Universidad de Concepción

Facultad de ciencias naturales y oceanográficas

Doctorado en Oceanografía

ROL DEL OCÉANO Y EL CLIMA EN LA MODULACIÓN DEL GRADIENTE LATITUDINAL DEL RADIOCARBONO ATMOSFÉRICO EN EL HEMISFERIO SUR

Tesis presentada a la Facultad de Ciencias Naturales y Oceanográficas de la Universidad de Concepción para optar al grado de Doctor en Oceanografía

POR SANTIAGO EDUARDO ANCAPICHÚN HERNÁNDEZ

Profesor Guía Ricardo Hernan De Pol Holz

Abril 2022

Concepción, Chile

DEDICATORIA

La presente tesis se la dedico a Loreto Morales y Santiago Ancapichún Hernández

AGRADECIMIENTOS

A mi familia por su apoyo y amor incondicional.

A Loreto por estar a mi lado en las buenas y malas, por escucharme y ayudarme a ver más allá siempre.

Al Dr. Ricardo De Pol Holz por ser mi apoyo académico; por las oportunidades y experiencias que van mucho más allá de lo académico.

A la Dra. Silvana Collado y al Dr. Duncan Christie por su apoyo académico durante el desarrollo de la tesis.

A todas las personas que me ayudaron en mi formación inicial, partiendo por los Drs. José Garcés-Vargas y Patricio Manriquez, quienes me mostraron los quehaceres de un científico.

A las fuentes de financiamiento estatal: Beca Doctorado Nacional CONICYT Nº 21140422 y FONDECYT 11150710. Y por lo tanto, a todos los que componen y hacen girar los engranajes de este modesto pero aguerrido país.

A la Universidad de Magallanes por su constante apoyo científico y técnico durante mi formación.

TABLA DE CONTENIDO

ÍNDICE DE ILUSTRACIONES

RESUMEN GENERAL

ROL DEL OCÉANO Y EL CLIMA EN LA MODULACIÓN DEL GRADIENTE LATITUDINAL DEL RADIOCARBONO ATMOSFÉRICO EN EL HEMISFERIO SUR.

Por Santiago Eduardo Ancapichún Hernández.

Profesor Guía: Ricardo De Pol Holz

Director de Tesis: Wolfgang Schneider

Fecha: 03/01/2022

Del total global de átomos de carbono (C), el 98.89% son átomos de ^{12}C (isótopo liviano), 1.11% de ^{13}C (isótopo pesado no radiactivo) y solo un 10^{-10} % corresponden a átomos de ^{14}C (isótopo pesado radiactivo). El átomo de ^{14}C tiene una tasa de decaimiento radiactivo que es constante y aleatoria. Al decaer, se desintegra en partículas beta (-β) y átomos de nitrógeno. Cuando el átomo de ^{14}C atmosférico es asimilado por algún ser vivo en sus estructuras sólidas, la concentración del ^{14}C de estas estructuras disminuye a través del tiempo debido al decaimiento radiactivo, lo que se asocia a un envejecimiento. Al utilizar una curva de calibración, el ^{14}C ha sido ampliamente utilizado para datar materia orgánica.

Los árboles asimilan los isótopos de C formando anillos de crecimiento anuales, los cuales registran las proporciones isotópicas atmosféricas de C, siendo claves para la construcción de las curvas de calibración. Es así como los anillos de árboles son excelentes testigos de la variabilidad a través del tiempo del ^{14}C atmosférico. En este sentido, se han constatado tres mecanismos naturales que modulan la variabilidad del ^{14}C atmosférico: i) la producción de ^{14}C en la estratósfera-baja, ii) el intercambio de C entre reservorios y iii) el transporte y mezcla de parcelas de aire. Por otro lado, existen dos mecanismos/eventos antropogénicos que han afectado significativamente los niveles de $\Delta^{14}C$ atmosférico (que es la proporción ^{14}C:^{12}C corrigiendo el fraccionamiento isotópico dependiente de la masa y reincorporando el ^{14}C perdido producto del decaimiento radiactivo): i) la quema de combustibles fósiles y ii) la detonación de armas termonucleares. De este modo, los anillos de crecimiento anuales de los árboles han sido utilizados para el estudio de estos mecanismos. No obstante, en las costas de Sudamérica frente al océano Pacífico Sudoriental, no existen registros de ^{14}C atmosférico, siendo una interrogante i) las concentraciones de ^{14}C atmosférico presentes en esta región, ii) su variabilidad a través del tiempo y iii) los principales mecanismos que la modulan.

La presente tesis, además de mejorar significativamente las curvas de calibración del hemisferio sur, estudió la variabilidad a través del tiempo y los

principales mecanismos que afectan al $\Delta^{14}C$ atmosférico frente al océano Pacífico Sudoriental, a través del estudio de cuatro nuevos registros de $\Delta^{14}C$ atmosférico.

De este modo, se encontró la ocurrencia de un notable gradiente latitudinal de $\Delta^{14}C$ atmosférico positivo de norte a sur a lo largo de las costas de Sudamérica occidental, el cual presentó ciertas excepciones asociadas al efecto del transporte y mezcla de parcelas de aire y al intercambio de C entre reservorios. Se determinó que los principales moduladores de las concentraciones de $\Delta^{14}C$ atmosférico de Sudamérica tropical fueron el intercambio de carbono entre la atmósfera, la biósfera amazónica y el océano subtropical y los patrones de circulación atmosférica tropical. Por otro lado, la surgencia de aguas profundas y viejas, empobrecidas en ^{14}C debido al decaimiento radioactivo, afectaron significativamente los niveles de $\Delta^{14}C$ atmosférico sobre el océano austral disminuyendo los niveles de $\Delta^{14}C$. Los niveles de $\Delta^{14}C$ atmosférico de las latitudes medias y altas del hemisferio sur permitieron estudiar en detalle la variabilidad a través del tiempo de las emisiones de CO_2 del océano austral. De este modo, se encontró una notable, y sin precedentes, variabilidad interanual de las emisiones de CO_2 del océano austral.

Concluimos que las concentraciones de ^{14}C atmosférico a lo largo del océano Pacífico Sudoriental trazan importantes mecanismos del sistema climático terrestre como lo son i) el flujo del carbono entre la atmósfera, biósfera e

hidrósfera, ii) los patrones de circulación atmosférica y iii) la surgencia de aguas profundas y viejas del océano austral.

ABSTRACT

OCEAN AND CLIMATE ROLE ON THE MODULATION OF THE LATITUDINAL ATMOSPHERIC RADIOCARBON GRADIENT IN THE SOUTHERN HEMISPHERE

By Santiago Eduardo Ancapichún Hernández.

Professor guide: Ricardo De Pol Holz

Thesis director: Wolfgang Schneider

Date: 03/01/2022

The most abundant carbon (C) isotope is the ^{12}C (light isotope, 98.89 %), the ^{13}C represents 1.11 % of all C isotopes (heavy isotope), and ^{14}C is the 10^{-10} % of all C isotopes (radioactive-heavy isotope). The ^{14}C atom has a constant decay rate through aleatory radioactive B-decay. Atmospheric ^{14}C atom is assimilated into all biological life. Then, the ^{14}C concentration in organic materials decreases over time because of the radioactive decay once assimilation stops. This ^{14}C level decrease is associated with aging. The ^{14}C has been widely used to date organic materials. Trees assimilate C isotopes to form grown annual rings, which record the atmospheric C isotopic proportion and are key for calibration curve construction.

Thereby, the tree rings are excellent witnesses of the atmospheric ^{14}C variability through time. In this sense, three natural mechanisms that modulate atmospheric ^{14}C variability have been found: i) ^{14}C production in the low-

stratosphere, ii) C exchange between reservoirs, and iii) air parcels transport and mixing. On the other hand, there are two anthropogenic mechanisms/events that have been affected atmospheric $\Delta^{14}C$ levels (the deviation from an atmospheric standard and corrected for fractionation): i) burning of ^{14}C-free fossil fuel and ii) thermonuclear detonations. Thereby, annual tree rings have been widely used to study these mechanisms. However, atmospheric ^{14}C records along the margins of the southeast Pacific Ocean are lacking, which beg the question how i) atmospheric ^{14}C concentration in this region, ii) its atmospheric ^{14}C variability, and iii) mostly important mechanisms that modulate atmospheric ^{14}C concentration in this region.

The present thesis improves the Southern Hemisphere calibration curve through the development of four new atmospheric $\Delta^{14}C$ records. Moreover, this thesis studied the variability through time and the most important mechanism that affected atmospheric $\Delta^{14}C$ levels in the Southeast Pacific Ocean.

We found a noticeable latitudinal atmospheric $\Delta^{14}C$ gradient, positive north to south along the coast of western South America, which presents some exceptions associated with air parcels mixing and transport and the C exchange between reservoirs. We determine that the principal modulators of atmospheric $\Delta^{14}C$ levels from tropical South America were the C exchange between the atmosphere, the amazon biosphere, and subtropical ocean, and the atmospheric circulation patterns. On the other hand, the upwelling of old and

deep water, ^{14}C-poor because of radioactive decay, significantly affected the atmospheric $\Delta^{14}C$ concentrations above the Southern Ocean, decreasing the $\Delta^{14}C$ levels. The atmospheric $\Delta^{14}C$ concentration of Southern Hemisphere mid and high latitudes allows us to study in deep the variability through the time of the Southern Ocean CO_2 emissions. Thereby, we found a noticeable, and without precedents, interannual variability of the Southern Ocean CO_2 emissions.

We conclude that the atmospheric ^{14}C concentration along the southeastern Pacific Ocean traces important mechanisms of the earth climatic system such as i) the C fluxes between atmosphere, biosphere, and hydrosphere, ii) the atmospheric circulation patterns, and iii) the upwelling of old and deep waters in the Southern Ocean.

1 INTRODUCCIÓN GENERAL

Del total global de átomos de carbono (C), el 98.89% son átomos de ^{12}C (isótopo liviano), 1.11% de ^{13}C (isótopo pesado no radiactivo) y solo un 10^{-10} % corresponden a átomos de ^{14}C (isótopo pesado radiactivo) (Schuur et al. 2016). El átomo de ^{14}C tiene una tasa de decaimiento radiactivo que es constante y aleatoria. Al decaer, se desintegra en partículas beta (-β) y átomos de nitrógeno. Willard Frank Libby y colaboradores diseñaron un método con el cual se establece la edad de estructuras biológicas sólidas de acuerdo a su proporción isotópica ^{14}C:^{12}C. Cuando el átomo de ^{14}C atmosférico es asimilado por algún ser vivo (edad cero), y es incorporado para formar estructuras sólidas (huesos, anillos de árboles, etc.), la concentración del ^{14}C de estas estructuras disminuye a través del tiempo debido al decaimiento radiactivo, lo que se asocia a un envejecimiento (Libby 1952). Con el objetivo de estimar la edad aproximada de estas estructuras biológicas sólidas, su concentración de ^{14}C es medida y comparada con una curva de calibración. Las curvas de calibración se basan en las concentraciones de ^{14}C de estructuras sólidas de edades conocidas, como por ejemplo los anillos de crecimiento de los árboles.

Los árboles asimilan los isótopos de C formando anillos de crecimiento anuales, los cuales registran las proporciones isotópicas atmosféricas de C presentes durante la temporada de crecimiento. Es así como los anillos de árboles son excelentes testigos de la variabilidad a través del tiempo del ^{14}C atmosférico (Stuiver y Braziunas 1993; Schuur et al. 2016). Además de ser útiles para la datación de materia orgánica, las concentraciones de ^{14}C atmosféricas registradas por anillos de árboles son un poderoso trazador de distintos mecanismos naturales y artificiales. Con el objetivo de trazar la variabilidad de ^{14}C atmosférico modulada por mecanismos naturales y artificiales, las proporciones isotópicas ^{14}C:^{12}C se expresan como $\Delta^{14}C$. A pesar de que el $\Delta^{14}C$ se puede definir de muchas formas, con ecuaciones y simbologías diversas, los componentes de estas ecuaciones son los mismos, resultando en la convergencia del resultado final (el valor de $\Delta^{14}C$) (Stuiver y Polach 1977). Con el objetivo de definir de forma sencilla e intuitiva al $\Delta^{14}C$, aquí nosotros definimos al $\Delta^{14}C$ como la proporción ^{14}C:^{12}C corrigiendo el fraccionamiento isotópico dependiente de la masa (basado en ^{13}C) y reincorporando el ^{14}C perdido producto del decaimiento radiactivo (Stuiver y Polach 1977) (ver metodología del capítulo I). En este sentido, se han constatado tres mecanismos naturales que modulan la variabilidad del $\Delta^{14}C$ atmosférico: i) la producción de ^{14}C en la estratosfera-baja, ii) el intercambio de

C entre reservorios y iii) el transporte y mezcla de parcelas de aire. Por otro lado, existen dos mecanismos/eventos antropogénicos que han afectado significativamente los niveles de $\Delta^{14}C$ atmosférico: i) la quema de combustibles fósiles y ii) la detonación de armas termonucleares.

En la naturaleza, el ^{14}C se produce en la estratósfera-baja y troposfera-alta, como resultado de la interacción entre los átomos de nitrógeno y los rayos cósmicos (Masarik y Beer 1999). La producción natural de ^{14}C es modulada principalmente por la actividad solar y el campo magnético terrestre (Stuiver et al. 1991; Stuiver y Braziunas 1993; Hughen et al. 2004). Una vez producido el átomo de ^{14}C, éste es oxidado rápidamente a dióxido de carbono ($^{14}CO_2$) y es desplazado de la estratósfera-baja a la troposfera durante los meses de primavera, a través de la circulación atmosférica. El aporte primaveral de ^{14}C de la estratósfera-baja a la troposfera es un importante mecanismo natural que modula las concentraciones de ^{14}C atmosférico, el cual ocurre en latitudes altas y medias. Es conocido que la asimetría interhemisférica de este mecanismo es muy pequeña (Levin et al. 2010), por lo que no afecta a los gradientes inter-hemisféricos de $\Delta^{14}C$ atmosférico. Es así como, tanto las concentraciones de ^{14}C atmosférico del hemisferio Norte (INTCAL20; Reimer et al. 2020) como las del hemisferio Sur (SHCAL20; McCormac et al. 2013; Hogg et al. 2020), presentan una variabilidad multidecadal muy similar entre sí durante el periodo

preindustrial (antes de 1830), la cual es modulada principalmente por este mecanismo (figura 1) (Stuiver y Quay 1981). Subsecuentemente, en la troposfera, el $^{14}CO_2$ es incorporado al ciclo global del C, el cual continuamente intercambia C entre los distintos reservorios: la atmósfera, litósfera, biósfera e hidrósfera (Randerson et al. 2002; Levin et al. 2010). Por lo tanto, debido a que el ^{14}C se produce en la estratósfera-baja, en la atmósfera se encuentra la mayor proporción isotópica ^{14}C:^{12}C del planeta (en condiciones naturales).

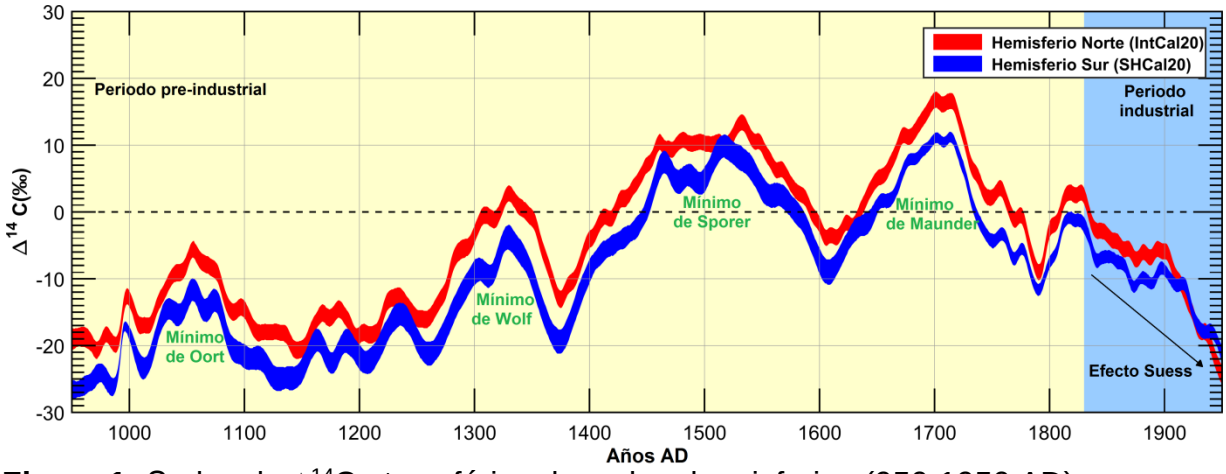

Figura 1: Series de $\Delta^{14}C$ atmosférico de ambos hemisferios (950-1950 AD), con una resolución temporal de cinco años. La línea gruesa de color rojo representa los valores de $\Delta^{14}C$ atmosférico del hemisferio norte (± 1 σ; IntCal20; Reimer et al. 2020), mientras que la línea gruesa azul representa los valores de $\Delta^{14}C$ atmosférico del hemisferio sur (± 1 σ; SHCal20; Hogg et al. 2020). El área de color pastel muestra el periodo de tiempo que corresponde al periodo pre-industrial (1830 hacia el pasado). El área azul claro muestra el periodo industrial (1830 a 1950). Además se indica el momento aproximado en el que ocurrieron los mínimos solares (letras color verde), los cuales modularon las concentraciones de ^{14}C atmosférico.

El intercambio de carbono entre reservorios es otro importante mecanismo natural que ha afectado los niveles de $\Delta^{14}C$ atmosférico. El reservorio de C atmosférico intercambia C con la litósfera, biósfera e hidrósfera, lo que afecta bilateralmente los niveles de $\Delta^{14}C$ de cada reservorio. En el océano austral, la variabilidad del $\Delta^{14}C$ atmosférico es modulada por la surgencia oceánica de aguas profundas, las cuales provienen de la superficie del océano Atlántico, se han hundido y han sido transportadas a través de la circulación termohalina durante cientos a miles de años (Weaver et al. 1993; Braziunas et al. 1995). Estas aguas profundas y viejas son ricas en carbono inorgánico disuelto (CID) debido a la acción de la bomba biológica (Damon et al. 1989; Manning et al. 2002; Rodgers et al. 2011). Estas antiguas masas de agua al volver a estar en contacto con la atmósfera, intercambian enormes cantidades de dióxido de carbono (CO_2) con la troposfera debido al efecto de los fuertes vientos australes (Schimel et al. 2001; Feely et al. 1999; Rodgers et al. 2011). El CID oceánico presenta un valor de $\Delta^{14}C$ menor que el atmosférico, debido al decaimiento radiactivo del ^{14}C (figura 2). De este modo, la mezcla del CO_2 de origen oceánico con el C atmosférico, provoca una disminución en los valores del $\Delta^{14}C$ atmosférico austral (Braziunas et al. 1995).

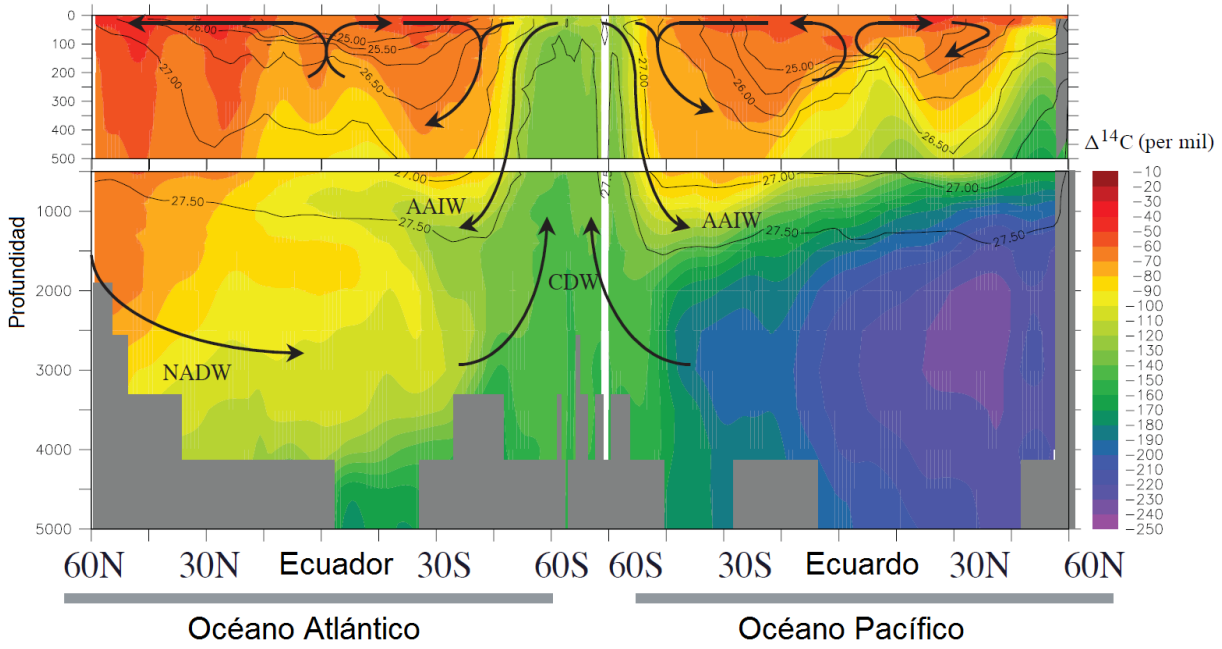

Figura 2: Modelación de los niveles de $\Delta^{14}C$ a lo largo de los océanos Pacífico y Atlántico para el periodo pre-bomba (per mil). Figura extraída de Rodgers et al. (2011), basada en la modelación de Key et al. (2004) de los datos de GLODAP (Olsen et al., 2020). Además, se observan se observan las distintas masas de agua que afectan los niveles de $\Delta^{14}C$ del océano austral: Agua intermedia antártica (AAIW), agua circumpolar profunda (CDW), y agua profunda del Atlántico norte (NADW).

Al analizar series de tiempo de $\Delta^{14}C$ en anillos de árboles de todo el globo, estudios previos han observado una notable diferencia de $\Delta^{14}C$ atmosférico entre el hemisferio norte y el hemisferio sur (figura 1; Siegenthaler et al. 1980;

Stuiver y Quay 1980; Reimer et al. 2004), donde el hemisferio norte ha presentado valores de $\Delta^{14}C$ atmosférico mayores que el hemisferio sur. Rodgers et al. (2011) estudiaron este gradiente inter-hemisférico para el periodo 950-1830 utilizando modelos acoplados océano-atmosféricos, determinando que la variabilidad de la diferencia de $\Delta^{14}C$ inter-hemisférica observada se explica por el intercambio de CO_2 de origen oceánico-austral con la atmósfera, y el efecto sobre el intercambio de C océano-atmósfera de la velocidad y estrés del viento. Su modelo-acoplado evidenció que la disminución del gradiente inter-hemisférico durante el periodo de transición entre la anomalía cálida medieval y la pequeña edad del hielo (año 1375), puede explicarse por una disminución del estrés y la velocidad del viento sobre el océano austral. Esto provocó un menor intercambio de CO_2 entre el océano (con bajos valores de $\Delta^{14}C$) y la atmósfera, lo que disminuyó la magnitud del gradiente inter-hemisférico de 6.63 a 4.48 ‰. Por otro lado, la biósfera terrestre es otro importante reservorio de C, el cual afecta los niveles de $\Delta^{14}C$ atmosférico al intercambiar CO_2 con la atmósfera (Stuiver y Braziunas 1993; Randerson et al. 2002; Levin et al. 2010; Graven et al. 2012). Dependiendo de la ubicación latitudinal, los bosques presentan distintas velocidades de asimilación y respiración del CO_2. Estas diferencias en las velocidades de intercambio de C pueden producir cambios en los niveles de $\Delta^{14}C$ atmosférico (Randerson et al. 2002). Una vez asimilado en sus estructuras biológicas sólidas, el C demora

algunos años en ser respirado (reingresado a la atmósfera), y si el $\Delta^{14}C$ reingresado tiene un valor distinto al valor 'actual' de $\Delta^{14}C$ atmosférico, su reintegración podría producir variaciones sobre el $\Delta^{14}C$ atmosférico local (Randerson et al. 2002; Levin et al. 2010).

El tercer mecanismo natural que ha afectado al $\Delta^{14}C$ atmosférico, es el transporte y mezcla de parcelas de aire, el cual puede causar una concentración inusual de ^{14}C en una región y un tiempo determinado, no afectando al equilibrio de gran escala (Hua et al. 2004). Hua y colaboradores (2004), especularon sobre este mecanismo y sus posibles implicancias, pero no lograron cuantificar su efecto sobre el $\Delta^{14}C$ atmosférico. Posteriormente, Hua y Barbetti (2007) determinaron el efecto del transporte y mezcla de parcelas de aire sobre el $\Delta^{14}C$ atmosférico tropical del hemisferio norte, concluyendo que el aporte de masas de aire provenientes del hemisferio sur disminuyen los niveles de $\Delta^{14}C$ en latitudes tropicales del hemisferio norte. Luego, Hua et al. (2012) evidenciaron el efecto de este mecanismo sobre el $\Delta^{14}C$ atmosférico en el hemisferio sur (Indonesia). El registro que analizaron presentó valores anuales de $\Delta^{14}C$ mayores en comparación a otros registros del hemisferio sur. Esta diferencia la atribuyeron a la influencia del monzón de invierno asiático, el cual transportó parcelas de aire con altos niveles de $\Delta^{14}C$ atmosférico provenientes del hemisferio norte hacia Indonesia, enriqueciendo en ^{14}C a los anillos de

árboles de esta región. A diferencia de los otros mecanismos, el efecto del transporte y mezcla de parcelas de aire sobre el $\Delta^{14}C$ atmosférico es difícil de cuantificar, por ello no ha sido estudiado en detalle.

Respecto a los mecanismos/eventos antropogénicos que afectan las concentraciones de ^{14}C atmosférico, la quema de combustibles fósiles es un fuerte modulador de las concentraciones de ^{14}C atmosférico. La quema de combustibles fósiles comenzó durante el inicio de la revolución industrial, aproximadamente entre 1820 y 1840, lo que provocó la liberación hacia la atmósfera de grandes cantidades de CO_2. El CO_2 liberado por la quema de combustibles fósiles tiene una nula concentración de ^{14}C (Suess 1955). Esta nula concentración de ^{14}C ocurre debido a que el tiempo de formación del petróleo (millones de años) es mucho mayor al tiempo en que los átomos de ^{14}C decaen completamente (la probabilidad de que un átomo de ^{14}C no haya decaído en 57300 años es de 0.1%) (Schuur et al. 2016). Al mezclarse este CO_2 de origen fósil con el C atmosférico, la atmósfera se envejece aparentemente al disminuir sus proporciones ^{14}C:^{12}C, al igual que los valores de $\Delta^{14}C$ (McCormac et al. 1998; Marland 2008). Suess (1955) probó este mecanismo, mostrando la ocurrencia de una tendencia negativa del $\Delta^{14}C$ atmosférico entre 1820 y 1954 (figura 1). Hoy esta tendencia negativa de $\Delta^{14}C$ atmosférico producida por la quema de combustibles fósiles se conoce como

‘’efecto Suess’’. De este modo, se ha establecido que el $\Delta^{14}C$ atmosférico es un poderoso trazador de las emisiones de CO_2 producto de la quema de combustibles fósiles (Randerson et al. 2002; Turnbull et al. 2009; Graven et al. 2012; Hou et al. 2020; Niu et al. 2021).

Otro mecanismo/evento antropogénico que ha afectado los niveles de $\Delta^{14}C$ atmosférico han sido las detonaciones termonucleares atmosféricas ocurridas, en su mayoría, en el hemisferio norte. Estas ocurrieron principalmente durante los años 1945 y 1963, afectando fuertemente los niveles de $\Delta^{14}C$ atmosférico durante el periodo bomba (1945-1985; Enting 1982). No obstante, se observó un incremento significativo del $\Delta^{14}C$ atmosférico entre los años 1954 y 1955 (Reimer et al. 2004; Hua et al. 2013). Estas detonaciones liberaron partículas similares a los rayos cósmicos, que generaron enormes cantidades de ^{14}C, acumulando ^{14}C en la estratósfera (Hesshaimer y Levin 2000). El exceso de ^{14}C estratosférico ingresó a latitudes altas y medias de la troposfera del hemisferio norte, durante los meses de primavera, a través de la circulación atmosférica (Stuiver et al. 1991). Luego, el exceso de ^{14}C fue transportado gradualmente hacia latitudes más australes. Una vez en la troposfera Ecuatorial, el exceso de ^{14}C fue transportado hacia el hemisferio sur, evidenciando un tiempo de mezcla inter-hemisférico de alrededor de un año (Lal y Rama 1966; Nydal 1968). De este modo, un gran y persistente gradiente

latitudinal de $\Delta^{14}C$ atmosférico fue observado en todo el globo durante los años 1955-1972, el cual se reconoce como un periodo de máximos gradientes latitudinales (Hua et al. 2013).

Con el objetivo de disponer de curvas de calibración para datar la materia orgánica y el estudio del ciclo global de C después de 1950, Hua y colaboradores (2013) establecieron distribuciones zonales homogéneas de $\Delta^{14}C$ atmosférico para el periodo bomba, dividiendo latitudinalmente al globo en 5 zonas. Ellos describieron al hemisferio sur extra tropical (zona SH 1-2) como una región en que el $\Delta^{14}C$ troposférico presentó valores homogéneos durante el periodo bomba (figura 3). Sin embargo, en sus datos de $\Delta^{14}C$ atmosférico de la zona SH 1-2 no se dispuso de ningún registro dendrocronológico ubicado en Sudamérica ni en latitudes australes del hemisferio sur (45-65ºS). Esta homogeneidad del $\Delta^{14}C$ atmosférico planteada por Hua et al. (2013), se contrapone a lo observado por Stuiver y Braziuras (1998), para el periodo pre-bomba, en donde encontraron un patrón heterogéneo en los valores de $\Delta^{14}C$ atmosférico austral. Por lo tanto, para dilucidar esta disyuntiva es indispensable disponer de nuevos registros de $\Delta^{14}C$ atmosférico, de alta resolución temporal y de distintas regiones del hemisferio sur.

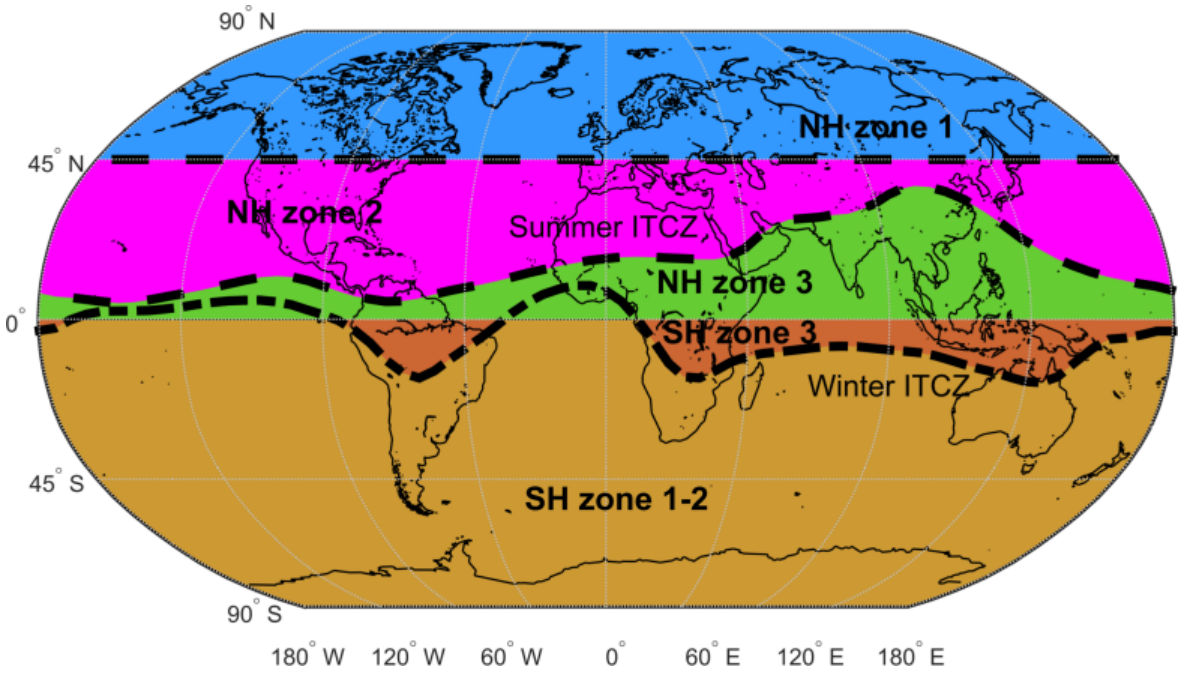

Figura 3: Globo dividido en cinco zonas con valores de $\Delta^{14}C$ atmosférico significativamente distintos (1950-1985; Hua et al. 2013). Latitudes septentrionales presentan los valores más elevados de $\Delta^{14}C$ atmosférico, mientras que latitudes más australes presentan los valores más bajos de $\Delta^{14}C$ atmosférico. De acuerdo a Hua et al. (2013), en latitudes medias y tropicales los valores de $\Delta^{14}C$ atmosférico son modulados por la circulación atmosférica (ITCZ de verano e invierno).

En el hemisferio norte, el $\Delta^{14}C$ atmosférico alcanzó un valor máximo (*Bomb-peak*) a mediados del año 1963 ($\Delta^{14}C$ = 980 ‰; Hua et al. 2013),

mientras que en el hemisferio sur, el $\Delta^{14}C$ atmosférico alcanzó un valor máximo a fines del año 1965 ($\Delta^{14}C$ = 671 ‰; Hua et al. 2013). Luego de alcanzar el valor máximo, el $\Delta^{14}C$ atmosférico comenzó a declinar debido a una paulatina disminución de las detonaciones termonucleares atmosféricas, y a la acción del intercambio de C entre la atmósfera y los otros reservorios de carbono, como el océano y la biósfera (Randerson et al. 2002). El océano y la biósfera han removido paulatinamente el ^{14}C-bomba de la atmósfera, a través de la formación de aguas profundas y asimilación de isótopos de ^{14}C en estructuras biológicas sólidas, entre otros. A su vez, la quema de combustibles fósiles también contribuyó a la disminución de los valores de $\Delta^{14}C$ atmosférico, lo cual fue más evidente durante el periodo post-bomba (1985 al presente) (Levin et al. 2010; Graven et al. 2012; Hou et al. 2020; Niu et al., 2021).

Durante el periodo bomba la diferencia de $\Delta^{14}C$ entre la atmósfera y los otros reservorios de carbono se amplificó, lo cual provocó que el intercambio de C entre reservorios amplificara su efecto sobre $\Delta^{14}C$ atmosférico (Kromer et al. 2001; Randerson et al. 2002; Levin et al. 2010; Graven et al. 2012). El *isoflux* es un término utilizado para trazar el efecto del intercambio de C entre la atmósfera y otros reservorios de C. El *isoflux* es el producto del flujo de CO_2 en una dirección y la diferencia isotópica entre la fuente (o sumidero) y la atmósfera (Schuur et al. 2016). Para el caso del intercambio de C océano-atmósfera,

durante el periodo pre-bomba, el *isoflux* global océano-atmósfera era pequeño y negativo de aproximadamente -5500 (Pg C ‰ $year^{-1}$), el cual causaba una disminución del $\Delta^{14}C$ global de 9 ‰ $year^{-1}$. No obstante, durante el periodo bomba, se amplificó el *isoflux* global océano-atmósfera a aproximadamente -54000 (Pg C ‰ $year^{-1}$), causando una disminución del $\Delta^{14}C$ atmosférico global de 80 ‰ $year^{-1}$ (Heimann y Maier-Reimer 1996; Key et al. 2004). Para el caso del intercambio de C biósfera-atmósfera, durante el periodo pre-bomba, el *isoflux* global biósfera-atmósfera era pequeño y negativo de aproximadamente -235 (Pg C ‰ $año^{-1}$), el cual causaba una disminución del $\Delta^{14}C$ global de 0.4 ‰ $año^{-1}$. No obstante, durante el periodo bomba, se amplificó el *isoflux* global biósfera-atmósfera a aproximadamente -30000 (Pg C ‰ $year^{-1}$), causando una disminución del $\Delta^{14}C$ atmosférico global de 44 ‰ $year^{-1}$ (Naegler y Levin 2009). Al mismo tiempo, el exceso de ^{14}C bomba atmosférico también produjo la amplificación del mecanismo de transporte y mezcla de parcelas de aire, en donde parcelas de aire provenientes del norte tuvieron una mayor concentración de ^{14}C que las masas de aire provenientes del sur (Hua et al. 2012).

A pesar de que el $\Delta^{14}C$ atmosférico registrado en los anillos de los árboles es indispensable para construir una confiable curva de calibración y que estos registros de ^{14}C pueden trazar importantes mecanismos climáticos y

eventos antropogénicos, actualmente no existen registros de $\Delta^{14}C$ atmosférico durante el periodo bomba y post-bomba en las costas de Sudamérica occidental. Debido a esto, las particularidades regionales del $\Delta^{14}C$ atmosférico en el Pacífico Sudoriental son una incógnita, tanto para el periodo bomba como para el periodo post-bomba. La ausencia de registros anuales contemporáneos, limita nuestro entendimiento de los mecanismos que afectan al $\Delta^{14}C$ atmosférico en esta región del globo, lo que impide realizar un análisis completo de la variabilidad de los niveles del $\Delta^{14}C$ atmosférico del hemisferio sur y del globo y sus moduladores climáticos. De hecho, el Modo Anular del Sur (MAS; oscilación océano-atmosférica que afecta a todo el hemisferio sur; Marshall 2003), afecta a los campos de presiones extratropicales de todo el hemisferio sur (Marshall 2003; Ancapichún y Garcés 2015). Cuando el MAS está en su fase positiva, las presiones de latitudes medias (40ºS) aumentan, provocando una intensificación de los anticiclones de esta franja, que modulan diversos eventos océano-atmosféricos. Además, un MAS positivo produce divergencia del transporte superficial cercano a la Antártida (surgencia oceánica), aumento de la intensidad de los vientos del oeste y aceleración de la corriente circumpolar (Thompson et al. 2011; DeVries et al. 2017). De hecho, recientes estudios han reportado los fuertes efectos del MAS sobre el intercambio de carbono océano-atmosférico, modulando el secuestro de CO_2 atmosférico de origen antropogénico y la emisión de CO_2 pobre en ^{14}C de origen oceánico (Le

Quéré et al. 2007; DeVries et al. 2017). Por otro lado, Turney y Palmer (2007) hipotetizaron que las variaciones en la surgencia ecuatorial, y el intercambio de carbono océano-atmósfera, influenciadas por El-Niño Oscilación del Sur (ENOS) podrían haber modulado al gradiente interhemisférico de $\Delta^{14}C$ atmosférico durante el periodo pre-industrial. Por lo tanto, el MAS o ENOS podrían modular las concentraciones de $\Delta^{14}C$ atmosférico en las costas de Sudamérica occidental, forzando al transporte y mezcla de parcelas de aire y el intercambio de carbono entre reservorios durante el periodo bomba y post-bomba.

Considerando lo mencionado anteriormente, a través del desarrollo de cuatro nuevos registros de $\Delta^{14}C$ atmosférico frente al Océano Pacífico Sudoriental, la presente tesis inicialmente evaluará si el conocimiento actual del $\Delta^{14}C$ atmosférico aplica para el océano Pacífico Sudoriental: i) bajos valores de $\Delta^{14}C$ atmosférico respecto al hemisferio norte durante el periodo bomba, y ii) ausencia de un gradiente latitudinal durante el periodo bomba sobre el océano Pacífico Sudoriental. Posteriormente, se determinarán los principales mecanismos climáticos que han afectado al $\Delta^{14}C$ atmosférico en Sudamérica occidental. **En particular, estudiaremos la relación que existe entre el $\Delta^{14}C$ atmosférico y los mecanismos que lo modulan, como el transporte y mezcla de parcelas de aire y el intercambio de C entre reservorios.** De este

modo, dado que algunas especies árboles chilenos pueden presentar dendrocronologías de varios miles de años (Lara y Villalba 1993), esta tesis representa el primer esfuerzo en desarrollar el potencial como trazador paleoclimático de los registros de $\Delta^{14}C$ atmosférico frente al océano Pacífico Sudoriental.

El objetivo general de la presente tesis es estudiar el rol del océano y el clima en la modulación del gradiente latitudinal del radiocarbono atmosférico en el hemisferio sur.

2 HIPÓTESIS Y OBJETIVOS ESPECÍFICOS.

Preguntas de investigación:

I) ¿Existe un gradiente latitudinal positivo de norte a sur en el océano Pacífico Sudoriental durante el periodo bomba?

II) ¿Cuáles son los principales mecanismos que influencian la variabilidad del $\Delta^{14}C$ atmosférico sobre el océano Pacífico Sudoriental?

III) ¿Existe alguna asociación entre la variabilidad del $\Delta^{14}C$ atmosférico en las costas chilenas y alguna oscilación climática del océano Pacífico Sudoriental?

Para poner a prueba el conocimiento actual del $\Delta^{14}C$ atmosférico en el hemisferio sur, se plantearon las siguientes hipótesis y objetivos específicos.

H1: Debido al efecto del océano Austral sobre los niveles de $\Delta^{14}C$ atmosférico, esperamos que los niveles de $\Delta^{14}C$ atmosférico de registros

australes tengan bajos valores en comparación a registros más septentrionales. De este modo, se podría observar un gradiente latitudinal de $\Delta^{14}C$ atmosférico estadísticamente significativo sobre el océano Pacífico Sudoriental durante el periodo bomba y post-bomba.

H2: El principal mecanismo que afectaría al $\Delta^{14}C$ atmosférico sobre el océano Pacífico Sudoriental es el intercambio de carbono entre reservorios, principalmente el intercambio de carbono atmósfera-océano dependiente del viento.

H3: La oscilación océano-atmosférica que mayormente modula la variabilidad del $\Delta^{14}C$ atmosférico sobre el Pacífico Sudoriental es el MAS, debido a su fuerte influencia sobre el Anticiclón del Pacífico Sur y el océano austral, modulando la surgencia de aguas profundas y pobres en radiocarbono y el intercambio de carbono océano-atmósfera.

Para evaluar las hipótesis mencionadas anteriormente en relación a la variabilidad del $\Delta^{14}C$ atmosférico y los mecanismos océano-atmosféricos que lo podrían modular, presentamos los siguientes objetivos específicos:

I. Estudiar a las diferencias de $\Delta^{14}C$ atmosférico entre distintas regiones del hemisferio sur, a través de diversas herramientas estadísticas.

II. Estudiar la influencia de los principales mecanismos moduladores del $\Delta^{14}C$ atmosférico i. e. transporte y mezcla de parcelas de aire, intercambio de carbono entre reservorios, entre otros, sobre la variabilidad y los gradientes latitudinales del $\Delta^{14}C$ atmosférico en el hemisferio sur.

III. Determinar si la surgencia de aguas profundas y viejas, mayormente modulada por el modo anular del sur, ha influenciado la variabilidad de los niveles del $\Delta^{14}C$ atmosférico en el hemisferio sur y a su vez desarrollar el potencial del $\Delta^{14}C$ atmosférico para trazar las emisiones de CO_2 del océano austral.

3 DESCRIPCIÓN GENERAL DE MATERIAL Y MÉTODOS.

3.1 Nuevos registros de $\Delta^{14}C$ atmosférico

Con el objetivo de estudiar a variabilidad del $\Delta^{14}C$ atmosférico a lo largo del hemisferio sur, se recolectaron tarugos de distintas especies de árboles a lo largo de las costas de Chile (figura 3). Estas especies registraron el $\Delta^{14}C$ atmosférico en sus anillos de crecimiento anuales, abarcando los años 1950-2016: *Polylepis tarapacana* fue recolectado por el Dr. Duncan Christie (20ºS), *Austrocedrus chilensis* fue recolectado por el Dr. Carlos Le Quesne (32ºS), *Fitzroya cupressoides* fue recolectado por el Dr. Antonio Lara (40ºS) y *Pilgerodendron uviferum* fue recolectado por el Dr. Juan Carlos Aravena (53ºS). Posterior a la recolección, se continuó con la extracción de holocelulosa y la combustión de las muestras, en las instalaciones de la Universidad de Concepción. La grafitización y análisis de radiocarbono fueron realizados en las instalaciones de Keck AMS de la Universidad de California en Irvine por la Dra. Silvana Collado y el Dr. Ricardo De Pol Holz.

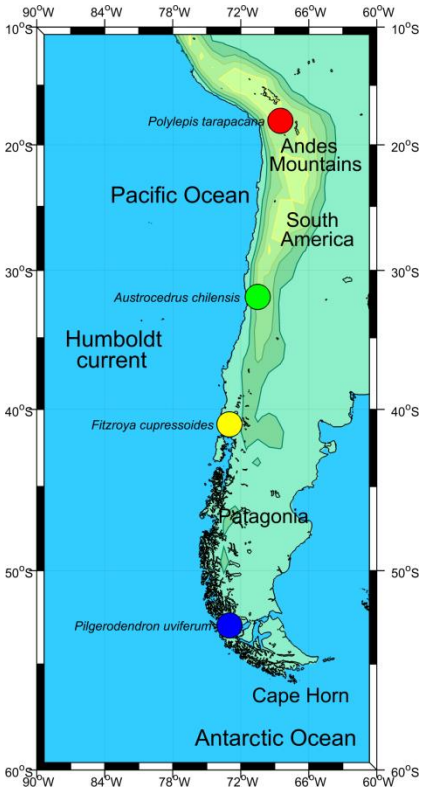

Figura 3: Océano Pacífico Sudoriental. Los círculos de colores representan la ubicación geográfica de cada dendrocronología utilizada: *Polylepis tarapacana* (20ºS, círculo rojo), *Austrocedrus chilensis* (32ºS, circulo verde), *Fitzroya cupressoides* (40ºS, amarillo) y *Pilgerodendron uviferum* (53ºS, circulo azul).

3.1.1 Registros de $\Delta^{14}C$ atmosférico en el hemisferio sur

Para estudiar la variabilidad del $\Delta^{14}C$ atmosférico a lo largo del hemisferio sur, se utilizaron registros y mediciones de otras regiones del hemisferio sur, como por ejemplo: i) Indonesia (5ºS; Hua et al. 2012), ii) Brasil (23º; Santos et

al. 2015), iii) Nueva Zelanda (41ºS; Turnbull et al. 2017) e iv) Islas Campbell (52ºS; Turney et al. 2018).

3.2 Modelo de transporte atmosférico

Para evaluar el mecanismo de transporte y mezcla de parcelas de aire y determinar la proveniencia geográfica del $^{14}CO_2$ almacenado en los anillos anuales de nuestros registros, se utilizó el modelo de transporte atmosférico Hybrid Single-Particle Lagrangian Integrated Trajectory (HYSPLIT) (Draxler y Taylor 1982; Draxler y Stunder 1988; Draxler y Hess 1998; Stein et al. 2015). El modelo HYSPLIT versión 4 es un completo sistema diseñado para calcular trayectorias simples y trayectorias hacia el pasado de las parcelas de aire, transporte atmosférico complejo, dispersión, transformaciones químicas y simulación de deposiciones. Los datos del reanálisis NCEP/NCAR fueron utilizados como datos de entrada para el modelo HYSPLIT (Kalnay et al. 1996).

3.3 Datos de reanálisis.

Con el objetivo de evaluar el mecanismo de transporte y mezcla de parcelas de aire y el intercambio de carbono entre reservorios, los datos de la presión del aire a nivel del mar (PA) y magnitud y dirección del viento (resolución espacial de 2.5º × 2.5º) se obtuvieron del proyecto de re análisis National Centers for Environmental Prediction/ National Center for Atmospheric Research (NCEP/NCAR). Este proyecto consiste en un modelo físico sometido a reajustes permanentes a través de la comparación entre datos in situ y satelitales de temperatura, vientos, presión y otros (Kalnay et al. 1996). Se utilizaron los datos de éste reanálisis debido a su alta confiabilidad y el periodo del que dispone, el cual es ideal para estudiar el periodo bomba (1945-1985).

3.4 Datos de flujo de CO_2 océano-atmósfera.

Para comparar nuestros resultados y evaluar el intercambio de carbono océano-atmósfera, se utilizaron las siguientes estimaciones del flujo de CO_2 océano-atmósfera basadas en distintas metodologías que abordan la reconstrucción de la pCO_2 sobre el océano: (i) modelo biogeoquímico acoplado a un modelo atmosférico de inversión que considera la profundidad de la capa de mezcla superficial del océano y mediciones de presión parcial de CO_2 sobre la superficie oceánica ($pCO_{2\ océano}$) (JENA-MLS: Rödenbeck et al. 2013), (ii) red

neuronal de un paso que relaciona no-linealmente a las variables de temperatura superficial, salinidad superficial, latitud, longitud y clorofila-a superficial con mediciones de $pCO_{2\ océano}$ (NIES-FNN; Zeng et al. 2014), iii) red neuronal de dos pasos, uno para desarrollar la climatología y otro para desarrollar las anomalías de $pCO_{2\ océano}$, el cual relaciona no-linealmente a la temperatura superficial, salinidad superficial, latitud, longitud, profundidad de la capa de mezcla, nivel del mar y clorofila-a superficial con mediciones de $pCO_{2\ océano}$ (CMEMS-FFNN; Devin-sommer et al. 2019), iv) estimación de $pCO_{2\ océano}$ usando *machine lerning*, con el cual se divide al océano en provincias biogeoquímicas a través del método *k-means* y luego se utilizan cuatro modelos estadísticos para ajustar los valores proyectados de $pCO_{2\ océano}$ con valores de mediciones *in situ* de $pCO_{2\ océano}$ (CSIR-ML6; Gregor et al. 2019), (v) modelos de regresiones lineales múltiples que asocian a la temperatura superficial, salinidad superficial, latitud, longitud, profundidad de la capa de mezcla, nivel del mar y clorofila-a superficial con el carbono inorgánico disuelto y mediciones de $pCO_{2\ océano}$ (JMA-MLR; Iida et al. 2020), vi) red neuronal de dos pasos acoplado a una división del océano en provincias biogeoquímicas para posteriormente relacionar diversas variables con mediciones de $pCO_{2\ océano}$ (MPI-SOMFFN; Landschützer et al. 2020).

4 RESULTADOS

4.1 Capítulo I

4.1.1Título manuscrito I: Radiocarbon bomb-peak signal in tree-rings from the tropical Andes register low latitude atmospheric dynamics in the Southern Hemisphere

Santiago Ancapichún[1], Ricardo De Pol-Holz[2*], Duncan A. Christie[3,4], Guaciara M. Santos[5], Silvana Collado-Fabbri[6], René Garreaud[4,7], Fabrice Lambert[4,8], Andrea Orfanoz-Cheuquelaf[4,7], Maisa Rojas[4,7], John Southon[5], Jocelyn C. Turnbull[9,10], and Pearce Paul Creasman[11]

[1]Postgraduate School in Oceanography, Faculty of Natural and Oceanographic Sciences, Universidad de Concepción, Concepción, Chile

[2]Centro de Investigación GAIA Antártica (CIGA) and Network for Extreme Environment Research (NEXER), Universidad de Magallanes, Punta Arenas, Chile

[3]Laboratorio de Dendrocronología y Cambio Global, Instituto de Conservación Biodiversidad y Territorio, Universidad Austral de Chile, Valdivia, Chile

[4]Center for Climate and Resilience Research (CR)[2], Chile

[5]Department of Earth System Science, University of California, Irvine, USA

[6]Fundación Crono Austral, Concepción, Biobio, Chile

[7]Department of Geophysics, Universidad de Chile, Santiago, Chile

[8]Department of Physical Geography, Pontificia Universidad Católica de Chile, Santiago, Chile

[9]GNS Science, Rafter Radiocarbon Laboratory, Lower Hutt, New Zealand

[10]CIRES, University of Colorado at Boulder, USA

4.1.2 Manuscrito publicado en Science of the total environment:

Ancapichún S, De Pol-Holz R, Christie DA, Santos GM, Collado-Fabbri S, Garreaud R, Lambert F, Orfanoz-Cheuquelaf A, Rojas M, Southon J, Turnbull JC, Creasman PP. 2021. Radiocarbon bomb-peak signal in tree-rings from the tropical Andes register low latitude atmospheric dynamics in the Southern Hemisphere. Science of the Total Environment 774:145126, doi:10.1016/j.scitotenv.2021.145126.

Declaración de contribución de Santiago Ancapichún Hernández.

Conceptualización, Metodología, Investigación, Análisis formal, escritura del draft original, Validación, Visualización, Investigación.

Graphical abstract

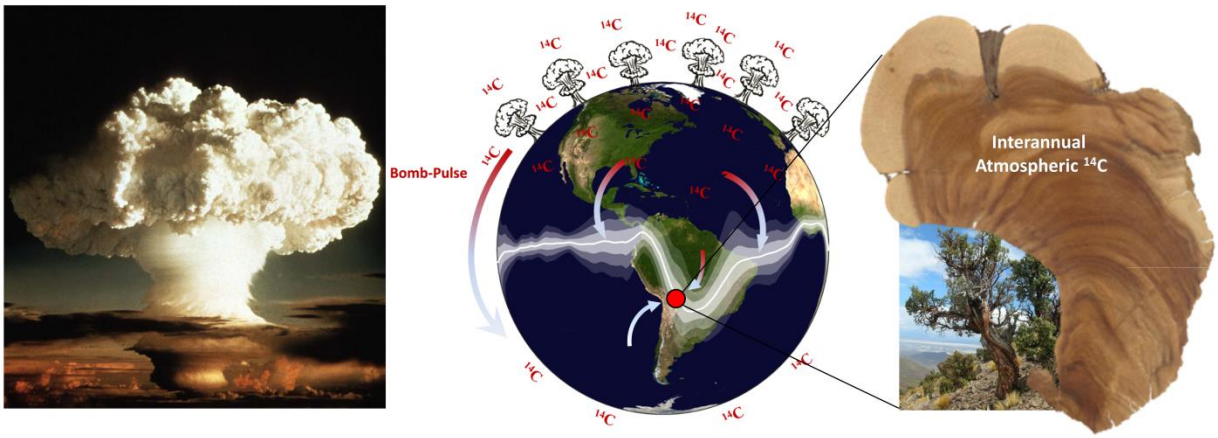

Abstract

South American tropical climate is strongly related to the tropical low-pressure belt associated with the South American monsoon system. Despite its central societal role as a modulating agent of rainfall in tropical South America, its long-term dynamical variability is still poorly understood. Here we combine a new (and world's highest) tree-ring ^{14}C record from the Altiplano plateau in the central Andes with other ^{14}C records from the Southern Hemisphere during the second half of the 20th century in order to elucidate the latitudinal gradients associated with the dissemination of the bomb ^{14}C signal. Our tree-ring ^{14}C record faithfully captured the bomb signal of the 1960's with an excellent match to atmospheric ^{14}C measured in New Zealand but with significant differences with a recent record from Southeast Brazil located at almost equal latitude.

These results imply that the spreading of the bomb signal throughout the Southern Hemisphere was a complex process that depended on atmospheric dynamics and surface topography generating reversals on the expected north-south gradient in certain years. We applied air-parcel modeling based on climate data to disentangle their different geographical provenances and their preformed (reservoir affected) radiocarbon content. We found that air parcel trajectories arriving at the Altiplano during the bomb period were sourced i) from the boundary layer in contact with the Pacific Ocean (41%), ii) from the upper troposphere (air above the boundary layer, with no contact with oceanic or continental carbon reservoirs) (38%) and iii) from the Amazon basin (21%). Based on these results we estimated the $\Delta^{14}C$ endmember values for the different carbon reservoirs affecting our record which suggest that the Amazon basin biospheric ^{14}C isoflux could have been reversed from negative to positive as early as the beginning of the 1970's. This would imply a much faster carbon turnover rate in the Amazon than previously modelled.

1. Introduction

Tree-rings have proven to faithfully record the ^{14}C content of the adjacent atmosphere, a powerful tracer for the study of atmospheric circulation, exchanges between carbon reservoirs such as the oceans and the biosphere,

ocean circulation, natural and man-made carbon emissions (Suess effect and nuclear power plants), and the global carbon cycle (Broecker et al., 1980; Hou et al., 2020; Hughen et al., 2004; Oeschger et al., 1975; Turnbull et al., 2006; Turnbull et al., 2009; Geller et al., 1997; Graven et al., 2012; Hesshaimer & Levin, 2000; Krakauer et al., 2006; Levin et al., 2010; Nydal & Lövseth, 1965; Nydal, 1968; Patra et al., 2011; Randerson et al., 2002; Hua et al., 2012). This is particularly so in the decade from the mid-1950s to the mid-1960s, when atmospheric radiocarbon levels almost doubled due to the large number of atmospheric thermonuclear bomb tests detonated in the northern hemisphere (NH) (Manning et al., 1990). The anthropogenically produced ^{14}C accumulated in the NH stratosphere and then gradually entered the troposphere via stratosphere-troposphere exchange processes at mid-to-high latitudes (Nydal & Lovseth, 1965). Once in the Equatorial troposphere, the air masses from the NH carrying the bomb-^{14}C signal were mixed with the low-^{14}C concentration air masses from the Southern Hemisphere (SH) (Lal & Rama, 1966; Nydal, 1968) through the latitudinal displacement of the Intertropical Convergence Zone (ITCZ). Thus, a large and persistent latitudinal gradient was generated around the globe during the so-called “bomb-period” (1950 – 1985; Hua et al., 2013).

Using tree-rings, Hua et al. (2012) found that atmospheric ^{14}C over Indonesia (5 ºS; Figure 1), was markedly higher than over the southern latitudes during the austral summer (December, January, and February; DJF). The

authors suggested that the influence of high ^{14}C-concentration northern air-masses enriched atmospheric ^{14}C above Indonesia (5ºS; Figure 1). The findings have meaningful paleoclimatic implications, since they establish the potential of atmospheric ^{14}C to trace changes on atmospheric patterns such as the shape and latitudinal variability of the ITCZ. Over large continental masses like Tropical South America (TSA), however, the narrow zonally extended ITCZ is not present and the atmospheric equivalent of a climatic equator is a ubiquitous tropical low-pressure belt (TLPB). During the austral summer, at the mature phase of the South American Monsoon (Fletcher, 1945; Tomas et al., 1999; Hastenrath & Polzin, 2004, Vuille et al., 2012), the TLPB reaches its southernmost latitudinal position above TSA –sometimes extending as far as 30° S, forming a 'U-shape' that encompasses the Amazon basin with a marked space-time variability (Figure 1). Therefore, well suited tropical ^{14}C archives have the potential to record past atmospheric circulation changes associated with the TLPB. However, ^{14}C studies in TSA are scarce because most of the tree-ring studies have been developed at mid to high latitudes (Boninsegna et al., 2009; Oliveira et al., 2009, 2010). Presently, the most complete ^{14}C-record for TSA is located in Brazil (22º S, 46 ºW; Santos et al., 2015), which shows similar ^{14}C values for the bomb-period than those from higher latitudes of the SH despite being under the influence of the TLPB (Figure 1). This evidences that latitudinal atmospheric ^{14}C differences not only depending on the latitudinal location of the record relative to

the TLPB, but also the potential effect of different carbon reservoirs. We believe it is crucial to provide new and continuous atmospheric ^{14}C record for TSA, especially from the period when the bomb-^{14}C excess amplified the signal of atmospheric-flow patterns and carbon reservoir effects (Hua et al., 2012; Heimann & Maier-Reimer, 1996; Key et al., 2004; Naegler & Levin, 2009).

Polylepis tarapacana, is a long-lived (≥700 years) tree species with well-defined annual rings extensively utilized for dendroclimatic studies (Morales et al., 2020). *P. tarapacana* inhabits the Altiplano (15-23°S; 68 ºW), a high-altitude semiarid plateau at 4,000 m above sea level (asl) in the tropical central Andes, and is considered the world's highest elevation tree. Besides these exceptional features, *P. tarapacana* is under the influence of particular atmospheric-flow patterns. The Altiplano separates the dry Atacama Desert from the wet influences of the Atlantic, which support the world's largest rainforest in the Amazon basin (Figure 1) (Garreaud et al., 2003). Locally, during DJF, the radiative heat from the Altiplano warms surface air masses, which ascend and enable the intrusion of moist air masses from the east, specifically from the Amazon basin, reducing the intrusion of dry air masses from the west and causing 70–90% of the Altiplano annual precipitation (Vuille et al., 2000; Vuille & Keiming, 2004; Garreaud et al., 2009). On a broader scale, Segura et al. (2020) identified a meridional circulation associated with the vertical flow of the western

Amazon convection that also affects the moisture transport towards the Altiplano.

Considering the U-shape of the TLPB, with its western flank coincident with the central Andes, air parcels arriving at the Altiplano from the northeast originated to the north of the TLPB are relatively wet and should have carried the bomb-^{14}C excess derived from nuclear testing. By the contrary, air parcels arriving to the Altiplano from the west (especially from the southwest) originated outside the TLPB and should carry low-moisture and low-^{14}C concentration from the extratropical SH. We thus expect that an increase in the arrival of eastern air parcels from the TLPB influence-region caused an increase in the atmospheric ^{14}C recorded by *P. tarapacana* relative to another SH records. To test our hypothesis and to get a better understanding of atmospheric ^{14}C variability over TSA, we have measured ^{14}C in *P. taparacana* annual rings from the bomb-period (1950 – 1985), compared it with other relevant SH ^{14}C records, and modelled the tropical atmospheric circulation in order to elucidate the main carbon reservoirs that could be affecting the *P. tarapacana* signal.

2. Materials and Methods

2.1 Altiplano tree-ring samples and radiocarbon analyses

P. tarapacana (Queñoa) is a small tree from the *Rosaceae* family with well-defined annual rings that grows at high altitudes (4,000–5,000 m asl) in the Central Andes region of Peru, Chile, Bolivia and Argentina. We sampled ^{14}C in the annual rings of a *P. tarapacana* during the 1950–1985 period from the Irruputuncu tree-ring site located at 4,324 m asl within the Altiplano region (20°S, 68°W). The Irruputuncu *P. tarapacana* tree-ring chronology was previously developed by cross-dating 111 tree-ring series within the site comprising 30,620 annual rings (Morales et al. 2020), and corroborated its annual resolution against 16 different *P. tarapacana* tree-ring sites which encompass 929 tree-ring series and 209,820 annual rings of the species across the Altiplano (Christie et al. 2009; Solíz et al. 2009; Morales et al. 2012; Li et al. 2013; Morales et al. 2015; Lima et al. 2016). Also, independent historical records from severe droughts and pluvials have been used to corroborate the annual nature of the *P. tarapacana* tree-ring network (Morales et al. 2020). Sample preparation was done by cutting dated tree-rings under a binocular microscope into annual rings using sterile ceramic knives over an acrylic table at the tree-ring lab of the Universidad Austral de Chile. Each annual wood segment was polished with diamond tools to remove the surface that was in contact with extraction and sanding tools. For studying post-bomb ^{14}C in tree-rings at annual resolution, it is extremely important to isolate the carbon assimilated in the corresponding growth year, as non-cellulosic compounds can be synthesized

the year after the ring formation or can be translocated between several rings (Anchukaitis et al. 2008; Santos et al., 2020). Therefore, we extracted the holocellulose of each *Polylepis* ring for ^{14}C measurements as it has been shown to be a useful way to remove any mobile carbon from other years (Capano et al., 2017; Santos et al., 2020). Briefly, tree-ring samples were chemically cleaned by a series of acid-base washes followed by the removal of lignin and other mobile carbon fractions through chlorine baths (Southon & Magana, 2010). The holocellulose was then combusted, and CO_2 was cryogenically separated and reduced to graphite by H_2 using FeO as a catalyst (Santos & Ormsby, 2013). The ^{14}C content of the graphite sample was measured at the AMS facility of the University of California at Irvine (Santos et al., 2004, 2007). Radiocarbon results are reported as $\Delta^{14}C$ values that are corrected for known age to 1950 according to convention (Stuiver & Polach, 1977). *P. tarapacana* growth is strongly related to temperature and precipitation occurring between December and February (DJF), therefore we assigned the calendar age of each ring as the SH dendro age plus one; e.g. the atmospheric ^{14}C stored in growing season of 1949-1950 was assigned to January 1st 1950. We use IAEA-C3 (cellulose) as well as holocellulose extracted from wood shaved from tree-rings of *Sequoia sempervirens* centered in year 1850 as secondary standards. Our full *P. tarapacana* $\Delta^{14}C$ record spans from 1950 to 2014, however, for the purpose of this article, we present here the data from 1950 to 1985. We measured

replicates of >10% of the samples and calculated error weighted averages for those years with more than one data point (Supplementary information). The pooled standard deviation based on all replicates produced for the 1950-2014 record is 5‰, whereas the higher variability associated with the 1950-1972 period increases our pooled standard deviation to 6.1‰.

2.2 Geographical provenance of air parcels

We used HYSPLIT to assess the potential geographical provenance of the air parcels that transported the $^{14}CO_2$ that was subsequently fixed in the *P. tarapacana* (and *A. angustifolia*) tree-rings (Draxler & Hess, 1998; Draxler & Stunder, 1988; Stein et al., 2015). The HYSPLIT model v.4 is a complete system designed to calculate simple air-parcel trajectories, complex transport, dispersion, chemical transformation, and depositional simulations. The NCEP/NCAR reanalysis was used as the input data of the HYSPLIT model (Kalnay et al., 1996). This is the only comprehensive climatological dataset covering the beginning of the bomb-testing period, and it is based on *in situ* observations and satellite data which have been proven to be reliable for the representation of atmospheric variables (Kalnay et al., 1996). On the other hand, the backward trajectories calculated using HYSPLIT are generated as a set of longitudinal, latitudinal, and altitudinal points based on an arbitrary number of hours into the past for a specific hour of the day (Draxler & Taylor, 1982). Previous studies have shown that 120 hours (5 days) is a suitable time-window

to overcome potential biases since shorter time-windows tend to show limited trajectories that are too close to the study site, and longer time-windows may be associated with major propagation errors (Scarchilli et al., 2011; Schlosser et al., 2008; Sinclair et al., 2013). A 5-day time window allows for ~35% of the original CO_2 to be exchanged with the local reservoir with the concomitant effect on the $\Delta^{14}C$ of the air parcel (supplementary information). In this way, we calculated 24 backward trajectories (one for each hour of the day) for each day of the growing season (December to February) between the years 1950 and 1985 (77,760 computed trajectories by each TSA record). Each backward trajectory describes the spatial displacement of air parcels during the 5-day time-window (see supplementary information for details).

In order to determine the latitudinal limits of the TLPB-influence and its space-time variability, we used the above sea-level pressure data from the National Center for Environmental Prediction/National Center for Atmospheric Research (NCEP/NCAR) Reanalysis dataset (Kalnay et al. 1996) (see supplementary information). Based on the air parcel position at hour –120, we detected three main geographical provenances that could have a potential isotopic fingerprint, i.e. Amazon basin, the lower troposphere over the extratropical Pacific Ocean and upper troposphere. The criteria for assigning air parcels to each of these geographical provenances is the following: i) air parcels that at hour –120 are located at a more northerly latitude than the average-

location of the TLPB – 2σ were assigned to the Amazon basin; ii) air parcels that at hour –120 are located to the south of the average-shape of the TLPB – 2 σ were assigned to the extratropical ocean and iii) the air parcels that at hour –120 are located at higher altitudes than the different atmospheric boundary layers (see Supplementary Information for details) were assigned to the upper troposphere. The contribution of air parcels from a geographical provenance is gauged by the percentage given by the number of air parcels positioned above a particular geographical provenance at hour –120 relative to the total number of air parcels in all of the backward trajectories.

2.3 $\Delta^{14}C$ endmembers

We use the term '$\Delta^{14}C$ endmember' to represent the preformed ^{14}C content of air parcels that characterizes a particular geographical provenance. In theory, air parcels from the TLPB influence-region must have a higher ^{14}C concentration than air parcels at latitudes further south than the TLPB influence-region. On the other hand, when a carbon reservoir exchanges CO_2 with its adjacent air parcel, this air parcel will acquire the $\Delta^{14}C$ fingerprint of the corresponding carbon reservoir. This influence of carbon reservoirs on air-parcels is called 'isoflux' (Turnbull et al., 2016). The isoflux is the product of the one-way gross CO_2 flux and the isotopic difference between the source (or sink) and the atmosphere. For example, if a given carbon reservoir has a significantly higher $\Delta^{14}C$ than the adjacent atmosphere, there will be a positive isoflux causing an increase in the

$\Delta^{14}C$ of the adjacent air parcel; and vice versa. During the bomb-testing period, the produced atmospheric ^{14}C excess exacerbated the isofluxes of each carbon reservoir due to the amplified isotopic difference between the carbon sources and sinks.

To assess the endmember $\Delta^{14}C$ of each geographical provenance affecting the Altiplano, we first obtained the interannual percentage contribution of air parcels from each geographical provenance using HYSPLIT as discussed in the previous section. Then, we chose selected ^{14}C records that are expected to directly or indirectly express the endmembers of the geographical provenances. For this, we assume that the raw $\Delta^{14}C$ of the records are a combination of different fractions of air masses with their corresponding endmember $\Delta^{14}C$ and that each carbon reservoir exchange with the adjacent air masses is constrained to the altitude of the boundary layer (Graven et al., 2012; Levin et al., 2010; Randerson et al., 2002). The generic equation that is used (see Hua & Barbetti, 2007) on the different records to assess the endmember values is:

$$C = n_1E_1 + n_2E_2 + \ ... + n_iE_i \qquad \text{(Equation 1)}$$

where C is the measured $\Delta^{14}C$ level for a specific site, E_i are the endmember $\Delta^{14}C$ levels for specific geographical provenances; and n_i are the

associated fractions of air masses contribution of a geographical provenance; hence:

$$n_1 + n_2 + \ ... + n_i = 1$$

As discussed later on, the HYSPLIT model results showed that for the Altiplano, the main geographical provenances are (i) the SH Pacific extratropical ocean, (ii) the Amazon basin and (iii) the upper troposphere. One of these, the Pacific extratropical ocean, can be assessed by using direct atmospheric $\Delta^{14}C$ measurements from Wellington (DJF), New Zealand (41° S, 174° E) (Rafter & Fergusson, 1959; Turnbull et al., 2017). The Amazon basin endmember is then calculated by using the *Araucaria angustifolia* record from the Atlantic forest biome in Southeast Brazil (22° S, 46° W) (Santos et al., 2015), which is located at a similar latitude than *P. tarapacana*, but whose main air parcel geographical provenances are the SH Atlantic extratropical ocean and Amazon basin. Once the Amazon basin endmember is calculated we derive the upper troposphere using our *P. tarapacana* ^{14}C record. Considering that the southwest region of both Atlantic and Pacific Oceans share latitudinal location, climatic settings, and reservoir effect, we justify our selection assuming no significant differences in atmospheric $\Delta^{14}C$ (Hua et al., 2013).

3 Results and Discussion

3.1 Atmospheric $\Delta^{14}C$ variability over the Altiplano and the SH

The new *P. tarapacana* ^{14}C record is shown in Figure 2. As expected, the annual chronology faithfully captured the bomb signal both in terms of timing and magnitude. The period 1950-1960 is characterized by rapid swings in the Altiplano $\Delta^{14}C$, reflecting the complicated Andean mixing of the initial bomb signal during this decade (see section 3.2). As shown by Turnbull et al. (2017), the bomb signal transported from the NH to the SH was lagged by about 1.4 years (one year according to our centering on 1st January; see supplementary information). The bomb-peak in the Altiplano is centered on the year 1966, occurring after large $\Delta^{14}C$-changes of more than 200 ‰ yr^{-1} during the period 1963-1966. This reflects the bomb-^{14}C excess produced by thermonuclear detonations in the NH, which resulted in local stratosphere $\Delta^{14}C$ values as high as 5,000–20,000 ‰ (Hesshaimer & Levin, 2000). Then, during the boreal spring and summer, this ^{14}C excess gradually entered the troposphere of the NH, causing a large peak of atmospheric ^{14}C observed at 47º N, Austria, in the year 1964 (Figure 2). This ^{14}C excess was subsequently transported south (Nydal, 1968), affecting first the equatorial region and then the Southern Hemisphere, reaching its maximum level there in 1965 (Indonesian record; Figure 2). As a result of this, a large and persistent north-south $\Delta^{14}C$ positive gradient was present in the global troposphere between 1950 and 1972, which we call the ‘maximum gradient period’ (MGP; Hua et al., 2013). In order to assess the full

geographical variability of the bomb signal in the SH, we constructed indices based on the ^{14}C differences between TSA tree-ring atmospheric $\Delta^{14}C$ records (Altiplano and Brazil) and two other records from locations representing different SH endmembers. These were *Tectona grandis* from Muna Island, southeast of Sulawesi, Indonesia (5° S, 122° E), located perennially north of the austral summer TLPB and strongly affected by the ^{14}C-enriched air masses of the NH and by the tropical ocean isoflux (Hua et al., 2012), and with air ^{14}C from Wellington, New Zealand, located perennially south of the TLPB and influenced by the negative extratropical ocean isoflux (Turnbull et al., 2017).

Figure 3 shows 5 indices constructed by subtracting the lower minus higher latitude $\Delta^{14}C$ records, as well as the magnitude of bomb energy released to the atmosphere through atmospheric nuclear bomb tests. Negative values in our indices are indicative of reversals in the expected north-south positive gradient, and as such, they imply the influence of carbon reservoirs or air parcel pathways. Indeed, TLPB index I (Indonesia – Altiplano, Figure 3a) shows some negative values during the beginning of the bomb peak (years 1950, 1951, 1956, and 1958), whereas the TLPB index II (Indonesia – Brazil, Figure 3b) is almost always positive during the MGP. However, the TLPB index II (Indonesia – Brazil) shows negative values between 1973 and 1978 (see section 3.2). The Altiplano tree-ring record has $\Delta^{14}C$ values that were up to 25 ‰ higher than Indonesia, which points to an enriched source of ^{14}C arriving at high altitude in

western TSA early in the bomb-period. The tropospheric altitude at which physical and chemical mixing occurs between the atmosphere and the Earth's surface varies between oceanic and continental regions; the marine and continental atmospheric boundary layers are located approximately 1 km and 1.5 km above the surface, respectively (Garratt, 1994; Zeng et al., 2004; Messager et al., 2012). Exchanges between carbon reservoirs and the lower troposphere are constrained to these boundary layers, and air parcels from the upper troposphere (higher altitudes than the upper limits of the boundary layers) have a different isotopic signal as they do not directly exchange CO_2 with the biosphere or the oceans, rather they are more influenced by long-range transport and also by natural cosmogenic ^{14}C production in the upper atmosphere. Therefore, considering the above and that several studies have described that high-altitude measurements have different $\Delta^{14}C$ levels than low-altitude measurements (Levin & Kromer, 2004; Turnbull et al., 2009; Graven et al., 2012), reversals in the expected north-south positive gradient found in the TLPB index I are likely explained by the influence of ^{14}C-enriched air parcels from the upper troposphere (see section 3.2). Both indices show a prominent positive peak in 1964, indicating the high ^{14}C signal from the NH arriving in Indonesia with a lag of about 1 year from the maximum ^{14}C production from weapon testing.

The extratropical index I (Altiplano – New Zealand) (figure 3c) shows slightly positive or near-zero values during the MGP, as expected from the north-south positive global gradient (Hua et al., 2013), except for 1964 where the Altiplano record shows higher $\Delta^{14}C$ levels than New Zealand (60 ‰). However, Extratropical index II (Brazil – New Zealand) (Figure 3d), shows slightly negative values during 1956-1962 and positive ones thereafter. This reversal in the expected pattern might be explained by the biospheric reservoir effect of the Amazon rainforest affecting the *A. angustifolia* site and/or a southern air parcel provenance. Naegler & Levin (2009) demonstrated that the radiocarbon isoflux from the biosphere to the troposphere was amplified from –235 ± 55 ‰ yr^{-1} up to –30,000 ± 6,000 ‰ yr^{-1} near the start of the bomb-period. The ocean-troposphere isoflux was also highly amplified from –5,500 ± 1,400 ‰ yr^{-1} during the pre-bomb-testing period to –54,000 ± 13,000 ‰ yr^{-1} near the start of the bomb-period (Heimann & Maier-Reimer, 1996; Key et al., 2004). However, while the Southern Ocean had a dominant role on the ocean-troposphere isoflux, the sub-tropical ocean had a small negative isoflux. This occurred because of the natural radioactive decay of ^{14}C in old water masses that have been transported by the thermohaline circulation and have upwelled in the Southern Ocean, and because of the relatively shallow mixed layers and limited vertical entrainment of pre-bomb water masses in the mid-ocean gyres (Braziunas et al., 1995; Randerson et al., 2002). In fact, Randerson et al. (2002)

modeled a zonal difference of the contribution of $\Delta^{14}C$ fluxes through the Amazon Rainforest and the Atlantic Ocean from the bomb-period, and theorized high tropospheric $\Delta^{14}C$ values over the tropical and extratropical Atlantic Ocean and low values over the Amazon Basin for the early bomb-period. This suggests that the Amazon biosphere-troposphere carbon exchange has played a dominant role in modulating the $\Delta^{14}C$ signal over Brazil. Therefore, reversals in the expected north-south positive gradient in extratropical Index II during the MGP can be explained by the more strongly negative isoflux generated by the carbon flux from the biosphere to the troposphere.

The TSA index (Altiplano – Brazil) (figure 3e), shows remarkably high variability throughout the MGP despite being almost a zonal gradient due to the similar latitude of both records. During the first part of the MGP, the index is characterized by positive values, but then a sharp decrease to very negative ones (up to -45 ‰) occurs right before the bomb peak, coinciding with the 1-year lagged bomb test maximum. These are clear indications of different air masses arriving in TSA at similar latitudes but different altitudes or different carbon-reservoirs affecting these air masses.

3.2 Air parcel ^{14}C affecting TSA tree-ring records.

Based on the Altiplano and Brazilian tree-rings ^{14}C record locations, HYSPLIT geographical provenance results show that the bulk of air parcels

arriving in TSA during the studied period came from the extratropical ocean and the TLPB influenced region of the Amazon basin (Figure 4). Additionally, the Altiplano receives an important contribution of air parcels coming from the upper troposphere of the tropical Pacific (ca. > 3 km, figure 4ce). Quantitatively, 41% derive from the extratropical ocean, 38% from the upper troposphere, and 21% from the Amazon Basin. For the *A. angustifolia* record of Santos et al., (2015) in Southeast Brazil, our analysis shows that 53% of the air parcels arrive from the extratropical ocean, 38% from the Amazon Basin, and only 9% from the upper troposphere. These results highlight the fact that the Altiplano has an additional source of air parcels that could explain the observed ^{14}C differences with *A. angustifolia*. While the extratropical ocean is a dominant source for both records, the Amazon biosphere-troposphere carbon exchange has also played an important role in modulating the $\Delta^{14}C$ signal over TSA. Irrespective of the altitude, our findings show clear summer east-west flows that determine the provenance of air parcels for the Altiplano (Figure 4 a). This is in general agreement with previous studies of the atmospheric circulation in the area (Apaéstegui et al., 2018; Garreaud, 1999; Lenters & Cook, 1997; Perry et al., 2014; Vuille & Keiming, 2004; Vuille et al., 2000). The interannual variability of air parcel geographical provenance (Figure 4g) shows that during the bomb-testing period, an increase in the upper-tropospheric contribution towards the Altiplano is associated with a decrease in contribution mainly from the

extratropical Pacific Ocean and secondarily from the Amazon Basin. This pattern is corroborated by correlation analysis of interannual air-parcel geographical provenance series that show a significant negative relationship between the upper-tropospheric contribution towards the Altiplano with the contribution from both the extratropical Pacific Ocean ($R = –0.85$; $p < 0.05$) and the Amazon basin ($R = –0.58$; $p < 0.05$). These results could be related to the vertical flow pattern described by Segura et al. (2020), where an increase of the upward flow in the western Amazon and the Altiplano generates an increase in moisture transport from the Amazon basin. By extension, our analysis also shows that a decrease in the upper troposphere contribution towards the Altiplano implies an increase of upward flow not only from the Amazon (Neukom et al., 2015; Vera et al., 2019), but also an intrusion of air parcels from the Pacific Ocean lower-troposphere. This is a novel mechanism that will be studied in more depth in future research, given the importance to understanding rainfall events in the Altiplano.

To test our hypothesis that an increase in air parcels from the TLPB influence-region during the bomb period should cause an increase in ^{14}C in tree-rings of *P. tarapacana* and *A. angustifolia* relative to other SH records, we compared both TLPB and Extratropical indices of figure 3 with the percentage of air parcels arriving from the Amazon basin at both locations (Figure 5a,b). If correct, our hypothesis predicts a decrease in the ^{14}C difference between

Indonesia and TSA records (TLPB indices) when the % of air parcels from the Amazon basin increases. In other words, there should be a negative correlation between the amount of air arriving from the Amazon basin and the TLPB indices 1 and 2. Conversely, there should be a positive correlation between the amount of air arriving from the Amazon basin and the extratropical indices, i.e. the $\Delta^{14}C$ difference between TSA records and New Zealand. However, following a first approach using Pearson's correlation coupled with Monte-Carlo analyses done separately for the MGP and post-MGP periods, there are no significant relationships between the air parcels that arrive at the TSA-records from the Amazon basin and the $\Delta^{14}C$-indices (see Supplementary information). Despite this apparent lack of mechanistic causality, we further calculated the $\Delta^{14}C$ endmember values affecting the TSA tree-ring records in order to better understand the atmospheric $\Delta^{14}C$ variability over TSA.

Using the "Wellington smoothed" $\Delta^{14}C$ record (Turnbull et al., 2017) as representative of the extratropical ocean (both Pacific and Atlantic) endmember, we used the *A. angustifolia* ^{14}C data to solve for the Amazon basin endmember, ignoring the negligible contribution of the upper troposphere (~2km) air parcels to that site. Subsequently, we use the calculated Amazon basin endmember together with the Wellington record and the Altiplano ^{14}C to solve for the upper troposphere endmember. The interannual evolution of these endmembers is shown in figure 5c. During the initial bomb rise (1956-1962), our estimated

Amazon $\Delta^{14}C$ shows the most depleted endmember values affecting both TSA tree-ring records while the upper troposphere contributes with highly ^{14}C-enriched air parcels to the Altiplano. From 1950-1962 the Amazon air parcel contribution to both Brazil and the Altiplano is moderate, with both locations showing the extratropical ocean as an important source of air (Figure 4 g,h). The low Amazon endmember values ($\Delta^{14}C < 0$ ‰) during the initial bomb-period are consistent with observational and model-based data that shows the effect of the biospheric negative ^{14}C isoflux on tropospheric air over the Amazon basin (Randerson et al., 2002) that could have lowered the original NH bomb signal. At the same time, the enriched northern sources affecting the upper troposphere during those years are probably related to bomb derived radiocarbon transported from the NH by the upward limb of the Hadley cell at the Equator and then to higher latitudes, without carbon-exchange with the SH ocean, to subsequently move downwards at the subtropics (20-30ºS) (Rind et al., 2001; Held & Hou, 1980; Quan et al., 2004). The interplay of these two extremes, and the transient changes in air parcel geographical provenance contribution from ocean-dominated to upper troposphere-dominated, probably explains the rather variable $\Delta^{14}C$ over the Altiplano and the unexpected negative values of the TLPB index I for the period before 1960. Between 1963 and 1964, air parcels arriving at the Altiplano from the Amazon Basin had higher ^{14}C concentrations than the air parcels from the upper troposphere. As previously explained, these

values are likely related to nuclear weapons testing and changes in the Amazon isoflux. The air parcels influencing the Brazilian tree-ring record were derived from lower altitudes and more northern latitudes than those arriving at the Altiplano. As such, the air parcels reflected in the Brazilian tree-ring record were more directly influenced by the bomb ^{14}C excess. Meanwhile the large negative Amazon isoflux observed during the early bomb-period was weakened, due to the gradual assimilation of bomb-^{14}C excess by the Amazon rainforest. Then, between 1965 and 1972 the Amazon and upper troposphere endmembers do not show large differences. However, from 1973 onwards, the Amazon endmember turns into the highest source of enriched ^{14}C, notably after the MGP. Carbon cycle modeling studies have suggested that the reversal (from negative to positive) of the Amazon biospheric isoflux occurred during the mid-80s as enriched bomb ^{14}C from previous decades was respired (Levin et al., 2010; Randerson et al., 2002). Our calculated Amazon endmember, however suggests that this reversal could have happened at least 10 years earlier. Although preliminary, new ^{14}C data from *Cedrela odorata* from the northeastern sector of the Amazon basin also point to an earlier isoflux reversal (Santos, unpublished results). Reasons for this discrepancy might be the coarse resolution of the modeling framework that could underestimate the carbon reservoir effect of the Amazon biosphere (Randerson et al., 2002) and/or the soil carbon turnover times that are poorly constrained in the model considering the

large Amazon respiration fluxes (Fan et al., 1990). Therefore, our results strongly suggest that when comparing the bomb signal in tree-ring records from different latitudes, the disruption on the expected north-south positive $\Delta^{14}C$ gradient global pattern could be associated to the altitude of a record, atmospheric circulation, and the carbon reservoirs upwind to the record.

4 Conclusions

The new *P. tarapacana* ^{14}C record faithfully captured the bomb signal both in terms of timing and magnitude. Atmospheric $\Delta^{14}C$ offsets between TSA and SH records provide evidence that the expected north-south positive $\Delta^{14}C$ gradient global pattern did not always occur. Despite being broadly applicable, global zoning according to regional $\Delta^{14}C$ concentrations and superficial atmospheric circulation is an oversimplification that needs to be reevaluated.

Our air parcel analyses demonstrated that TSA ^{14}C records are influenced by air parcels from three different geographical provenances. In agreement with previous studies, our $\Delta^{14}C$ estimations from these three geographical provenances suggest an important signal associated to isofluxes from these areas on air parcels. Hence, our findings suggest that when comparing the bomb signal in tree-ring records from different latitudes, the disruption on the expected north-south positive $\Delta^{14}C$ gradient global pattern could be associated

to the altitude of a record, atmospheric circulation, and the carbon reservoirs upwind to the record.

Acknowledgments

We would like to thank all the personnel at the Keck Radiocarbon Facility of the University of California, Irvine for their continuous support and laboratory help. Funding for this study came from the Chilean Agencia Nacional de Investigación y Desarrollo (ANID) Fondecyt grants #1140536, #1201810 and 1201411; ANID FONDAP 15110009 $(CR)^2$. SA was partially supported by the ANID doctoral scholarship 21140194.

Data Availability

The new Altiplano *P. taparacana* ^{14}C dataset can be found in the supplementary information.

References

Anchukaitis, K., Evans, M., Lang, T., Smith, D., Leavitt, S., & Schrag, D. (2008). Consequences of a Rapid Cellulose Extraction technique for Oxygen

isotope and radiocarbon analyses. *Analytical Chemistry*, 80(60), 2035-2041. https: //doi.org/10.1021/ac7020272.

Apaéstegui, J., Cruz, F., Vuille, M., Fohlmeister, J., Espinoza, J., Sifeddine, A., et al. (2018). Precipitation changes over the Eastern Bolivian Andes inferred from speleothem ($\delta^{18}O$) records for the last 1400 years. *Earth and planetary Letters*, 494, 124-134. https: //doi.org/10.1016/j.epsl.2018.04.048.

Braziunas, T., Fung, I., & Stuiver, M. (1995). The preindustrial atmospheric $^{14}CO_2$ latitudinal gradients as related to exchanges among atmospheric, oceanic, and terrestrial reservoirs. *Global Biogeochemical Cycles*, 9(4), 565-584. https: //doi.org/10.1029/95GB01725.

Broecker ,W., Peng, T.-H., & Engh, R. (1980). Modeling the carbon system. *Radiocarbon*, 22(3), 565-598. https: //doi.org/10.1017/S0033822200009966.

Capano, M., Miramont, C., Guibal, F., Kromer, B., Tune, T., Fagault, Y., et al. (2017). Wood ^{14}C Dating with AixMICADAS: Methods and application to tree-ring sequences from the Younger Dryas Event in the Southern French Alps. *Radiocarbon*, 60(01), 51-74. https: //doi.org/10.1017/rdc.2017.83.

Christie, D., Lara, A., Barichivich, J., Villalba, R., Morales, M., & Cuq, E. (2009). El Niño-Southern Oscillation signal in the world's highest-elevation tree-

ring chronologies from the Altiplano, Central Andes. *Palaeogeography, Palaeoclimatology, Palaeoecology,* 281(3-4), 309-3019. https: //doi.org/10.1016/j.palaeo.2007.11.013.

Draxler, R., & Hess, G. (1998). An Overview of the HYSPLIT_4 modeling system for trajectories, dispersión, and deposition. *Austrian Meteorological Magazine*, 47, 295-308. https: //doi.org/10.1016/S1352-2310(97)00457-3.

Draxler, R., & Stunder, J. (1988). Modeling the CAPTEX vertical tracer concentration profiles. *Journal of Applied Meteorology*, 27, 617-625. https: //doi:10.1175/1520-0450(1988)027<0617:mtcvtc>2.0.co;2.

Draxler, R., & Taylor, D. (1982). Horizontal dispersion parameters for long-range transport modeling. *Journal of Applied Meteorology*, 21, 367-372. https: //doi.org/10.1175/1520-0450(1982)021<0367:HDPFLR>2.0.CO;2.

Enting, I. (1982). Nuclear weapons data for use in carbon cycle modeling. Melbourne (Australia), CSIRO Division of atmospheric physics and technology.

Fan, S-M., Wofsy, S., Bakwin, P., Jacob, D., & Fitzjarrald, D. (1990). Atmosphere-biosphere exchange of CO_2 and O_3 in the central Amazon Forest. *Journal of Geophysical research: atmosphere*, 95, D10. https://doi.org/10.1029/JD095iD10p16851.

Fletcher, R. (1945). The general circulation of the tropical and equatorial atmosphere. *Journal of meteorology*, 2(3), 167-174. https: //doi.org/10.1175/1520-0469(1945)002<0167:TGCOTT>2.0.CO;2.

Garratt, J. (1994). Review: the atmospheric boundary layer. *Earth-Science Reviews*, 37, 89-134. https: //doi.org/10.1016/0012-8252(94)90026-4.

Garreaud, R. (1999). Multiscale analysis of summertime precipitation over the central Andes. *Monthly Weather Review*,127, 901-921. https: //doi.org/10.1175/15200493(1999)127<0901:MAOTSP>2.0.CO;2.

Garreaud, R., & Aceituno, P. (2001). Interannual rainfall variability over the South American Altiplano. *Journal of Climate,* 14, 2779-2789. https: //doi.org/10.1175/15200442(2001)014<2779:IRVOTS>2.0.CO;2.

Garreaud R., Vuille, M., & Amy, C. (2003). The climate of the Altiplano: observed current conditions and mechanisms of past changes. *Palaeogeography, Palaeoclimatology, Palaeoecology*, 194, 5-22. https: //doi.org/10.1016/S0031-0182(03)00269-4.

Garreaud, R., Vuille, M., Compagnucci, R., & Marengo, J. (2009). Present-day South American climate. *Palaeogeography, Palaeoclimatology, Palaeoecology*, 281, 180-195. https: //doi.org/10.1016/j.palaeo.2007.10.032.

Geller, L., Elkins, J., Lobert, J., Clarke, A., Hurst, D., Butler, J., et al. (1997). Tropospheric SF_6: Observed latitudinal distribution and trends, derived emissions and interhemispheric exchange time. *Geophysical Research Letter*, 24(6), 675-678. https: //doi.org/10.1029/97GL00523.

Graven, H., Guilderson, T., & Keeling, R. (2012). Observations of radiocarbon in CO_2 at seven global sampling sites in the Scripps flask network: Analysis of spatial gradients and seasonal cycles. *Journal of Geophysical Research*, 117, D02303. https: //doi.org/10.1029/2011JD016535.

Hastenrath, S., & Polzin, D. (2004). Dynamics of the surface wind field over the equatorial Indian Ocean, *Quarterly Journal of the Royal Meteorological Society*, 130, 503-517. https: //doi.org/10.1256/qj.03.79.

Heimann, M., & Maier-Reimer, E. (1996). On the relations between the oceanic uptake of CO_2 and its carbon isotopes. *Global Biogeochemical Cycles*, 10, 89-110. https: //doi.org/10.1029/95GB03191.

Held, I., & Hou, A. (1980). Nonlinear axially symmetric circulations in a nearly inviscid atmosphere. *Journal of the atmospheric science,* 37, 515-533. https: //doi.org/10.1175/1520-0469(1980)037<0515:NASCIA>2.0.CO;2.

Hesshaimer, V., & Levin, I. (2000). Revision of the stratospheric bomb $^{14}CO_2$ inventory. *Journal of Geophysical Research*, 105(D9), 11641-11658. https: //doi.org/10.1029/1999JD901134.

Hou, Y., Zhour, W., Cheng, P., Xiong, X., Du, H., Niu, Z., et al. (2020). ^{14}C-AMS measurements in modern tree rings to trace local fossil fuel-derived CO_2 in the greater Xi'an area, China. *Science of the total Environment*, 715, 136669. https: //doi.org/10.1016/j.scitotenv.2020.136669.

Hua, Q., & Barbetti, M. (2007). Influence of atmospheric circulation on regional $^{14}CO_2$ differences. *Journal of Geophysical Research*, 112(D19). https: //doi.org/10.1029/2006jd007898.

Hua, Q., Barbetti, M., Levchenko, V., Arrigo, R., Buckley, B., & Smith, A. (2012). Monsoonal influences on Southern Hemisphere $^{14}CO_2$. *Geophysical Research Letter*, 39, L19806. https: //doi.org/10.1029/2012GL052971.

Hua, Q., Barbetti, M., & Rakowski, A. (2013). Atmospheric Radiocarbon for the period 1950-2010. *Radiocarbon*, 55(4), 2059-2072. https: //doi.org/10.2458/azu_js_rc.v55i2.16177.

Hughen, K., Lehman, S., Southon, J., Overpeck, J., Marchal, O., Herring, C., et al. (2004). ^{14}C activity and global carbon cycle changes over the past

50,000 years. *Science*, 303(5655), 202-207. https: //doi.org/10.1126/science.1090300.

Kalnay, E., Kanamitsu, M., Kistler, R., Collins, W., Deaven, D., Gandin, L., et al. (1996). The NCEP/NCAR 40-Year Reanalysis Project. *Bulletin of the American Meteorological Society,* 77, 437-471. https: //doi.org/10.1175/1520-0477(1996)077<0437:TNYRP>2.0.CO;2.

Key, R., Kozyr, A., Sabine, C., Lee, K., Wanninkhof, R., Bulliste, J., et al. (2004). A global ocean carbon climatology: results from global data analysis project (GLODAP). *Global Biogeochemical Cycles*, 18(4), GB4031. https: //doi.org/10/1029/2004gb002247.

Krakauer, N., Randerson, J., Primeau, F., Gruber, N., & Menemenlis, D. (2006). Carbon isotope evidence for the latitudinal distribution and wind speed dependence of the air-sea gas transfer velocity. *Tellus*, 58(B), 390-417. https: //doi.org/10.1111/j.1600-0889.2006.00223.x.

Lal, D., & Rama (1966). Charasteristics of global tropospheric mixing based on Man-Made ^{14}C, ^{3}H, and ^{90}Sr. *Journal of Geophysical Research*, 71(12), 2865-2874. https: //doi.org/10.1029/JZ071i012p02865.

Lenters, J., & Cook, K. (1997). On the origin of the Bolivian High and related circulation features of South American climate. *Journal of the*

Atmospheric Science, 54, 656-677. https: //doi.org/10.1175/1520-0469(1997)054<0656:OTOOTB>2.0.CO;2.

Levin, I., Naegler, T., Kromer, B., Francey, R., Gomez-Pelaez, A., Steele, L., et al. (2010). Observations and modeling of the global distribution and long-term trend of atmospheric $^{14}CO_2$. *Tellus,* 62(1), 26-46. https: //doi.org/10.1111/j.1600-0889.2009.00446.x.

Levin, I., & Kromer, B. (2004). The tropospheric $^{14}CO_2$ level in mid-latitudes of the northern hemisphere (1959-2003). *Radiocarbon*, 46(03), 1261-1272. https: //doi.org/10.1017/s0033822200033130.

Levin, I., & Rödenbeck, C. (2007). Can the envisaged reductions of fossil fuel CO_2 emissions be detected by atmospheric observations?. *Naturwissenschaften*, 95, 203-208. https: //doi.org/10.1007/s00114-007-0313-4.

Manning, M., Lowe, D., Melhuish, W., Sparks, R., Wallace, G., Brenninkmeijer, C., & Mcgil, R. (1990). The use of radiocarbon measurements in atmospheric studies. *Radiocarbon,* 32, 37-58. https://doi.org/10.1017/S0033822200039941.

Marland, G., Boden, T., & Andres, R. (2006). Global, regional and national CO_2 emissions. In: Trends: A compendium of data on global change. Carbon

Dioxide information Analysis Center, Oak ridge national laboratory, Us Department of Energy, Oak Ridge, TN.

Messager, C., Speich, S., & Key, E. (2012). Marine atmospheric boundary layer over some Southern Ocean fronts during the IPY BGH 2008 cruise. *Ocean Science*, 8(6), 1001-1023. https: //doi.org/10.5194/os-8-1001-2012.

Morales, M., Christie, D., Argollo, J., Pacajes, J., Silva, J., Alvarez, C., et al. (2012). Precipitation changes in the South American Altiplano since 1300 AD reconstructed by tree-rings. *Climate of the Past*, 8, 653-666. https: //doi.org/10.5194/cp-8-653-2012.

Morales, M., Carilla, J., Grau, H.R., and Villalba, R. (2015). Multi-century lake area changes in the Southern Altiplano: a tree-ring-based reconstruction. *Climate of the Past*, 11, 1139-1152. https: //doi.org/10.5194/cp-11-1139-2015.

Morales, M.S., Cook, E.R., Barichivich, J., Christie, D.A., Villalba, R., LeQuesne, C., Srur, A.M., Ferrero, M.E., González-Reyes, A., Couvreux, F., Matovsky, V., Aravena, J.C., Lara, A., Mundo, I.A., Rojas, F., Prieto, M.R., Smerdon, J.E., Bianchi, L.O., Masiokas, M.H., Urrutia, R., Rodriguez-Catón, M., Muñoz, A.A., Rojas-Badilla, M., Alvarez, C., Lopez, L., Luckman, B., Lister, D., Harris, I., Jones, P.D., Williams, A.P., Velazquez, G., Aliste, D., Aguilera-Betti, I., Marcotti, E., Flores, F., Muñoz, T., Cuq, E. & Boninsegna, J.A. (2020). Six hundred years of South American tree rings reveal an increase in severe

hydroclimatic events since mid-20th century. *Proceedings of the National Academy of Sciences.* https: //doi.org/10.1073/pnas.2002411117.

Naegler, T., & Levin, I. (2009). Observation-based global biospheric excess radiocarbon inventory 1963-2005. *Journal of Geophysical Research*, 114, D17302. https: //doi.org/10.1029/2008JD011100.

Neukon, R., Rohrer, M., Calanca, P., Salzmann, N., Huggel, C., Acuña, D., et al. (2015). Facing unprecedented drying of the Central Andes? Precipitation variability over the period AD 1000-2100. *Environmental Research Lett*eres. https: //doi.org/10.1088/1748-9326/10/8/084017.

Nydal, R. (1968). Further investigation on transfer of radiocarbon in nature. *Journal of Geophysical Research*, 73(12), 3617-3635. https: //doi.org/10.1029/JB073i012p03617.

Nydal, R., & Lövseth, K. (1965). Distribution of radiocarbon from nuclear tests. *Nature,* 206, 1029-1031. https: //doi.org/10.1038/2061029a0.

Oeschger, H., Siegenthaler, U., Schotterer, U., & Gugelmann, A. (1975). A box-diffusion model to study the carbon dioxide exchange in nature. *Tellus*, 27(2), 168-192. https: //doi.org/10.1111/j.2153-3490.1975.tb01671.x.

Oliveira, J., Roig, F., & DePatta, V. (2010). Climatic signals in tree-rings of *Araucaria angustifolia* in the southern Brazillian highlands. *Austral Ecology*, 35, 134-147. https: //doi.org/10.1111/j.1442-9993.2009.02018.x.

Oliveira, J., Santarosa, E., DePatta, V., & Roig, F. (2009). Seasonal cambium activity in the subtropical rain forest tree *Araucaria angustifolia*. *Trees*, 23, 107-115. https: //doi.org/10.1007/s00468-008-0259-y.

Patra, P., Houweling, S., Krol, M., Bousquet, P., Belikov, D., Bergmann, D., et al. (2011). Transcom model simulations of CH_4 and related species: linking transport, surface flux and chemical loss with CH_4 variability in the troposphere and lower stratosphere. *Atmospheric Chemistry and Physics*, 11, 12813-12837. https: //doi.org/10.5194/acp-11-12813-2011.

Perry, L., Seimon, A., & Kelly, G. (2014). Precipitation delivery in the tropical high Andes of southern Peru: new findings and paleoclimatic implications. *International Journal of Climatology*, 34, 197-215. https: //doi.org/10.1002/joc.3679.

Quan, X., Diaz, H., & Hoerling, M. (2004). Change in the Tropical Hadley Cell since 1950. *Book: The Hadley Circulation: Present, Past and Future*, 85-120. https: //doi.org/10.1007/978-1-4020-2944-8_4.

Rafter, T., & Fergusson, G. (1959). Atmospheric radiocarbon as a tracer in geophysical circulation problems. United Nations Peaceful Uses of Atomic Energy, Pergamon Press, London.

Randerson, J., Enting, I., Schuur, E., Caldeira, K., & Fung, I. (2002). Seasonal and latitudinal variability of troposphere $\Delta^{14}CO_2$: Post bomb contributions from fossil fuels, oceans, the stratosphere, and the terrestrial biosphere. *Global biochemical Cycles*, 16(4), 59-1-59-19. https: //doi.org/10.1029/2002GB001876.

Rind, D., Lerner, J., & McLinden, C. (2001). Changes of tracer distributions in the doubled CO_2 climate. *Journal of Geophysical research: Atmospheres*, 106(D22), 28061-28079. https: //doi.org/10.1029/2001jd000439.

Ramsey, C., Plicht, J., & Weninger, B. (2001). 'Wiggle matching' radiocarbon dates. *Radiocarbon*, 43(2), 381-389.

Santos, G., Linares, R., Lisi, C., & Tomazello, M. (2015). Annual growth rings in a simple of Pananá pine (*Araucaria angustifolia*): Toward improving the ^{14}C calibration curve for the Southern Hemisphere. *Quaternary Geochronology*, 25, 96-103. https: //doi.org/10.1016/j.quageo.2014.10.004.

Santos, G., Moore, R., Southon, J., Griffin, S., Hinger, E., & Zhang, D. (2007). AMS ^{14}C sample preparation at the KCCAMS/UCI facility: status report

and performance of small samples. *Radiocarbon,* 49(2), 255-70. doi:10.1017/S0033822200042181.

Santos, G., & Ormsby, K. (2013). Behavioral variability in ABA chemical pretreatment close to the ^{14}C age limit. *Radiocarbon*, 55(2), 534-44. https: //doi.org/10.1017/S0033822200057660.

Santos, G., Granato-Souza, D., Maioli, A., Oelkers, R., & Andreu-Hayles, L. (2020). Radiocarbon analysis confirms annual periodicity in *Cedrela odorata* tree rings from the equatorial Amazon. *Quaternary Geochronology*, 28, 101079. https: //doi.org/10.1016/j.quageo.2020.101079.

Santos, G., Southon, J., Druffel-Rodriguez, K., Griffin, M., & Mazon, M. (2004). Magnesium perchlorate as an alternative water trap in AMS graphite simple preparation: a report on sample preparation at KCCAMS at the University of California, Irvine. *Radiocarbon,* 46(1), 165-73. https: //doi.org/10.1017/S0033822200039485.

Scarchilli, C., Frezzotti, M., & Ruti, P. (2011). Snow precipitation at four ice core sites in East Antarctica: Provenance seasonality a blocking factors. *Climate dynamic*, 37, 2107-2125. https: //doi.org/10.1007/s00382-010-0946-4.

Schlosser, E., Oeter, H., Mason-Delmonte, V., & Reijmer, C. (2008). Atmospheric influence on the deuterium excess signal in polar firn: Implications

for ice-core interpretation. *Journal Glaciology*, 54, 117-124. https: //doi.org/10.3189/002214308784408991.

Segura, H., Espinoza, J., Junquas, C., Lebel, T., Vuille, M., and Garreaud, R. (2020). Recent changes in the precipitation-driving processes over the southern tropical Andes/western Amazon. *Climate Dynamics*. https://doi.org/10.1007/s00382-020-05132-6.

Sinclair, K., Bertler, N., Trompetter, W., & Baisden, W. (2013). Seasonality of airmass pathways to coastal Antarctica: Ramifications for interpreting high-resolution ice core records. *Journal of Climate,* 26(6), 2065-2076. https: //doi.org/10.1175/JCLI-D-12-00167.1.

Southon, J., & Magana, A. (2010). A comparison of cellulose extraction and ABA pretreatment methods for AMS ^{14}C dating of ancient wood. *Radiocarbon,* 52(3), 1371-1379. https: //doi.org/10.1017/S0033822200046452.

Stein, A., Draxler, R., Rolph, G., Stunder, B., Cohen, M., & Ngan, F. (2015). NOAA's HYSPLIT atmospheric transport and dispersion modeling system, *Bulletin of the American Meteorological Society*, 96, 2059-2077. https: //doi.org/10.1175/BAMS-D-14-00110.1.

Stuiver, M., & Polach, H. (1977). Discussion: reporting of ^{14}C data. *Radiocarbon*, 19(3), 355-63. https: //doi.org/10.1017/S0033822200003672.

Takahashi, K., & Battisti, D. (2007). Processes controlling the mean tropical Pacific precipitation pattern. Part II: The SPCZ and the southeast Pacific dry zone. *Journal of Climate*, 20, 5696-5706. https: //doi.org/10.1175/2007JCLI1656.1.

Tomas, R., Holton, J., & Webster, P. (1999). The influence of cross-equatorial pressure gradients on the location of near-equatorial convection. *Quarterly Journal of the Royal Meteorological Society*, 125, 1107-1127. https: //doi.org/10.1002/qj.1999.49712555603.

Turnbull, J. C., H. D. Graven and N. Y. Krakauer (2016). Radiocarbon in the atmosphere. Radiocarbon and Climate Change. E. A. G. Schuur, E. R. M. Druffel and S. E. Trumbore, Springer International Publishing: 83-137.

Turnbull, J., Mikaloff, S., Ansell, I., Brailsford, G., Moss, R., Norris, M., et al. (2017). Sixty years of radiocarbon dioxide measurements at Wellington, New Zealand: 1954-2014. *Atmospheric Chemistry and Phys*ics, 17, 14771-14784. https: //doi.org/10.5194/acp-17-14771-2017.

Turnbull, J., Miller, J., Lehman, S., Tans, P., Sparks, R., & Southon, J. (2006). Comparison of $^{14}CO_2$, CO and SF_6 as tracers for determination of recently added fossil fuel CO_2 in the atmosphere and implications for biological CO_2 exchange. *Geophysical Research Letter*, 33, L01817. https: //doi.org/10.1029/2005GL024213.

Turnbull, J., Rayner, P., Miller, J., Naegler, T., Ciais, P., & Cozic, A. (2009). On the use of $^{14}CO_2$ as a tracer for fossil fuel CO_2: Quantifying uncertainties using an atmospheric transport model. *Journal of Geophysical Research*, 114, D22302. https: //doi.org/10.1029/2009JD012308.

Vera, C., Diaz, L., & Saurral, R. (2019). Influence of anthropogenically-Forced Global Warming and Natural climate variability in the rainfall changes observed over the South American Altiplano*. Frontiers in Environmental Sci*ence. https: //doi.org/10.3389/fenvs.2019.00087.

Vuille, M., Bradley, R., & Keimig, F. (2000). Interannual climate variability in the Central Andes and its relation to tropical Pacific and Atlantic forcing. *Journal of Geophysical R*esearch, 105, 12447-12460. https: //doi.org/10.1029/2000JD900134.

Vuille, M., Burns, S., Taylor, B., Cruz, F., Bird, B., Abbott, M., et al. (2012). A review of the South American monsoon history as recorded in stable isotopic proxies over the past two millennia. *Climate of the Past*, 8, 1309-1321. https: //doi.org/10.5194/cp-8-1309-2012.

Vuille, M., & Keimig, F. (2004). Interannual Variability of Summertime convective cloudiness and precipitation in the central Andes derived from ISCCP-B3 data. *Journal of Climate*, 17, 3334-3348. https: //doi.org/10.1175/1520-0442(2004)017<3334:IVOSCC>2.0.CO;2.

Zeng, X., Brunke, M., Zhou, M., Fairall, C., Bond, N., Lenschow, D., et al.(2004). Marine atmospheric boundary layer height over the eastern Pacific: Data analysis and model evaluation. *Journal of Climate*, 17, 4159-4170. https: //doi.org/10.1175/JCLI3190.1.

Figures

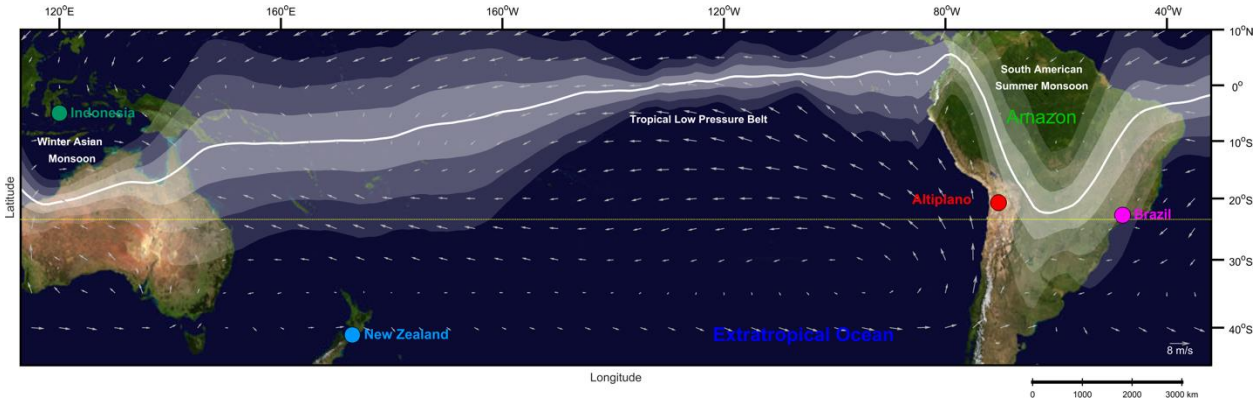

Figure 1. Locations of $\Delta^{14}C$ records used in our study: Altiplano (*Polylepis tarapacana*; 20 °S, red dot, this study); Indonesia (*Tectona grandis*; 5° S, green dot; Hua et al., 2012); Brazil (*Araucaria angustifolia*; 22° S; magenta dot; Santos et al., 2015); and New Zealand (atmospheric measurements from Wellington; 41 °S, blue dot; Turnbull et al., 2017). The white line represents the average (± 1 σ, ± 2 σ, and ± 3 σ) latitudinal positions of the Tropical Low-Pressure Belt (TLPB) drawn following the 1949-2019 averaged austral summer (DJF) minimum sea level pressure between 10° N and 35° S in the NCAR/NCEP reanalysis. White vectors show wind velocity and direction. The Tropic of Capricorn is shown with the yellow dotted line.

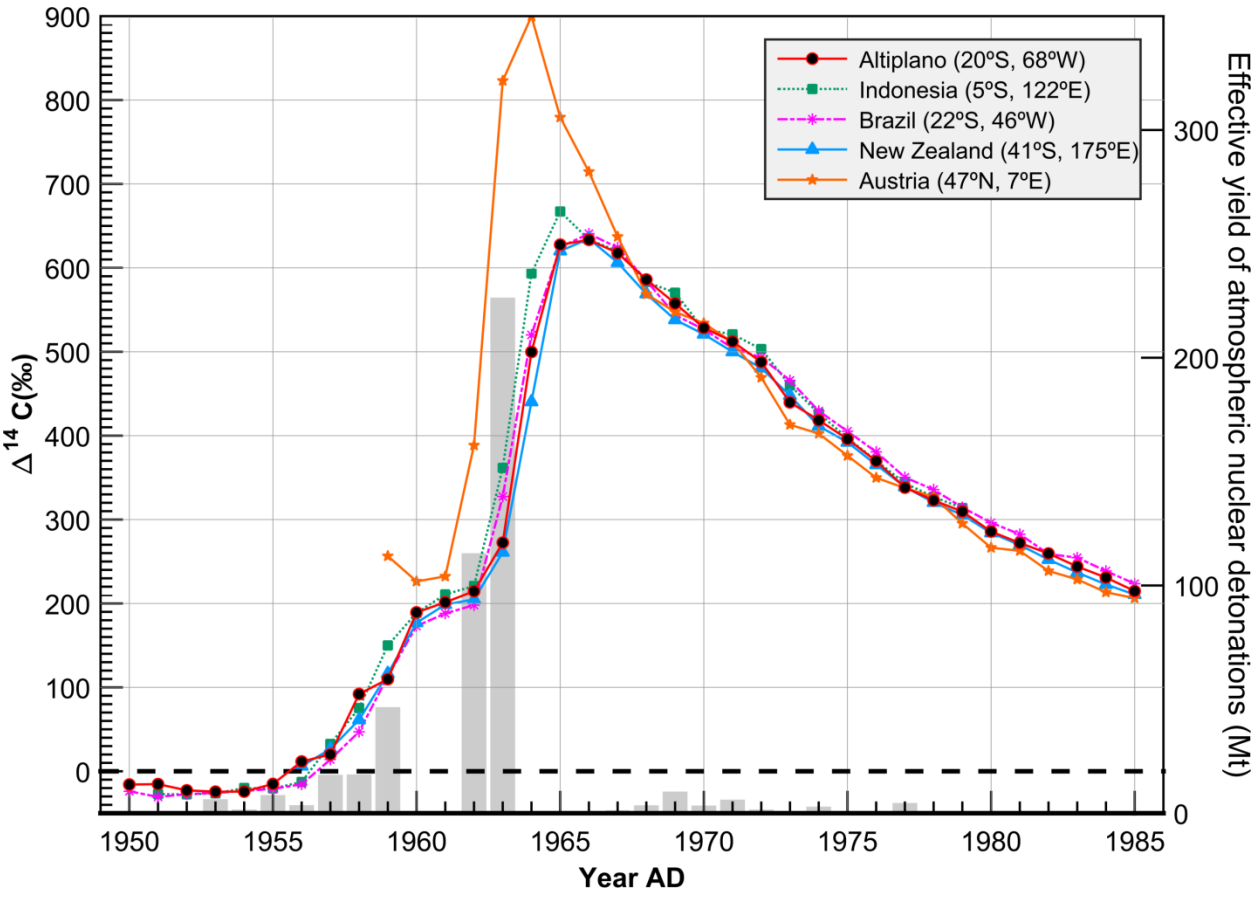

Figure 2. *Polylepis tarapacana* annual ^{14}C during the bomb-testing period (red line with black circles) is shown. For comparison, we include the December, January, and February average of the monthly seasonally detrended atmospheric $\Delta^{14}C$ from New Zealand (Turnbull et al., 2017; light blue line with triangles), *Araucaria angustifolia* $\Delta^{14}C$ record from Brazil (Santos et al., 2015; magenta broken line with asterisks) *Tectona grandis* $\Delta^{14}C$ record from Indonesia (Hua et al., 2012; green dotted line with squares), and Austria atmospheric $\Delta^{14}C$ summer measurements (Levin & Kromer, 2004; orange solid line with stars) representative of the midlatitude northern hemisphere. The grey bars show the effective yield in megatons of thermonuclear detonations during this period which is directly related to the quantity of ^{14}C atoms generated (Enting, 1982).

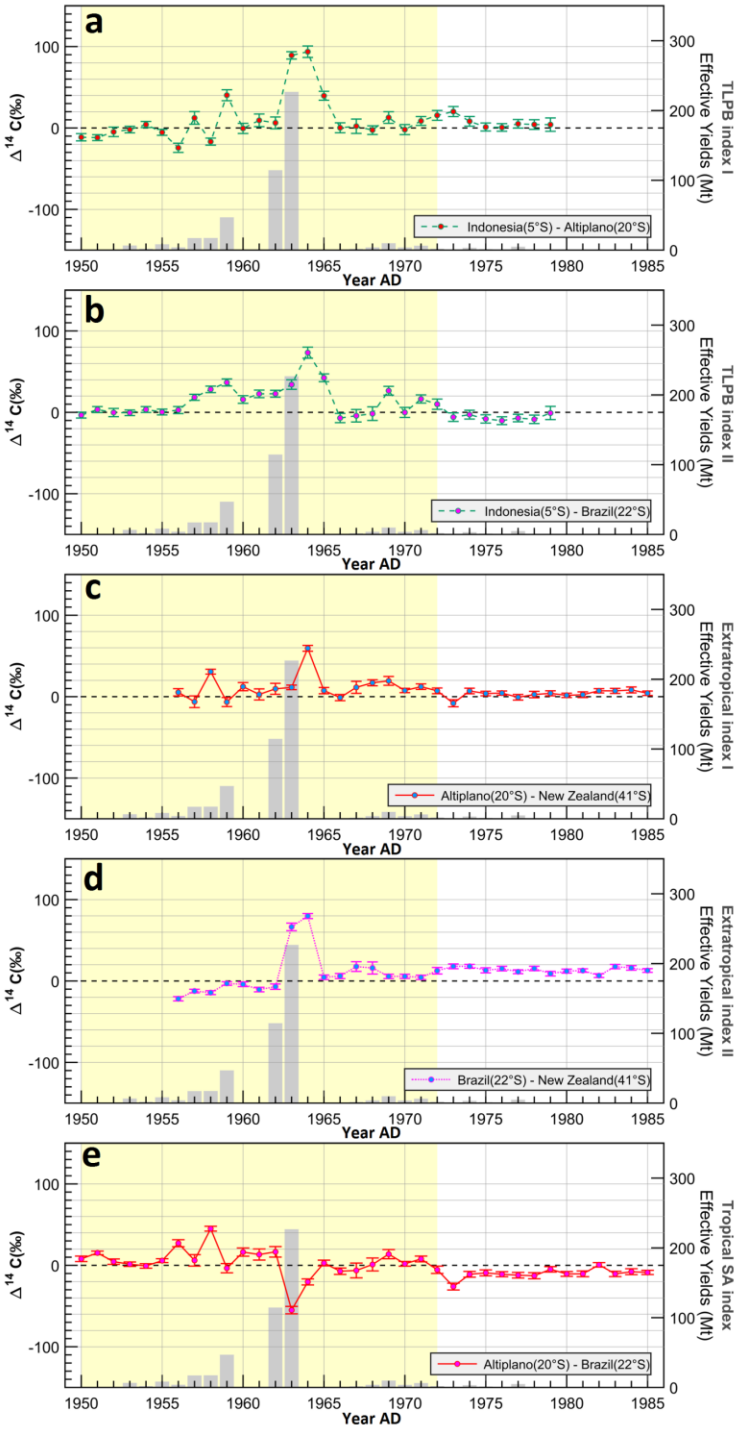
a
b
c
d
e
Δ14C(‰)
Effective Yields (Mt)
TLPB index I
TLPB index II
Extratropical index I
Extratropical index II
Tropical SA index
Year AD
Indonesia(5°S) - Altiplano(20°S)
Indonesia(5°S) - Brazil(22°S)
Altiplano(20°S) - New Zealand(41°S)
Brazil(22°S) - New Zealand(41°S)
Altiplano(20°S) - Brazil(22°S)

Figure 3. Indexes based on latitudinal $\Delta^{14}C$ differences (north – south): (a) TLPB index I = Indonesia - Altiplano; (b) TLPB index II = Indonesia - Brazil; (c) Extratropical index I = Altiplano - New Zealand; (d) Extratropical index II= Brazil - New Zealand and (e) TSA index Altiplano - Brazil. Colored area is the Maximum Gradient Period (MGP, Hua et al., 2013) and the dashed black line indicates $\Delta^{14}C = 0$. The magnitude of nuclear explosions during the bomb-testing period is also shown (grey bars, based on Enting, 1982).

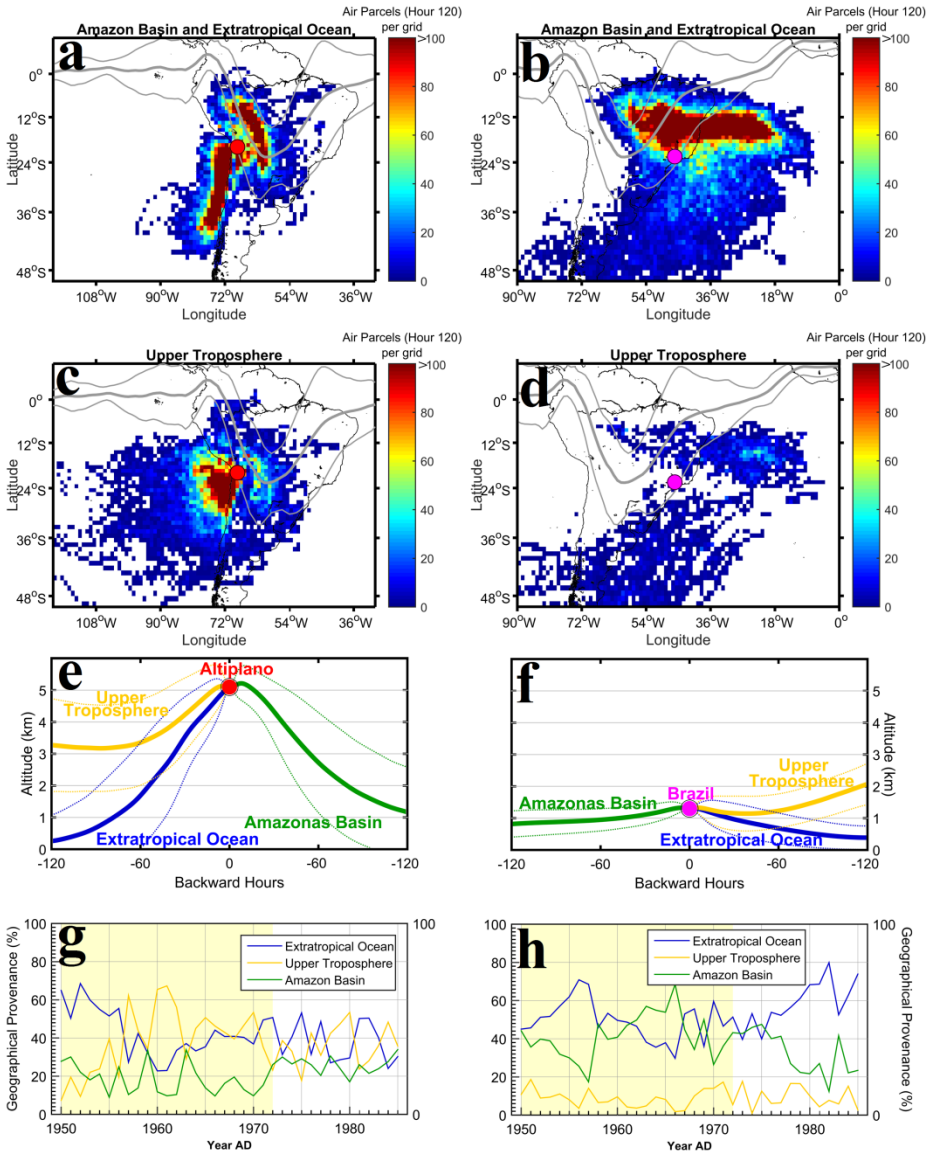

Figure 4. HYSPLIT backward trajectory analysis results for TSA. **(a)** Air parcel density arriving to the Altiplano from within the atmospheric boundary layers (see Supplementary information). The colorbar scale indicates the total number of air parcels located on each pixel grid (1º x 1º) at hour -120 during the entire study period (DJF, 1950 to 1985). The solid gray lines show the mean temporal shape of the Tropical Low-Pressure Belt ± 2σ of its spatial variability; **(b)** Same as (a) but for Southeast Brazil; **(c)** Same as (a); but for air parcels originating above the atmospheric boundary layers (see Supplementary information) **(d)** Same than (c) but for Southeast Brazil; **(e)** Mean altitude of the air-parcel trajectories that reached the Altiplano during the studied period (solid color lines) and its standard deviation (dotted color lines); **(f)** same that (e) but for Southeast Brazil; **(g)** air parcel contribution (%) of each geographical provenance arriving in the Altiplano during the studied period **(h)** same as (g) but for Southeast Brazil. The shaded yellow area highlights the maximum gradient period of 1950-1972.

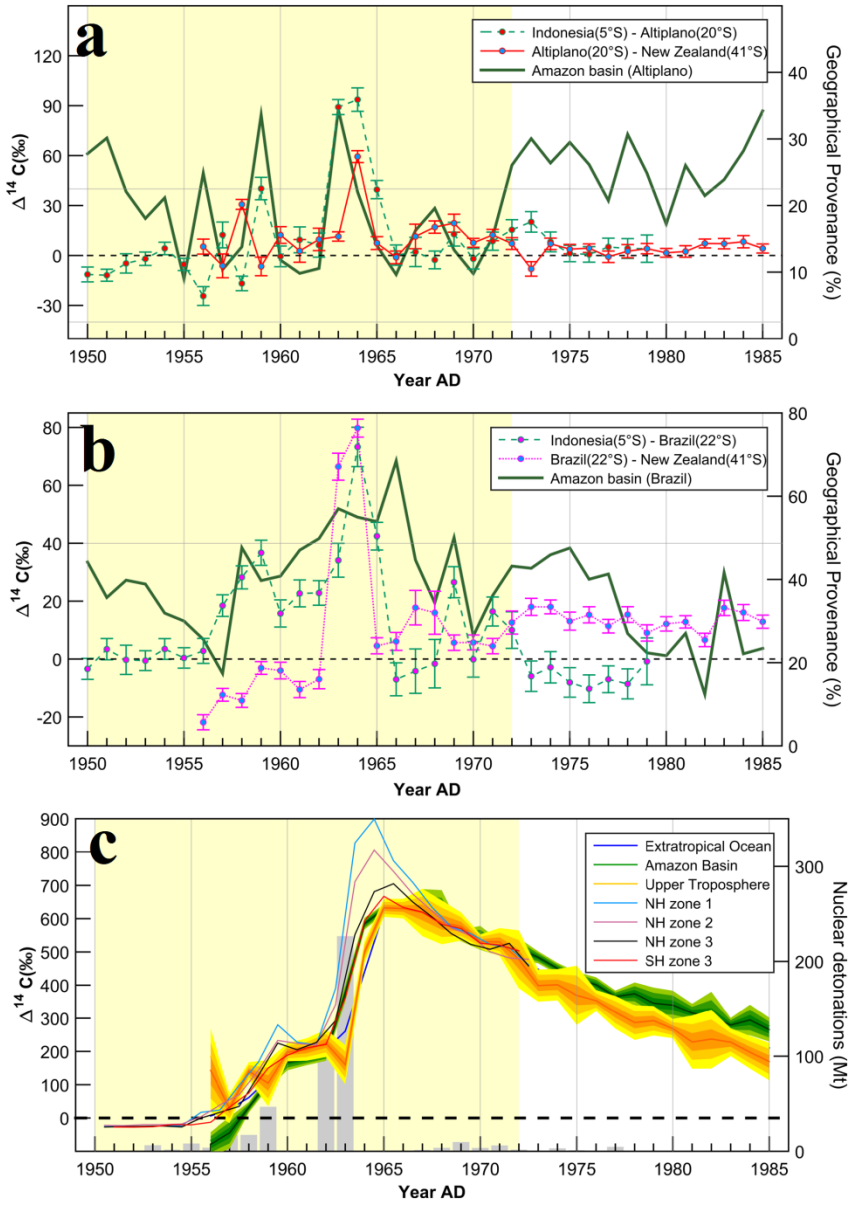

Figure 5. (**a**) Comparison between TLPB index I (green dashed line), Extratropical index I (red solid line) and the % of air parcels from the Amazon basin arriving in the Altiplano (green solid line); **(b)** Comparison between TLPB index II (green dashed line), Extratropical index II (red solid line) and the % of air parcels from the Amazon basin arriving to Southeast Brazil (green solid line); **(c)** Calculated $\Delta^{14}C$ endmember values for TSA (Extratropical Ocean is the New Zealand atmospheric detrended record) together with radiocarbon latitudinal

zones (Hua et al., 2013). Using the errors of each record were calculated the possible maximum and minimum values for the estimation of both Amazon and Upper troposphere endmembers (± 1σ, ± 2σ, and ± 3σ are represented by shaded colors of the same tinge).The magnitude of nuclear explosions during the bomb-testing period (grey bars, based on Enting, 1982) is also shown. The dashed horizontal line indicates $\Delta^{14}C = 0$. The shaded area highlights the Maximum Gradient Period (MGP).

Supporting Information for

Radiocarbon bomb-peak signal in tree-rings from the tropical Andes register low latitude atmospheric dynamics in the Southern Hemisphere

Santiago Ancapichún[1], Ricardo De Pol-Holz[2*], Duncan A. Christie[3,4], Guaciara M. Santos[5], Silvana Collado-Fabbri[6], René Garreaud[4,7], Fabrice Lambert[4,8], Andrea Orfanoz-Cheuquelaf[4,7], Maisa Rojas[4,7], John Southon[5], Jocelyn C. Turnbull[9,10], and Pearce Paul Creasman[11]

[1]Postgraduate School in Oceanography, Faculty of Natural and Oceanographic Sciences, Universidad de Concepción, Concepción, Chile

[2]Centro de Investigación GAIA Antártica (CIGA) and Network for Extreme Environment Research (NEXER), Universidad de Magallanes, Punta Arenas, Chile

[3]Laboratorio de Dendrocronología y Cambio Global, Instituto de Conservación Biodiversidad y Territorio, Universidad Austral de Chile, Valdivia, Chile

[4]Center for Climate and Resilience Research (CR)[2], Chile

[5]Department of Earth System Science, University of California, Irvine, USA

[6]Fundación Crono Austral, Concepción, Biobio, Chile

[7]Department of Geophysics, Universidad de Chile, Santiago, Chile

[8]Department of Physical Geography, Pontificia Universidad Católica de Chile, Santiago, Chile

[9]GNS Science, Rafter Radiocarbon Laboratory, Lower Hutt, New Zealand

[10]CIRES, University of Colorado at Boulder, USA

[11]American Center for Oriental Research (ACOR), Amman, Jordan

*Corresponding author: Dr. Ricardo De Pol-Holz, Av. Bulnes 01855, Punta Arenas, Chile (ricardo.depol@umag.cl)

1 Introduction

This supplementary information contains an overview of the material and methods used to produce the figures and statistical results given in the main paper. As such, this material intentionally contains some repetition from the main paper and additional methodological details for users of the dataset.

The supplementary material and methods section explains in detail the *Polylepis tarapacana* $\Delta^{14}C$ record, HYSPLIT processes, and supplementary data.

Figure S1 shows an evaluation of the ring counts by the timing of the ^{14}C bomb spike

Figure S2 shows a regional summer-meteorology, focused on the TLPB's shape.

Figure S3 shows maps of *P. tarapacana's* location, altitude, and *P. tarapacana's* images.

Figure S4 shows the lowest interannual above sea-level pressure series and precipitation.

Figure S5 shows HYSPLIT backward trajectory analysis results for Altiplano

Figure S6 shows HYSPLIT backward trajectory analysis results for Brazil.

Figure S7 shows air parcel contribution comparison between different hours.

Table S1 shows the linear regression coupled to Monte-Carlo method (1950-1972).

Table S2 shows the linear regression coupled to Monte-Carlo method (1973-1985).

References are in the main article.

2 Material and methods

This study is the first time that tree-rings of *P. tarapacana* are used for radiocarbon analysis. For this reason, we evaluated the ring counting by analyzing the timing of the ^{14}C-bomb spike compared to atmospheric measurements in New Zealand. Figure S1 shows that by shifting our chronology in ±1 yr, there is a clear mismatch with the DJF average of the monthly seasonally detrended atmospheric Δ^{14}C from Turnbull et al., (2017), hence confirming the accuracy of our year-to-year ring counting as well as DJF as the average wood-tissue growth period (Christie et al., 2009). Dendrochronologists have used *P. tarapacana* successfully as a summer (DJF) precipitation proxy due to its reliable interannual ring-growth pattern (Morales et al., 2012).

2.1 Southern hemisphere Δ^{14}C-records

In order to detect differences between our *P. tarapacana* and other Δ^{14}C series of the Southern Hemisphere (affected by different carbon reservoirs), we used the following data:

Tectona grandis: Teak is one of very few tropical tree species producing tree rings with annual growth. The tree-ring core was extracted from Muna

Island off southeastern Sulawesi in Indonesia (5º S, 122º E). During the growing season (the rainy months from November to April), Muna Island is strongly influenced by the Winter Asian Monsoon. Due to the location of this atmospheric $\Delta^{14}C$ series, it was described that during the bomb-period it was influenced by the ^{14}C-enriched air of the northern hemisphere (Hua et al., 2012). Tree-ring data are commonly plotted in the middle of the growing period. Specifically, in Hua et al. (2012), Teak was plotted on Jan-Feb of each year (growth_end plus 0.08 year). Hence, Teak recorded atmospheric ^{14}C from 1951.08 to 1979.08. Here, we plotted and used data aligned to 1 Jan of each year. Thus, the bomb-peak on Teak occurred in 1965 with $\Delta^{14}C$ = 667.1. Data available at: https://agupubs.onlinelibrary.wiley.com/action/downloadSupplement?doi=10.1029%2F2012GL052971&file=grl29580-sup-0002-ds01.txt.

Araucaria angustifolia: The Paraná pine (also called the candelabra tree) site used in our study is located in the Atlantic forest biome of the Municipality of Camanducaia (22º 50' S, 46º 04' W) in Minas Gerais, Brazil's southeastern highlands (Santos et al., 2015). Ring counting shows that this tree species can reach several hundred years of age (Oliveira et al., 2010). Growth months of *Araucaria angustifolia* were aligned with the summer season (Nov to Feb), that is the rainy season. Santos et al. (2015) found a good alignment from growth_start year plus 0.95 years (1927.95 – 1997.95). Here, we align this data

to 1 Jan of the growth_end year. Due to the good agreement between duplicates and time series Araucaria data, we averaged the duplicates using weight mean calculations. The error between duplicates was calculated using standard error calculations. The outlayer UCIAMS116680, was not considered for the averaging. The bomb-peak on Paraná pine occurred in 1966 with $\Delta^{14}C$=640.7.

Atmospheric measurements from Wellington: The first Atmospheric $\Delta^{14}C$ measurements were begun at Wellington, New Zealand in 1954, aiming to better understand carbon exchange processes (Turnbull et al., 2017). Samples from 15 December 1954 to 5 June 1987 were collected at Makara, on the south-west coast of the North Island of New Zealand (41.25º S, 174.69º E). Samples since 8 July 1988 have been collected at Baring Head on the south coast of the lower North Island and 23 km south-east of Makara (41.41º S, 174.87º E). We use summer months (DJF) from BHD_monthly_smooth_curve (the series of D14C_trend), due to its high similitude with the curve of the SH zone 1-2 (Hua et al., 2013). We align the average of the summer months to 1 Jan of each year. Thus, the bomb-peak on Wellington occurred in 1966 with $\Delta^{14}C$=634.6.

2.2 Tropical Low-Pressure Belt (TLPB)

The ITCZ definition as an atmospheric circulation-boundary between the northern and southern hemisphere that covers tropical latitudes around the globe (Linacre and Geerts, 1997) has been applied on several radiocarbon/atmospheric-circulation related studies (Hua et al., 2012; Hua et al., 2013). However, the ITCZ concept represents a meteorological phenomenon occurring over the oceans (see Vuille et al. 2012). Over continental masses like TSA however, the ITCZ definition is not as straightforward. Considering that TSA's topography affects the precipitation regime and generate spatial irregularity on winds, and that the convergence of trade winds from the northern and southern hemisphere occurring at tropical latitudes are associated with a low-pressure zone, we propose for this study the Tropical Low-Pressure Belt (TLPB) as a reliable indicator of the atmospheric circulation-boundary between hemispheres (Fletcher, 1945; Tomas et al., 1999; Hastenrath & Polzin, 2004).

In order to determine the latitudinal limits of the TLPB influence and determine its spatio-temporal variability, we used the above sea-level pressure data from the National Center for Environmental Prediction/National Center for Atmospheric Research (NCEP/NCAR) Reanalysis dataset (Kalnay et al. 1996), which have a spatial-resolution of 2.5º latitude x 2.5º longitude. In addition, in order to obtain the same spatial resolution between our air parcel fields (section 2.5) and the above sea-level pressure, the raw data from the reanalysis NCEP/NCAR was remodeled into a matrix of 1º latitude x 1º longitude.

Considering austral summer as the growing season of *P. tarapacana*, we studied summer months (D, J, F) from years 1949 to 2019. Based on the average of the above sea-level pressure data from the studied period, we developed a map that shows the spatial pattern of the minimum pressures above the TSA (Figure S2). We found an absence of low pressures at north of 10º N, therefore we considered this latitude as the north limit of the TLPB. On the other hand, the southern limit was established at 35ºS, according to the evidence of the map and considering that low pressures on TSA during the mature phase of the South American Monsoon (D, J, F) can reach latitudes near 30ºS (Vera et al. 2006). South of 35ºS we could observe low pressure levels, but these are related to the austral low-pressure belt. In this way, after the evaluation of the above sea-level pressure pattern, we established the zonal lowest-pressure values between the latitudes 10º N-35º S for each summer month of each year studied. In order to minimize the outlier-effect produced by low spatial-resolution of the reanalysis NCEP/NCAR on the latitudinal position of the TLPB, we smooth our data using a moving average of 10 points. The averaged location and variability (standard deviation) of the TLPB were calculated using summer months (D, J, F) from 1949 to 2019.

2.3 Bomb-pulse

The bomb pulse at the SH is proportional to the energy released by thermonuclear detonations: the effective yield in megatons (Enting 1982; Hua et

al., 2013). This ^{14}C excess produced in the NH generated a large and persistent global latitudinal gradient (Hua et al., 2013). Using the data from Enting (1982), we averaged the monthly data from each year (January to December), generating an annual series. Because the bomb-^{14}C excess produced during an entire year is recorded by tree-rings only on the growing season (DJF for the SH), the annual series was align to Jan 1st of the next year.

2.4 GP of air parcels using HYSPLIT

To assess the GP of the air parcels that potentially transported the $^{14}CO_2$ that was subsequently fixed in the *P. tarapacana* tree-rings through photosynthesis; we used HYSPLIT (Draxler & Hess, 1998; Draxler & Stunder, 1988; Stein et al., 2015). The HYSPLIT model v. 4 is a complete system designed to calculate simple air-parcel trajectories, complex transport, dispersion, chemical transformation, and depositional simulations. The NCEP/NCAR reanalysis data were used as the input data of the HYSPLIT model (Kalnay et al., 1996). This is the only comprehensive climatological dataset covering the beginning of the bomb-testing period, and it is based on *in situ* observations and satellite data which have been proven to be reliable for the representation of atmospheric variables (Kalnay et al., 1996). On the other hand, the backward trajectories calculated using HYSPLIT are generated as a set of

longitudinal, latitudinal, and altitudinal data based on an arbitrary number of hours into the past for a specific hour of the day (Draxler & Taylor, 1982).

Previous studies have shown that -120 hours (5 days) is a suitable time-window to overcome potential biases since shorter time-windows tend to show limited trajectories that are too close to the study site, and longer time-windows may be associated with major propagation errors (Scarchilli et al., 2011; Schlosser et al., 2008; Sinclair et al., 2013). In addition, considering that the atmosphere had 360 kg C/ha^3 (at 300 ppmv) and that the Amazon biosphere respire 25.7 kg C/ha per night (10 hours) (Fan et al., 1990), we estimated that the Amazon biosphere respired about 35% of the CO_2 of an hypothetic air parcel of 1 ha^3. This estimation suggests that the Amazon biosphere could cause a strong reservoir effect on air parcels positioned above the Amazon basin along 5 days. Besides, for our study, in longer time-windows the footprints being much diffuse, because air parcels that in hour -120 were located in the Amazon basin changed to the Extratropical ocean resulting in a assign-wrong reservoir effect (Figure S5 and S6).

In the main paper different calculation based on the use of one backward trajectory by each hour of the day was made, therefore, 24 backward trajectories per day were modeled. The large climatic extremes that occur at the Altiplano drive the daily biological cycle of *P. tarapacana*. Is known that during both morning and afternoon *P. tarapacana* is biologically active, avoidance activating

during the leftover of the day where extremes both high and low temperatures occur. The precise hour when *P. tarapacana* takes the atmospheric CO_2 varies between days, because depend of weather conditions. Therefore, in the main study we used overall hour of the day. However, to evaluate if there are differences in the contribution of air parcels of each geographical provenance calculated using different hours of the day, the contribution of air parcels was calculated using 24 hours per day (main study) and 1 hour per day (midday) (figure 7S). This comparison shows that together ways to calculate the contribution of air parcels presented similar values between them. Therefore, we conclude that the use of 1 hour or 24 hours per day isn't relevant for the development of our study and that the use of one series or another doesn't cause large differences in our analysis.

Each backward trajectory (77,760) described the spatial displacement of air parcels during a determinate time-window (120 hours). However, the low topographic resolution of the HYSPLIT model does not fully represent the complex topography of the Altiplano, having a default altitude of approximately 3 km at the location of our record (4,324 m asl). If the default altitude (3 km) is used, the air-parcel backward trajectory analysis ignores the regional topographic effect, giving incorrect displacement into the mountains (Figure S3). Therefore, following Stein et al., (2015), and evaluating the topography of the region, we used 550 hPa (5,000 m approximately) as the starting point of the air-

parcel analysis to ensure the reliable performance of the HYSPLIT model. Using our analysis, we identified the main GP of the air parcels at hour –120 for each backward trajectory. For example, if a cluster of air parcels that at hour –120 was identified as being located above the Amazon basin, we assigned it a GP of the Amazon basin. Therefore, the contribution of air parcels from an established GP is represented by the percentage given by the number of air parcels positioned above a particular GP at hour –120 relative to the total number of air parcels in all of the backward trajectories.

Considering that South American Monsoon delivers water to the Amazon biosphere and that monsoonal influence is associated with low pressures at sea level on TSA (Figure S4), the Amazon basin GP corresponds to the –2 σ of the TLPB position over TSA. On the other hand, the tropospheric altitude at which physical and chemical mixing occurs between the atmosphere and the Earth's surface varies between areas of oceans and continents. The marine atmospheric boundary layer occurs approximately 1 km above the Pacific Ocean (900 hPa; Zeng et al., 2004). The marine atmospheric boundary layer occurs approximately 1.3 km above the Atlantic Ocean (850 hPa; Messager et al., 2012). The atmospheric boundary layer occurs approximately 1.5 km above continents (Garratt, 1994).

2.5 Linear regression coupled to Monte-Carlo method

For radiocarbon studies, the goal of the Monte-Carlo method is to consider data error, that has each radiocarbon measurements, in several statistical analyses such as Chi-square (Ramsey et al., 2001). Each radiocarbon value is accompanied by its measurement error (± σ), based on the fact that this error has a Gaussian probability of occurs, it is 68 % probable that the radiocarbon measured being between ± 1 σ and 95 % probable that the radiocarbon measured being between ± 2. In our study, the Monte-Carlo method allows us to create a set of ‘’n’’ probable radiocarbon series (considering each annual value) for each radiocarbon index (n = 10000). At the same time, we made a Pearson correlation analysis between each probable radiocarbon series and the contribution of air parcels that came from the Amazon basin. Thereby, a set of R coefficients were obtained with its respective p-values. Then, to obtain the probability that there is a significant relationship between our radiocarbon indexes and the air parcels Amazon contribution, the number of significant correlations were divided by the total number of probable radiocarbon series created. Our analyses demonstrate that there is a low-probability to obtain a significant relationship between the Amazon air parcel contribution and ^{14}C indexes.

3 Figures and Tables

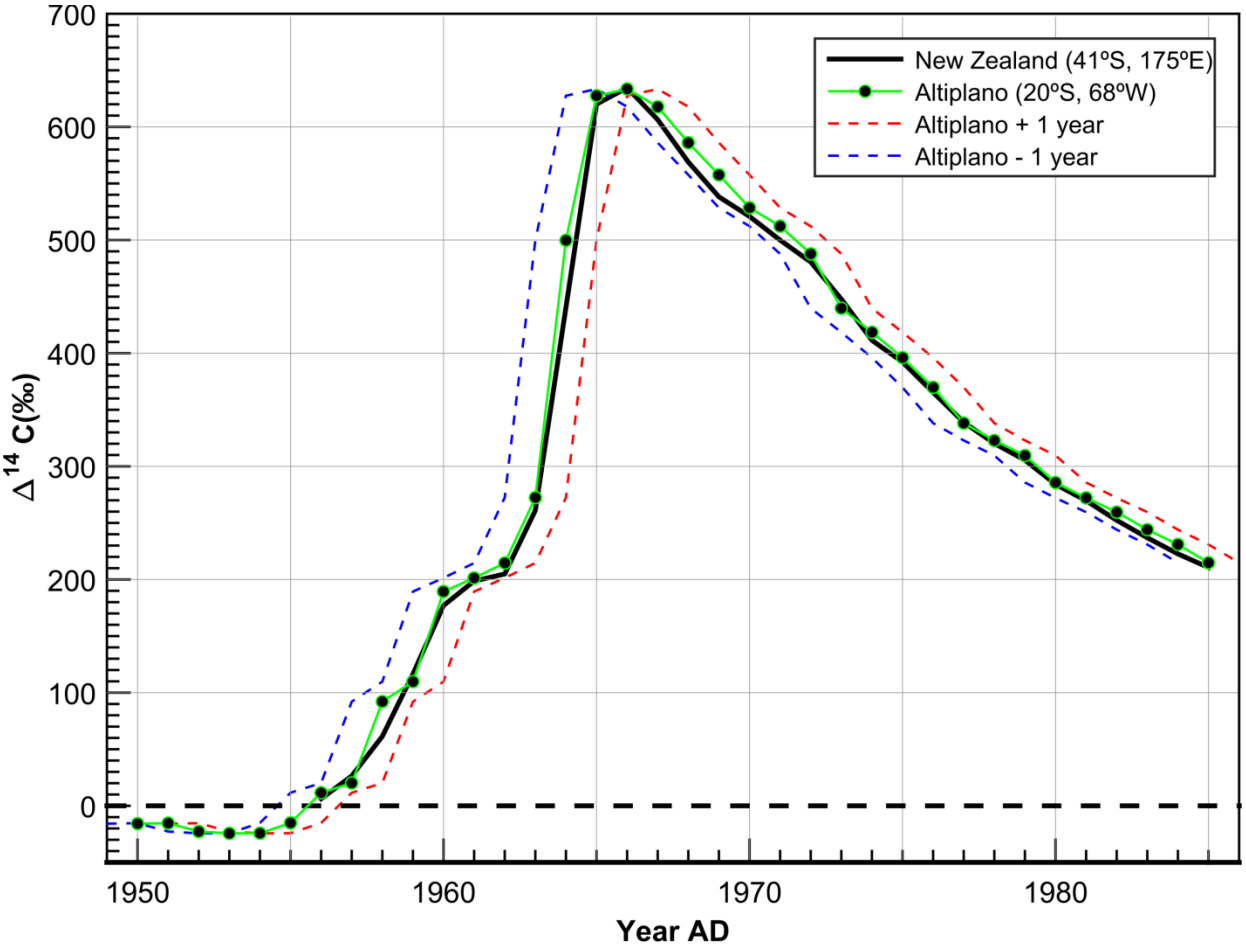

Figure S1. Evaluation of tree ring counts for the Altiplano. Black lines are curves of New Zealand. Green line is the tree ring data from the Altiplano, using the assigned ring counts. Blue and red dashed lines are the tree ring data shifted by one year in either direction. Adjustments in either direction clearly misalign the upswing of the bomb pulse and the timing of the peak $\Delta^{14}CO_2$ values. In the later part of the record, since 1973, the trend through time is smaller, but the blue points (shifted one year older) consistently underestimate the *P. tarapacana* values throughout the record. While, the red points (shifted one year younger) overestimate the *P. tarapacana* values throughout the record.

There is excellent agreement between the *P. tarapacana* record with New Zealand atmospheric $\Delta^{14}C$ measurements, giving us confidence that the ring counts are correct in this case.

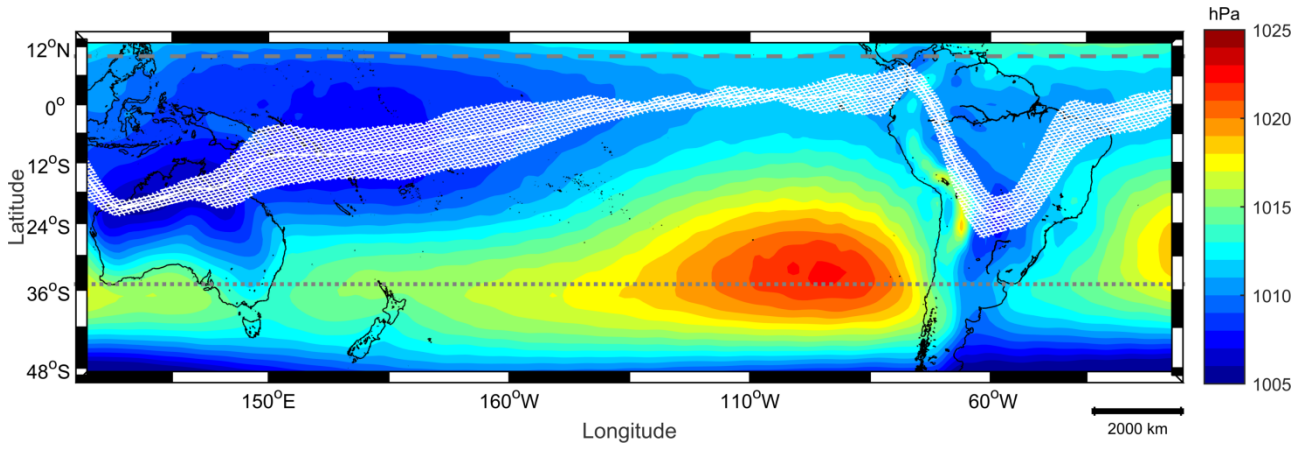

Figure S2. Averaged above sea-level pressure (color) and the TLPB (=solid white line; σ = dashed white area). Using the NCEP/NCAR reanalysis data from December, January, and February from the year 1949 to 2019, variables were calculated. The dashed and dotted grey lines represent latitudinal-limits to calculate the TLPB: 10º N and 35º S, respectively.

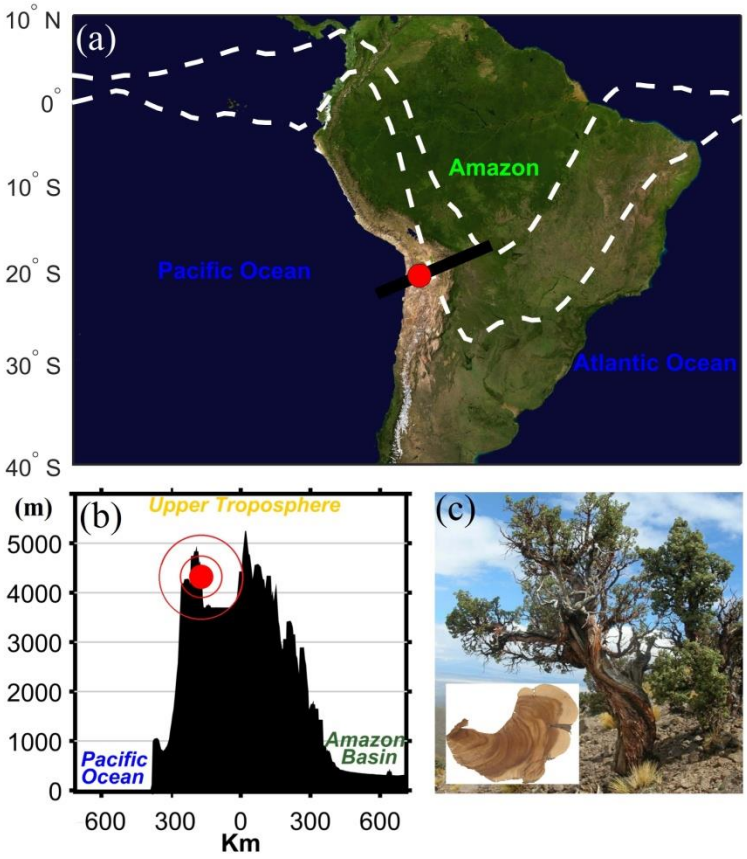

Figure S3. (a) White dashed lines show the TLPB region of influence (± 1 σ) and the red circle shows the location of *P. tarapacana*. (b) The profile shows the altitudinal location of Altiplano's record corresponding to the black solid line in (a) based on ETOPO1. (c) Tree of *Polylepis tarapacana* with its annual tree-rings.

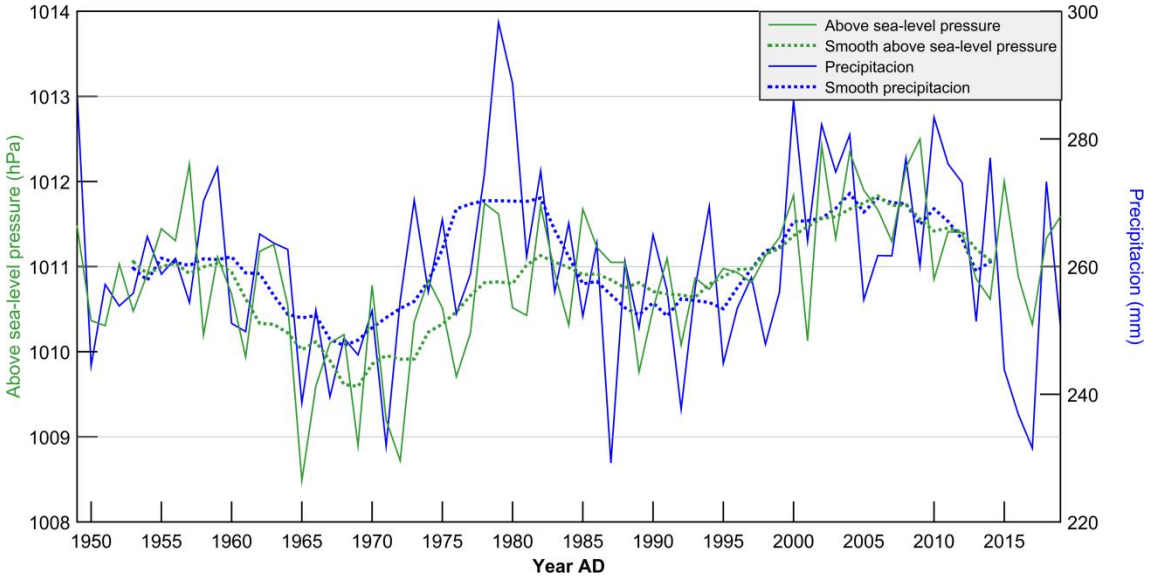

Figure S4. (Left) The lowest interannual above sea-level pressure on 5° S-35° S and 68° W-50° W (D, J, F) (green line) and its decadal smooth line (dotted green line). (Right) The interannual series (D, J, F) of the mean precipitation over the core monsoon region (Vuille et al., 2012) (blue line) and its decadal smooth line (dotted blue line). The Pearson's correlation between interannual series is 0.44 ($p \leq 0.05$) and the Pearson's correlation between decadal series is 0.76 ($p \leq 0.05$). Precipitation data was obtained from CRU TS4.00 dataset.

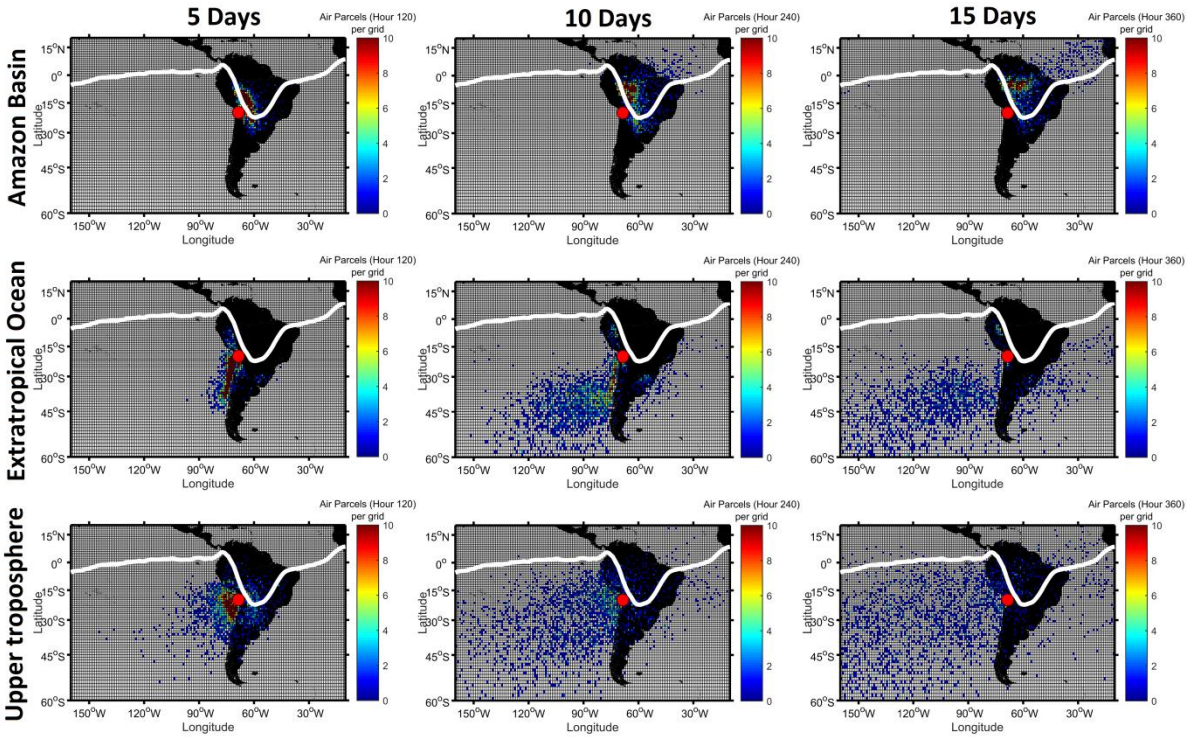

Figure S5. HYSPLIT backward trajectory analysis results for Altiplano (1 hour per day, midday). Air parcel density arriving to the Altiplano. The colorbar scale indicates the total number of air parcels located on each pixel grid (1º x 1º) at hour -120 during the entire study period (DJF, 1950 to 1985). The solid white lines show the mean temporal shape of the Tropical Low-Pressure Belt ± 2σ of its spatial variability.

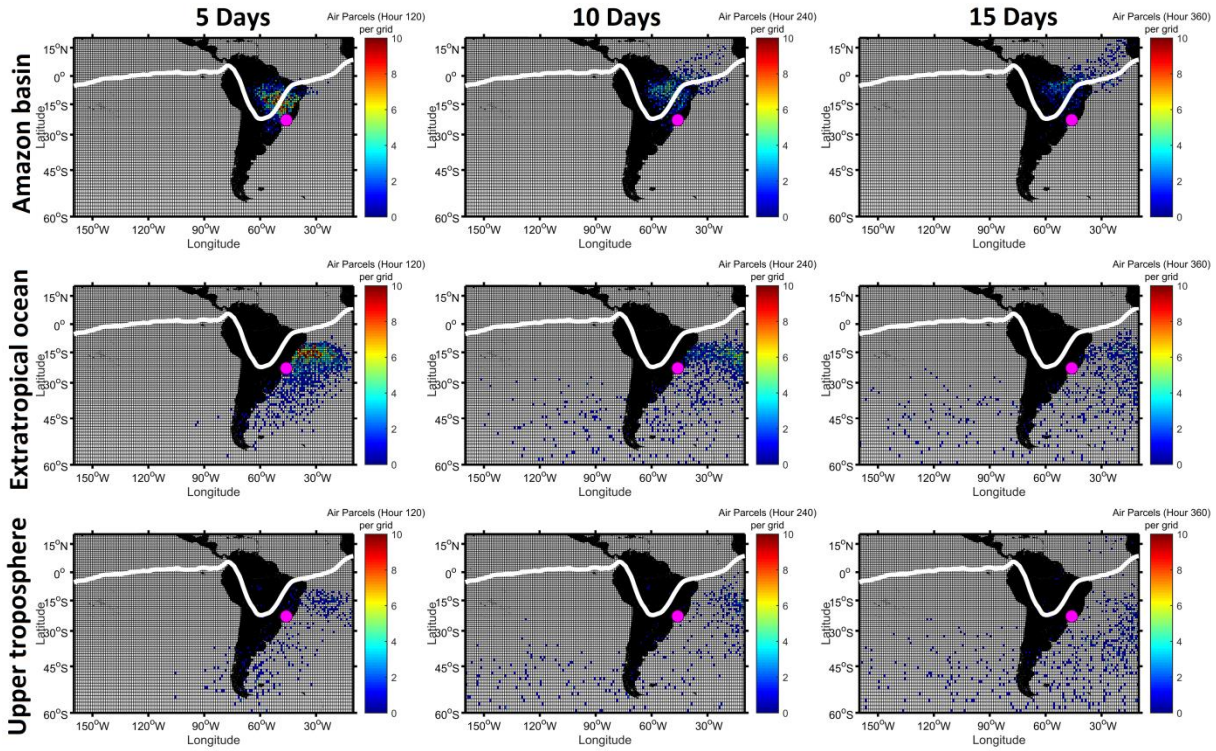

Figure S6. HYSPLIT backward trajectory analysis results for Brazil (1 hour per day, midday). Air parcel density arriving to the Brazil. The colorbar scale indicates the total number of air parcels located on each pixel grid (1º x 1º) at hour -120 during the entire study period (DJF, 1950 to 1985). The solid white lines show the mean temporal shape of the Tropical Low-Pressure Belt ± 2σ of its spatial variability.

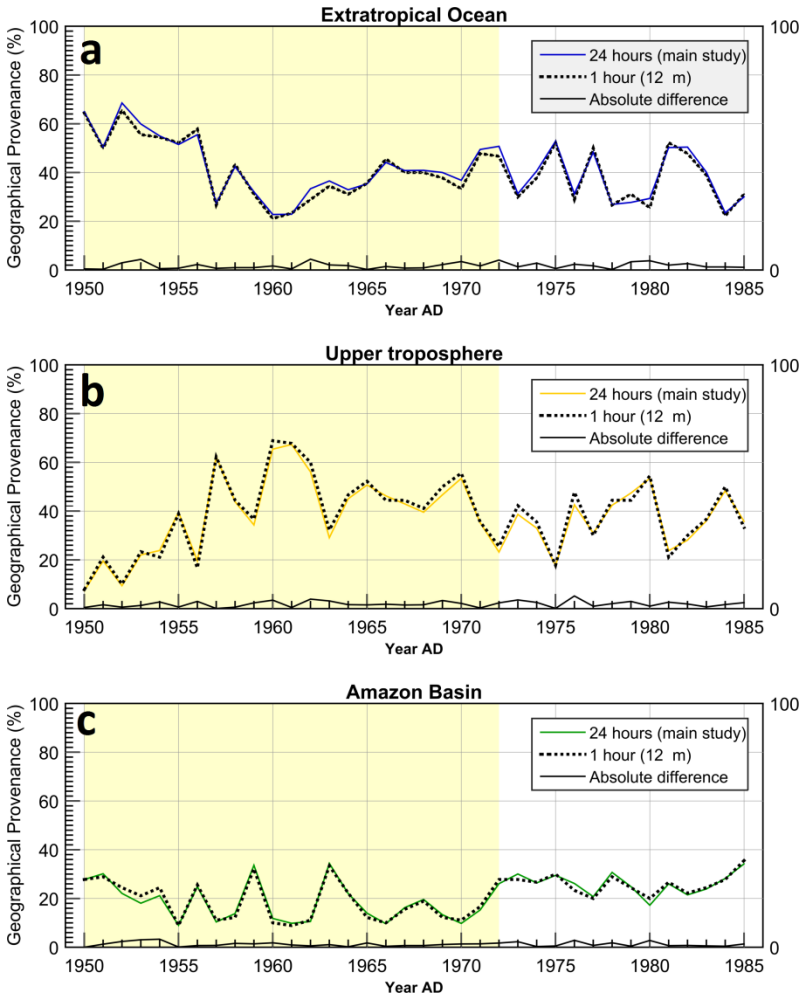

Figure S7. Color lines represents air parcel contribution (%) of each geographical provenance arriving in the Altiplano during the studied period using 24 hours per day: **(a)** Extratropical Ocean, **(b)** Upper troposphere, and **(c)** Amazon basin. Black dotted lines represent the air parcel contribution (%) of each geographical provenance arriving in the Altiplano using one hour per day (midday). Black solid lines show the absolute difference between air parcel contribution (%) derived from 24 hours per day and air parcel contribution (%) derived from 1 hour per day. The shaded yellow area highlights the maximum gradient period of 1950-1972.

Table S1

Linear regression coupled to Monte-Carlo method: MGP (1950-1972)

Amazon contribution vs:	Max R	Min R	Probability (%)
TLPB index I	0.61	0.41	8
Extratropical index I	-0.47	-0.52	0
TLPB index II	0.64	0.41	18.7
Extratropical index II	0.59	0.46	28

Note: Using Monte-Carlo techniques we produce a whole set of possible ^{14}C values for the samples measured and possible coefficient of correlation (R) values. The possible ^{14}C values follow a normal distribution probability between $\pm 2\ \sigma$.

Table S2

Linear regression coupled to Monte-Carlo method: Post-MGP (1973-1985)

Amazon contribution vs:	Max R	Min R	Probability (%)
TLPB index I	0.93	-0.96	2.5
Extratropical index I	0.77	-0.82	1.6
TLPB index II	0.95	-0.96	5.3

Extratropical index II	0.85	-0.66	7

Note: Using Monte-Carlo techniques we produce a whole set of possible ^{14}C values for the samples measured and possible coefficient of correlation (R) values. The possible ^{14}C values follow a normal distribution probability between $\pm 2\ \sigma$.

4.2 Capítulo II

4.2.1 Título manuscrito II: Atmospheric radiocarbon for the period 1950-2019

Quan Hua[1,*], Jocelyn C Turnbull[2,3], Guaciara M Santos[4], Andrzej Z Rakowski[5], Santiago Ancapichún[6,7], Ricardo De Pol-Holz[7], Samuel Hammer[8], Scott J Lehman[9], Ingeborg Levin[8], John B Miller[10], Jonathan G Palmer[11,12], Chris SM Turney[11,12]

[1]Australian Nuclear Science and Technology Organisation, Locked Bag 2001, Kirrawee DC, NSW 2232, Australia

[2]Rafter Radiocarbon Laboratory, GNS Science, Lower Hutt, New Zealand

[3]CIRES, University of Colorado, Boulder, Colorado, USA

[4]Earth System Science, University of California, Irvine, B321 Croul Hall, Irvine CA 92697-3100, USA

[5]Institute of Physics, Center for Science and Education, Silesian University of Technology, 44-100 Gliwice, Poland

[6]Postgraduate School in Oceanography, Faculty of Natural and Oceanographic Sciences, Universidad de Concepción, Concepción, Chile

[7]Centro de Investigación GAIA Antártica (CIGA) and Network for Extreme Environment Research (NEXER), Universidad de Magallanes, Punta Arenas, Chile.

[8]Institut für Umweltphysik, Heidelberg University, INF 229, 69120 Heidelberg, Germany

[9]INSTAAR, University of Colorado, Boulder, Colorado CO 80309-0450, USA

[10]NOAA Earth System Research Laboratory, Boulder, Colorado, USA

[11]ARC Centre of Excellence for Australian Biodiversity and Heritage, School of Biological, Earth and Environmental Sciences, University of New South Wales, NSW 2052, Australia

[12]Chronos ^{14}Carbon-Cycle Facility and Changing Earth, University of New South Wales, NSW 2052, Australia

*Corresponding author. Email: qhx@ansto.gov.au

4.2.2 Estado manuscrito aceptado en la revista Radiocarbon

Declaración de contribución de Santiago Ancapichún Hernández.

Conceptualización, Metodología, Investigación, Análisis formal, Visualización.

ABSTRACT

This paper presents a compilation of atmospheric radiocarbon for the period 1950-2019, derived from atmospheric CO_2 sampling and tree rings from clean-air sites. Following the approach taken by Hua et al. (2013), our revised and extended compilation consists of zonal, hemispheric and global ^{14}C data sets, with monthly data sets for 5 zones (Northern Hemisphere zones 1, 2 and 3, and Southern Hemisphere zones 3 and 1-2). Our new compilation includes smooth curves for zonal data sets that are more suitable for dating applications than the previous approach based on simple averaging (Hua et al. 2013). Our new radiocarbon dataset is intended to help facilitate the use of atmospheric bomb ^{14}C in carbon cycle studies and to accommodate increasing demand for accurate dating of recent (post-1950) terrestrial samples.

KEYWORDS: Bomb radiocarbon; bomb peak; atmospheric carbon dioxide; tree rings; the global carbon cycle

INTRODUCTION

Radiocarbon or ^{14}C is naturally produced in the upper atmosphere by the interaction of the secondary neutron flux from cosmic rays with atmospheric nitrogen-14 (^{14}N; Libby 1952). Following its production and oxidation to carbon

dioxide (CO_2), ^{14}C enters the biosphere and oceans via photosynthesis and air-sea gas exchange, respectively, providing a supply of ^{14}C that approximately compensates for the decay of the existing ^{14}C in terrestrial and marine organisms. This forms the basis for the traditional radiocarbon dating ca. 50,000 years back before 1950.

Radiocarbon is also produced anthropogenically. Atmospheric nuclear weapon testing mostly in the late 1950s and early 1960s produced large fluxes of thermal neutrons, which reacted with atmospheric ^{14}N to form ^{14}C (Libby 1956; Rafter and Fergusson 1957). The excess ^{14}C produced by atmospheric nuclear detonations or bomb ^{14}C was mostly injected into the stratosphere and subsequently transported to the troposphere, which together with fossil-fuel emissions, atmospheric circulation patterns and rapid exchanges between the global carbon reservoirs shaped the tropospheric $\Delta^{14}C$ levels during the past ca. 70 years. We note that $\Delta^{14}C$ used in this paper is the fractionation- and age-corrected deviation from the standard pre-industrial ^{14}C content in atmospheric CO_2, which is the Δ term of Stuiver and Polach (1977). Atmospheric $\Delta^{14}CO_2$ (or atmospheric $\Delta^{14}C$ in short) followed a decreasing trend from ca. 1900 due to the Suess effect (Suess 1955), started increasing in 1955, then reached its maximum levels in 1963-1964 in the Northern Hemisphere (NH) and 1964-1965 in the Southern Hemisphere (SH), and has decreased approximately exponentially since then (e.g. Levin and Hesshaimer 2000; Hua et al. 2003;

Turney et al. 2018). Rapid exchange between the atmosphere, and the terrestrial biosphere and oceans resulted in substantial decreases in atmospheric $\Delta^{14}C$ and increases in $\Delta^{14}C$ of the surface ocean during the mid-1960s to mid-1980s, allowing the use of bomb ^{14}C to study air-sea exchange of CO_2, ocean circulation, and the global carbon cycle (Nydal 1968; Oeschger et al. 1975; Druffel and Suess 1983; Levin and Hesshaimer 2000; Randerson et al. 2002; Hua et al. 2003; Key et al. 2004; Krakauer et al. 2006; Naegler 2009; Levin et al., 2010). Large differences in atmospheric $\Delta^{14}C$ levels during the post-1955 period also enable the use of bomb ^{14}C as a powerful dating tool, which can deliver dating accuracies of one to a few years for recent terrestrial samples (Hua and Barbetti 2004).

Several compilations of recent atmospheric □^{14}C for use in carbon cycle modelling and/or age calibration have been carried out previously. Based on a small number of atmospheric, tree-ring and organic samples, Tans (1981) performed the earliest compilation of recent atmospheric □^{14}C for the period 1954-1977 for use in carbon model calculations. Recently, Graven et al. (2017) created annual atmospheric □^{14}C datasets for 3 regions (NH north of 30°N, tropics between 30°N-30°S and SH south of 30°S) for the period 1850-2015 for use in the Coupled Model Intercomparison Project 6 (CMIP6). For the period 1950-2015, this compilation was derived from tree-ring □^{14}C data and a large number of atmospheric □^{14}C records. Goodsite et al. (2001) brought together

recent atmospheric $\Delta^{14}C$ for the NH for use in ^{14}C dating of their peat cores from Denmark. This atmospheric $\Delta^{14}C$ curve was based on a limited number of atmospheric sampling, tree-ring records and organic samples north of 27°N during 1950-1998. In addition, Hua and Barbetti (2004) compiled summer and monthly atmospheric $\Delta^{14}C$ data for the period 1955-2001 for use in carbon cycle modelling and ^{14}C dating, respectively. The authors defined zonal distributions of bomb $\Delta^{14}C$ (3 zones in the NH and 1 zone for the SH) during the bomb peak period, reflecting major zones of atmospheric circulation. This compilation, derived from a large number of atmospheric and tree-ring records and measurement of organic materials, provided zonal, hemispheric and global summer $\Delta^{14}C$ data sets, and 4 zonal data sets with (mostly) monthly resolution. Hua et al. (2013) subsequently defined another zone for the SH, increasing the number of discrete atmospheric zones from 4 to 5. They refined the dataset of Hua and Barbetti (2004), resulting in compiled summer and (mostly) monthly $\Delta^{14}C$ data sets for 1950-2011.

In this paper, we present a new compilation of atmospheric $\Delta^{14}C$ for the period 1950-2019, which is an extended and revised version of the compilation of Hua et al. (2013) with the addition of recent data from 4 atmospheric sampling records and 11 new tree-ring records. We provide two datasets, one for summertime and the other with monthly resolution for each year of record. The compiled zonal, hemispheric and global summer data are intended for use in

carbon model calculations, while zonal monthly data were constructed to facilitate the dating of recent organic materials. We also incorporate curve fitting to smooth the data and make it more appropriate for dating applications, because this method delivers continuous datasets with suppressed outliers and clear seasonal cycles for the periods covered by atmospheric $\Delta^{14}C$ records.

DATA SETS USED FOR THE COMPILATION

Selection Criteria

The current compilation is based on representative radiocarbon measurement series from tree rings and direct atmospheric CO_2 sampling from clean-air sites and rural areas, which are not strongly affected by local fossil-fuel emissions or nuclear facilities. This primary data selection criterion is similar to that adopted by Hua and Barbetti (2004) and Hua et al. (2013).

For tree rings, two additional selection criteria were employed. One of them is on tree-ring chronologies to ensure that selected tree rings are properly dated. This criterion involves tree-ring dating by (i) using the dendrochronological method of cross-dating, which is comprised of multiple trees and often multiple tree radii or tree cores per tree collected, measured and their ring-widths pattern matched from the same location (e.g., Speer 2010), or

(ii) ring counting within the sample by applying a similar type of dendro-analytical process to match ring-width variations within two or more tree radii. The other criterion relates to tree-ring pre-treatment for radiocarbon analysis. Only tree rings with sufficient pre-treatment to remove non-structural carbon (NSC) compounds (Carbone et al. 2013), and extract holocellulose or alpha-cellulose, which mostly reflects atmospheric $\Delta^{14}C$ at the time of tree growth, were selected for analysis.

Atmospheric CO_2 sampling

Atmospheric $\Delta^{14}C$ data sets selected for the study include those used in Hua et al. (2013) and recent data from Schauinsland (Germany; 48°N, 8°E; 2004-2016; Hammer and Levin 2017), Jungfraujoch (Switzerland; 46°N, 8°E; 2004-2019; Hammer and Levin 2017; Emmenegger et al. 2020), Niwot Ridge (USA; 40°N, 106°W; 2007-2018; Lehman et al. 2013; Lehman and Miller 2019), and Wellington (New Zealand; 41°S 175°E; 2012-2019; Turnbull et al. 2017). Revisions of the Wellington data for the periods 1990-1993 and 1995-2005, reported in Turnbull et al. (2017), were also incorporated into this compilation.

As there are strong influences of fossil-fuel combustion in winters for Kasprowy Wierch from Poland (49°N, 20°E) in Central Europe (Zimnoch et al. 2012), only the summer $\Delta^{14}C$ data from this record was included in Hua et al. (2013). Because this record is quite short, spanning only 2008-2009, and there

are now 2 additional data sets from Central Europe (Schauinsland and Jungfraujoch), the decision was made to exclude the Kasprowy Wierch data set from the current study.

Tree rings

Our study employs 22 tree-ring records, consisting of 11 from Hua et al. (2013) and 11 new ones. Four tree-ring data sets employed in Hua et al. (2013) were omitted from our compilation as they failed to satisfy our selection criteria. The Kiel record (Germany; 54°N, 10°E; 1955-1964) is one of the rejected series because there was no supporting information on the tree-ring dating (Willkomn and Erlenkeuser 1968) and our pre-treatment criterion was not satisfied (only acid-alkali-acid (AAA) pre-treatment was used; H. Erlenkeuser, personal communication June 2020). The other three data sets all failed the tree-ring pre-treatment criterion. They include Gifu (Japan; 36°N, 138°E; 1955-1959; Nakamura et al. 1987a,b) and Saigon (Vietnam; 11°N, 107°E; 1962, 1964-1967; Kikata et al. 1992, 1993) using the AAA pre-treatment method, and Agematsu (Japan; 36°N, 138°E; 1960-1967, 1969) using Soxhlet solvent extraction followed by AAA (Muraki et al. 1998).

Recently published tree-ring ^{14}C data sets included in our compilation are Scots pine (*Pinus sylvestris*) from central Norway (63°16'N, 10°27'E, 1953-1965; Svarva et al. 2019), oak (*Quercus borealis*) from Eastern Jutland, Denmark

(56°11'N, 10°13'E; 1954-1970; Kudsk et al. 2018), white oak (*Quercus garryana*) from western Oregon, USA (45°07'N, 123°27'W; 1950-1952 and 1960-1969; Cain et al. 2018), Douglas fir (*Pseudotsuga menziesii*) from northeastern Mexico (23°49′N, 99°50′W; 1950-2002; Beramendi-Orosco et al. 2018), Japanese cedar (*Cryptomeria japonica*) from Fukushima, Japan (37.01°N, 140.81°E; 1984-1994; Xu et al. 2015), *Polylepis tarapacana* from Irruputuncu, Altiplano, Chile (22°S, 68°W; 1950-2014; Ancapichún et al. 2021), *Araucaria angustifolia* from Camanducaia, Brazil (22°50'S, 46°04'W; 1927-1997; Santos et al. 2015), *Pinus radiata* and *Agathis australis* from Wellington, New Zealand (41°S 175°E; 1950-2011; Turnbull et al. 2017), and *Dracophyllum spp.* from Campbell Island, New Zealand (52.554°S, 169.133°E; 1953-2011; Turney et al. 2018).

Two data sets on oak (*Quercus borealis*) from Uppsala, Sweden (60°0'N, 17°38'E; 1951-1967 and 1980-1981; Olsson and Possnert 1992) and Sitka spruce (*Picea sitchensis*) from Washington state, USA (47°57'N, 124°33'W; 1962-1964; Grootes et al. 1989), which were inadvertently omitted from the previous compilations (Hua and Barbetti 2004; Hua et al. 2013), are now also included in the current study. The Washington Sitka spruce sub-annual tree-ring samples have recently been remeasured at the National Laboratory for Age Determination in Trondheim. These new, unpublished $\Delta^{14}C$ results are similar to those published in Grootes et al. (1989) but have much higher precision (H. Svarva, M.-J. Nadeau and P. Grootes, personal communication July 2020). We,

therefore, used these new data instead of the published original data for our compilation.

Kudsk et al. (2018) compared $\Delta^{14}C$ of earlywood (EW) and latewood (LW) of their Danish oak (1954-1970) record and the Swedish oak record (1951-1967 and 1980-1981) of Olsson and Possnert (1992) with the compiled monthly NH zone 1 data of Hua et al. (2013) derived from atmospheric sampling (1959-2009). They reported that the LW fraction of the two records formed in June-July (mid-summer), while the EW fraction of the Danish and Swedish records contained carbon assimilated in spring and probably from the previous year, respectively. As the timing of the LW formation is similar to that of tree-ring growth seasons (see later discussion), only the LW ^{14}C data of these two oak records were included in the compilation.

Xu et al. (2015) measured ^{14}C in EW, LW and (whole) annual rings of a Japanese cedar located ca. 50 km southwest of the Fukushima Dai-ichi Nuclear Power Plant during the period 1984-2013 to see whether there was a significant release of anthropogenic ^{14}C from the power plant accident in 2011. Only the tree-ring ^{14}C data for the period before the accident, which agree well with the compiled NH zone 2 data of Hua et al. (2013), are included here. To be consistent, the data of the whole ring in 1994 and LW fraction from 1984 to 1989 were used although $\Delta^{14}C$ values of these LW samples and their associated EW samples are similar.

For the sub-annual Norwegian tree-ring record (8 incremental samples per year) of Svarva et al. (2019), the first and last increments of each annual tree ring were excluded from our analyses. This is because of the possibility of cross-ring-boundary sampling resulting in unreliable $\Delta^{14}C$ values, especially for the bomb peak period (Svarva et al. 2019).

All atmospheric and tree-ring ^{14}C records used for our compilation are shown in Table 1 and illustrated in Figure 1.

ZONAL ATMOSPHERIC □^{14}C AND BOUNDARIES

As a result of aboveground nuclear detonations mostly in the NH, the majority of bomb ^{14}C resided in the northern stratosphere during the years of atmospheric nuclear testing and several years after the 1963 Nuclear Test Ban Treaty (ca. 1955-1967) (Telegadas 1971; Hesshaimer and Levin 2000). Bomb ^{14}C was injected into the troposphere through the mid- to high-latitude tropopause gaps during the springtime of each hemisphere. The seasonality of this exchange led to a ^{14}C disequilibrium between the stratosphere and the troposphere during this period (Hesshaimer and Levin 2000), which was employed for constraining parameters related to atmospheric transport across the tropopause (Hesshaimer 1997). At the same time, the excess-^{14}C injection from the stratosphere also created large ^{14}C gradients between tropospheric

high and low latitudes, and between the northern and southern troposphere (Hua and Barbetti 2007; Hua et al. 2012), which are valuable for modelling tropospheric air mass transport. Excess ^{14}C was subsequently transferred southwards and the spatial distribution of atmospheric radiocarbon during this period is strongly influenced by atmospheric transport and mixing through the large-scale wind systems including monsoon circulation (Hua and Barbetti 2007; Levin et al. 2010; Hua et al. 2012). This spatial distribution seems to be further characterized by 5 zones of different $\Delta^{14}C$ levels (NH zones 1, 2 and 3, and SH zones 3 and 1-2; see Figure 1) that decrease from north to south (Hua et al. 2013). NH zone 1 in northern mid- to high latitudes, where most of the excess ^{14}C from the stratosphere was injected into the troposphere (e.g., Levin et al. 1985; Nydal and Gislefoss 1996), had the highest $\Delta^{14}C$ values during this period. Meanwhile, at the same time, SH zone 1-2 covering most of the SH recorded the lowest $\Delta^{14}C$ values, and the other zones recorded intermediate $\Delta^{14}C$ levels. The intra-hemispheric differences in atmospheric $\Delta^{14}C$ were substantially reduced in the late 1960s and early 1970s (Telegadas 1971; Manning et al. 1990) as a result of atmospheric mixing, and from 1973 onwards there have been similar $\Delta^{14}C$ values between locations within each hemisphere (Hua et al. 2013). Similar to Hua et al. (2013), in this current study we employed the five-zone pattern of atmospheric $\Delta^{14}C$, which broadly reflects major zones of

atmospheric circulation, with different zonal $\Delta^{14}C$ levels for 1950-1972 and very similar zonal $\Delta^{14}C$ values in each hemisphere for 1973-2019.

Figure 1 shows the zonal boundaries. The boundary between NH zone 2 and NH zone 3 is defined as the mean position of the convergence of northeasterly trade winds from the northern subtropics and winds from the northern and southern tropics during June, July and August (JJA). This convergence, known as the Inter-Tropical Convergence Zone (ITCZ), is associated with a low-pressure band (tropical low pressure belt (TLPB); Ancapichún et al. 2021). However, as ITCZ is a marine phenomenon and is not well defined over the continents (e.g., Vuille et al 2012; Marsh et al. 2018), in this paper we use TLPB instead of ITCZ concerning the wind convergence associated with the low-pressure band. During December, January and February (DJF), the TLPB has a southward position, which is the convergence of winds from the northern tropics and easterly winds from the southern tropics and subtropics (Hogg et al. 2020; Ancapichún et al. 2021). The mean DFJ position of the TLPB in the eastern and central Pacific and the Atlantic is located in the NH. Therefore, for these regions SH zone 3 was not defined and the equator was employed as the boundary between NH zone 3 and SH zone 1-2. The mean DJF position of the TLPB in the western Pacific, the Indian Ocean and South America is located in the SH and was used as the boundary between SH zone 3 and SH zone 1-2. It is worth noting that lower $\Delta^{14}C$ values over the

Southern Ocean, related to upwelling of ^{14}C-depleted deeper waters, (ca. 3-6‰ during the late 1980s – the 2000s) compared to SH sub-tropical and temperate sites are well documented (Levin et al. 2010; Graven et al. 2012b; Turney et al. 2016) and there is some suggestion that it would be appropriate to define these areas as two separate zones. However, for the intended application of dating terrestrial materials, this applies only to a very limited subset of locations south of ca. 50°S. In addition, only a small amount of data is currently available for this region and highlights the need for further work over the Southern Ocean. Therefore, in the current compilation, results from SH zones 1 and 2 are binned into a single $\Delta^{14}C$ zone, SH zone 1-2.

The new tree-ring record from Irruputuncu, Altiplano, Chile at 20°S, 68°W (Ancapichún et al. 2021) is located close to the western edge of the South American 'V-shaped' boundary between SH zone 3 and SH zone 1-2 derived from the NCEP/NCAR sea level pressure data (Kalnay et al. 1996) (Figure 1). Despite a minor portion of the air parcels (21%) reaching Irruputuncu from the Amazon basin (SH zone 3), its tree-ring $\Delta^{14}C$ values are similar to those from Wellington, New Zealand (Ancapichún et al. 2021) located in SH zone 1-2. Thus, appropriate development of new tree-ring records from low to mid-latitude regions is necessary as a means to better define the areas affected by changes in the mean TLPB position.

The boundary between NH zone 1 and NH zone 2 was previously defined based on limited ^{14}C records in mid- to high northern latitudes during the bomb peak period. According to Hua and Barbetti (2004) and Hua et al. (2013), this boundary around 40°N is located south of China Lake (CL; 35°32'N, 117°41'W) but north of Santiago de Compostela (42°53'N, 8°26'W). With the recent availability of the tree-ring record from western Oregon, USA (45°07'N, 123°27'W; 1960-1969; Cain et al. 2018) and the inclusion of a short tree-ring data set from Washington state, USA (47°57'N, 124°33'W; 1962-1964; Grootes et al. 1989), the position of this boundary in north-western America can be refined.

Hua and Barbetti (2004) suggested that the CL atmospheric record (1963-1968) belonged to NH zone 1, based on the fact that the average of monthly $\Delta^{14}C$ differences between CL and NH zone 1 data, and between CL and NH zone 2 data are negligible and large, respectively. It is worth noting that higher $\Delta^{14}C$ values of the CL record compared to those of other atmospheric data sets at similar latitudes in NH zone 2 are not likely due to influences of nearby Nevada bomb tests on CL (see discussion later).

Figure 2 shows monthly $\Delta^{14}C$ differences between NH zone 1 and CL, and between NH zone 2 and CL. The CL $\Delta^{14}C$ values are similar to NH zone 1 values and higher than NH zone 2 values mostly during winter-spring (grey stripes in Figure 2), but lower than NH zone 1 values and similar to NH zone 2

values during summer-autumn (white stripes in Figure 2) except for late 1967-1968 due to reduced $\Delta^{14}C$ differences between regions in the late 1960s. These observations support large seasonal variations of the polar jet in north-western America as discussed in the literature (e.g., Barton and Ellis 2009; Pena-Ortiz et al. 2013). They also indicate that during the bomb peak period the polar jet moved southwards as far as south of CL in winter-spring and CL received air masses from the north containing higher $\Delta^{14}C$ values than southern air-masses, while in summer-autumn the polar jet travelled northwards resulting in a contribution of the southern air masses to CL.

In contrast, an oak tree from western Oregon, located northwest of CL, with radial growth during spring-late autumn has $\Delta^{14}C$ values close to those of NH zone 2 rather than NH zone 1 (Cain et al. 2018; Figure 3). The authors used the Pacific North American (PNA) index, representing a record of large-scale weather patterns that describe the placement of the polar and sub-tropical jets, to explain some relatively low values of their tree-ring $\Delta^{14}C$. They showed that monthly PNA index values for March-June were negative in 1962-1964, coinciding with relatively low tree-ring $\Delta^{14}C$ values during April-June of 1962-1964. This suggests during this period both the polar and sub-tropical jets moved northwards and their tree rings reflected carbon uptake from air masses coming from the south containing lower bomb $\Delta^{14}C$ values.

Furthermore, $\Delta^{14}C$ values of Sitka spruce tree rings from Washington state (Grootes et al. 1989) located north of the Oregon tree rings are similar to NH zone 1 values based on atmospheric records (Figure 3). Large seasonal variation in the position of the polar jet in north-western America discussed above means that the boundary between NH zone 1 and NH zone 2 varies seasonally. However, with the $\Box^{14}C$ data during the bomb peak currently available for this region (CL atmospheric record, and Oregon and Washington tree-ring data) and for our practical purposes, the boundary between NH zone 1 and NH zone 2 is considered to be located between the two tree-ring sites and south of CL (see Figure 1). More tree-ring records in north-western America are useful for further refinement of the position of the boundary between NH zone 1 and NH zone 2 in this region.

One may argue that higher $\Delta^{14}C$ values of the CL record (1963-1968) compared to those of other atmospheric data sets at similar latitudes, belonging to NH zone 2, are due to influences of Nevada bomb tests on CL. There were quite a number of low-yield atmospheric nuclear bomb tests at Nevada (36.6 – 37.2°N, 115.9 – 116.4°W) during 1951-1958 and 1962 (UNSCEAR, 2000). In 1962, there were only 4 atmospheric nuclear weapon tests in July with a detonation yield ranging from 5 to 20 kton each. The Nevada test sites are located northeast of CL (35°32'N, 117°41'W). Low-yield atmospheric nuclear bomb tests have a tendency to substantially contribute to local/regional areas

(e.g., Enting 1982). If this were the case for these Nevada bomb tests in 1962, their contribution to CL would be clearly seen in 1962 and approximately one year after the tests (i.e., 1963). This is because atmospheric transport is quite fast, which is ca. 1 year from northern mid-latitudes to northern tropics based on the timing of the bomb ^{14}C peaks in atmospheric sampling (August 1963 in Vermunt, Austria (Levin and Kromer 2004) and July 1964 in Dakar, Senegal (Nydal and Lövseth 1996)) for example. However, the two earliest CL $\Delta^{14}C$ values available in 1963 are similar to NH zone 2 values (Figure 2). In addition, CL $\Delta^{14}C$ values are higher than NH zone 2 values during winter-spring seasons in 1964-1965 (Figure 2), 2-3 years after the tests. These indicate that relatively high CL $\Delta^{14}C$ values during the bomb peak period are unlikely due to the contribution of the 1962 Nevada nuclear bomb tests.

COMPILATION METHODS

Timing of tree-ring growth seasons

Growth seasons of different tree-ring species in different regions employed in our compilation are not identical, but they are similar (e.g., Hua et al. 2012; Cain et al. 2018; Turney et al. 2018; Svarva et al. 2019; Ancapichún et al. 2021). The duration of growing seasons can also vary slightly from one year to another. However, tree growth follows a similar pattern of slow increment at

the start (early spring to early summer) and end (late summer to autumn) of a growing season, while fast increment occurs during summer (Grootes et al. 1989; Hua et al. 2000; Turnbull et al. 2017; Cain et al. 2018; Kudsk et al. 2018; Svarva et al. 2019). This also applies to tropical tree rings used in the current compilation for which most growth occurs in summer rainy seasons (e.g., Hua et al. 2000, 2012). In addition, for each annual ring, wood material away from the ring boundaries is usually sampled for ^{14}C analysis (e.g., Hua et al. 1999, 2012) to avoid potential cross-ring-boundary issues. Thus the material of each ring selected for ^{14}C analysis is mainly the portion of wood growing in summer in both hemispheres (May-August or the middle of the current year for the NH, and November-February or the beginning of the following year for the SH). This simple approach allows for estimation of hemispheric and global summer means from tree-ring $\Delta^{14}C$ values and associated atmospheric $\Delta^{14}C$ values in addition to the construction of the zonal estimates.

Compiled data

Our compilation provides both summer and monthly results. The summer data were derived from atmospheric sampling and tree-ring records using a simple averaging method. Monthly data were primarily based on atmospheric sampling, with tree-ring data only used when atmospheric CO_2 data were not available, mostly during the pre-bomb and early bomb period. A curve fitting method was employed to construct monthly results.

Summer data

Zonal, hemispheric and global summer data sets were compiled. Five separate zonal data sets (3 for the NH and 2 for the SH) were constructed for the period 1950-1972. Due to similar $\Delta^{14}C$ values between locations in each hemisphere from 1973 onwards (Hua et al. 2013), 3 identical zonal data sets for the NH and 2 identical zonal data sets for the SH were compiled. We modified the methods employed by Hua et al. (2013) for the construction of these summer data sets, which are described below.

The mean value for summers (May-August for the NH (Hua and Barbetti 2004; Hammer and Levin 2017) and November-February for the SH (Hua and Barbetti 2004)) for an atmospheric $\Delta^{14}C$ record for a particular year was calculated only if there were data available for at least 3 out of 4 months for the season. The mean summer value for a particular zone in a particular year was then calculated with weight being the uncertainty associated with the summer mean of the individual record (atmospheric sampling or tree rings).

As the surface areas covered by the three NH zones are different in size (Figure 1), summer mean values for the NH for the period 1950-1972 were calculated from the 3 zonal summer means, with weights being the percentages of zonal surface areas (ca. 17%, 46%, and 37% for NH zones 1, 2, and 3, respectively). The same approach was employed for the calculation of summer

mean values for the SH for 1950-1972 with the percentages of zonal surface areas for SH zones 3 and 1-2 being ca. 15% and 85%, respectively. For the period 1973-2019, hemispheric summer mean values are actual zonal summer values.

Two zonal (SH zones 3 and 1-2) data sets for boreal summers were also compiled to construct the global boreal summer data set. For 1950-1972, the global boreal summer means were calculated using the 5 zonal (boreal summer) data sets with weights being the percentages of zonal surface areas mentioned above. For the period 1973-2019, the global boreal summer means were calculated using the 2 hemispheric data sets for boreal summers.

Monthly data

Five zonal monthly data sets were constructed using the ccgcrv curve fitting method (Thoning et al. 1989) to output smooth curves at monthly resolution. The data used for the curve fitting were primarily atmospheric records. When atmospheric records were not available (e.g., mostly the pre-bomb and early bomb period), average zonal summer data and/or sub-annual tree-ring data were employed. In addition, to avoid possible discontinuities between our NH monthly data sets and IntCal20 curve (Reimer et al. 2020) when they are used together for dating, we included the raw IntCal20 data for 1940-1950 in our curve fitting. The same approach was applied for the

construction of the SH monthly data sets by including the raw SHCal20 data for 1940-1950 (Hogg et al. 2020).

To develop the smooth curves, all data for a given zonal data set were compiled, then a smooth curve was created following the method of Turnbull et al. (2017). Each data set was split into six time intervals (1940-1955, 1954-1966, 1965-1973, 1972-1990, 1989-2006 and 2005-2020) to allow the seasonal cycle and long-term trend to vary through time. A Monte-Carlo method with 1,000 iterations was used to create a smooth curve for each time interval, with uncertainty assigned from the scatter of the Monte-Carlo simulation. For each of the 1,000 simulations, the ^{14}C value for each date sampled is re-assigned randomly according to the normal distribution described by the mean and reported standard deviation of the measurement. A curve is fitted to each of the 1,000 simulations, then the mean and standard deviation are calculated for each time step from the spread of the 1,000 fitted curves. In this simulation, input data was at its native resolution (i.e. every raw data point was included), and the fitted curves were output at monthly resolution.

Finally, all sixtime intervals were spliced together, averaging across the overlap periods, to produce a smooth curve fit for the entire period. Alternative curve fitting methods do allow varying seasonal cycles (e.g., Pickers et al. 2015), but require gap filling with interpolated data, which introduces a different set of biases.

For the pre-bomb and early bomb period and a short period 1970-1972 in NH zone 3 when only tree-ring data were available (except for SH zone 1-2 where atmospheric data were available), it is not possible to derive a seasonal cycle from the (summertime only) tree-ring data. It is also inappropriate to assign the seasonal cycle for the latter time period, as it is clear that the $\Delta^{14}C$ seasonal cycle changed dramatically with the inputs of bomb ^{14}C. Therefore, we chose not to assign any seasonal cycle to these periods, instead of interpolating the interannual trend to provide monthly $\Delta^{14}C$ values.

RESULTS AND DISCUSSION

Many plants and some animals depend on the carbon formed during the summer growing season, making the compiled zonal summer data sets appropriate for use in radiocarbon dating of these sample types. However, for other plants and vegetation, whose main growing seasons are different such as early-spring for leaves, autumn plants/seeds and winter wheat/rice, the zonal summer data sets are not useful for dating of these materials. Vegetation in the aseasonal tropics between ~5°N and ~5°S, growing almost all year round, is also in this category. In addition, humans and animals, who consume foods mostly imported from around the globe, may not be accurately dated using the zonal summer data sets. We, therefore, take a simple and consistent approach,

and recommend the compiled zonal monthly data sets should be used for dating of all recent samples.

Similar to the previous compilations (Tans 1981; Hua and Barbetti 2004; Hua et al. 2013, Graven et al. 2017), we aimed to provide compiled $\Delta^{14}C$ data sets with annual resolution for use in carbon cycle modelling. Summer data sets were chosen as their raw data were the only data available for the whole period of interest, 1950-2019. In addition, an advantage of these summer data sets is that they can be extended back in time using compatible tree-ring based IntCal20 or SHCal20 data, if longer data sets are required for modelling studies. The zonal monthly data sets were constructed for dating purposes as discussed above. However, they can be used for carbon modelling if it requires higher temporal resolution.

Compiled zonal atmospheric $\Delta^{14}C$ data sets for NH zones 1, 2 and 3 for boreal summers (May-August) for the period 1950-2019 are presented in Supplementary Table S1a, while compiled zonal atmospheric $\Delta^{14}C$ data sets for SH zones 3 and 1-2 for austral summers (November-February) are reported in Supplementary Table S1b. All the compiled zonal $\Delta^{14}C$ data sets are illustrated in Figure 4a. Compiled hemispheric $\Delta^{14}C$ data sets for boreal and austral summers are also reported in Supplementary Table S1a and Table S1b, respectively, while the compiled global atmospheric $\Delta^{14}C$ data set for boreal summers is presented in Supplementary Table S1c. The compiled hemispheric

and global atmospheric $\Delta^{14}C$ data sets for 1950-2019 are also depicted in Figure 4b.

Our compiled summer $\Delta^{14}C$ data sets have good agreement with those of Hua et al. (2013) for the overlapping periods (1950-2010 for the NH and 1950-2011 for the SH; see Supplementary Figures S1a-h). The compilation by Graven et al. (2017) for 1950-2015 consists of annual $\Delta^{14}C$ data for 3 different regions, NH north of 30°N (NH>30°N), 30°N-30°S and SH south of 30°S (SH>30°S), with the timing of each data point being in the middle of a year. For ease of comparison with our compiled data for the SH with each data point being the beginning of the following year, the compiled data for 2 regions 30°N-30°S and SH>30°S from Graven et al. (2017) were linearly interpolated (see Supplementary Figures S2c-d). In general, we find good concordance between our and their compiled $\Delta^{14}C$ data (Supplementary Figures S2a-d), although the spatial coverage of the study regions in these two studies are not the same.

Compiled zonal data sets at monthly resolution for 1940-2019, in $\Delta^{14}C$ and $F^{14}C$ (Reimer et al. 2004), are reported in Supplementary Tables S2a-e. These data in $F^{14}C$ are also shown in Figure 5. The ccgcrv curve fitting method used for the compilation of monthly data sets in this study has a couple of advantages compared to the weighted average methods used by Hua et al. (2013). First, the curve fitting method smooths the noise associated with the relatively large uncertainties assigned to individual measurements, resulting in

smoother compiled data with clear seasonal cycles for the periods covered by atmospheric $\Delta^{14}C$ records (Figures 5 and 6a-e). Second, the compiled extended monthly data sets of Hua et al. (2013) have different temporal resolutions with monthly data for the periods covered by atmospheric $\Delta^{14}C$ records and annual summer data outside these periods. Meanwhile, the compiled data sets in the current study have a monthly resolution for the whole study period of 1940-2019 (see Figures 6a-e; Supplementary Tables S2a-e). Thus the curve fitting method used in the present study resulted in improved zonal monthly data sets and consequently improved radiocarbon dating of recent terrestrial samples.

Good agreement between the compiled monthly data sets and IntCal20 or SHCal20 is observed for the overlapping period (1940-1950) (Supplementary Figures S3a-e), indicating the continuity between these data sets when they are used together for radiocarbon dating. We recommend that when calibrations span the pre- and post-bomb periods, users replace the IntCal20 or SHCal20 data for 1940-1950 with the compiled monthly data for 1940-1950 to avoid discontinuities between the datasets.

The compiled monthly data sets for the NH zones in this study agree well with those of Hua et al. (2013) for the overlapping period (1950-2009) (Figures 6a-c). It should be noted that the Monte-Carlo simulation associated with the curve fitting method assigns smaller uncertainties than the standard deviations that were assigned in the previous study.

For the SH zones, a similar pattern is observed except during 1990-1993 (Figures 6d-e). With the revision of the Wellington atmospheric □ ^{14}C record for 1990-1993 (Turnbull et al. 2017), our compiled monthly $F^{14}C$ data for the SH zones for this period are lower than those of the 2013 data (Figures 6d-e). This means anomalously high $F^{14}C$ values for this period, which previously appeared in the 2013 data for the SH zones, no longer exist in our compiled monthly data. Similarly, anomalously high $\Delta^{14}C$ values for 1990-1993, previously appearing in the compiled summer data of Hua et al. (2013) for the SH zones, are also not evident in our compiled summer data (see Supplementary Figures 2d-e).

The compiled monthly $F^{14}C$ data are mostly based on atmospheric records, but they are derived from tree-ring records when atmospheric sampling is not available (Figures 6a-e). The use of tree-ring data to extend the compiled monthly atmospheric-based data is an advantage. However, tree rings do not fully represent atmospheric $\Delta^{14}C$ levels when these levels change substantially and quickly, although tree-ring $\Delta^{14}C$ follows atmospheric $\Delta^{14}C$ very well with a delay of no more than ca. 2 weeks for Washington Sitka spruce (Grootes et al. 1989) or 5-6 weeks for Tasmanian Huon pine (Hua et al. 2000). For example, atmospheric $F^{14}C$ (and consequently $\Delta^{14}C$) in NH zone 1 peaks in 1963 (Figure 5) but tree-ring $\Delta^{14}C$ in this zone reaches its maximum in 1964 (Figure 4a). Another example, which can be seen in Figure 3, indicates that sub-annual tree-ring $\Delta^{14}C$ for the NH zones 1 and 2 during 1963-1964 do not cover the full

ranges of their associated atmospheric $\Delta^{14}C$ values. These differences are likely due to growing seasons, which are only a portion of a year, seasonal averaging or insufficient sampling resolution for tree rings. Substantial changes in atmospheric $\Delta^{14}C$ levels occur during the early bomb period and the bomb peak period. During these periods, needles/leaves of early spring, autumn plants/seeds and winter wheat/rice incorporate atmospheric $\Delta^{14}C$ values at the time of growth, which may be substantially different from those of annual and/or sub-annual tree rings. This issue, therefore, should be considered or recognized when dating such samples for the periods that the compiled monthly ^{14}C data are derived from tree-ring records such as 1955-1959 for NH zone 1, 1955-1963 for NH zones 2 and 3, and especially 1955-1972 for SH zone 3 (see Figures 6a-d).

After reaching its peak levels, atmospheric $\Delta^{14}C$ in the NH and SH has decreased since 1963-1964 and 1964-1965, respectively. Decreases in atmospheric $\Delta^{14}C$ from the mid-1960s to mid-1980s are mainly due to rapid exchange between the atmosphere and the biosphere and oceans (Oeschger et al. 1975; Druffel and Suess 1983; Levin and Hesshaimer 2000), while combustion of fossil fuels free of ^{14}C is the main causal factor for the $\Delta^{14}C$ decline since the late 1980s and early 1990s (Levin et al. 2010; Graven et al. 2012a). Since the early and late 2000s, the atmospheric $\Delta^{14}C$ values have been lower than those of the surface waters in the North and South Pacific Gyres,

respectively, indicating the oceans might become a net ^{14}C source (instead of a net ^{14}C sink) of the atmosphere (Andrews et al. 2016, 2021; Wu et al. 2021).

The last data points in our compiled monthly data at 2019.375 have respective $F^{14}C$ values of 1.0084 and 1.0195 for the NH and SH (see Supplementary Tables 2a-e), which are very close to the pre-bomb $F^{14}C$ value of slightly lower than 1. This indicates that clean-air $F^{14}C$ is likely to reach the pre-bomb value in the early 2020s, which is similar to the estimation of Graven (2015) and Sierra (2018). If this occurs, radiocarbon dating of a single terrestrial sample having $F^{14}C$ lower than 1 delivers two possible ages: pre-1955 and the early 2020s or after. Graven (2015) discussed issues of radiocarbon dating of single samples with different scenarios of fossil-fuel emissions, suggesting that the radiocarbon method may not provide definitive ages for samples up to 2000 years old under a worst-case, high-emission scenario from fossil fuels. To avoid these issues, radiocarbon dating of a series of samples in sequence with known chronological ordering (e.g., samples from a sediment profile or along the growth axis of a tree) combined with other isotopic studies should be employed. Constraints in the chronological ordering of measured radiocarbon ages (or $F^{14}C$ values) of the sequence samples give a much better indication (than that of a single sample) on their calendar ages, resulting in more definite ages for each sample in the sequence (e.g., Goslar et al. 2005; Yeloff et al. 2006; Hua 2009; Santini et al. 2013). As fossil fuels are not only depleted in ^{14}C ($F^{14}C$ = 0 and

$\Delta^{14}C$ = -1000‰) but also in ^{13}C ($\delta^{13}C$ = -28‰, which is ~20‰ lighter than atmospheric $\delta^{13}C$), the decline of $\delta^{13}C$ due to fossil fuel input can be very useful to distinguish between the two possible ages (Köhler 2016). For example, if measured $\delta^{13}C$ values of dated C3 and C4 plant samples are lower than their present-day ranges of -34 to -22‰ (Diefendorf et al. 2010; Kohn 2010; Basu et al. 2015) and -16 to -10‰ (Cerling and Harris 1999; Basu et al. 2015), respectively, these samples are formed or grown in this decade or after. Otherwise, the samples are of ancient origin.

CONCLUSION AND FUTURE RESEARCH

A comprehensive compilation of clean-air $\Delta^{14}C$ for the period 1950-2019 is presented. The compilation consists of zonal, hemispheric and global summer $\Delta^{14}C$ data sets for use in regional and global carbon cycle studies. Compiled monthly $F^{14}C$ (and $\Delta^{14}C$) data sets for 5 different zones (3 in the NH and 2 in the SH) are also reported. These monthly data sets are used as zonal radiocarbon calibration curves in the CALIBomb (http://calib. org/CALIBomb/) and OxCal (http://c14.arch.ox.ac.uk/calibration.htlm) programs for age calibration of dated terrestrial samples formed after 1955.

Atmospheric and tree-ring $\Delta^{14}C$ records selected for our compilation are not distributed evenly around the globe (Figure 1). The majority of the records

are from Europe, north-western America and East Asia for the NH, and New Zealand, south-eastern Australia and Antarctica for the SH. Future research efforts should focus first on new sites for better determination of zonal boundaries for improved bomb radiocarbon dating. They include southern Europe, north-eastern America, northern China and southern Russia for NH zone 1 – NH zone 2 boundary; central America, north-central Africa and northern China for NH zone 2 – NH zone 3 boundary; and south America, south-central Africa and northern Australia for SH zone 3 – SH zone 1-2 boundary. Tree rings during the bomb peak period from these new sites are useful for the determination of zonal boundaries. The quality of tree-ring $\Delta^{14}C$ data should also be considered by applying the dendrochronological methods for tree-ring dating instead of ring counting, specifying how wood material is sampled and employing sufficient sample pre-treatment to extract holocellulose or alpha-cellulose for ^{14}C analysis.

For periods not covered by atmospheric records (the early bomb period for NH zones 1, 2 and 3, and 1955-1972 for SH zone 3; see Figures 6a-d), the compiled monthly $F^{14}C$ data sets are currently based on tree rings. Therefore, for these periods, $\Delta^{14}C$ data from archived seasonal plants, seeds, wheat, rice, etc., whose growth seasons are different than summer (the main growing season of tree rings), should be useful for the improvement of the compiled zonal monthly data sets.

Finally, some records used here are relatively short, or need to be replicated and/or possibly revised. Data were produced before methodological and instrumentation updates, without clear data-quality information or data replication (see details in references therein - Table 1). With the purpose of data enhancement and enrichment, follow-up studies on existing sites should be encouraged to corroborate atmospheric ^{14}C records, following the criteria layout here. Future compilations would require further screening of data sets and aggregation of new records.

APPENDIX

Our compiled monthly data sets end at 2019.375 (Supplementary Table S2a-e), meaning that dating of organic samples formed after this time cannot be carried out using these data. However, if the compiled data are extended to the more recent time by extrapolating, age estimation of the above samples can be performed.

We tried to fit the compiled monthly data sets for the NH zones from the 1980s onwards using an exponential trend line and employed it to extend the data beyond 2019. The best fit or highest R^2 value of the exponential trend line ($y = ae^{bx}$, with a = 7112.83757 ± 0.03923 and b = -0.00439 ± 0.00002) was achieved when the period of 1993-2019 was used. For the SH zones, the best fit

was achieved when the period of 1994-2019 was employed. The constant parameters associated with the exponential trend line for the SH zones are a = 4271.92875 ± 0.03494 and b = -0.00413 ± 0.00002.

These exponential trend lines are recommended for use in extrapolating the zonal monthly data sets of the current compilation to no more than 5 years after 2019 for age estimation due to uncertain future emissions of fossil fuels (e.g., Graven 2015; Köhler 2016). However, users of these data should be aware that age estimation beyond the currently compiled data sets is considered as qualitative age approximation. Accurate age determination of organic samples formed after 2019 can only be achieved when a future compilation of atmospheric $\Delta^{14}C$ data extended beyond 2019 is available, probably in several years from now.

ACKNOWLEDGEMENTS

We thank S. Hankin for the preparation of Figure 1, H. Erlenkeuser for the pre-treatment of Kiel tree rings, S. Xu for the dating of Fukushima tree rings, and H. Svarva, M.-J. Nadeau and P. Grootes for their generous provision of unpublished ^{14}C data on sub-annual Washington Sitka spruce measured at the National Laboratory for Age Determination in Trondheim. We would also like to thank P. Grootes for useful discussions and comments on age calibration using

compiled monthly $\Delta^{14}C$ data derived from tree rings. We also acknowledge two anonymous reviewers and the Associate Editor, P. Reimer, for their valuable comments, which improved the manuscript.

REFERENCES

Ancapichún S, De Pol-Holz R, Christie DA, Santos GM, Collado-Fabbri S, Garreaud R, Lambert F, Orfanoz-Cheuquelaf A, Rojas M, Southon J, Turnbull JC, Creasman PP. 2021. Radiocarbon bomb-peak signal in tree-rings from the tropical Andes register low latitude atmospheric dynamics in the Southern Hemisphere. Science of the Total Environment 774:145126, doi:10.1016/j.scitotenv.2021.145126.

Andrews AH, Siciliano D, Potts DC, DeMartini EE, Covarrubias S. 2016. Bomb radiocarbon and the Hawaiian Archipelago: coral, otoliths and seawater. Radiocarbon 58:531-548.

Andrews AH, Prouty NG, Cheriton OM. 2021. Bomb-produced radiocarbon across the South Pacific Gyre – A new record from American Samoa with utility for fisheries science. Radiocarbon, doi:10.1017/RDC.2021.51

Barton NP, Ellis AW. 2009. Variability in wintertime position and strength of the North Pacific jet stream as represented by re-analysis data. International Journal of Climatology 29:851-862, doi:10.1002/joc.1750.

Basu S, Agrawal S, Sanyal P, Mahato P, Kumar S, Sarkar A. 2015. Carbon isotopic ratios of modern C3–C4 plants from the Gangetic Plain, India and its implications to paleovegetational reconstruction. Palaeogeography, Palaeoclimatology, Palaeoecology 440: 22-32.

Berger R, Libby WF. 1966. UCLA radiocarbon dates V. Radiocarbon 8:467-497.

Berger R, Libby WF. 1967. UCLA radiocarbon dates VI. Radiocarbon 9:477-504.

Berger R, Libby WF. 1968. UCLA radiocarbon dates VIII. Radiocarbon 10(2):402-416.

Berger R, Libby WF. 1969. UCLA radiocarbon dates IX. Radiocarbon 11(1):194-209.

Berger R, Fergusson GJ, Libby WF. 1965. UCLA radiocarbon dates IV. Radiocarbon 7:336-371.

Berger R, Jackson TB, Michael R, Suess HE. 1987. Radiocarbon content of tropospheric CO_2 at China Lake, California 1977-1983. Radiocarbon 29(1):18-23.

Beramendi-Orosco LE, Johnson KR, Noronha AL, González-Hernández G, Villanueva-Díaz J. 2018. High precision radiocarbon concentrations in tree rings from Northeastern Mexico: A new record with annual resolution for dating the recent past. Quaternary Geochronology 48:1-6, doi:10.1016/j.quageo.2018.07.007.

Cain WF, Griffin S, Druffel-Rodriguez KC, Druffel ERM. 2018. Uptake of carbon for cellulose production in a white oak from Western Oregon, USA. Radiocarbon 60(1):151-158, doi:10.1017/RDC.2017.82.

Carbone M, Czimczik C, Keenan T, Murakami P, Pederson N, Schaberg P, Xu X, Richardson A. 2013. Age, allocation and availability of nonstructural carbon in mature red maple trees. New Phytologist 200:1145-1155, doi:10.1111/nph.12448.

Cerling TE, Harris JM. 1999. Carbon isotope fractionation between diet and bioapatite in ungulate mammals and implications for ecological and paleoecological studies. Oecologia 120:347-363.

Damon PE, Cheng S, Linick TW. 1989. Fine and hyperfine structure in the spectrum of secular variations of atmospheric ^{14}C. Radiocarbon 31(3):704-718.

Diefendorf AF, Mueller KE, Wing SL, Koch PL, Freeman KH. 2010. Global patterns in leaf ^{13}C discrimination and implications for studies of past and future climate. Proceedings of the National Academy of Sciences 107: 5738-5743.

Druffel EM, Suess HE. 1983. On the radiocarbon record in banded corals: exchange parameters and net transport of $^{14}CO_2$ between atmosphere and surface ocean. Journal of Geophysical Research 88(C2):1271-1280.

Emmenegger L, Leuenberger M, Steinbacher M., ICOS RI. 2020. ICOS ATC ^{14}C Release, Jungfraujoch (10.0 m), 2016-01-04–2019-08-12, https://hdl.handle.net/11676/X-lXPKZlO4DWX7wncsLQ7akY

Enting IG. 1982. Nuclear weapons data for use in carbon cycle modeling. CSIRO Division of Atmospheric Physics Technical Paper No. 44. Melbourne: CSIRO.

Goodsite ME, Rom W, Heinemeier J, Lange T, Ooi S, Appleby PG, Shotyk W, van der Knaap WO, Lohse C, Hansen TS. 2001. High-resolution

AMS ^{14}C dating of post-bomb peat archives of atmospheric pollutants. Radiocarbon 43(2B): 495-515.

Goslar T, van der Knaap WO, Hicks S., Andrič M, Czernik J, Goslar E, Räsänen S, Hyötylä , H., 2005. Radiocarbon dating of modern peat profiles: pre and post-bomb ^{14}C variations in the construction of age-depth models. Radiocarbon 47: 115-134.

Graven HD. 2015. Impact of fossil fuel emissions on atmospheric radiocarbon and various applications of radiocarbon over this century. Proceedings of National Academy of Sciences USA 112:9542-9545, doi:10.1073/pnas.1504467112.

Graven HD, Guilderson TP, Keeling RF. 2012a. Observations of radiocarbon in CO_2 at La Jolla, California, USA 1992-2007: analysis of the long-term trend. Journal of Geophysical Research 117: D02302, doi:10.1029/2011JD016533.

Graven HD, Guilderson TP, Keeling RF. 2012b. Observations of radiocarbon in CO_2 at seven global sampling sites in the Scripps flask network: analysis of spatial gradients and seasonal cycles. Journal of Geophysical Research 117: D02303, doi:10.1029/2011JD016535.

Graven H, Allison CE, Etheridge DM, Hammer S, Keeling RF, Levin I, Meijer HAJ, Rubino M, Tans PP, Trudinger CM, Vaughn BH, White JWC. 2017. Compiled records of carbon isotopes in atmospheric CO_2 for historical simulations in CMIP6. Geoscientific Model Development 10:4405-4417, doi:10.5194/gmd-10-4405-2017.

Grootes PM, Farwell GW, Schmidt FH, Leach DD, Stuiver M. 1989. Rapid response of tree cellulose radiocarbon content to changes in atmospheric $^{14}CO_2$ concentration. Tellus 41B:134-148.

Hammer S, Levin I. 2017. Monthly mean atmospheric $\Delta^{14}CO_2$ at Jungfraujoch and Schauinsland from 1986 to 2016, https://doi.org/10.11588/data/10100.

Hertelendi E, Csongor E. 1982. Anthropogenic ^{14}C excess in the troposphere between 1951 and 1978 measured in tree rings. Radiochemical and Radioanalytical Letters 56:103-110.

Hesshaimer V. 1997. Tracing the global carbon cycle with bomb radiocarbon. PhD thesis, University of Heidelberg, Heidelberg, Germany.

Hesshaimer V, Levin I. 2000. Revision of the stratospheric bomb $^{14}CO_2$ inventory. Journal of Geophysical Research 105:11,641-11,658.

Hogg A, Heaton TJ, Hua Q, Palmer JG, Turney CSM, Southon J, Bayliss A, Blackwell PG, Boswijk G, Bronk Ramsey C, Pearson C, Petchey F, Reimer P, Reimer R, Wacker L. 2020. SHCal20 Southern Hemisphere calibration, 0-55,000 years cal BP. Radiocarbon 62(4):759-778, doi:10.1017/RDC.2020.59.

Hua Q. 2009. Radiocarbon: A chronological tool for the recent past. Quaternary Geochronology 4: 378-390, doi:10.1016/j.quageo.2009.03.006.

Hua Q, Barbetti M. 2004. Review of tropospheric bomb radiocarbon data for carbon cycle modeling and age calibration purposes. Radiocarbon 46(3):1273-1298.

Hua Q, Barbetti M. 2007. Influence of atmospheric circulation on regional $^{14}CO_2$ differences. Journal of Geophysical Research 112: D19102, doi:10.1029/2006JD007898.

Hua Q, Barbetti M, Worbes M, Head J, Levchenko VA. 1999. Review of radiocarbon data from atmospheric and tree ring samples for the period 1945-1997 AD. IAWA Journal 20:261-283.

Hua Q, Barbetti M, Jacobsen GE, Zoppi U, Lawson EM. 2000. Bomb radiocarbon in annual tree rings from Thailand and Tasmania. Nuclear Instruments and Methods in Physics Research B 172(1-4):359-365.

Hua Q, Barbetti M, Zoppi U, Chapman DM, Thomson B. 2003. Bomb radiocarbon in tree rings from northern New South Wales, Australia: implications for dendrochronology, atmospheric transport and air-sea exchange of CO_2. Radiocarbon 45(3):431-447.

Hua Q, Barbetti M, Zoppi U. 2004. Radiocarbon in annual tree rings from Thailand during the pre-bomb period, AD 1938-1954. Radiocarbon 46(2):925-932.

Hua Q, Barbetti M, Levchenko VA, D'Arrigo RD, Buckley BM, Smith AM. 2012. Monsoonal influences on Southern Hemisphere $^{14}CO_2$. Geophysical Research Letters 39: L19806, doi:10.1029/2012GL052971.

Hua Q, Barbetti M, Rakowski AZ. 2013. Atmospheric radiocarbon for the period 1950-2010. Radiocarbon 55:2059-2072, doi:10.2458/azu_js_rc.v55i2.16177.

Kalnay E, Kanamitsu M, Kistler R, Collins W, Deaven D, Gandin L, Iredell M, Saha S, White G, Woollen J, Zhu Y, Chelliah M, Ebisuzaki W, Higgins W, Janowiak J, Mo KC, Ropelewski C, Wang J, Leetmaa A, Reynolds R, Jenne R, Joseph D. 1996. The NCEP/NCAR 40-year reanalysis project. Bulletin of the American Meteorological Society 77:437-471, doi:10.1175/1520-0477(1996)077<0437:TNYRP>2.0.CO;2.

Key RM, Kozyr A, Sabine CL, Lee K, Wanninkhof R, Bullister JL, Feely RA, Millero FJ, Mordy C, Peng T-H. 2004. A global ocean carbon climatology: Results from Global Data Analysis Project (GLODAP). Global Biogeochemical Cycles 18: GB4031, doi:10.1029/2004gb002247.

Kikata Y, Yonenobu H, Morishita F, Hattori Y. 1992. ^{14}C concentrations in tree stems. Bulletin of the Nagoya University Furukawa Museum 8:41-46. In Japanese.

Kikata Y, Yonenobu H, Morishita F, Hattori Y, Marsoem SN. 1993. ^{14}C concentrations in tree stems I. Mokuzai Gakkaishi 39(3):333-337. In Japanese.

Kohn MJ. 2010. Carbon isotope compositions of terrestrial C3 plants as indicators of (paleo)ecology and (paleo)climate. Proceedings of the National Academy of Sciences 107: 19,691-19,695.

Köhler P. 2016. Using the Suess effect on the stable carbon isotope to distinguish the future from the past in radiocarbon. Environmental Research Letters 11: 124016, doi:10.1088/1748-9326/11/12/124016

Krakauer NY, Randerson JT, Primeau FW, Gruber N, Menemenlis D. 2006. Carbon isotope evidence for the latitudinal distribution and wind speed

dependence of the air-sea gas transfer velocity. Tellus 58B: 390-417, doi:10.1111/j.1600-0889.2006.00223.x

Kudsk SGK, Olsen J, Nielsen LN, Fogtmann-Schulz A, Knudsen MF, Karoff C. 2018. What is the carbon origin of early-wood? Radiocarbon 60(5):1457-1464, doi:10.1017/RDC.2018.97

Lehman SJ, Miller JB, Wolak C, Southon J, Tans PP, Montzka SA, Sweeney C, Andrews A, LaFranchi B, Guilderson TP, Turnbull JC. 2013. Allocation of terrestrial carbon sources using $^{14}CO_2$: Methods, measurement, and modelling. Radiocarbon 55:1484-1495, doi:10.1017/S0033822200048414.

Lehman SJ, Miller JB. 2019. University of Colorado, Institute of Alpine and Arctic Research (INSTAAR), Radiocarbon Composition of Atmospheric Carbon Dioxide ($^{14}CO_2$) from the NOAA GML Carbon Cycle Cooperative Global Air Sampling Network, 2003-2018, Version: 2020-03-12.

Levin I, Hesshaimer V. 2000. Radiocarbon – a unique tracer of global carbon cycle dynamics. Radiocarbon 42(1):69-80.

Levin I, Kromer B. 1997. Twenty years of atmospheric $^{14}CO_2$ observations at Schauinsland station, Germany. Radiocarbon 39(2):205-218.

Levin I, Kromer B. 2004. The tropospheric $^{14}CO_2$ level in mid-latitudes of the Northern Hemisphere (1959-2003). Radiocarbon 46(3):1261-1272.

Levin I, Kromer B, Schoch-Fischer H, Bruns M, Münnich M, Berdau D, Vogel JC, Münnich KO. 1985. 25 years of tropospheric ^{14}C observations in central Europe. Radiocarbon. 27: 1-19.

Levin I, Kromer B, Francey RJ. 1996. Continuous measurements of ^{14}C in atmospheric CO_2 at Cape Grim. In: Francey RJ, Dick AL, Derek N, editors. Baseline Atmospheric Program Australia 1994-1995. Melbourne: CSIRO. p 106-107.

Levin I, Kromer B, Francey RJ. 1999. Continuous measurements of ^{14}C in atmospheric CO_2 at Cape Grim, 1995-1996. In: Grass JL, Derek N, Tindale NW, Dick AL, editors. Baseline Atmospheric Program Australia 1996. Melbourne: Bureau of Meteorology and CSIRO Atmospheric Research. p 89-90.

Levin I, Naegler T, Kromer B, Diehl M, Francey RJ, Gomez-Pelaez AJ, Steele LP, Wagenbach D, Weller R, Worthy DE. 2010. Observations and modelling of the global distribution and long-term trend of atmospheric $^{14}CO_2$. Tellus B 62(1):26-46.

Levin I, Kromer B, Steele LP, Porter LW. 2011. Continuous measurements of ^{14}C in atmospheric CO_2 at Cape Grim, 1997-2008. In: Derek N, Krummel PB, editors. Baseline Atmospheric Program Australia 2007-2008. Melbourne: Australian Bureau of Meteorology and CSIRO Marine and Atmospheric Research. p 56-59.

Libby WF. 1952. Radiocarbon dating. Chicago: University of Chicago Press.

Libby WF. 1956. Radioactive fallout and radioactive strontium. Science 123(3199): 657-660, doi:10.1126/science.123.3199.657.

Manning MR, Lowe DC, Melhuish WH, Sparks RJ, Wallace G, Brenninkmeijer CAM, McGrill RC. 1990. The use of radiocarbon measurements in atmospheric studies. Radiocarbon 32(1):37-58.

Marsh EJ, Bruno MC, Fritz SC, Baker P, Capriles JM, Hastorf CA. 2018. IntCal, SHCal, or a mixed curve? Choosing a ^{14}C calibration curve for archaeological and paleoenvironmental records from Tropical South America. Radiocarbon 60:925-940.

Meijer HAJ, Pertuisot MH, van der Plicht J. 2006. High accuracy ^{14}C measurements for atmospheric CO_2 samples by AMS. Radiocarbon 48(3):355-372.

Muraki Y, Kocharov G, Nishiyama T, Naruse Y, Murata T, Masuda K, Arslanov KhA. 1998. The new Nagoya radiocarbon laboratory. Radiocarbon 40(1):177-182.

Murphy JO, Lawson EM, Fink D, Hotchkis MAC, Hua Q, Jacobsen GE, Smith AM, Tuniz C. 1997. ^{14}C AMS measurements of the bomb pulse in N- and S-hemisphere tropical trees. Nuclear Instruments and Methods in Physics Research B 123(1-4):447-450.

Naegler T. 2009. Reconciliation of excess ^{14}C-constrained global CO_2 piston velocity estimates. Tellus B 61(2):372-384, doi:10.1111/j.1600-0889.2008.00408.x

Nakamura T, Nakai N, Ohishi S. 1987a. Applications of environmental ^{14}C measured by AMS as a carbon tracer. Nuclear Instruments and Methods in Physics Research B 29(1-2):355-360.

Nakamura T, Nakai N, Kimura M, Ohishi S, Hattori Y, Kikata Y. 1987b. Variations in ^{14}C concentrations of tree rings (1945-1983). Chikyu-Kagaku (Geochemistry) 21:7-12. In Japanese.

Nydal R. 1968. Further investigation on the transfer of radiocarbon in nature. Journal of Geophysical Research 73(12):3617-3635.

Nydal R, Gislefoss JS. 1996. Further application of bomb ^{14}C as a tracer in the atmosphere and ocean. Radiocarbon 38(3):389-406.

Nydal R, Lövseth K. 1996. Carbon-14 measurement in atmospheric CO_2 from Northern and Southern Hemisphere sites, 1962-1993. Carbon Dioxide Information Analysis Center, World Data Center-A for Atmospheric Trace Gases, Oak Ridge National Laboratory, Tennessee.

Oeschger H, Siegenthaler U, Schotterer U, Gugelmann A. 1975. A box diffusion model to study the carbon dioxide exchange in nature. Tellus 27(2):168-192.

Olsson IU, Possnert G. 1992. ^{14}C Activity in different sections and chemical fractions of oak tree rings, AD 1938-1981. Radiocarbon 34(3):757-767.

Park JH, Kim JC, Cheoun MK, Kim IC, Youn M, Liu YH, Kim ES. 2002. ^{14}C level at Mt Chiak and Mt Kyeryong in Korea. Radiocarbon 44(2):559-566.

Pena-Ortiz C, Gallego D, Ribera P, Ordonez P, Alvarez-Castro MDC. 2013. Observed trends in the global jet stream characteristics during the second half of the 20th century. Journal of Geophysical Research: Atmospheres 118:2702-2713, doi:10.1002/jgrd.50305.

Pickers PA, Manning AC. 2015. Investigating bias in the application of curve fitting programs to atmospheric time series. Atmospheric Measurement Techniques. 8(3):1469-1489.

Rafter TA, Ferguson GJ. 1957. "Atom bomb effect" – Recent increase of carbon-14 content of the atmosphere and biosphere. Science 126(3273):557-558, doi:10.1126/science.126.3273.557.

Rakowski AZ, Nadeau M-J, Nakamura T, Pazdur A, Paweczyk S, Piotrowska N. 2013. Radiocarbon method in environmental monitoring of CO_2 emission. Nuclear Instruments and Methods in Physics Research B 294:503-507.

Randerson JT, Enting IG, Schuur EAG, Caldeira K, Fung IY. 2002. Seasonal and latitudinal variability of troposphere $\Delta^{14}CO_2$: post bomb contributions from fossil fuels, oceans, the stratosphere, and the terrestrial biosphere. Global Biogeochemical Cycles 16(4):1112, doi:10.1029/2002GB001876.

Reimer PJ, Brown TA, Reimer RW. 2004. Discussion: reporting and calibration of post-bomb ^{14}C data. Radiocarbon 46(3):1299-1304.

Reimer PJ, Austin WEN, Bard E, Bayliss A, Blackwell PG, Bronk Ramsey CB, Butzin M, Cheng H, Edwards RL, Friedrich M, Grootes PM,

Guilderson TP, Hajdas I, Heaton TJ, Hogg AG, Hughen KA, Kromer B, Manning SW, Muscheler R, Palmer JG, Pearson C, van der Plicht J, Reimer RW, Richards DA, Scott EM, Southon JR, Turney CSM, Wacker L, Adolphi F, Büntgen U, Capano M, Fahrni SM, Fogtmann-Schulz A, Friedrich R, Köhler P, Kudsk S, Miyake F, Olsen J, Reinig F, Sakamoto M, Sookdeo A, Talamo S. 2020. The IntCal20 Northern Hemisphere radiocarbon age calibration curve (0-55 cal kBP). Radiocarbon 62(4):725-757.

Santini NS, Hua Q, Schmitz N, Lovelock CE. 2013. Radiocarbon dating and wood density chronologies of mangrove trees in arid Western Australia. PloS ONE 8(11): e80116, doi:10.1371/journal.pone.0080116.

Santos, G.M., Linares, R., Lisi, C.S., Tomazello Filho, M. 2015. Annual growth rings in a sample of Parana pine (Araucaria angustifolia): Toward improving the ^{14}C calibration curve for the Southern Hemisphere. Quaternary Geochronology 25:96-103, doi:10.1016/j.quageo.2014.10.004.

Sierra CA. 2018. Forecasting atmospheric radiocarbon decline to pre-bomb values. Radiocarbon 60(4):1055-1066, doi:10.1017/RDC.2018.33.

Speer JH. 2010. Fundamentals of tree-ring research. University of Arizona Press, 368 pp., ISBN 978-0-8165-2684-0.

Stuiver M, Polach HA. 1977. Discussion: reporting of ^{14}C data. Radiocarbon 19(3):353-363.

Stuiver M, Reimer PJ, Braziunas TF. 1998. Radiocarbon age calibration for terrestrial and marine samples. Radiocarbon 40(3):1127-1151.

Suess HE. 1955. Radiocarbon concentration in modern wood. Science 122: 415-417.

Svarva H, Grootes P, Seiler M, Stene S, Thun T, Værnes E, Nadeau M-J. 2019. The 1953-1965 rise in atmospheric bomb ^{14}C in Central Norway. Radiocarbon 61(6):1765-1774, doi: 10.1017/RDC.2019.98.

Tans P. 1981. A compilation of bomb ^{14}C data for use in global carbon model calculations. In: Bolin B, editor. Carbon Cycle Modeling (Scope 16). New York: John Wiley and Sons. p 131-157.

Telegadas K. 1971. The seasonal atmospheric distribution and inventories of excess carbon-14 from March 1955 to July 1969. US Atomic Energy Commission Report HASL-243.

Thoning KW, Tans PP, Komhyr WD. 1989. Atmospheric carbon dioxide at Mauna Loa Observatory 2, Analysis of the NOAA GMCC data, 1974-1985. Journal of Geophysical Research 94: 8549-8563.

Turnbull JC, Lehman SJ, Miller JB, Sparks RJ, Southon JR, Tans PP. 2007. A new high precision $^{14}CO_2$ time series for North American continental air. Journal of Geophysical Research 112:D11310, doi:10.1029/2006JD008184.

Turnbull JC, Mikaloff Fletcher SE, Ansell I, Brailsford GW, Moss RC, Norris MW, Steinkamp K. 2017. Sixty years of radiocarbon dioxide measurements at Wellington, New Zealand: 1954-2014. Atmospheric Chemistry and Physics17:14771-14784, doi:10.5194/acp-17-14771-2017.

Turney CSM, Palmer J, Hogg A, Fogwill CJ, Jones RT, Bronk Ramsey C, Fenwick P, Grierson P, Wilmshurst J, O'Donnell A, Thomas ZA, Lipson M. 2016. Multidecadal variations in Southern Hemisphere atmospheric ^{14}C: Evidence against a Southern Ocean sink at the end of the Little Ice Age CO_2 anomaly. Global Biogeochemical Cycles 30:211-218, doi:10.1002/2015GB005257.

Turney CSM, Palmer J, Maslin M, Hogg A, Fogwill CJ, Southon J, Fenwick P, Helle G, Wilmshurst J, McGlone M, Bronk Ramsey C, Thomas Z, Lipson M, Beaven B, Jones RT, Andrews O, Hua Q. 2018. Global peak in atmospheric radiocarbon defines the onset of Anthropocene Epoch in 1965. Scientific Reports 8:3293, doi:10.1038/s41598-018-20970-5.

UNSCEAR. 2000. United Nations Scientific Committee on the Effects of Atomic Radiation UNSCEAR 2000 Report to the General Assembly, with Scientific Annexes volume I: Sources and Effects of Ionizing Radiation, https://www.unscear.org/docs/publications/2000/UNSCEAR_2000_Report_Vol.I.pdf

Vogel JC, Marais M. 1971. Pretoria radiocarbon dates I. Radiocarbon 13(2):378-394.

Vuille M, Burns SJ, Taylor BL, Cruz FW, Bird BW, Abbott MB, Kanner LC, Cheng H, Novello VF. 2012. A review of the South American monsoon history as recorded in stable isotopic proxies over the past two millennia. Climate of the Past 8: 1309-1321, doi:10.5194/cp-8-1309-2012

Willkomm H, Erlenkeuser H. 1968. University of Kiel radiocarbon measurements III. Radiocarbon 10(2):328-332.

Xu S, Cook GT, Cresswell AJ, Dunbar E, Freeman SPHT, Hastie H, Hou X, Jacobsson P, Naysmith P, Sanderson DCW. 2015. Radiocarbon concentration in modern tree rings from Fukushima, Japan. Journal of Environmental Radioactivity 146:67-72, doi:10.1016/j.jenvrad.2015.04.004

Wu Y, Fallon S J, Cantin N E, Lough J M. 2021. Surface ocean radiocarbon from a Porites coral record in the Great Barrier Reef: 1945-2017. Radiocarbon, doi:10.1017/RDC.2020.141

Yamada Y, Yasuike K, Komura K. 2005. Temporal variation of carbon-14 concentration in tree-ring cellulose for the recent 50 years. Journal of Nuclear and Radiochemical Sciences 6(2):135-138.

Yeloff D, Bennett KD, Blaauw M, Mauquoy D, Sillasoo Ű, van der Plicht J, van Geel B. 2006. High precision ^{14}C dating of Holocene peat deposits: a comparison of Bayesian calibration and wiggle-matching approaches. Quaternary Geochronology 1: 222-235.

Zimnoch M, Jelen D, Galkowski M, Kuc T, Necki J, Chmura L, Gorczyca Z, Jasek A, Rozanski K. 2012. Partitioning of atmospheric carbon dioxide over Central Europe: insights from combined measurements of CO_2 mixing ratios and their carbon isotope composition. Isotopes in Environmental and Health Studies 48(3):421-433.

Figure captions

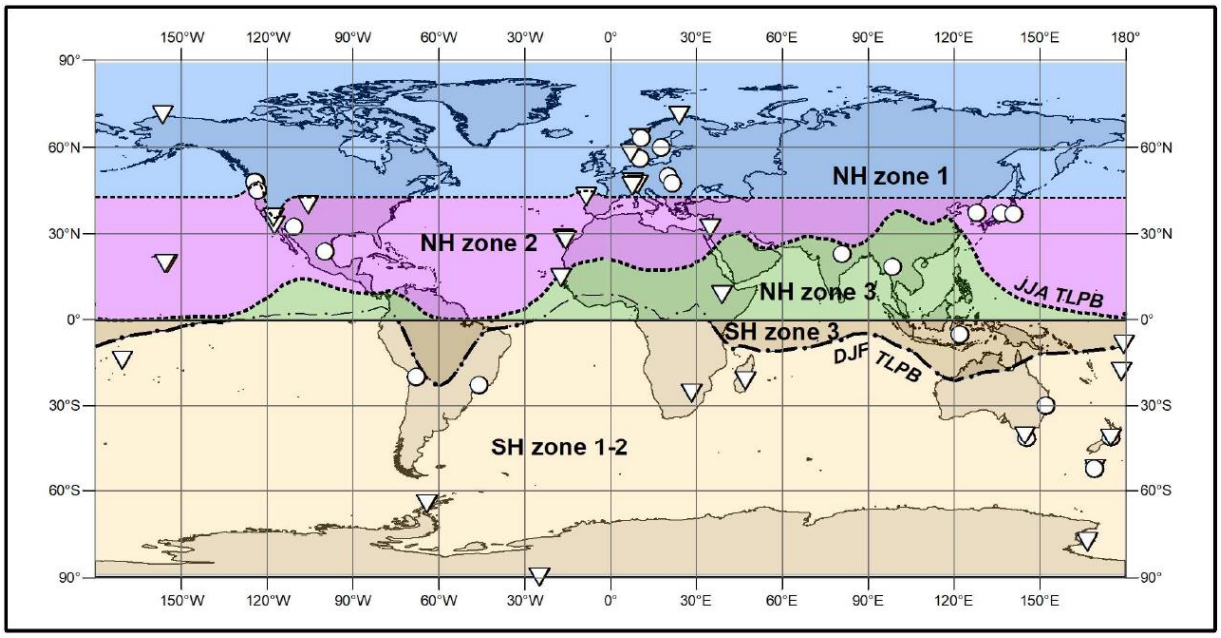

Figure 1 – World map showing the zones and locations of atmospheric CO_2 sampling (triangles) for ^{14}C analysis and $\Delta^{14}C$ tree-ring records (circles) used for our compilation. The mean positions of the TLPB during December-February (DJF) and June-August (JJA) are based on the NCEP/NCAR sea level pressure data (Kalnay et al. 1996) for 1949-2019.

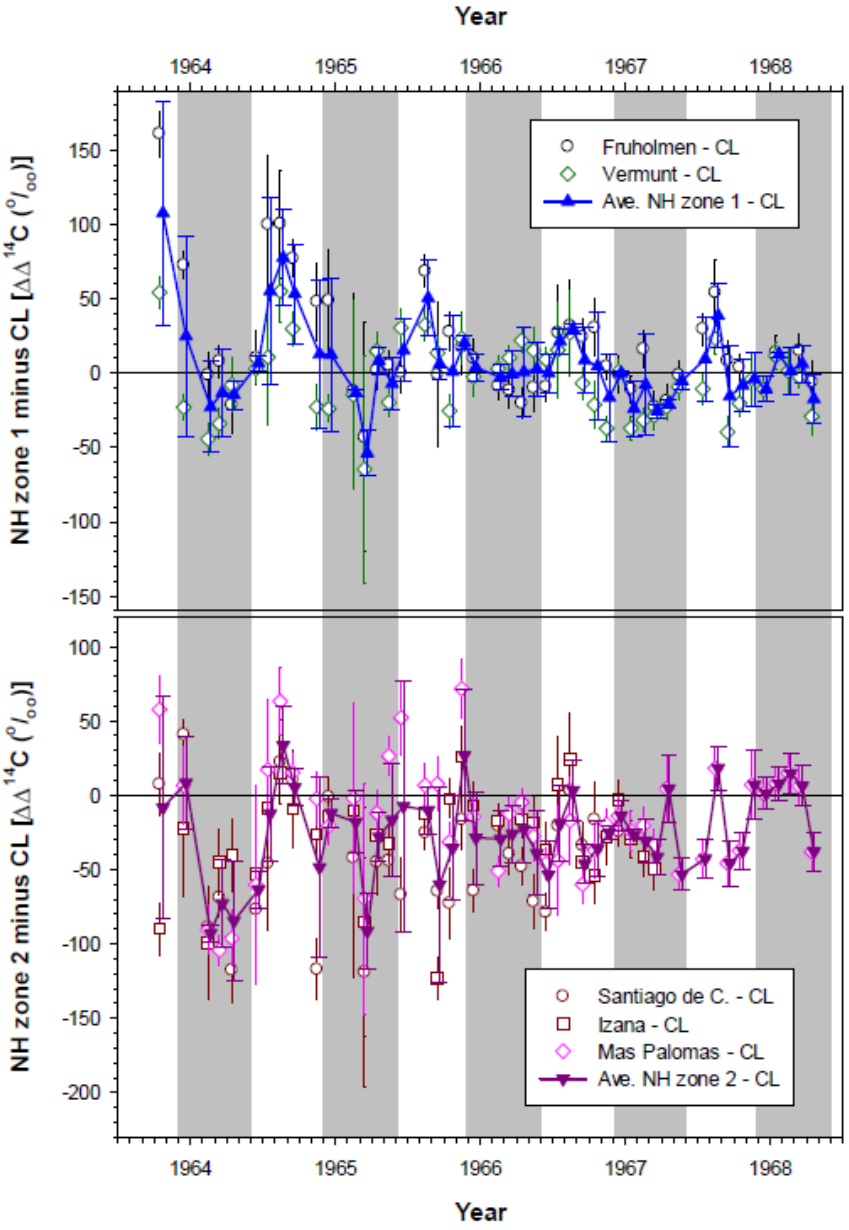

Figure 2 – Monthly $\Delta^{14}C$ differences between atmospheric records in NH zones 1 and 2, and China Lake (CL). Data sources of these atmospheric records are Berger et al. (1965) and Berger and Libby (1966, 1967, 1968, 1969) for CL, Levin and Kromer (2004) for Vermunt, and Nydal and Lövseth (1996) for Fruholmen, Santiago de Compostela, Izaña and Mas Palomas. Grey and white stripes represent winter-spring and summer-autumn, respectively.

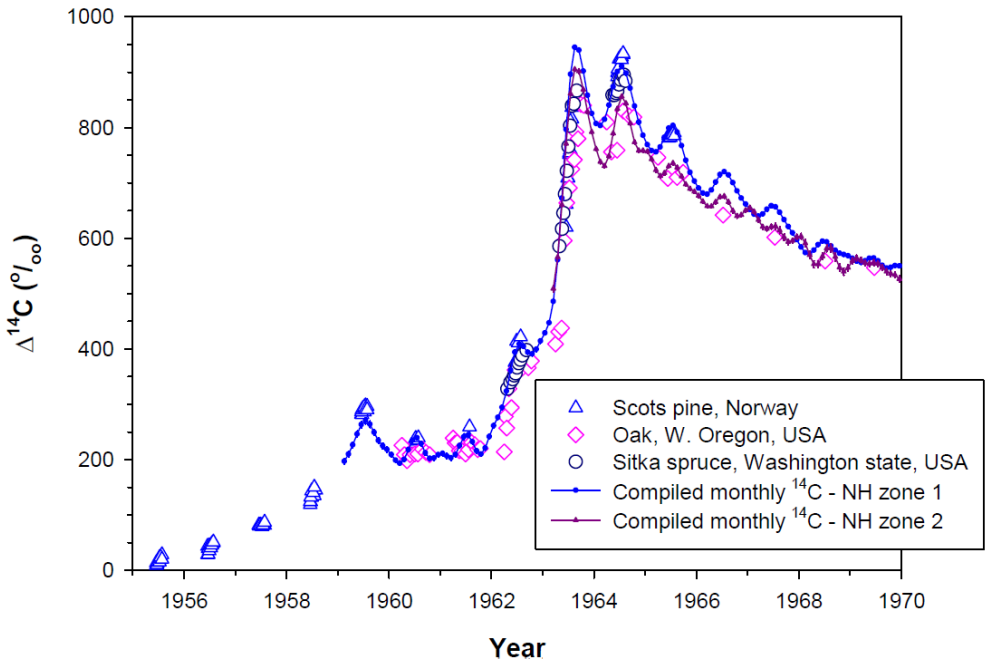

Figure 3 – Tree-ring $\Delta^{14}C$ values from Scots pine (Norway; Svarva et al. 2019), oak (western Oregon, USA; Cain et al. 2018) and Sitka spruce (Washington state, USA; Grootes et al. 1989) versus compiled monthly $\Delta^{14}C$ data for NH zones 1 and 2 derived from atmospheric records (see discussions later on the construction of these compiled data).

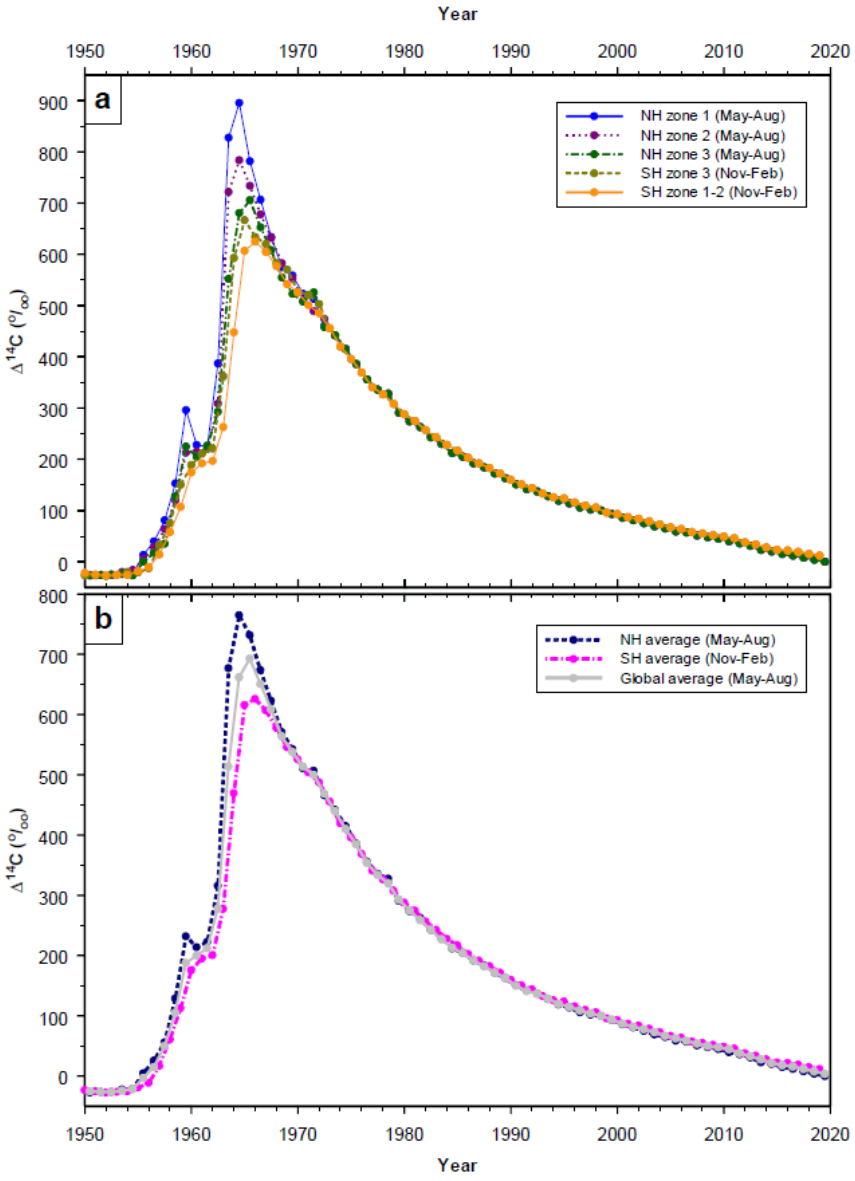

Figure 4 – Compiled zonal **(a)**, and hemispheric and global **(b)** summer atmospheric $\Delta^{14}C$ curves. The compiled data sets are reported in Supplementary Tables S1a-c.

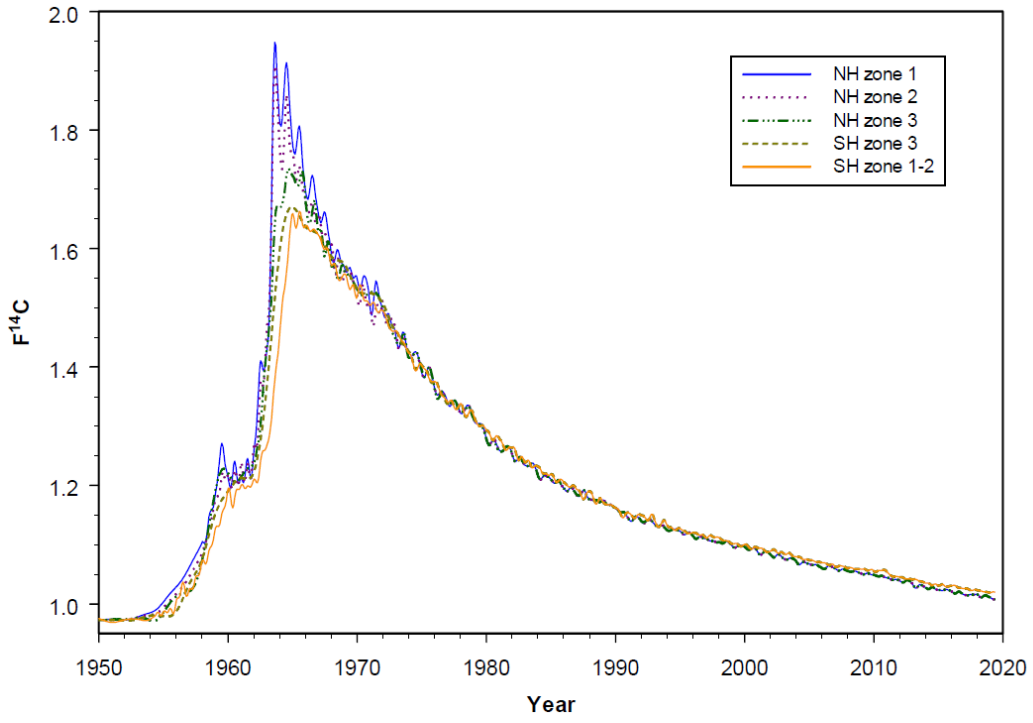

Figure 5 – Compiled monthly atmospheric $F^{14}C$ curves for 5 different zones. The compiled data sets are presented in Supplementary Tables S2a-e.

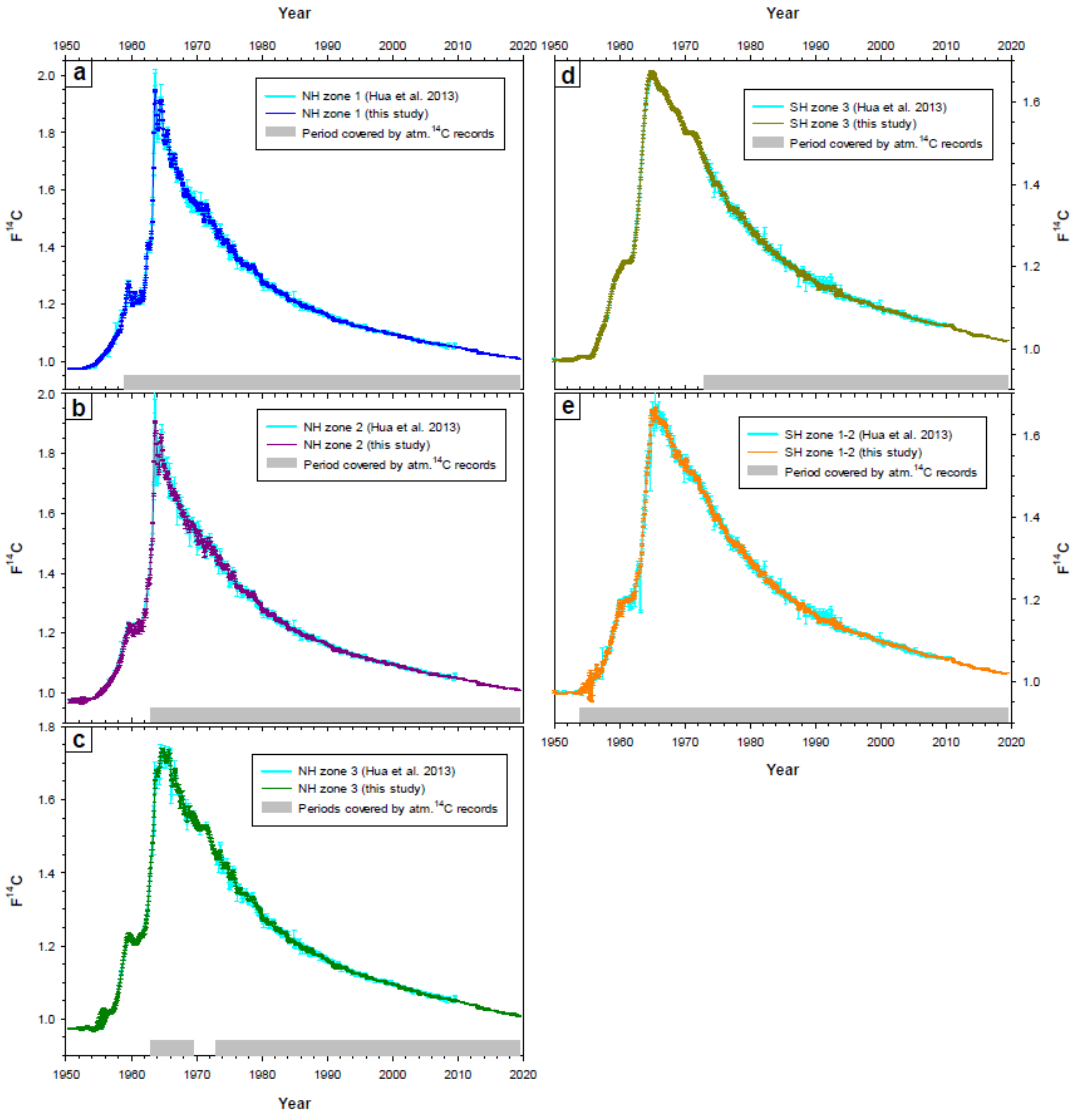

Figure 6 – Our compiled monthly atmospheric $F^{14}C$ curves versus those of Hua et al. (2013).

PERIOD 1973-2019	
NH (NH zones 1, 2 and 3)	**SH (SH zones 3 and 1-2)**
Atmospheric records	***Atmospheric records***
Fruholmen, Norway (71°06'N, 23°59'E; 1973-1993) [1]	Cape Matatula, American Samoa (14.25°S, 170.57°W; 2001-2007) [31]
Point Barrow (Alaska; 71.38°N, 156.47°W; 1985-1991 [27] & 1999-2007 [28]), Niwot Ridge (Colorado; 40.05N, 105.58W; 2003-2018) [29], China Lake (California; 35°32'N, 117°41'W; 1977-1983) [30], and Kumukahi and Mauna Loa (Hawaii; 19.52-53°N, 154.82-155.58°W; 2001-2007) [31], USA	Suva, Fiji (18.1°S, 178.4°E; 1973-1975) [20]
Vermunt, Austria (47°4'N, 9°34'E; 1973-1986) [2]	Fianarantsoa, Madagascar (21°27'S, 47°05'E; 1973-1978) [1]
Schauinsland, Germany (47°55'N, 7°55'E; 1976-2016) [32]	Pretoria, South Africa (25°43'S, 28°21'E; 1973-1994) [21]
Jungfraujoch, Switzerland (46°33'N, 7°42'E; 1986-2019) [32-33]	Cape Grim, Australia (40°41'S, 144°41'E; 1994-2008) [36]
Izaña (28°22'N, 16°30'W; 1976-1990) and Mas Palomas (27°45'N, 15°40'W; 1973), Spain [1]	Wellington (41.25-41°S, 174.69-87°E; 1973-2019) [22] and Campbell Is. (52.5°S, 169.2°E; 1973-1977) [20], New Zealand
Tree rings	Palmer Station (64°46'27"S, 64°03'14"W; 2005-2007) [31], South Pole (89.98°S, 24.80°W; 1984-1992 [27] & 1999-2007 [31]) and Scott Base (77.9°S, 166.7°E; 1973-1976) [20], Antarctica
Uppsala, Sweden (60°0'N, 17°38'E; 1980-1981) [5]	***Tree rings***
Schauinsland, Germany (48°N, 8°E; 1974-1985) [34]	Muna Is., Indonesia (5°S, 122°E; 1973-1979) [19]
Niepolomice, Poland (50°2′N, 20°13′E; 1973-2003) [7]	Irruputuncu, Altiplano, Chile (20°S, 68°W; 1973-2014) [23]
NE Hungary (47°35'N, 21°35'E; 1973-1978) [10]	Camanducaia, Brazil (22°50'S, 46°04'W; 1973-1997) [24]
NE Mexico (23°49′N, 99°50′W; 1973-2002) [13]	Armidale (30°S, 152°E; 1973-1977) [25] and Tasmania (41°41'S, 145°18'E; 1973-1976) [17], Australia
Shika-machi (37.1°N, 136.5°E; 1973-1999) [14] and Fukushima (37.01°N, 140.81°E; 1984-1989 & 1994) [35], Japan	Wellington (41.25-33°S, 174.87°E; 1973-2012) [22] and Campbell Is. (52.554°S, 169.133°E; 1973-2011) [26], New Zealand
Mts Chiak and Kyeryon, South Korea (37°20-23′N, 128°03-04′E; 1975-2000) [15]	
Mandla, India (23°N, 81°E; 1980) [16]	
Doi Inthanon, Thailand (18°33'N, 98°34'E; 1973-1975) [17]	

Note: [1] = Nydal and Lövseth (1996); [2] = Levin and Kromer (2004); [3] = Berger et al. (1965) and Berger and Libby (1966, 1967, 1968, 1969); [4] = Svarva et al. (2019); [5] = Olsson and Possnert (1992); [6] = Kudsk et al. (2018); [7] = Rakowski et al. (2013); [8] = Stuiver et al. (1998); [9] = Grootes et al. (1989); [10] = Hertelendi and Csongor (1982); [11] = Cain et al. (2018); [12] = Damon et al. (1989); [13] = Beramendi-Orosco et al. (2018); [14] = Yamada et al. (2005); [15] = Park et al. (2002); [16] = Murphy et al. (1997); [17] = Hua et al. (2000); [18] = Hua et al. (2004); [19] = Hua et al. (2012); [20] = Manning et al. (1990); [21] = Vogel and Marais (1971); [22] = Turnbull et al. (2017); [23] = Ancapichún et al. (2021); [24] = Santos et al. (2015); [25] = Hua et al. (2003); [26] = Turney et al. (2018); [27] = Meijer et al. (2006); [28] = Graven et al. (2012a); [29] = Turnbull et al. (2007), Lehman et al. (2013), and Lehman and Miller (2019); [30] = Berger et al. (1987); [31] = Graven et al. (2012b); [32] = Levin and Kromer (2004), and Hammer and Levin (2017); [33] = Emmenegger et al. (2020); [34] = Levin and Kromer (1997); [35] = Xu et al. (2015); and [36] = Levin et al. (1996, 1999, 2011).

Table 1 – Atmospheric and tree-ring $\Delta^{14}C$ records used for the compilation of summer and monthly data sets.

Supplementary Information

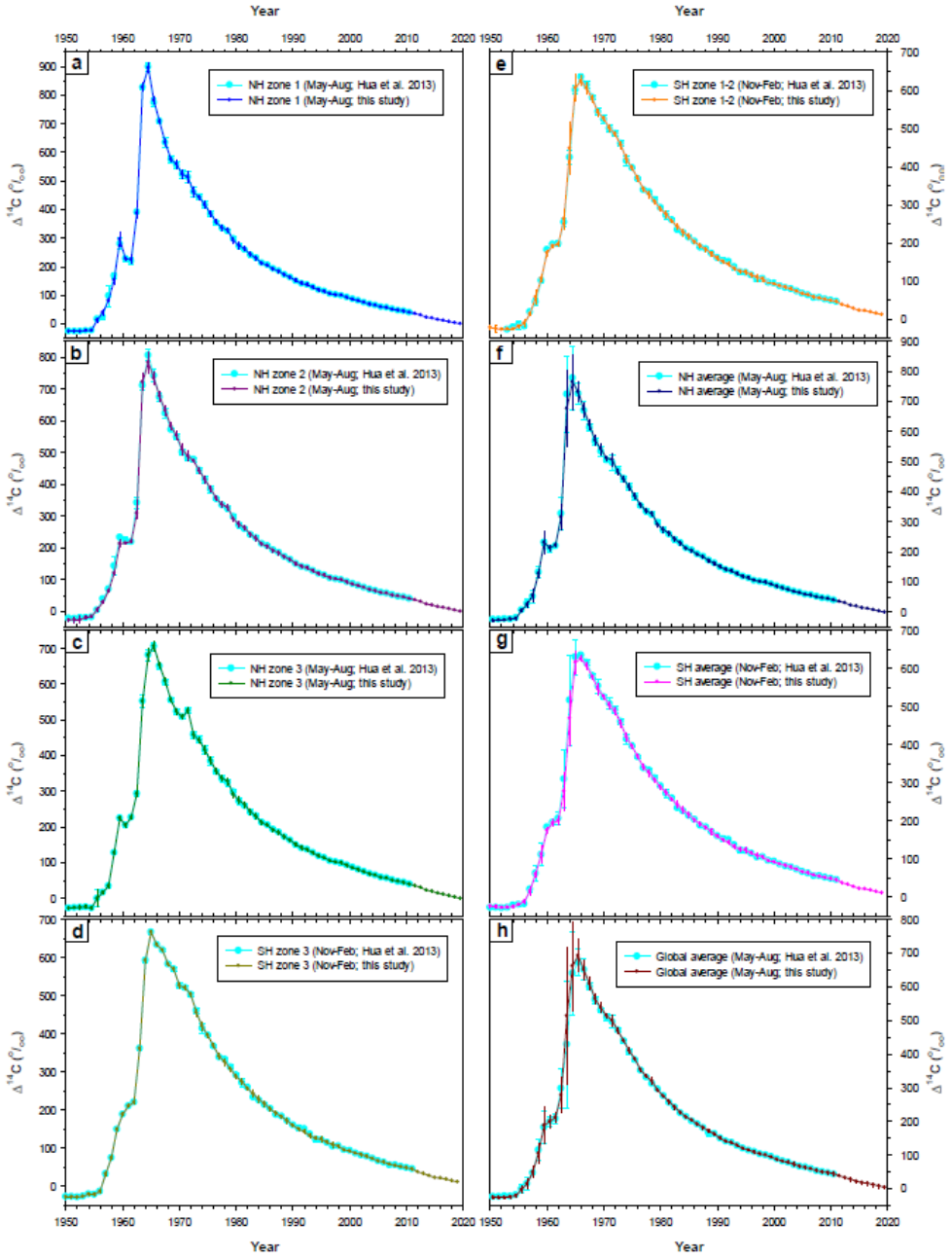

Supplementary Figure S1a-h – Our compiled zonal, hemispheric and global summer $\Delta^{14}C$ curves versus those of Hua et al. (2013).

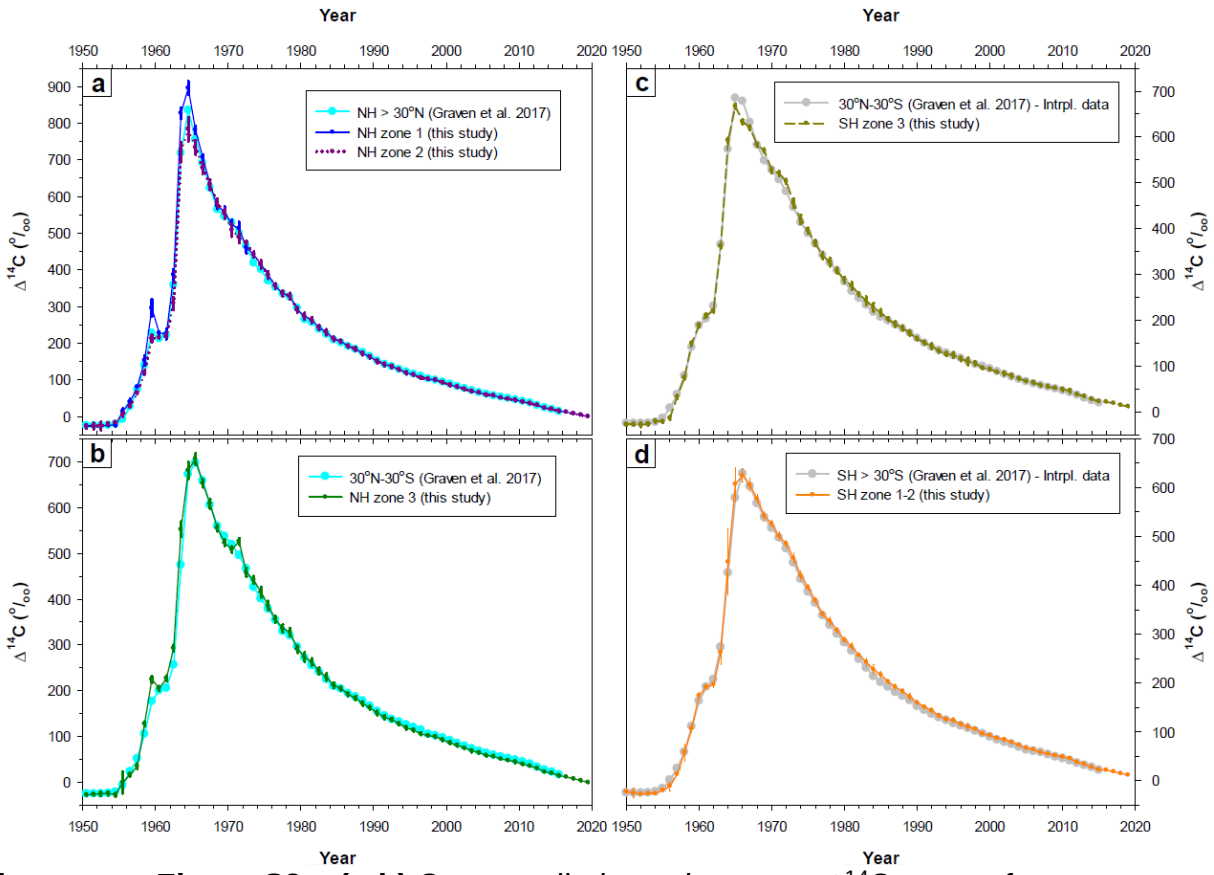

Supplementary Figure S2 – **(a-b)** Our compiled zonal summer $\Delta^{14}C$ curves for the NH versus compiled $\Delta^{14}C$ data of Graven et al. (2017), **(c-d)** Our compiled zonal summer $\Delta^{14}C$ curves for the SH versus interpolated values of the compiled $\Delta^{14}C$ data of Graven et al. (2017). The latter data were linearly interpolated in order to get the same timing for both compiled data sets for ease of comparison.

Supplementary Table S1 – **(a)** Zonal and hemispheric $\Delta^{14}C$ (‰) for the NH for boreal summers (May-Aug), **(b)** Zonal and hemispheric $\Delta^{14}C$ (‰) for the SH for austral summers (Nov-Feb), and **(c)** Global $\Delta^{14}C$ (‰) for boreal summers (May-Aug).

Supplementary Table S2 – **(a)** Monthly ^{14}C data for NH zone 1, **(b)** Monthly ^{14}C data for NH zone 2, **(c)** Monthly ^{14}C data for NH zone 3, **(d)** Monthly ^{14}C data for SH zone 3, and **(e)** Monthly ^{14}C data for SH zone 1-2.

4.3 Capítulo III

4.3.1 Título manuscrito III: Large interannual variability of the Southern Ocean CO_2 outgassing revealed by atmospheric ^{14}C levels.

Santiago Ancapichún[1,2], et al

[1]Postgraduate School in Oceanography, Faculty of Natural and Oceanographic Sciences, Universidad de Concepción, Concepción, Chile

[2]Centro de Investigación GAIA Antártica (CIGA) and Network for Extreme Environment Research (NEXER), Universidad de Magallanes, Punta Arenas, Chile

*Corresponding author: Ricardo De Pol-Holz, ricardo.depol@umag.cl

4.3.2 Manuscrito en preparación.

Declaración de contribución de Santiago Ancapichún Hernández.

Conceptualización, Metodología, Investigación, Análisis formal, escritura del draft original, Validación, Visualización, Investigación.

Highlights:

- New Southern Hemisphere tree-ring ^{14}C records captured the bomb period timing and magnitude

- The $\Delta^{14}C$ gradient in the Southern Hemisphere traces the ocean outgassing of CO_2

- The ocean outgassing of CO_2 ^{14}C-based reveals large interannual variability and a negative trend.

Abstract

The Southern Ocean is an important sink of anthropogenic carbon. However, recent studies have found a strong weakening uptake of atmospheric CO_2 trend in the 1990s related to an increase in the Outgassing of CO_2 (OC), followed by a reinvigoration in the 2000s. Measurements used to trace the air-sea CO_2 flux are sparse in time and space, being necessary to develops new approaches to find a consensus. In this sense, the atmospheric ^{14}C offers a promising alternative tracer. Throughout upwelling, ^{14}C-depleted deepwater emerges to the Southern Ocean surface and exchanges CO_2 with the troposphere bringing it CO_2 with low ^{14}C levels. Thus, the Southern tropospheric ^{14}C concentration is sensitive to ocean OC changes. Here, we present the first

outgassing record of CO_2 in the Southern Ocean derived from three new annual resolution ^{14}C tree-ring records across the Southeast Pacific Coast (32°-54°S). Our ^{14}C-records faithfully captured the bomb signal both in terms of timing and magnitude and show significant latitudinal $\Delta^{14}C$ differences across our 32°-54°S gradient. In addition when compared to previous records at similar austral latitudes at the other rim of the Pacific they show no zonal atmospheric $\Delta^{14}C$ differences suggesting a strong effect of the OC. The OC based on ^{14}C traces an unprecedented large interannual variability of the ocean OC, but doesn't show a clear decadal pattern. Moreover, the OC based on ^{14}C traces a progressive decrease in the ocean OC in agreement with OC estimations based on pCO_2 products. This negative trend potentially is associated with the increase in the atmospheric pCO_2 caused by the emission of anthropogenic CO_2.

Keywords

Radiocarbon

Tree-rings

Carbon reservoir effect

Southern Ocean ventilation

Outgassing of natural CO_2

1. INTRODUCTION

Up nearly 40% of anthropogenic carbon stored in oceans has been taken by the Southern Ocean (Mikaloff Fletcher et al., 2006; Khatiwala et al., 2009; DeVries 2014). The Southern Ocean's role for the global exchange of water between ocean surface-interior, referred to as Southern Ocean ventilation, is a key process in the carbon and energy balance of the earth. This process is a direct consequence of its unique circulation zonally unbound by continental barriers and forced by the Southern Westerly Winds (SWW; Figure 1) (Marshall & Speer 2012; Morrison et al., 2015). The SWW drives an intense divergence on the oceanic surface at ~ 60°S, generating upwelling of deepwater with low initial anthropogenic CO_2 concentration and a large amount of dissolved inorganic carbon (DIC) (Lovenduski & Gruber 2005). The upwelled deepwater is transported northward, exposing it to the atmosphere in a region of high-wind speed that causes large ocean-atmosphere CO_2 exchange. Thereby, south of ~ 45 °S, there is a band of high-outgassing of oceanic CO_2 and high-uptake of atmospheric CO_2 (Sabine et al., 2004; Mikaloff Fletcher et al., 2007; Gruber et al., 2009; Takahashi et al., 2009; Sallée et al., 2012; Bopp et al., 2015).

Several modeling studies based on CO_2 partial pressure have reported that in recent times, the Southern Ocean air-sea CO_2 flux has been characterized by decadal variability, showing a strong weakening uptake of atmospheric CO_2 trend in the 1990s followed by a reinvigoration in the 2000s (Landschützer et al.,

2013; Rödenbeck et al., 2014; Munro et al., 2015). Using a global inverse model coupled with a carbon cycling model, DeVries et al. (2017) found that in the 1990s, a strong upwelling of high CO_2 partial pressure (pCO_2) deepwater was caused by a strengthening of the meridional overturning circulation forced by a southward shift and strengthening of the SWW. This upwelling of high pCO_2 deepwater led to a strong-outgassing of natural CO_2 coupled with a low-uptake of anthropogenic CO_2, thus a weaker sink for atmospheric CO_2. In the 2000s, the meridional overturning circulation slowed, leading to a reduced upwelling of high pCO_2 deepwater that produced a reduction in the outgassing of natural CO_2 and a slight increase in the uptake of anthropogenic CO_2, which explains the observed increase in the total uptake of atmospheric CO_2 (DeVries et al., 2017). The above study evidences the close relationship between the total uptake of atmospheric CO_2 and the Southern Ocean ventilation, where the upwelling of high pCO_2 water, relative to the atmospheric pCO_2, supports the outgassing of oceanic CO_2 against the uptake of atmospheric CO_2 because the ocean-atmosphere pCO_2 difference is the force governing the exchange of CO_2 across the air-sea interface (Garbe et al., 2014; Wanninkhof 2014). However, pCO_2 measurements and other datasets are sparse in time and space. Most surface ocean pCO_2-based studies suggest a substantial amount of interannual to decadal variability from the period 1989-2018, indicating a more variable air-sea CO_2 flux than those suggested by model-based assessments (Fay & Mckinley,

2013; Rödenbeck et al., 2013; Fay et al., 2014; Zeng et al., 2014;Gregor et al., 2019; Landschützer et al., 2020; Iida et al., 2020; Chau et al., 2020). Moreover, the variability of the oceanic sink for CO_2 at decadal timescales found by inverse models and hindcast simulations have revealed large differences between estimations (Wanninkhof et al., 2013; Ishii et al., 2014). Therefore, it is essential to develop new approaches to determine recent changes in the air-sea CO_2 exchange in the Southern Ocean region for future climate change-based scenarios. In this sense, an integrated analysis of the atmospheric ^{14}C content in the Southern Hemisphere offers a promising research avenue.

The ^{14}C initially formed in the atmosphere is uptaken by the ocean and transported in its interior with the thermohaline circulation for centuries to millennia (Weaver et al., 1993; Braziunas et al., 1995). As a result of the natural radioactive decay of the ^{14}C, the Southern Ocean deep water masses have a low ^{14}C:^{12}C isotopic ratio relative to the atmosphere (commonly expressed as $\Delta^{14}C$, i.e., the deviation from an atmospheric standard and corrected for fractionation) (Stuiver & Polach, 1977; Key et al. 2004; Graven et al., 2012). As described above, upwelling of this high pCO_2, low anthropogenic CO_2, and ^{14}C-depleted deepwater to the Southern Ocean surface drives an exchange of the ocean CO_2 with the troposphere, diluting the $\Delta^{14}CO_2$ of the atmosphere (Braziunas et al., 1995; Randerson et al., 2002). Therefore, the Southern

tropospheric ^{14}C concentration is sensitive to variations of the Southern Ocean ventilation being and indicator of the ocean CO_2 outgassing.

Atmospheric ^{14}C patterns are precisely recorded by the photosynthetic assimilation of atmospheric CO_2 by trees and registered in their annual growth rings, turning trees into excellent annual records of past atmospheric $\Delta^{14}CO_2$ (Hua et al., 2013; Turnbull et al., 2017). Recent studies have traced CO_2 emissions of mega-cities through time using tropospheric $\Delta^{14}C$ recorded by trees (Niu et al., 2021; Xiong et al., 2021). Despite the atmospheric ^{14}C potential to trace recent changes in the outgassing of oceanic CO_2 within the region of influence of the Southern Ocean ventilation, there is only one tree-ring site registering the annual Southern atmospheric ^{14}C levels south of 45 °S (Campbell Island; 52.5 °S; Turney et al., 2018; Figure 1). On the other hand, there are few mid-latitude SH annual atmospheric ^{14}C-records being scarce records without Amazon biospheric influence (Santos et al., 2015; Turnbull et al., 2017; Ancapichun et al., 2021). This scarcity of appropriate records has hampered the potential use of tree-ring $\Delta^{14}C$ as an air-sea CO_2 exchange tracer. Meanwhile, several modeling studies have shown low atmospheric $\Delta^{14}C$ levels above the Southern Ocean relative to mid-latitudes from last decades (Randerson et al., 2002; Turnbull et al., 2009; Levin et al., 2010), which, to our knowledge, have not been confirmed by tree-ring records. Therefore, it is crucial to develop new high-resolution in situ records of atmospheric $\Delta^{14}C$ levels across

the SH to trace and understand the temporal variability of the outgassing of oceanic CO_2 at this remote region.

Here we determine the temporal variability of the Southern Ocean CO_2 outgassing utilizing three new annual resolution ^{14}C tree-ring records from the Southeast Pacific margin spanning the period 1950 to 2016. Two of this records are located at SH's mid-latitudes, specifically in Central Chile (CC; 32 °S) and Valdivian Rainforest (VR; 40 °S; Figure 1), and the other is located within the Southern Ocean region in the Strait of Magellan (SoM; 53.5 °S; Figure 1), representing the world's southernmost ^{14}C tree-ring record. We use these records to estimate the annual CO_2 emissions in the Southern Ocean region during the last 40 years.

2. METHODS

2.1. South Pacific tree-ring samples and radiocarbon analyses

We determined the ^{14}C content in the annual tree-rings from three sites located along the south east Pacific coast during 1950-2016 of the following tree species: *Austrocedrus chilensis* in Central Chile (33°S), *Fitzroya cupressoides* in northern Patagonia (40°S) and *Pilgerodendron uviferum* in southern tip of Patagonia (53°S). At each of these three sites ^{14}C were measured from one individual tree that were previously annually cross-dated against the existing site ring-ring width chronology of El Asiento (33°S, LeQuesne et al. 2016), Mirador

(40°S, Urrutia et al. 2015), and Mount Tarn (53°S, Holz et al. 2018). All these tree species and tree-ring sites have been extensively used in tree-ring studies, and its exactly annual dating corroborated against a massive tree-ring networks (Morales et al. 2020). The information of ^{14}C tree-ring records from Campbell Island and New Zealand is available in the section S2.1.

Sample preparation was done by cutting dated tree-rings under a binocular microscope into annual rings using sterile ceramic knives over an acrylic table at the tree-ring lab of the Universidad Austral de Chile and Universidad de Magallanes. Each annual wood segment was polished with diamond tools to remove the surface that was in contact with extraction and sanding tools. For studying post-bomb ^{14}C in tree-rings at annual resolution, it is extremely important to isolate the carbon assimilated in the corresponding growth year, as non-cellulosic compounds can be synthesized the year after the ring formation or can be translocated between several rings (Anchukaitis et al. 2008; Santos et al., 2020). Therefore, we extracted the holocellulose of each annual ring for ^{14}C measurements as it has been shown to be a useful way to remove any mobile carbon from other years (Capano et al., 2017; Santos et al., 2020). Briefly, tree-ring samples were chemically cleaned by a series of acid-base washes followed by the removal of lignin and other mobile carbon fractions through chlorine baths (Southon & Magana, 2010). The holocellulose was then combusted, and CO_2 was cryogenically separated and reduced to graphite by H_2 using FeO as a

catalyst (Santos & Ormsby, 2013). The ^{14}C content of the graphite sample was measured at the AMS facility of the University of California at Irvine (Santos et al., 2004, 2007). We use IAEA-C3 (cellulose) as well as holocellulose extracted from wood shaved from tree-rings of *Sequoia sempervirens* centered in the year 1850 as secondary standards.

The growing season of *A. chilensis* (Villalba 1994; LeQuesne et al., 2006), *F. cupressoides* (Urrutia et al., 2015) and *P. uviferum* (Aravena, 2007; Weitzenkamp et al., 2007) occurs during the late spring and summer months of the SH (October to March), the same period as the ^{14}C *Dracophylum sp.* tree-ring record from Campbell Island in the south-west (Turney et al., 2018). We assigned the calendar age of each annual ring as the SH dendro age plus one (e.g. the atmospheric ^{14}C stored in the growing season of 1949-1950 was assigned to January 1st 1950). Our full *P. uviferum* and *F. cupressoides* $\Delta^{14}C$ records span from 1950 to 2016, while *A. chilensis* spans from 1950 to 2002. We measured replicates of >10% of the samples and calculated error weighted averages for those years with more than one data point (see supplementary information). The pooled standard deviation based on all replicates produced for the 1950-2016 record is 3.5‰ for *P. uviferum* whereas the higher variability associated with the 1950-1972 period increases our pooled standard deviation to 8.7‰. Similar results were found for *F. cupressoides* and *A. chilensis* (see supplementary information).

2.2. Geographical provenance of air parcels to tree-ring sites.

We used HYSPLIT model v.4 to assess the geographical provenance of the air parcels that potential transported the $^{14}CO_2$ subsequently fixed in the Strait of Magellan, Campbell Island, New Zealand, and Valdivian Rainforest ^{14}C tree-ring sites utilized on this study (Draxler & Hess, 1998; Draxler & Stunder, 1988; Stein et al., 2015). HYSPLIT is a complete system designed to calculate simple air-parcel trajectories, complex transport, dispersion, chemical transformation, and depositional simulations. The backward trajectories calculated using HYSPLIT are generated as a set of longitudinal, latitudinal, and altitudinal data based on an arbitrary number of hours into the past for a specific hour of the day (Draxler & Taylor, 1982). Previous studies have shown that 120 hours (5 days) is a suitable time-window to overcome potential biases since shorter time-windows tend to show limited trajectories that are too close to the study site, and longer time-windows may be associated with major propagation errors (Scarchilli et al., 2011; Schlosser et al., 2008; Sinclair et al., 2013). Ancapichun et al. (2021) demonstrated that calculate one backward trajectory by day (specifically in midday) is enough to represent the general geographical provenance pattern for a studied site. In this way, we calculated 1 backward trajectory (at mid-day) for each day of the growing season (October to March) between the years 1950 and 2016 (12,127 computed trajectories by each tree-ring record). Each backward trajectory describes the spatial displacement of air

parcels during the 5-day time-window. The NCEP/NCAR reanalysis was used as the input data of the HYSPLIT model (Kalnay et al., 1996). This is the only comprehensive climatological dataset covering since the beginning of the bomb-testing period, and it is based on *in situ* observations and satellite data which have been proven to be reliable for the representation of atmospheric variables (Kalnay et al., 1996). Finally, we also utilized the NCEP/NCAR reanalysis data to determine the latitudinal profiles of wind magnitudes and northward Ekman transport, which are decisive variables in air-sea CO_2 exchange and upwelling mechanisms.

2.3. Tracing the Southern Ocean CO_2 outgassing.

We estimated the atmospheric CO_2 concentration that comes from the Southern Ocean (CSO) to infer the temporal variability of the Southern Ocean CO_2 outgassing. An increase (decrease) in the CSO values would indicate an intensification (weakening) in the upwelling of deep-water masses with high pCO_2, an increase (weakening) in the Southern Ocean outgassing of oceanic CO_2, and a decrease (increase) in the Southern Ocean atmospheric CO_2 uptake. The CSO was calculated based on the equation given by Levin et al. (2003), which has been successfully used to trace CO_2 emissions from megacities (Niu et al., 2021; Xiong et al., 2021):

$$CSO = \frac{\text{Atm. } CO_{2\text{background}} * (\text{Atm. } \Delta^{14}C_{\text{source}} - \text{Atm. } \Delta^{14}C_{\text{background}})}{\text{Ocean } \Delta^{14}C_{\text{source}} - \text{Atm. } \Delta^{14}C_{\text{source}}} \quad (1)$$

Where the Atm. $\Delta^{14}C_{source}$ is the atmospheric ^{14}C content above the Southern Ocean (from the source zonal band; see below) inferred by averaging our ^{14}C tree-ring record from Strait of Magellan and the ^{14}C tree-ring record from Campbell Island developed by Turney et al. (2018) with a weight mean and standard error. The Atm. $\Delta^{14}C_{background}$ is the atmospheric ^{14}C content above the Southern Hemisphere mid-latitudes (the background zonal band), which was obtained from the compilation of tree-ring ^{14}C from New Zealand (Turnbull et al., 2017), Valdivian Rainforest, and Central Chile. Ocean $\Delta^{14}C_{source}$ is the ^{14}C content of the Southern Ocean shallow water (< 50 m deep) from October to March derived from GLODAP (Olsen et al., 2020) (Figure S2, section S2.2). The Atm. $CO_{2background}$ is the carbon dioxide content (*ppm*) above SH's mid-latitudes (the background zonal band) during October to March obtained from the Earth System Research Laboratories (ESRL) surface marine boundary layer CO_2 product (Dlugokencky et al., 2017) (Figure S3 and Figure S4, section S2.3). The CSO was calculated annually since 1973 when the maximum gradient period ended and, therefore, the annual influence of thermonuclear detonation pulses are absent (Hua et al., 2013; Ancapichun et al., 2021; see section 3.2). A complete description of the source and the background zonal bands is presented in section 3.2 and section S2.4. The CSO values and uncertainties

were obtained using equation 1 coupled with Monte-Carlo simulations (section S2.5). On the other hand, through a sensibility test, we found that values and uncertainties of the CSO estimation are mostly determined by the values and uncertainties of the tree-ring ^{14}C measurements, and secondly by the values and uncertainties of the ^{14}C content of the Southern Ocean shallow water and carbon dioxide content above SH's mid-latitudes (Figure S5; section S2.5). In the years 2014 to 2016, the values and uncertainties of the ^{14}C content of the Southern Ocean shallow water produce high uncertainties in our CSO estimations (Figure S5). The above occurs due to the progressive atmospheric ^{14}C decrease caused mostly by the carbon exchange between reservoirs. Thus, Atm. $\Delta^{14}C_{source}$ values are similar to the uncertainties of Ocean $\Delta^{14}C_{source}$, producing high uncertainties in the calculation. Therefore, our CSO estimation spans the years 1973 to 2013. On the other hand, it is important to mention that several studies have demonstrated that the atmospheric ^{14}C recorded by trees is influenced by i) the growth season, ii) carbon reservoirs or anthropogenic activities affecting air masses that arrive to a tree, and iii) provenance of air masses (Hua et al., 2012; Niu et al., 2021; Ancapichun et al., 2021). Therefore, when compile a set of records from each SH's zonal band: i) reduces the particular uncertainties associated with individual records and, ii) reveals a common atmospheric ^{14}C zonal pattern.

To trace the outgassing of oceanic CO_2 using atmospheric ^{14}C, we transform the atmospheric CO_2 concentration that comes from the Southern Ocean (CSO) to Petagrams of carbon (PgC). Our assumptions are that i) based on HYSPLIT analyses and the fact that the atmospheric layers close to the ocean have more oceanic carbon, the atmospheric layer strongly influenced by the outgassing of oceanic CO_2 corresponds to 100 meters, thus the volume where the CSO occurs corresponds to the source zonal band area (5.17×10^{13} m^2) multiplied with 100 meters, and ii) The density of carbon dioxide is 1.836 kg m^{-3}.

2.4. Air-sea CO_2 fluxes.

To compare our outgassing of oceanic CO_2 based on ^{14}C estimation with recent air-sea CO_2 flux based on pCO_2-products, we use the Harmonized ensemble data of the air-sea CO_2 flux based on observation pCO_2 products (Seaflux; Fay et al., 2021). This ensemble product was meant to facilitate the use of the air-sea CO_2 flux estimates based on pCO_2 observations in assessment studies of the global carbon cycle. This ensemble was harmonized by area correction and consistent scaling of gas exchange. Thus, this ensemble data product accounts for the diversity of the underlying mapping methodologies. The Seaflux uses six global observation-based mapping products and five wind products (section S2.6). More details are available in Fay et al. (2021).

3. RESULTS AND DISCUSSION

3.1. The atmospheric ^{14}C variability. Our three annually resolved ^{14}C tree-ring records (Figure 2) reveal an abrupt increase in atmospheric ^{14}C levels from the mid-1950s derived from the large number of atmospheric thermonuclear bomb tests detonated in the northern hemisphere during the so-called ‘’bomb-period’’ (1950-1985; Manning et al., 1990). It is worth noting that the subantarctic ^{14}C *P. uviferum* tree-ring record from the Strait of Magellan faithfully captured the bomb signal in terms of timing and magnitude, representing the world's southernmost ^{14}C marker of the bomb-period (Figure 2). As shown by Turnbull et al. (2017), the propagation of the bomb signal from the NH to the Southern Ocean was lagged by about 1.4 years. The maximum annual ^{14}C concentration (*bomb-peak*) in our ^{14}C records occurred in 1966 after large $\Delta^{14}C$-changes of more than 300 ‰ yr^{-1} during the 1963-1966 period. The *bomb-peak* timing of the southeast Pacific is in agreement with Campbell Island and New Zealand ^{14}C records, supporting the ideas that there are not zonal offsets in the Southern Hemisphere (Hogg et al., 2013) and that the peak in atmospheric $\Delta^{14}C$ recorded in the remote Southern Ocean region is indeed a candidate to demarcate the beginning of the Anthropocene (Turney et al., 2018). The period 1967-2016 is characterized by a steady decrease in atmospheric $\Delta^{14}C$ as a result of the ban on surface bomb tests, the burning of the ^{14}C-free fossil fuel, and the carbon exchange between the atmosphere and other carbon

reservoirs such as the Southern Ocean (Randerson et al., 2002; Levin et al., 2010; Graven et al., 2012).

3.2. Southern Hemisphere atmospheric ^{14}C gradients. The atmospheric $\Delta^{14}C$ difference between the Strait of Magellan (53.8 °S, 71° W) and Campbell Island (52.5° S, 169° E; Turney et al., 2018) regions is very low (Figure 2; Figure S6a; section S2.5), which indicates a similar atmospheric ^{14}C concentration between these two regions. This result is supported by a paired sample t-test coupled with the Monte-Carlo method, which showed a low probability level that the atmospheric $\Delta^{14}C$ difference between Strait of Magellan and Campbell Island regions is different from zero (level of probability = 4 %). This result suggests the absence of zonal atmospheric ^{14}C differences at ~52.5-53.8° S, agreeing with Hogg et al. (2013). The absence of Southern zonal offsets is explained by the atmospheric circulation, with latitudinal atmospheric mixing occurring for about months and zonal atmospheric mixing occurring in a few weeks (Jacob 1999). On the other hand, both the Strait of Magellan and Campbell Island records have noticeable differences with the other SH's mid-latitude $\Delta^{14}C$ records, revealing a north-south positive $\Delta^{14}C$ gradient in the SH during the studied period. Throughout paired sample t-tests coupled with the Monte-Carlo method, we confirm these findings (Figure S6b; section S2.5), obtaining a high probability level that the atmospheric $\Delta^{14}C$ offset between SH's mid-latitude and Southern Ocean $\Delta^{14}C$ records are different to zero (level of

probability > 99 %). Therefore, we report for the first time significant tropospheric ^{14}C differences between SH's mid and southern latitudes from recent decades. Thus, we confirm previous ocean-atmosphere model studies which found lower tropospheric ^{14}C concentration above the Southern Ocean relative to subtropical latitudes associated with bomb pulses flushes from NH and the Southern Ocean ventilation influence (Randerson et al., 2002; Turnbull et al., 2009).

From 1950 to 1972, the atmospheric ^{14}C offset between mid-latitudes and the Southern Ocean records shows maximum values (Figure S6b), evidencing the bomb pulses flushes from northern to southern latitudes agreeing with similar latitudinal ^{14}C patterns described by Hua et al. (2013). From 1973 to 2016, despite the absence of northern bomb ^{14}C-pulses, the Southern Ocean records still show lower $\Delta^{14}C$ levels than mid-latitudes, evidencing the strong effect of the Southern Ocean outgassing of oceanic CO_2 on the Southern troposphere (Braziunas et al., 1995; Randerson et al., 2002; Key et al., 2004; Turnbull et al., 2009; Levin et al., 2010; Graven et al., 2012). In fact, through the calculation of the backward air parcel trajectories of each southern record location (Strait of Magellan and Campbell Island), we found that air parcels that transported the $^{14}CO_2$ came from latitudes between ~45-65 °S and low altitudes (within the marine boundary layer) (Figure S7 and S8; section S2.8). Along the 45-65 °S zonal band, strong winds (> 11 m s^{-1}) force northward Ekman transport (~ 0.1 m^2 s^{-1}), which moves shallow-waters northward, generating deep-water

upwelling (Lovenduski & Gruber 2005) (Figure S9). Subsequently, these strong winds cause high ocean-atmosphere CO_2 exchange, leading to high-outgassing of natural ^{14}C-depleted CO_2, explaining the lower southern tropospheric $\Delta^{14}C$ levels relative to mid latitudes (Randerson et al., 2002; Turnbull et al., 2009). On the other hand, during the early spring, high-$\Delta^{14}C$ air masses subside from the upper troposphere in absence of carbon exchange with other reservoirs (Randerson et al., 2002; Turnbull et al., 2017). Therefore, for the period 1973 to the present, we can assume that the only source of air parcels with high $\Delta^{14}C$ levels for the SH's extratropical latitudes is the upper troposphere and that the only process that could cause low $\Delta^{14}C$ levels in the SH's high-latitudes is the CO_2 outgassing of the Southern Ocean. Considering the processes and characteristics described above and the rapid zonal atmospheric mixing (Jacob 1999), to estimate the CO_2 contribution to the source atmospheric CO_2 concentration that comes from the Southern Ocean (CSO; equation 1), we established the background region as the SH's zonal band between 20-45 °S and the source region as the SH's zonal band between 45-65 °S (see methods and supplementary information; Figure S10a; Figure S10b).

3.3. The outgassing of oceanic CO_2 based on ^{14}C. The outgassing of oceanic CO_2 based on ^{14}C has positive values through time with a weighted mean of 0.09 ± 0.001 PgC (Figure 3). This result reveals the strong and

persistent CO_2 emissions from the Southern Ocean during the studied period and suggests a persistent influence of the Southern Ocean upwelling of deep-waters. Recent studies have reported a negative total air-sea CO_2 flux along the Southern Ocean (CO_2 into the ocean; Landschützer et al., 2020; Watson et al., 2020), but it is important to take into account that the total air-sea CO_2 flux that occurs along the Southern Ocean represents the integrated air-sea CO_2 flux of the natural and anthropogenic CO_2 (Landschützer et al., 2020). We show in the supplementary information (Figure S11), the Southern Ocean (45-65 °S; source zonal band) is characterized by areas of positive and negative air-sea CO_2 fluxes, corresponding to regions of outgassing of oceanic CO_2 and uptake of atmospheric CO_2, respectively. Thereby, the upwelling of high pCO_2 deepwater leads to the outgassing of oceanic CO_2 against a low uptake of atmospheric CO_2 because the ocean-atmosphere pCO_2 difference is the force governing the exchange of CO_2 across the air-sea interface (Garbe et al., 2014; Wanninkhof 2014; DeVries et al., 2017). In fact, we found a high positive correlation between the CO_2 flux out of the Southern Ocean (outgassing of oceanic CO_2 based on pCO_2 products) and the into CO_2 flux the Southern Ocean (section S2.6; Figure S12 and Table S1). Therefore, the outgassing of oceanic CO_2 based on ^{14}C also traces indirectly the interannual variability of the into the Southern Ocean atmospheric CO_2 flux along with the source zonal band (CO_2 into the ocean).

In order to compare our estimations of oceanic CO_2 outgassing based on atmospheric ^{14}C with independent approaches, we calculated the total summer CO_2 flux out of the Southern Ocean along the zonal band (45-65 °S) based on six surface ocean pCO_2 mapped products and five different wind products (Fay et al., 2021; see section 2.4) (Figure 3). In general, pCO_2-based products show persistent outgassing of oceanic CO_2 through time (weighted mean = 0.05 ± 0.005 PgC) in line with the persistent influence of Southern Ocean deep-water upwelling. However, the ^{14}C-based summer emissions are on average 0.04 PgC higher than those based on pCO_2. This could be associated with the assumption from our estimation; therefore, in the following paragraphs, we are going to analyze the interannual variability and trend of our estimation.

At interannual scale, the outgassing of oceanic CO_2 based on atmospheric ^{14}C shows values that varies from 0 to ~0.4 PgC between years (for example, 2011/2012 years), revealing a large interannual variability of the outgassing of oceanic CO_2. This substantial amount of interannual variability hasn't been reported previously. The few pCO_2-based products that show marked interannual variability, but smaller than the ^{14}C-based product, are the JMA-MLR and the JENA-MLS pCO_2-based products (Table S2). MPI-SOMFFN, CMEMS-FFN, NIES-FNN, and CSIR-ML6 pCO_2-based products show an even smaller interannual variability of the outgassing of oceanic CO_2 than our ^{14}C-based product, exposing discrepancies. On the other hand, the outgassing of oceanic

CO_2 based on atmospheric ^{14}C reveals some years of near to zero outgassing of oceanic CO_2: 1989, 2003, 2010, 2011, and 2013 (values near to 0 PgC). Previous studies have demonstrated that years of low Southern Ocean outgassing of oceanic CO_2 are explained by weakening Southern Ocean ventilation, which means a weak upwelling of high pCO_2 deepwater that favors the flux of carbon from atmosphere to the Ocean (DeVries et al., 2017). However, the only outgassing of oceanic CO_2 series derived from a pCO_2-based product that had values near to zero is CSIR-ML6 showing minimum values in the years 1989, 1993, 2010, and 2013 (similar to the ^{14}C-based product). Discrepancies exposed above could be explained by the interpolation methods used by the others pCO_2-based studies, which, in general, are accompanied by systematic-smooth procedures in the pCO_2 data, losing the large natural variability of the surface ocean pCO_2. Therefore, we found a higher than expected interannual variability of the outgassing of oceanic CO_2 that haven't been reported previously, suggesting an underestimation of the interannual variability of the outgassing of oceanic CO_2 traced by pCO_2-based products.

Our ^{14}C-based estimation represents the first outgassing record of oceanic CO_2 further back the 1980s, extending more than a decade this information and providing a multidecadal perspective to better understand recent changes and trends in Southern Ocean air-sea carbon fluxes. During the 70s, the Southern Ocean emitted a large amount of CO_2 to the atmosphere (Weight mean = 0.1

PgC) similar to the 80s decade (0.1 PgC) (Figure 3). The 80s and 90s show a decrease in the outgassing of oceanic CO_2 based on atmospheric ^{14}C from 0.1 to 0.095 PgC, respectively, followed by a decade of lower values (2000s weight mean = 0.09 PgC). These results suggest a transition period between the 80s to 90s decades when the outgassing of oceanic CO_2 decreased (-0.005 PgC). In agreement with previous studies that had reported a reinvigoration of the atmosphere to ocean CO_2 flux in the 2000s accompanied by a decrease of the outgassing of oceanic CO_2 (MPI-SOMFFN pCO_2-based product), our ^{14}C-based estimation showed a decrease during the transition 90s to 2000s, evidencing a decrease in the outgassing of oceanic CO_2 (Landschützer et al., 2014; DeVries et al., 2017; Watson et al., 2020). However, we report a lower than expected decrease in the outgassing of oceanic CO_2 from the transition period 90s to 2000s (decrease of -0.005 PgC). In fact, the Southern Ocean CO_2 flux derived from MPI-SOMFFN is the only pCO_2-based product that had a noticeable decadal variation, revealing discrepancies of the out the Southern Ocean CO_2 flux derived from different pCO_2-based products. Thus, surprisingly, our ^{14}C-based product and almost overall the pCO_2-based products, excluding the MPI-SOMFFN, didn't reveal a clear decadal pattern but show a marked negative trend.

The outgassing of oceanic CO_2 based on atmospheric ^{14}C reveals a negative trend from 1973 to 2013 years (Table S2; Figure 3), suggesting a

progressive decrease in the outgassing of oceanic CO_2. This negative trend also is found in the out the Southern Ocean CO_2 flux derived from different pCO_2-based products (Table S3; Figure 3). Previous studies have suggested that the Southern Ocean outgassing of oceanic CO_2 variability is dominated by two forcings: the anthropogenic CO_2 emissions and the Southern Annular Mode (SAM) that is the dominant mode of climate variability in the southern high latitudes (Marshall et al., 2003). The recent increase in anthropogenic CO_2 emissions has caused an increase in the atmospheric pCO_2, which by itself favors the atmosphere to the ocean CO_2 flux (Garbe et al., 2014; Wanninkhof 2014). The recent decades positive trend of the SAM have forced an intensification of the Southern overturning circulation, causing the strengthening of the upwelling of high pCO_2 deepwater, which by itself favors the ocean to the atmosphere CO_2 flux (Le Quéré et al., 2007; DeVries et al., 2017). Therefore, the negative trend showed by both the outgassing of oceanic CO_2 based on atmospheric ^{14}C and pCO_2-products is the result of these forcings and suggests that the increase of the atmospheric CO_2 is the main driver of the outgassing of oceanic CO_2 trend (Gruber et al., 2009; Ridge & McKinley 2020). The extrapolation of this negative trend suggests a possible near to zero Southern Ocean outgassing of oceanic CO_2 in the future, agreeing with recent projections (Kessler & Tjiputra 2016; Ridge & McKinley 2020). However, it is important to consider the unprecedented large interannual variability traced by the

outgassing of oceanic CO_2 based on the atmospheric ^{14}C, which suggest that still in a near to zero Southern Ocean outgassing of oceanic CO_2 scenario, the Southern Ocean would present years of high outgassing of oceanic CO_2 and, therefore, lower than expected ocean CO_2-uptake.

4. CONCLUSIONS

Comparisons between SH's records located in similar latitudes but different longitudes reveal the absence of zonal atmospheric $\Delta^{14}C$ differences from the bomb and post-bomb periods. However, we found significant atmospheric $\Delta^{14}C$ differences between mid-latitudes and southern records that are explained by the Southern Ocean ventilation influence, corroborating previous based-model study's findings.

Atmospheric $\Delta^{14}C$ levels from SH's tree-ring records are a reliable tracer for the outgassing of oceanic CO_2 showing an unprecedented-traced noticeable interannual variability. The ^{14}C-based product and out the Ocean CO_2 flux traces by surface ocean pCO_2 mapped products show negative trends that suggest a progressive decrease of the outgassing of oceanic CO_2 that potentially it is explained by the increase in the atmospheric pCO_2 caused by the emission of anthropogenic CO_2.

5. REFERENCES

Ancapichún S., De Pol-Holz R., Christie D., Santos, G., Collado-Fabbri, S., Garreaud, R., et al. (2021). Radiocarbon bomb-peak signal in tree rings from the tropical Andes register low latitude atmospheric dynamics in the Southern Hemisphere. *Science of the Total Environment* 774 (2021) 145126. doi:10.1016/j.scitotenv.2021.145126.

Anchukaitis, K., Evans, M., Lang, T., Smith, D., Leavitt, S., & Schrag, D. (2008). Consequences of a Rapid Cellulose Extraction technique for Oxygen isotope and radiocarbon analyses. *Analytical Chemistry*, 80(60), 2035-2041. doi:10.1021/ac7020272.

Atlas, R., Hoffman, R., Ardizzone, J., Leidner, S., Jusem, J., Smith, D., & Gombos, D. (2011). A cross-calibrated, multiplatform ocean surface wind velocity product for meteorological and oceanographic applications. *Bulletin of the American Meteorological Society*, *92*(2), pp.157-174. doi:10.1175/2010BAMS2946.1, 2011.

Aravena, J. (2007). Reconstructing climate variability using tree rings and glacier fluctuations in the southern Chilean Andes. *PhD Thesis,* Faculty of Graduate Studies, University of Western Ontario, Canada.

Bannister, J., Donoso, P., & Bauhus, J. (2012). Persistence of the Slow Growing Conifer *Pilgerodendron uviferum* in Old-Growth and Fire-Disturbed Southern Bog Forests. *Ecosystems*, 15(7), 1158–1172. doi:10.1007/s10021-012-9574-7.

Bopp, L., Lévy, M., Resplandy, L., & Sallée, J. (2015). Pathways of anthropogenic carbon subduction in the global ocean. *Geophysical Research Letter*, 42, 6416–6423. doi:10.1002/2015gl065073.

Braziunas, T., Fung, I., & Stuiver., M. (1995). The preindustrial atmospheric $^{14}CO_2$ latitudinal gradient as related to exchanges among atmospheric, oceanic, and terrestrial reservoirs. *Global Biogeochemical Cycles*, 9, 565–584. doi:10.1029/95gb01725.

Capano, M., Miramont, C., Guibal, F., Kromer, B., Tune, T., Fagault, Y., et al. (2017). Wood ^{14}C Dating with AixMICADAS: Methods and application to tree-ring sequences from the Younger Dryas Event in the Southern French Alps. *Radiocarbon*, 60(01), 51-74. doi:10.1017/rdc.2017.83.

Chau, T., Gehlen, M., & Chevallier, F. (2021). Global Ocean Surface Carbon Product MULTIOBS_ GLO_BIO_CARBON_SURFACE_REP_015_008, E.U. Copernicus Marine Service Information, available at: https://resources.marine.copernicus.eu/documents/PUM/CMEMS-MOB-PUM-015-008.pdf, last access: 11 January 2021.

DeVries, T. (2014). The oceanic anthropogenic CO_2 sink: storage, air-sea fluxes, and transports over the industrial era. *Global Biogeochemical Cycles*, 28, 631–647. doi:10.1002/2013gb004739.

DeVries, T., Holzer, M., & Primeau, F. (2017). Recent increase in oceanic carbon uptake driven by weaker upperocean overturning. *Nature*, 542, 215–218. doi:10.1038/nature21068.

Dlugokencky, E. & Tans, P. (2020). Trends in atmospheric carbon dioxide, National Oceanic and Atmospheric Administration, Earth System Research Laboratory (NOAA/ESRL), available at: http://www.esrl.noaa.gov/gmd/ccgg/trends/global.html, last access: 16 October 2020.

Donoso, C., Lara, A., Escobar, B., Premoli, A., & Souto, C. (2006). *Fitzroya cupressoides* (molina) I.M. johnst. In: Donoso, C. (Ed.), Las especies arbóreas de los bosques templados de Chile y Argentina. *Autoecología. Maria Cuneo Ediciones, Valdivia, Chile,* 68–81.

Draxler, R., & Hess, G. (1998). An Overview of the HYSPLIT_4 modeling system for trajectories, dispersión, and deposition. *Austrian Meteorological Magazine*, 47, 295-308. doi:10.1016/S1352-2310(97)00457-3.

Draxler, R., & Stunder, J. (1988). Modeling the CAPTEX vertical tracer concentration profiles. *Journal of Applied Meteorology*, 27, 617-625. doi:10.1175/1520-0450(1988)027<0617:MTCVTC>2.0.CO;2.

Draxler, R., & Taylor, D. (1982). Horizontal dispersion parameters for long-range transport modeling. *Journal of Applied Meteorology*, 21, 367-372. doi:10.1175/1520-0450(1982)021<0367:HDPFLR>2.0.CO;2.

Enting, I. (1982). Nuclear weapons data for use in carbon cycle modeling. Melbourne (Australia), CSIRO Division of atmospheric physics and technology.

Fay, A.., & McKinley, G. (2013). Global trends in surface ocean *p*CO2 from in situ data. *Global Biogeochemical Cycles*, *27*, 541–557. doi:10.1002/gbc.20051.

Fay, A., McKinley, G., & Lovenduski, N. (2014). Southern Ocean carbon trends: Sensitivity to methods. *Geophysical Research Letter*, *41*, 6833–6840. doi:10.1002/2014GL061324.

Fay, A., Gregor, L., Landschützer, P., McKinley, G., Gruber, N., Gehlen, M., et al. (2021). Harmonization of global surface ocean pCO2 mapped products and their flux calculations; an improved estimate of the ocean carbon sink. *Earth System Science Data***.** doi:10.5194/essd-2021-16.

Garbe, C., Rutgersson, A., Boutin, J., Leeuw, G., Delille, B., Fairall, C., et al. (2014). Transfer across the air-sea interface, in: Ocean-Atmosphere Interactions of Gases and Particles, edited by: Liss, P. S. and Johnson, M. T., *Springer*, Berlin, Heidelberg, 55–112, 2014.

Graven, H., Guilderson, T., & Keeling, R. (2012). Observations of radiocarbon in CO_2 at seven global sampling sites in the Scripps flask network: Analysis of spatial gradients and seasonal cycles. *Journal of Geophysical Research*, 117, D02303. doi:10.1029/2011JD016535.

Gruber, N., Gloor, M., Mikaloff-Fletcher, S., Doney, S., Dutkiewicz, S., Follows, M., et al. (2009). Oceanic sources, sinks, and transport of atmospheric CO_2. *Global Biogeochemical Cycles*, 23, GB1005. doi:10.1029/2008gb003349.

Gregor, L., Lebehot, A., Kok, S., & Scheel Monteiro, P. (2019). A comparative assessment of the uncertainties of global surface ocean CO2 estimates using a machine-learning ensemble (CSIR-ML6 version 2019a) – have we hit the wall*?. Geoscience Model Development*, 12, 5113–5136. doi:10.5194/gmd-12-5113-2019.

Hersbach, H., Bell, B., Berrisford, P., Hirahara, S., Horányi, A., Muñoz-Sabater, J., et al. (2020). The ERA5 global reanalysis. *Quaternary Journal Royal Meteorology Society.* 146, 1999–2049. doi: 10.1002/qj.3803, 2020.

Hogg, A., Turney, C., Palmer, J., Cook, E., & Buckley, B. (2013). Is there any evidence for regional atmospheric 14C offsets in the southern hemisphere?. *Radiocarbon*, Vol 55, Nr 4, 2013, p 2029–2034. doi:10.2458/azu_js_rc.v55i2.16104.

Holz, A., Hart, S., Williamson, G., Veblen, T., & Aravena, J. (2018). Radial growth response to climate change along the latitudinal range of the world's southernmost conifer in southern South America. *Journal of Biogeography*, 45(5), 1140–1152. doi:10.1111/jbi.13199.

Hua, Q., Barbetti, M., Levchenko, V., Arrigo, R., Buckley, B., & Smith, A. (2012). Monsoonal influences on Southern Hemisphere $^{14}CO_2$. *Geophysical Research Letter*, 39, L19806. doi:10.1029/2012GL052971.

Hua, Q., Barbetti, M., & Rakowski, A. (2013). Atmospheric Radiocarbon for the period 1950-2010. *Radiocarbon*, 55(4), 2059-2072. doi:10.2458/azu_js_rc.v55i2.16177.

Iida, Y., Takatani, Y., Kojima, A. & Ishii, M. (2020). Global trends of ocean CO2 sink and ocean acidification: an observation based reconstruction of surface ocean inorganic carbon variables. *Journal of Oceanography*, pp.1-36. doi:10.1007/s10872-020-00571-5, 2020.

Ishii, M., et al. (2014). Air-sea CO2 flux in the Pacific Ocean for the period 1990–2009. *Biogeosciences*, *11*, 709–734. doi:10.5194/bg-11-709-2014.

Jacob, D.J. 1999. Introduction to atmospheric chemistry. Princeton, NJ, USA: Princeton University Press.

Kalnay, E., Kanamitsu, M., Kistler, R., Collins, W., Deaven, D., Gandin, L., et al. (1996). The NCEP/NCAR 40-Year Reanalysis Project. *Bulletin of the American Meteorological Society,* 77, 437-471. doi:10.1175/1520-0477(1996)077<0437:TNYRP>2.0.CO;2.

Kanamitsu, M., Kumar, A., Juang, H., Schemm, J., Wang, W., Yang, et al. (2002). NCEP dynamical seasonal forecast system 2000. *Bulletin of the American Meteorological Society*, *83*(7), pp.1019-1038. doi:10.1175/1520-0477(2002)083<1019:NDSFS>2.3.CO;2.

Kessler, A., & Tjiputra, J. (2016). The Southern Ocean as a constraint to reduce uncertainty in future ocean carbon sinks. *Earth System Dynamics, 7(2), 295–312.* doi:10.5194/esd-7-295-2016.

Key, R., Kozyr, A., Sabine, C., Lee, K., Wanninkhof, R., Bulliste, J., et al. (2004). A global ocean carbon climatology: results from global data analysis project (GLODAP). *Global Biogeochemical Cycles*, 18(4), GB4031. doi:10/1029/2004gb002247.

Khatiwala, S., Tanhua, T., Mikaloff-Fletcher, S., Gerber, M., Doney, S., et al. (2013). Global ocean storage of anthropogenic carbon. *Biogeosciences*, 10:2169–91. doi:10.5194/bg-10-2169-2013.

Kobayashi, S., Ota, Y., Harada, Y., Ebita, A., Moriya, M., Onoda, H., et al. (2015). The JRA-55 Reanalysis: General Specifications and Basic Characteristics. *Journal Meteorological Society Japan*., 93, 5–48. doi:10.2151/jmsj.2015-001.

Landschützer, P., Gruber, N., Bakker, D., Schuster, U., Nakaoka, S., Payne, M., et al. (2013). A neural network-based estimate of the seasonal to inter-annual variability of the Atlantic Ocean carbon sink. *Biogeosciences*, 10, 7793–7815. doi:10.5194/bg-10-7793-2013.

Landschützer, P., Gruber, N., & Bakker, D. (2020). An observation-based global monthly gridded sea surface pCO2 product from 1982 onward and its monthly climatology (NCEI Accession 0160558). Version 5.5. NOAA National Centers for Environmental Information. https://www.ncei.noaa.gov/access/ocean-carbon-data system/oceans/SPCO2_1982_present_ETH_SOM_FFN.html. Dataset. doi.org:10.7289/V5Z899N6.

Le Quéré, C., Rödenbeck, C., Buitenhuis, E., Conway, T., Langenfelds, R., Gómez, A., et al. (2007). Saturation of the Southern Ocean CO2 Sink Due to

Recent Climate Change. *Science* 316, 1735 (2007). doi:10.1126/science.1136188.

LeQuesne, C., Stahle, D., Cleaveland, M., Therrell, M., Aravena, J., & Barichivich, J. (2006). Ancient *Austrocedrus* tree-ring chronologies used to reconstruct Central Chile precipitation variability from A.D.1200 to 2000. *Journal of Climate,* 19(22), 5731–5744*.* doi:10.1175/jcli3935.1.

Levin, I., Kromer, B., Schmidt, M., & Sartorius, H. (2003). A novel approach for independent budgeting of fossil fuel CO_2 over Europe by $^{14}CO_2$ observation. *Geophysical Research Letters*, 30(23), 2194. doi:10.1029/2003GL018477.

Levin, I. & Kromer, B., (2004). The tropospheric 14CO2 level in mid-latitudes of the northern hemisphere (1959-2003)**.** *Radiocarbon*, Vol 46, Nr 3, 2004, p 1261–1272. doi:10.1017/S0033822200033130.

Levin, I., Naegler, T., Kromer, B., Francey, R., Gomez-Pelaez, A., Steele, L., et al. (2010). Observations and modeling of the global distribution and long-term trend of atmospheric $^{14}CO_2$. *Tellus,* 62(1), 26-46. doi:10.1111/j.1600-0889.2009.00446.x.

Lovenduski, N., & Gruber, N. (2005). Impact of the Southern Annular Mode on Southern Ocean circulation and biology. *Geophysical Research Letter*, 32, L11603. doi:10.1029/2005gl022727.

Manning, M., Lowe, D., Melhuish, W., Sparks, R., Wallace, G., Brenninkmeijer, C., & Mcgil, R. (1990). The use of radiocarbon measurements in atmospheric studies. *Radiocarbon,* 32, 37-58. doi:10.1017/S0033822200039941.

Marshall, G. (2003). Trends in the southern annular mode from observations and reanalyses. *Journal of Climate* 16: 4134–4143. doi:10.1175/1520- 0442(2003)016<4134:Titsam>2.0.Co;2.

Marshall, J., & Speer, K. (2012). Closure of the meridional overturning circulation through Southern Ocean upwelling. *Nature Geoscience*, 5, 171–180. doi:10.1038/ngeo1391.

Messager, C., Speich, S., & Key, E. (2012). Marine atmospheric boundary layer over some Southern Ocean fronts during the IPY BGH 2008 cruise. *Ocean Science*, 8(6), 1001-1023. doi:10.5194/os-8-1001-2012.

Mikaloff-Fletcher, S., Gruber, N., Jacobson, A., Doney, S., Dutkiewicz, S., Gerber, M., et al. (2006). Inverse estimates of anthropogenic CO_2 uptake, transport, and storage by the ocean. *Global Biogeochemical Cycles*, 20, GB2002. doi:10.1029/2005gb002530.

Mikaloff-Fletcher, S., Gruber, N., Jacobson, A., Gloor, M., Doney, S., Dutkiewicz, S., et al. (2007). Inverse estimates of the oceanic sources and sinks

of natural CO_2 and the implied oceanic carbon transport. *Global Biogeochemical Cycles*, 21, GB1010. doi:10.1029/2006gb002751.

Morales, M. S., Cook, E. R., Barichivich, J., Christie, D. A., Villalba, R., LeQuesne, C., … Boninsegna, J. A. (2020). Six hundred years of South American tree rings reveal an increase in severe hydroclimatic events since mid-20th century. *Proceedings of the National Academy of Sciences*, 117(29), 16816–16823. doi:10.1073/pnas.2002411117.

Morrison, A., Frölicher, T., & Sarmiento, J. (2015). Upwelling in the Southern Ocean. *Physics Today*, 68, 27–32. doi:10.1063/PT.3.2654.

Munro, D., Lovenduski, N., Takahashi, T., Stephens, B., Newberger, T., & Sweeney, C. (2015). Recent evidence for a strengthening CO_2 sink in the Southern Ocean from carbonate system measurements in the Drake Passage (2002–2015). *Geophysical Research Letter*, 42, 7623–7630. doi:10.1002/2015gl065194.

Niu, Z., Feng, X., Zhour, W., Wang, P., Liu, Y., Lu, X., Du, H., et al. (2021). Tree-ring $\Delta^{14}C$ time series from 1948 to 2018 at a regional background site, China: Influences of atmospheric nuclear weapons tests and fossil fuel emissions. *Atmospheric Environment* 118156. doi:10.1016/j.atmosenv.2020.118156.

Ramsey, C., van der Plicht, J., & Weninger, B. (2001). “Wiggle Matching” Radiocarbon Dates. *Radiocarbon*, 43(2A), 381–389. doi:10.1017/s0033822200038248.

Randerson, J., Enting, I., Schuur, E., Caldeira, K., & Fung, I. (2002). Seasonal and latitudinal variability of troposphere $\Delta^{14}CO_2$: Post bomb contributions from fossil fuels, oceans, the stratosphere, and the terrestrial biosphere. *Global Biochemical Cycles*, 16(4), 59-1-59-19. doi:10.1029/2002GB001876.

Ridge, S., & McKinley, G. (2020). Advective controls on the North Atlantic Anthropogenic carbon sink. *Global Biochemical Cycles*. doi:10.1029/2019GB006457.

Rödenbeck, C., Keeling, R., Bakker, D., Metzl, N., Olsen, A., Sabine, C., & Heimann, M. (2013). Global surface-ocean pCO2 and sea–air CO2 flux variability from an observation-driven ocean mixed-layer scheme. *Ocean Science*, 9, 193–216. doi:10.5194/os-9-193-2013, 2013.

Rödenbeck, C., Bakker, D., Metzl, N., Olsen, A., Sabine, C., Cassar, N., et al. (2014). Interannual sea–air CO_2 flux variability from an observation-driven ocean mixed-layer scheme. *Biogeosciences*, 11, 4599–4613. doi:10.5194/bg-11-4599-2014.

Sabine, C., Feely, R., Gruber, N., Key, R., Lee, K., Bullister, J., et al. (2004). The oceanic sink for anthropogenic CO_2. *Science*, 305, 367–71. doi:10.1126/science.1097403.

Sallée, J., Matear, R., Rintoul, S., & Lenton, A. (2012). Localized subduction of anthropogenic carbon dioxide in the Southern Hemisphere oceans. *Nature Geoscience*, 5, 579–584. doi:10.1038/ngeo1523.

Santos, G., Linares, R., Lisi, C., & Tomazello, M. (2015). Annual growth rings in a simple of Pananá pine (*Araucaria angustifolia*): Toward improving the ^{14}C calibration curve for the Southern Hemisphere. *Quaternary Geochronology*, 25, 96-103. doi:10.1016/j.quageo.2014.10.004.

Santos, G., Granato-Souza, D., Maioli, A., Oelkers, R., & Andreu-Hayles, L. (2020). Radiocarbon analysis confirms anual periodicity in *Cedrela odorata* tree rings from the equatorial Amazon. *Quaternary Geochronology*, 28, 101079. doi:10.1016/j.quageo.2020.101079.

Santos, G., & Ormsby, K. (2013). Behavioral variability in ABA chemical pretreatment close to the ^{14}C age limit. *Radiocarbon*, 55(2), 534-44. doi:10.1017/S0033822200057660.

Santos, G., Southon, J., Druffel-Rodriguez, K., Griffin, M., & Mazon, M. (2004). Magnesium perchlorate as an alternative water trap in AMS graphite

simple preparation: a report on sample preparation at KCCAMS at the University of California, Irvine. *Radiocarbon,* 46(1), 165-73. doi:10.1017/S0033822200039485.

Santos, G., Moore, R., Southon, J., Griffin, S., Hinger, E., & Zhang, D. (2007). AMS ^{14}C sample preparation at the KCCAMS/UCI facility: status report and performance of small samples. *Radiocarbon,* 49(2), 255-70. doi:10.1017/S0033822200042181.

Scarchilli, C., Frezzotti, M., & Ruti, P. (2011). Snow precipitation at four ice core sites in East Antarctica: Provenance seasonality a blocking factors. *Climate dynamic*, 37, 2107-2125. doi:10.1007/s00382-010-0946-4.

Schlosser, E., Oeter, H., Mason-Delmonte, V., & Reijmer, C. (2008). Atmospheric influence on the deuterium excess signal in polar firn: Implications for ice-core interpretation. *Journal Glaciology*, 54, 117-124. doi:10.3189/002214308784408991.

Sinclair, K., Bertler, N., Trompetter, W., & Baisden, W. (2013). Seasonality of airmass pathways to coastal Antarctica: Ramifications for interpreting high-resolution ice core records. *Journal of Climate,* 26(6), 2065-2076. doi:10.1175/JCLI-D-12-00167.1.

Southon, J., & Magana, A. (2010). A comparison of cellulose extraction and ABA pretreatment methods for AMS ^{14}C dating of ancient wood. *Radiocarbon,* 52(3), 1371-1379. doi:10.1017/S0033822200046452.

Stein, A., Draxler, R., Rolph, G., Stunder, B., Cohen, M., & Ngan, F. (2015). NOAA's HYSPLIT atmospheric transport and dispersion modeling system, *Bulletin of the American Meteorological Society*, 96, 2059-2077. https: //doi.org/10.1175/BAMS-D-14-00110.1.

Stuiver, M., & Polach, H. (1977). Discussion: reporting of ^{14}C data. *Radiocarbon*, 19(3), 355-63. doi:10.1017/S0033822200003672.

Olsen, A., et al. (2020). An updated version of the global interior ocean biogeochemical data product, GLODAPv2.2020. *Earth System Science Data*, 12, 3653–3678, 2020. doi:10.5194/essd-12-3653-2020.

Takahashi, T., Sutherland, S., Wanninkhof, R., Sweeney, C., Feely, R., Chipman, D., et al. (2009). Climatological mean and decadal change in surface ocean pCO_2, and net sea–air CO_2 flux over the global oceans. *Deep-Sea Research II*, 56, 554–577. doi:10.1016/j.dsr2.2008.12.009.

Turnbull, J., Mikaloff, S., Ansell, I., Brailsford, G., Moss, R., Norris, M., et al. (2017). Sixty years of radiocarbon dioxide measurements at Wellington, New

Zealand: 1954-2014. *Atmospheric Chemistry and Phys*ics, 17, 14771-14784. doi:10.5194/acp-17-14771-2017.

Turnbull, J., Rayner, P., Miller, J., Naegler, T., Ciais, P., & Cozic, A. (2009). On the use of $^{14}CO_2$ as a tracer for fossil fuel CO_2: Quantifying uncertainties using an atmospheric transport model. *Journal of Geophysical Research*, 114, D22302. doi:10.1029/2009JD012308.

Turney, C., Palmer, J., Hogg, A., Fogwill, J., Jones, R., et al. (2016). Multidecadal variations in Southern Hermisphere atmospheric ^{14}C: Evidence against a Southern Ocean sink at the end of the Little Ice Age CO2 anomaly. *Global Biogeochemical Cycles*, 30. Doi:10.1002/2015GB005257.

Turney, C., Palmer, J., Maslin, M., Hogg, A., Fogwill, C., Southon, J., et al. (2018). Global Peak in Atmospheric Radiocarbon Provides a Potential Definition for the Onset of the Anthropocene Epoch in 1965. *Scientific Reports*, 8, 1. doi:10.1038/s41598-018-20970-5

Urrutia-Jalabert, R., Rossi, S., Deslauriers, A., Malhi, Y., & Lara, A. (2015). Environmental correlates of stem radius change in the endangered *Fitzroya cupressoides* forests of southern Chile. *Agricultural and Forest Meteorology*, 200, 209–221. doi:10.1016/j.agrformet.2014.10.001.

Villalba, R. (1994). Tree-ring and glacial evidence for the medieval warm epoch and the little ice age in southern South America*. Climatic Change,* 26(2-3), 183–197. doi:10.1007/bf01092413.

Watson, A., Schuster, U., Shutler, J., Holding, T., Ashton, I., Landschützer, P., Woolf, D., & Goddijn-Murphy, L. (2020). Revised estimates of ocean-atmosphere CO2 flux are consistent with ocean carbon inventory*. Nature Communication*s, 11, 1–6. doi:10.1038/s41467-020-18203-3, 2020.

Wanninkhof, R., et al. (2013). Global ocean carbon uptake: Magnitude, variability and trends. *Biogeosciences*, *10*, 1983–2000. doi:10.5194/bg-10-1983-2013.

Wanninkhof, R. (2014). Relationship between wind speed and gas exchange over the ocean revisited. *Limnolody Oceanography-Metheorology*., 12, 351–362. doi:10.4319/lom.2014.12.351, 2014.

Weaver, A., Marotzke, J., Cummins, P., & Sarachik, E. (1993). Stability and Variability of the Thermohaline Circulation. *Journal of Physical Oceanography, 23(1), 39–60.* doi:10.1175/1520-0485(1993)023<0039:savott>2.0.co.

Weitzenkamp, B., Schneider, C., Kilian, R., Spiecker, H., & Kahle, H. (2007). Regional climate and tree growth at Gran Campo Nevado, Chilean

Patagonia. *Geophysical Research Abstracts*, Vol. 9, 09332, 2007SRef-ID: 1607-7962/gra/EGU2007-A-09332.

Xiong , X., Zhou , W., Hou , X., P., H., Zhao , X., et al. (2021). Time series of atmospheric $\Delta^{14}CO_2$ recorded in tree rings from Northwest China (1957-2015). *Chemosphere* 272 (2021) 129921. doi: 10.1016/j.chemosphere.2021.129921.

Zeng, J., Nojiri, Y., Landschützer, P., Telszewski, M., & Nakaoka, S. (2014). A global surface ocean fCO2 climatology based on a feed-forward neural network. *Journal of Atmospheric Oceanic Technology.*, *31*, 1838–1849. doi:10.1175/JTECH-D-13-00137.1.

6. FIGURES

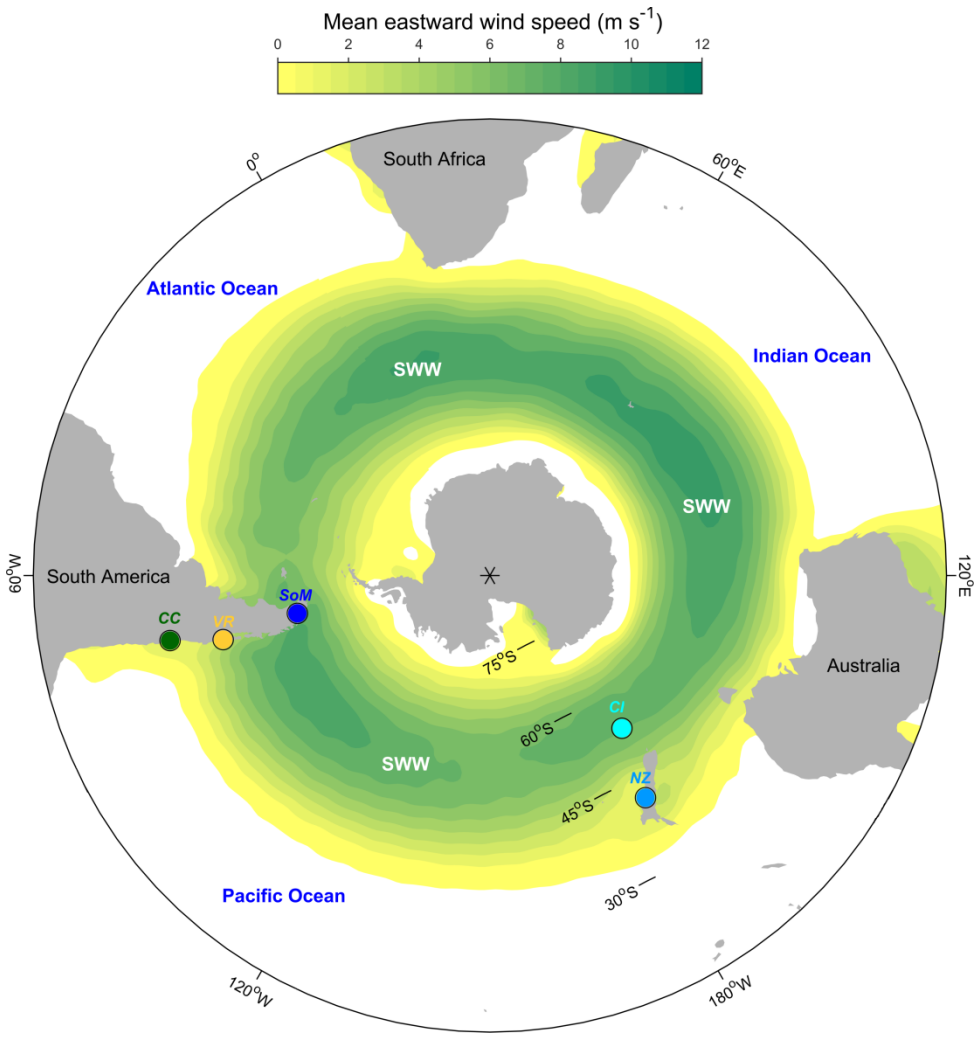

Figure 1. Locations of $\Delta^{14}C$ tree-ring records: Central Chile (*A. chilensis;* 32 °S, CC; green dot; this study); Valdivian Rainforest (*F. cupressoides;* 40 °S, VR; yellow dot; this study); New Zealand (*A. australis;* 41 °S, NZ; light blue dot; Turnbull et al., 2017); Campbell Island (*Dracophylum sp.*; 52.5 °S, CI; cyan dot; Turney et al., 2018); and Strait of Magellan (*P. uviferum*; 53.8 °S, SoM; blue dot; this study). Colored areas represent the mean eastward wind speed (m s^{-1}) calculated from the austral growing season (October to March) zonal winds at 10 meters above sea level from the years 1950 to 2016. Wind data from NCAR/NCEP reanalysis (Kalnay et al., 1996).

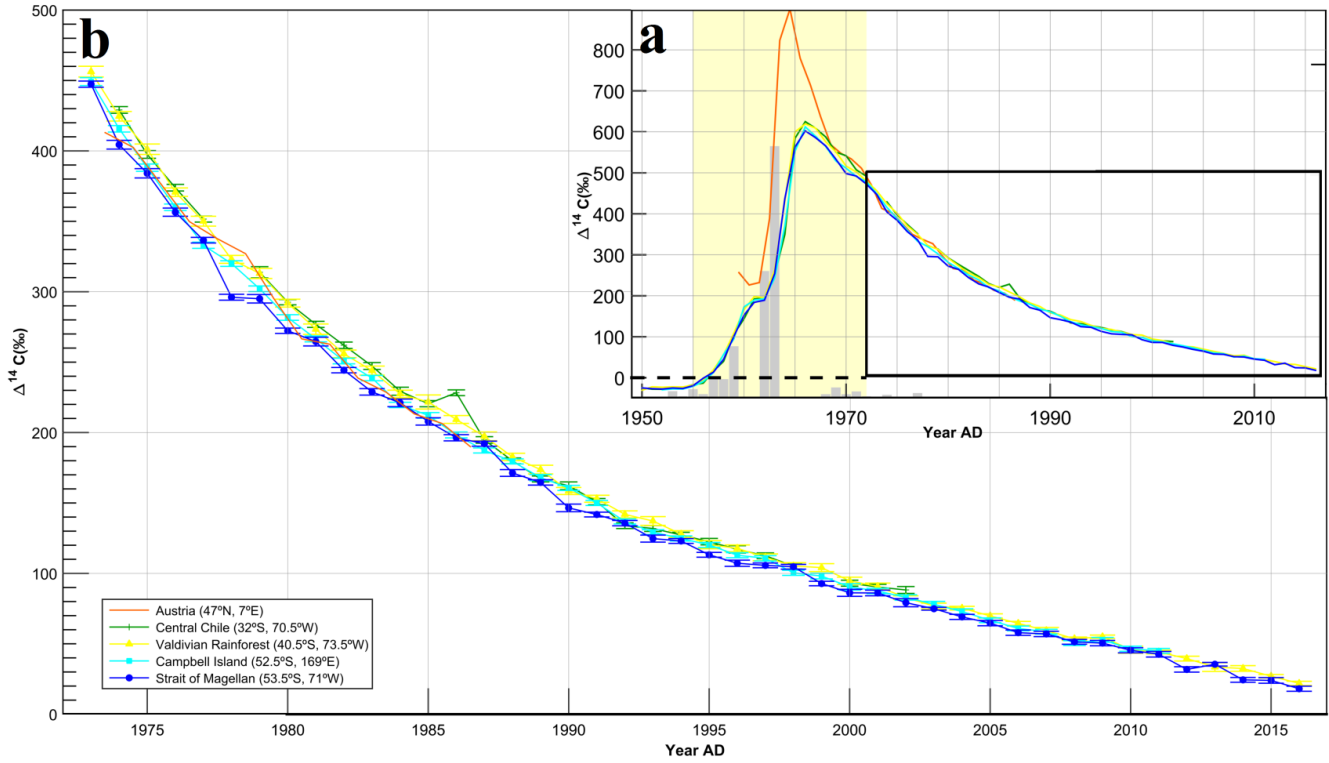

Figure 2. *Pilgerodendrun uviferum* (Strait of Magellan; black line with blue circles), *Fitzroya cupressoides* (Valdivian Rainforest Ecoregion; black dotted line with yellow circles), and *Austrocedrus chilensis* (Central Chile; a green dotted line with green cross) annual ^{14}C records from the bomb and post-bomb testing period are shown. For comparison, we include the *Dracophyllum sp.* $\Delta^{14}C$ record from Campbell Island (Turney et al., 2018; cyan line with squares), and Austria atmospheric $\Delta^{14}C$ summer measurements (Levin and Kromer, 2004; orange solid line). The colored area represents the Maximum Gradient Period (MGP), and the dashed black line indicates $\Delta^{14}C= 0$. The grey bars show the effective yield in megatons of thermonuclear detonations during this period which is directly related to the quantity of ^{14}C atoms generated (Enting, 1982).

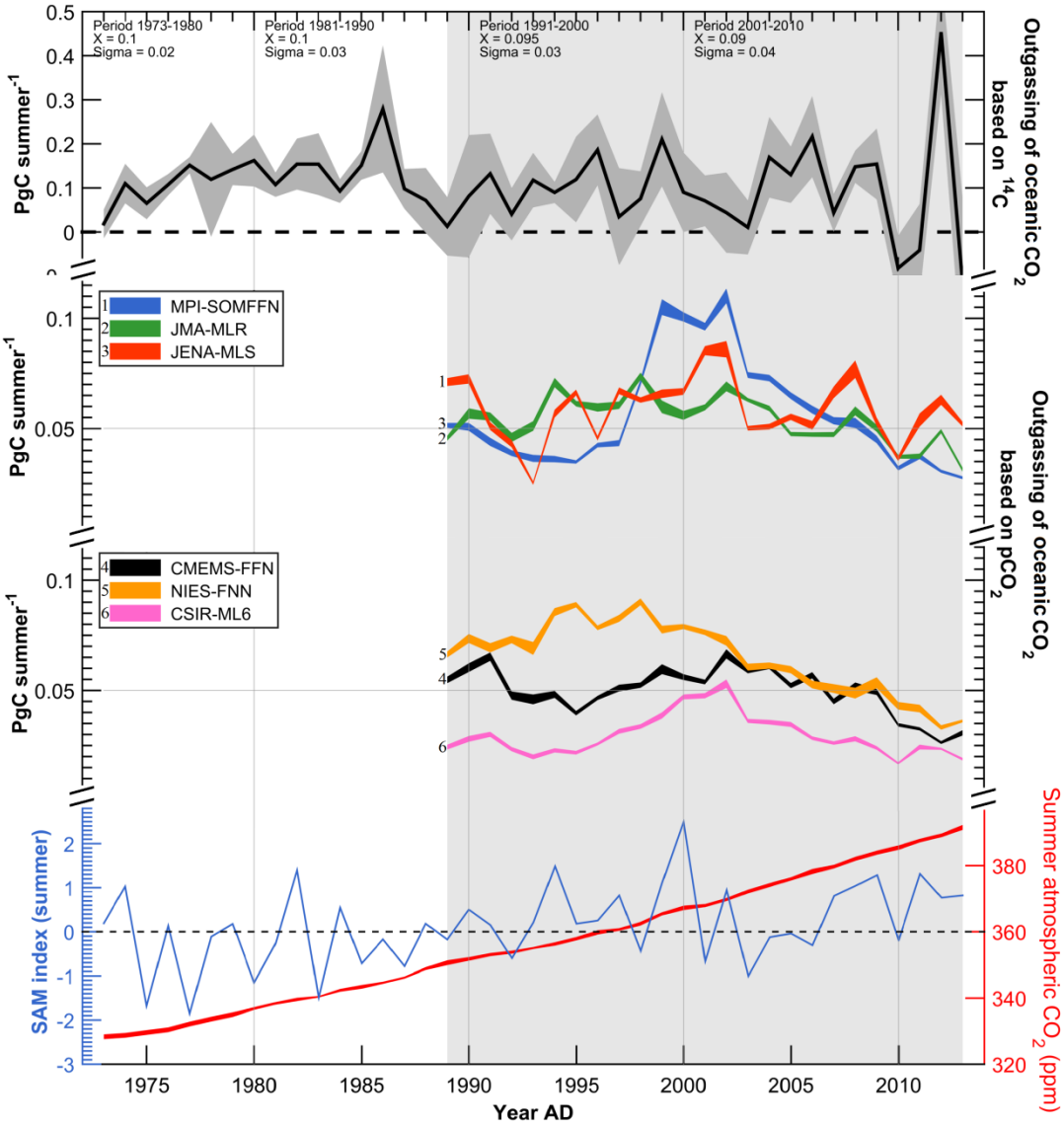

Figure 3. (**a**) The Southern Ocean outgassing of oceanic CO_2 (PgC) time series based on atmospheric ^{14}C levels inferred from tree-ring registries. The time series and uncertainties were calculated using equation 1 coupled to the Monte-Carlo method (section S2.8). X and sigma represent average and standar deviation from each decade (period). **(b)** Southern Ocean CO_2 flux (outgassing of oceanic CO_2) derived from different pCO_2 products: MPI-SOMFFN (Landschützer et al., 2020), JMA-MLR (Iida et al., 2020), JENA-MLS (Rödenbeck et al., 2013), CMEMS-FFNN (Chau et al., 2020), NIES-FNN (Zeng et al., 2014), and CSIR-ML6 (Gregor et al., 2019). Uncertainties are the

standard deviation calculated from different Southern Ocean CO_2 fluxes derived from five different wind products: Cross-calibrated Multi-Plataform v2 (CCMPV2; Atlas et al., 2011), ECMWF Reanalysis 5th Generation (ERA5; Hersbarch et al., 2020), Japanese 55-year Reanalysis (JRA55; Kobayashi et al., 2015), NCEP-NCAR reanalysis 1 (NCEP1; Kalnay et al., 1996), NCEP-NCAR reanalysis 2 (NCEP2; Kanamitsu et al., 2002). We calculated the outgassing of oceanic CO_2 through the sum of positive CO_2 flux values occurring in the source zonal band during October to March months by each year (aligned to 1st January). Thus, the outside the Southern Ocean CO_2 units are in PgC summer^{-1}. **(c)** Southern Annular Mode index (SAM; Marshall et al., 2003) and atmospheric CO_2 in the source zonal band (*ppm*) calculated from the October to March months by each year (aligned to 1st January). See supplementary information for detail.

Supporting Information for

LARGE INTERANNUAL VARIABILITY OF THE SOUTHERN OCEAN CO_2 OUTGASSING TRACED BY ATMOSPHERIC ^{14}C LEVELS

Santiago Ancapichún[1,2], et al

[1]Postgraduate School in Oceanography, Faculty of Natural and Oceanographic Sciences, Universidad de Concepción, Concepción, Chile

[2]Centro de Investigación GAIA Antártica (CIGA) and Network for Extreme Environment Research (NEXER), Universidad de Magallanes, Punta Arenas, Chile

1 Introduction

This supplementary information contains an overview of the material, methods, and results used to produce the figures and statistical results given in the main paper. As such, this material intentionally contains some repetition from the main paper and additional methodological details for users of the dataset.

The supplementary material and methods section explains in detail Southeast Pacific Ocean $\Delta^{14}C$ records, HYSPLIT processes, out the Southern Ocean CO_2 flux calculation, and supplementary data.

Figure S1 shows Southeast Pacific Ocean $\Delta^{14}C$ records.

Figure S2 shows ocean $\Delta^{14}C_{source}$ records.

Figure S3 and Figure S4 show the procedures to obtain Atm. $CO_{2background}$ series.

Figure S5 shows a sensibility test from equation 1.

Figure S6 shows zonal and latitudinal atmospheric ^{14}C differences.

Figure S7 and Figure S8 show air parcel trajectory analyses.

Figure S9 shows the latitudinal profiles of wind, Ekman transport, and surface ocean $\Delta^{14}C$ levels.

Figure S10 shows background and source zonal-band and input used in equation 1.

Figure S11 and Figure S12 show air-sea CO_2 fluxes.

Table S1 and Table S2 show Pearson correlations and slope analyses.

References are in the main article.

2 Material, methods, and results.

2.1 Southern hemisphere Δ^{14}C-records

In this article we present three new high-resolution atmospheric ^{14}C tree-ring-based records from *Austrocedrus chilensis*, *Fitzroya cupressoides*, and *Pilgerodendron uviferum* (Figure S1). Pooled standard deviations calculated from our records are presented in the supplementary excel file.). The *A. chilensis* tree-ring site (El Asiento) is located at mid-latitudes in central Chile at 1700 m asl (32 °S, 70 °W) and 57 km from the Pacific coast. The *A. chilensis* tree-ring chronologies are among the most climate-sensitive tree-ring records from the Andes and individuals can reach 1500 years-old (LeQuesne et al., 2006). The *F. cupressoides* tree-ring site (Mirador) is located in the Alerce Costero National Park in northern Patagonia at 800 m asl (40 °S, 73 °W) and 18 km from the Pacific coast. *F. cupressoides* is a slow-growth giant conifer that can reach heights of 50 meters (Donoso et al., 2006), endemic from the temperate rainforest of southern South America and can reach up to 3600 years-old (Lara and Villalba, 1993; Lara et al., 2020). Finally, the *P. uviferum* tree-ring site (Mount Tarn) is located in southern extreme Patagonia by the coast of the Strait of Magellan at 300 m asl (53 °S, 71 °W). *P. uviferum* ("Ciprés de las Guaitecas") is a mid-size tree from the *Cupressaceae* family with well-

defined annual rings that grows in Patagonia, which has been extensively used for tree-ring studies (Banister et al., 2012; Holz et al. 2018). It can reach >880 years-old and represent the world's southernmost conifer with populations up to 55 °S (Holz et al. 2018).

Campbell Island tree-ring record: The *Dracophyllum sp.* is one of the very few subantarctic tree species and has tree rings with annual growth. Turney et al. (2018) extracted the tree-ring core from Campbell Island (Southeast Harbour; 52.5 °S, 169 °E), a New Zealand subantarctic island. Therefore, the $\Delta^{14}C$ recorded by the *Dracophyllum sp.* tree is strongly influenced by the Southern Ocean conditions. The ^{14}C values across the inferred period of tree growth (October-March) were extracted using the calibration software OxCal 4.2 (Turney et al., 2018). Here, we align this data to 1st Jan of the growth_end year. The bomb-peak on the *Dracophyllum sp.* tree occurred in 1966 with $\Delta^{14}C$=612.0. This dataset spans the period 1952 to 2011, with continuous annual data.

New Zealand tree-ring record*:* We use the collected cores from near the Baring Head sampling station (41 °S, 174 °E) from New Zealand (Turnbull et al., 2017). A longer record was obtained from two specimens that were planted in 1919 and 1920. *Agathis australis* is a long-lived high-density softwood species

that has been widely used in dendrochronology and radiocarbon calibration studies. As in Turnbull et al. (2017), we align this data to 1st Jan of the growth_end year. Thus, the bomb-peak in New Zealand occurred in 1966 with $\Delta^{14}C$=610.9. This dataset spans the period 1951 to 2012, without continuous annual data.

2.2 Surface Ocean ^{14}C concentration in the source zonal band

Surface Ocean ^{14}C data were obtained from the Global Ocean Data Analysis Project (GLODAP; Olsen et al., 2020; https://www.glodap.info/). In order to obtain the Surface Ocean ^{14}C concentration in the source zonal-band (Depth < 50 meters), we found ^{14}C data of the Surface Ocean (Depth < 50 meters) from summer months (growing season: October to March) from years 1973 to 2016. Then, to obtain the interannual series and its associated uncertainties, we adjust the best linear fit to the data, and subsequently, we calculate the uncertainties based on the ^{14}C data and the best linear fit (Figure S2). We didn't use the ^{14}C values from the 2011 year because of its large dispersion compared to another annual ^{14}C data. In Figure S2g, the Ocean $\Delta^{14}C_{source}$ annual values and its annual uncertainties are shown.

2.3 Atmospheric CO_2 in the background zonal band

To calculate the atmospheric CO_2 levels in the background zonal-band, we use the NOAA greenhouse gas marine boundary layer reference (Dlugokencky et al., 2017; https://gml.noaa.gov/ccgg/mbl/mbl.html). We chose the NOAA greenhouse gas marine boundary layer reference dataset because has been widely used on carbon cycle studies, and is based on CO_2 measurements ignoring regions strongly affected by high fossil fuel emissions.

To obtain the annual CO_2 levels in the background zonal-band, we calculate the monthly average of the CO_2 concentration between 20.5 and 44.4 °S. Then, we calculate the average and standard deviation from the months October to March, which corresponds to the growing season of our ^{14}C records and, therefore, corresponds to the time window when atmospheric ^{14}C was recorded (Figure S3). Initially, the atmospheric CO_2 in the background zonal band spans the period 1980-2016.

Then, to extend our ^{14}C-bassed estimation, we made a linear interpolation based on Mauna Loa atmospheric CO_2 measurements (https://gml.noaa.gov/ccgg/trends/) (Figure S4) extending the atmospheric CO_2 in the background zonal band until 1973. In Figure S4b, the Atm. $CO_{2background}$ annual values and their annual uncertainties are shown, spanning the year 1973 to 2016.

2.4 Atmospheric ^{14}C in the background and source zonal band.

The atmospheric ^{14}C levels in the background and source zonal bands were calculated, compiling a ^{14}C record from each zonal band. To compile, we calculated the weight mean and standard error from each set of ^{14}C records.

The atmospheric ^{14}C levels from the background zonal-band were calculated using New Zealand, Central Chile, and Valdivian Rainforest records. The atmospheric ^{14}C levels from the source zonal-band were calculated using Campbell Island and Strait of Magellan records.

It is important mentioned that several studies demonstrated that the atmospheric ^{14}C recorded by trees is influenced by i) different growing season time-lapses, ii) different carbon reservoirs or anthropogenic activities affecting air masses that arrive at a tree, and iii) different provenance of air masses (Hua et al., 2012; Niu et al., 2021; Ancapichun et al., 2021). Therefore, the compile a high number of records from each SH's zonal-band going to i) reduce the atmospheric ^{14}C regional patterns associated with each record and ii) reveal a common atmospheric ^{14}C zonal pattern.

2.5 The atmospheric CO_2 concentration that comes from the Southern Ocean and Paired sample T-test calculations using Monte-Carlo method.

For Earth system studies, the goal of the Monte-Carlo method is to consider data error that could have each measurement in several statistical analyses such as Chi-square (Ramsey et al., 2001). For example, each radiocarbon value is accompanied by its measurement error (± σ), since this error has a Gaussian probability, it is 68 % probable that the radiocarbon measured being between ± 1 σ and 95 % probable that the radiocarbon measured being between ± 2. Thus, the Monte-Carlo method allows us to create a set of ‘’n’’ probable radiocarbon series for mid and southern latitudes (considering each annual uncertainty value; n = 10,000) atmospheric ^{14}C values.

We made a paired sample T-test analysis between each probable radiocarbon series of mid and southern latitudes atmospheric ^{14}C values, where test the null-hypothesis that pair-wise $\Delta^{14}C$ difference between mid-latitudes and Southern regions has a mean equal to zero (Figure S6, equation 1).

$$t = \frac{X - m}{\frac{s}{\sqrt{n}}} \quad (1)$$

Where X is the sample mean, m is the hypothesized population mean, s is the sample standard deviation, and n is the sample size. Under the null

hypothesis, the test statistic has Student's t distribution with n-1 degrees of freedom.

Thereby, a set of hypothesis null accepted were obtained. Then, to obtain the probability that the atmospheric $\Delta^{14}C$ difference between mid-latitudes and Southern regions has a mean equal to zero, the number of null hypotheses accepted were divided by the total number of probable radiocarbon series created and multiplied by 100. The same analysis was used to study ^{14}C differences between the Strait of Magellan and Campbell Island. These methods only can be executed using the ^{14}C series without annual gaps.

On the other hand, despite that we determined, from the studied period, that atmospheric ^{14}C concentrations from Strait of Magellan (SoM) and Campbell Island (CI) are not statistically different between them, we found some exceptional years when atmospheric ^{14}C concentration from Strait of Magellan was different (± 2 σ) from Campbell Island (Figure S6a). Specifically, we found that the atmospheric ^{14}C concentration from Campbell Island tended to have exceptional years of higher atmospheric ^{14}C concentration than the Strait of Magellan. Two mechanisms could produce this pattern i) different atmospheric circulation patterns between regions (Hua et al., 2012; Ancapichun et al., 2021) and ii) different upwelling regimens in each ocean basin (Braziunas et al., 1995; Randerson et al., 2002; Turnbull et al., 2009). Through HYSPLIT air parcel analyses, we found that the atmospheric circulation patterns from each region of

the studied records are closely similar between them (Figure S7). This analysis evidenced that air parcels that arrived at CI and SoM records share the latitudinal band from where they come. However, the ocean basins from where came air parcels, which arrived at CI and SoM records, show different air-sea CO_2 flux patterns (Figure S11). Specifically, the South Pacific Ocean shows a noticeable CO_2 flux out the ocean than the eastern South Indian Ocean. Therefore, the exceptional years when Campbell Island had a higher atmospheric ^{14}C concentration than the Strait of Magellan could be explained by years of high out the ocean CO_2 flux in the South Pacific Ocean and low out the ocean CO_2 flux in the eastern Indian Ocean. This difference of air-sea CO_2 flux out the Ocean could explain the pre-industrial zonal atmospheric ^{14}C offset between Campbell Island (53°S) and Tierra del Fuego (54°S) found by Turney et al., (2016), when compared the NH radiocarbon curve with SH radiocarbon curves based on tree-ring records.

We use the Monte-Carlo method to calculate the atmospheric CO_2 concentration that comes from the Southern Ocean (CSO): weight mean and standard error. Considering that each component of our equation 1 has an associated uncertainty, we executed 10,000 times the equation 1, generating 10,000 CSO estimation series based on the uncertainties of overall the components of equation 1. Then, we calculated the average and standard deviation of each year of the set of CSO estimation series. Thus, we obtained a

CSO estimation that considered the uncertainties of overall the components from which it was calculated.

To understand the influence of each component in our equation 1, we made a sensibility test using the Monte-Carlo method (Figure S5). We did the same procedure as above, but we systematically excluded the uncertainties of each component, leading to only one source of uncertainty. Thus, we obtained the uncertainties of the estimation associated with each component of equation 1. Moreover, we understood the influence of each component in the estimation of the CSO. Through this analysis, we determine that the ^{14}C measurement uncertainties were the main source of uncertainty in our estimation from the 1973-2013 period. From 2014 to 2016, we found that uncertainties associated with the shallow water Southern Ocean ^{14}C levels values were the main source of uncertainty and that these uncertainties were too large to obtain a reliable CSO estimation during these years. Therefore, we only show the period when the CSO shows the lowest uncertainties (1973-2013).

2.6 Out the Southern Ocean CO_2 flux based on pCO_2 mapped products.

To compare our Southern Ocean outgassing of oceanic CO_2 based on ^{14}C with recent air-sea CO_2 flux pCO_2-based products, we use the Harmonized

ensemble data of the air-sea CO_2 flux based on observation-based pCO_2 products (Seaflux; Fay et al., 2021). This ensemble product is meant to facilitate the use of the pCO_2 observation-based ocean flux estimates in assessment studies of the global carbon cycle. This ensemble was harmonized by area correction and consistent scaling of gas exchange. Thus, the ensemble data product accounts for the diversity of the underlying mapping methodologies. The Seaflux use six global observation-based mapping products: CMEMS-FFNN (Chau et al., 2020), CSIR-ML6 (Gregor et al., 2019), JENA-MLS (Rödenbeck et al., 2013), JMA-MLR (Iida et al., 2020), MPI-SOMFFN (Landschützer et al., 2020), and NIES-FNN (Zeng et al., 2014). Additionally, the air-sea CO_2 flux can be calculated used five different wind product: Cross-calibrated Multi-Plataform v2 (CCMPV2; Atlas et al., 2011), ECMWF Reanalysis 5th Generation (ERA5; Hersbarch et al., 2020), Japanese 55-year Reanalysis (JRA55; Kobayashi et al., 2015), NCEP-NCAR reanalysis 1 (NCEP1; Kalnay et al., 1996), NCEP-NCAR reanalysis 2 (NCEP2; Kanamitsu et al., 2002). Thus, we use these datasets to calculate the air-sea CO_2 flux from October to March months (growing season months), where positive values represent the outgassing of oceanic CO_2.

2.7 Effective yield of atmospheric nuclear detonation calculations.

The bomb pulse at the SH is proportional to the energy released by thermonuclear detonations: the effective yield in megatons (Enting 1982; Hua et al., 2013). This ^{14}C excess produced in the NH generated a large and persistent global latitudinal gradient (Hua et al., 2013). Using the data from Enting (1982), we averaged the monthly data from each year (January to December), generating an annual series. The bomb-^{14}C excess produced during an entire year is recorded by tree-rings during the growing season (October to March). Therefore, the annual series were aligned to Jan 1st of the next year.

2.8 Geographical Provenance of air parcels using HYSPLIT

To study the air parcel GP, we developed a frequency analysis (see HYSPLIT user's guide; https://www.arl.noaa.gov/documents/reports/hysplit_user_guide.pdf). The first is to count the number of trajectories that fall within each grid (1 degree) cell that covers the area. The trajectory frequency (F) is just the sum of the number of trajectories (T) that passed through each (i, j) grid cell divided by the total number (N) of trajectories analyzed:

$$F_{i,j} = 100 \, \Sigma \, T_{i,j} / N \quad (2)$$

Our air parcel frequency analyses (equation 2) show that air parcels influencing atmospheric $\Delta^{14}C$ in Campbell Island and Strait of Magellan came from further south latitudes (45-65 °S; Figures S7. This result suggests that Campbell Island and Strait of Magellan records are potentially influenced by the Southern Ocean sea-air CO_2 exchanges processes.

On the other hand, the tropospheric altitude at which physical and chemical mixing occurs between the atmosphere and the Earth's surface varies between areas of oceans and continents. The marine atmospheric boundary layer in the Southern Ocean occurs approximately 2 km above the Ocean (800 hPa; Messager et al., 2012). Therefore, air parcels located in hour -120 upper the marine atmospheric boundary layer were considered as upper tropospheric air parcels, which potentially no exchanged carbon with the ocean. Meanwhile, air parcels located in hour -120 lower the marine atmospheric boundary layer were considered as lower tropospheric air parcels, which potentially exchanged carbon with the ocean.

Figure S8 demonstrates that air parcels affecting atmospheric $\Delta^{14}C$ records used in our study mostly came from lower altitudes, specifically, inside the marine atmospheric boundary layer influence altitudes. Therefore, $\Delta^{14}C$ records

used in our study are strongly affected by the ocean-atmosphere CO_2 exchange (Southern Ocean ^{14}C fingerprint).

3 Figures

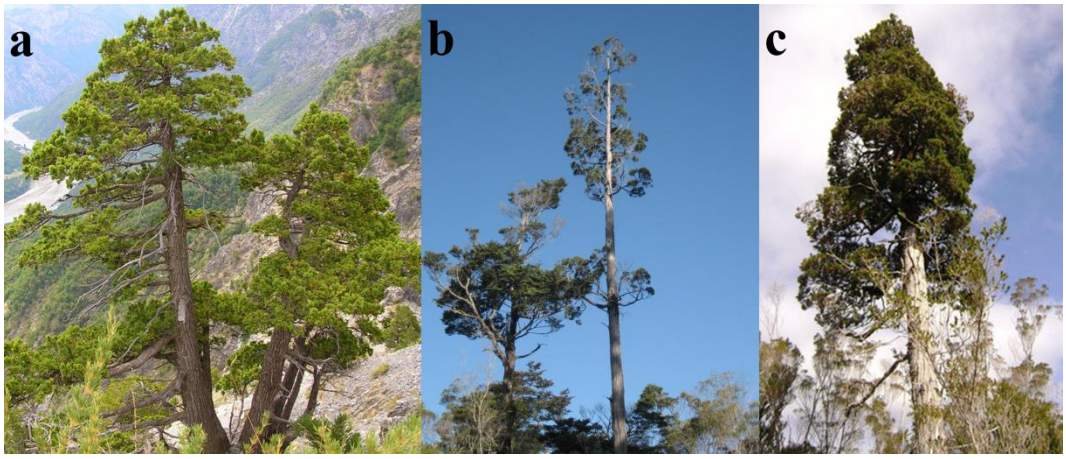

Figure S1. Tree individuals of (a) *Austrocedrus chilensis*, (b) *Fitzroya cupressoides*, and (c) *Pilgerodendron uviferum*.

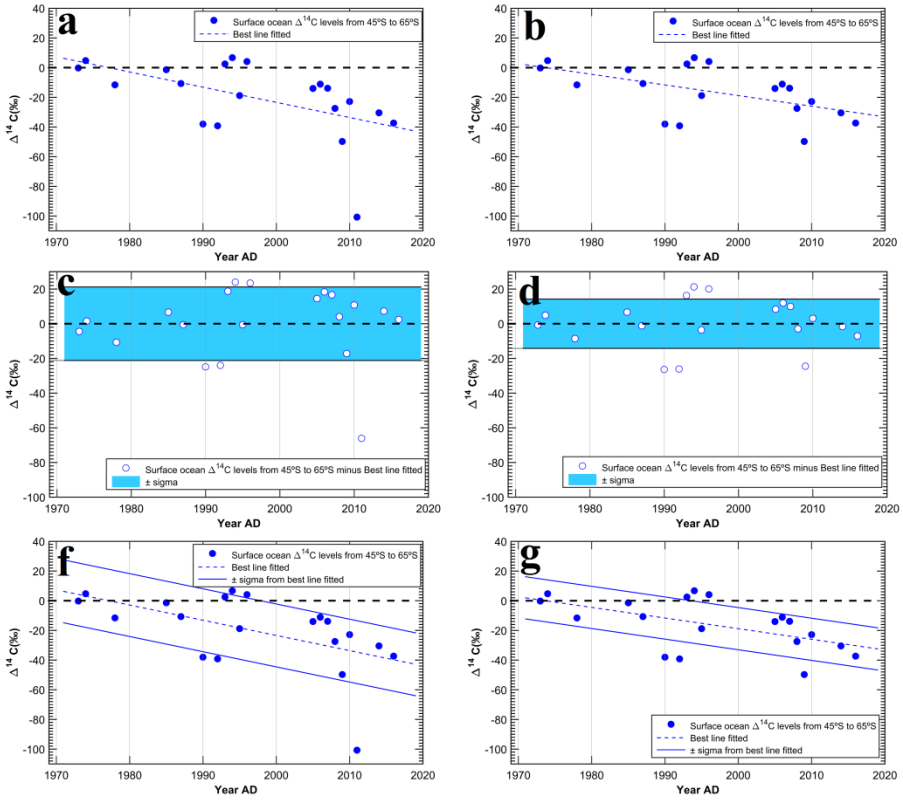

Figure S2: Calculation procedures to obtain the annual Surface Ocean ^{14}C level series from the source zonal-band with its respective uncertainties values. Figures (a), (c), and (f) show the annual Surface Ocean ^{14}C level series from the source zonal-band obtained from the overall data. Figures (b), (d), and (g) show the annual Surface Ocean ^{14}C level series from the source zonal-band obtained from the overall data excluding the 2011 year ^{14}C value. (a) and (b) show the Surface Ocean ^{14}C annual levels (average from October to March) from 45-65 °S and its best linear fit. (c) and (d) show the subtract between the Surface Ocean ^{14}C annual levels (average from October to March) from 45-65 °S and its best linear fit. The blue area represents the standard deviation calculated using the subtract values resulted. (f) and (g) show the annual Surface Ocean ^{14}C level (dashed blue line) and its uncertainties (solid blue line). Figure (g) shows the best linear fitted and the standard deviation calculated in the above steps, which are the component used in our CSO estimation as Ocean $\Delta^{14}C_{source}$.

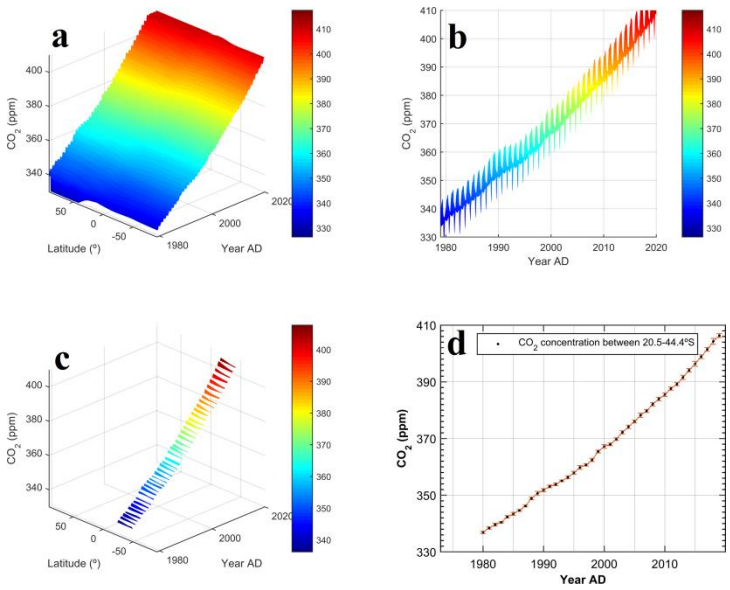

Figure S3: (a) CO_2 concentration obtained from the NOAA greenhouse gas marine boundary layer reference through latitude and time. (b) Same than (a) but only through time. (c) Dataset used in our study. (d) October to March average of the CO_2 concentration above the background zonal-band, bars represents the uncertainties.

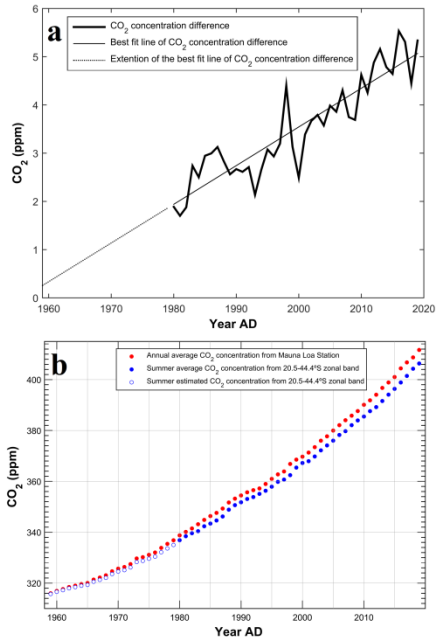

Figure S4: (a) CO_2 concentration difference between the summer annual averages of the CO_2 concentration above the background zonal-band derived from the NOAA greenhouse gas marine boundary layer reference and Mauna Loa CO_2 measurements (solid thick line). The dashed line represents the best linear fit adjusted to the difference between the summer annual average of the CO_2 concentration above the background zonal-band derived from the NOAA greenhouse gas marine boundary layer reference and Mauna Loa CO_2 measurements. The dotted line represents the extended best linear fit through time. (b) Damped blue circles represent the estimated summer CO_2 concentration above the background zonal-band obtained through a linear interpolation based on Mauna Loa CO_2 measurements. Blue damped and filled circles are the Atm. $CO_{2background}$ used in equation 1.

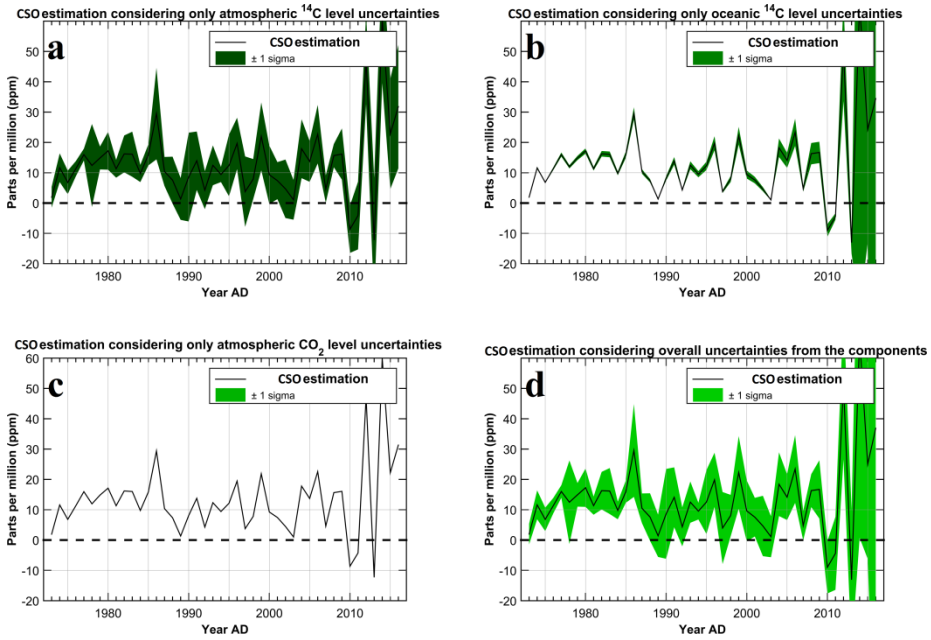

Figure S5. The atmospheric CO_2 concentration that comes from the Southern Ocean (CSO) calculated using equation 1 coupled with Monte-Carlo method: **(a)** Considering only atmospheric ^{14}C level uncertainties, **(b)** Considering only oceanic ^{14}C level uncertainties, **(c)** Considering only atmospheric CO_2 level uncertainties, and **(d)** Considering overall uncertainties from the components (CSO used in the main article).

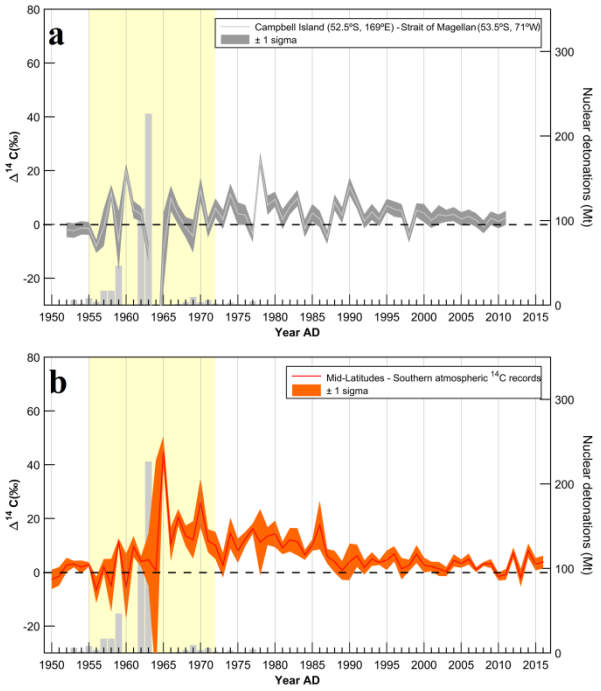

Figure S6: Atmospheric ^{14}C differences between SH's ^{14}C records. Sigma values were calculated as the square root of the sum of square errors. (a) The atmospheric ^{14}C difference between Campbell Island and Strait of Magellan records. (b) The atmospheric ^{14}C difference between compiled (Through a weight mean and standard error, similar to Hua et al., (2013)) Mid-Latitudes and Southern records. The colored light-yellow area represents the Maximum Gradient Period (MGP), and the dashed black line indicates $\Delta^{14}C= 0$. The grey bars show the effective yield in megatons of thermonuclear detonations during this period which is directly related to the quantity of ^{14}C atoms generated (Enting, 1982).

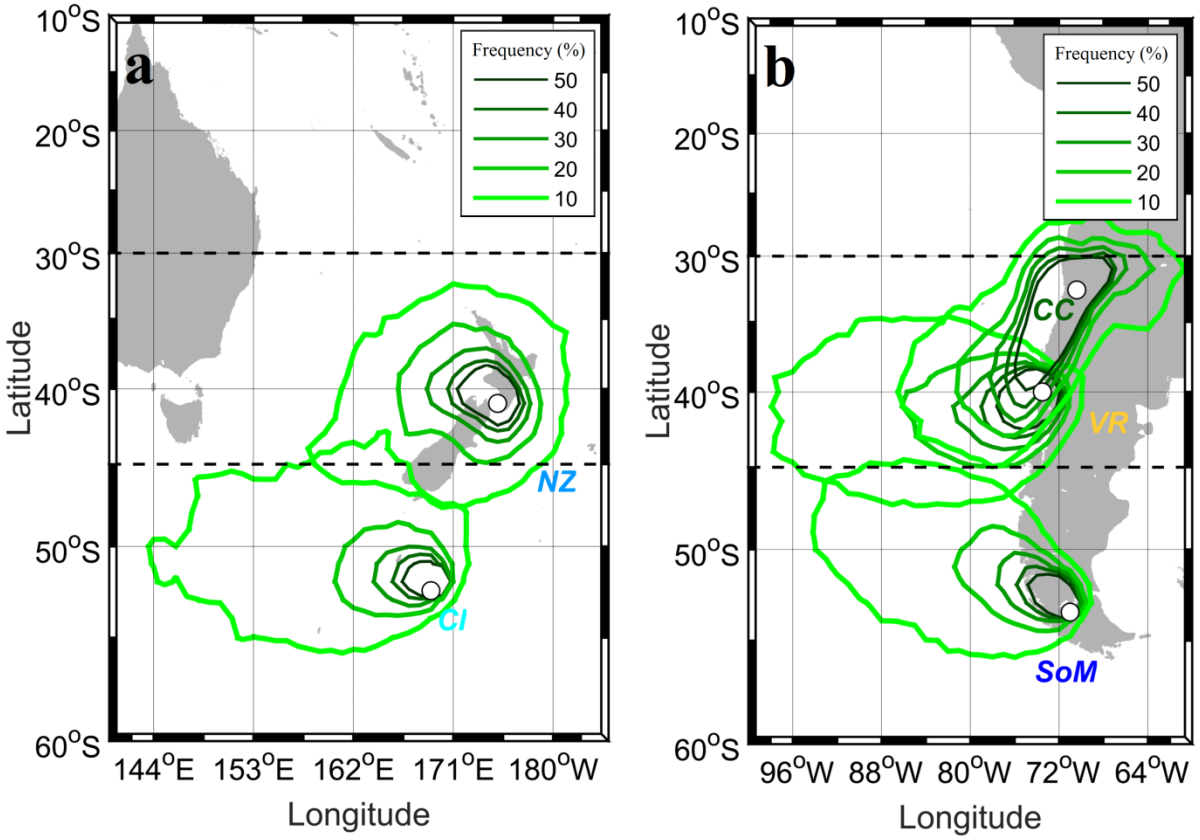

Figure S7. HYSPLIT backward trajectory analysis results for Southern ^{14}C records. Air parcel density arriving at records studied. The color lines indicate the total frequency of air parcels located on each pixel grid (1º x 1º) at hours 1 to 120 during the entire study period (ONDJFM, 1949 to 2020) (see HYSPLIT manual: Frequency analysis).

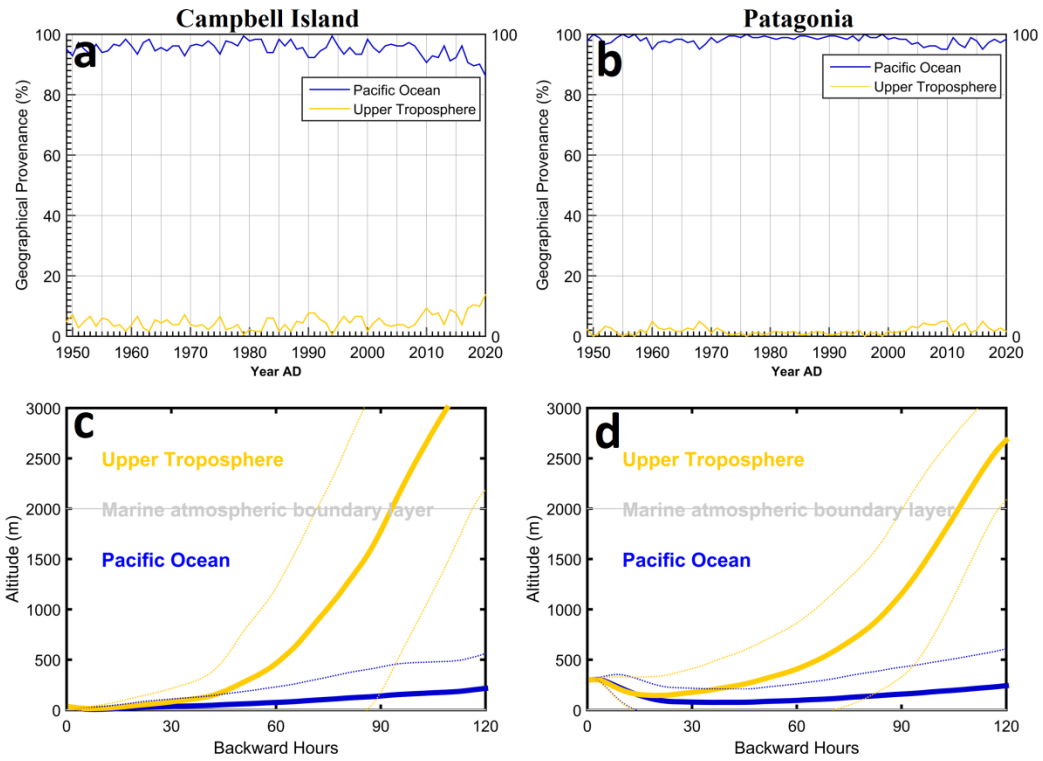

Figure S8. (a) air parcel contribution (%) of each geographical provenance arriving in the Campbell Island during the studied period **(b)** same as (a) but for Patagonia. **(c)** Mean altitude of the air-parcel trajectories that reached the Campbell Island record during the studied period (solid color lines) and its standard deviation (dotted color lines); **(d)** same that (c) but for Patagonia.

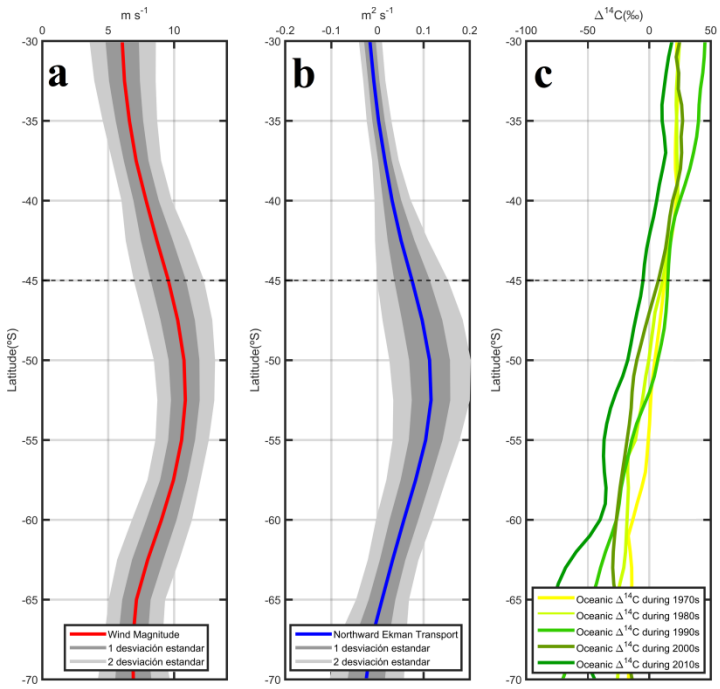

Figure S9: Latitudinal profiles represent the zonal average of (**a**) wind magnitude, (**b**) northward Ekman transport, and (**c**) latitudinal profile of zonal average of surface oceanic ^{14}C levels (< 50 m) through decades. Wind magnitude and northward Ekman transport profiles were calculated using the NCEP/NCAR dataset (Kalnay et al., 1997) and equations used in Ancapichun et al. (2015). Decadal ocean-surface $\Delta^{14}C$ data were obtained from GLODAP (Olsen et al., 2020) and were smoothed throughout the latitude. To make these calculations, we only used the dataset from October to March months from the years 1950 to 2016. The dashed line shows the latitudinal limits between the background and the zonal band.

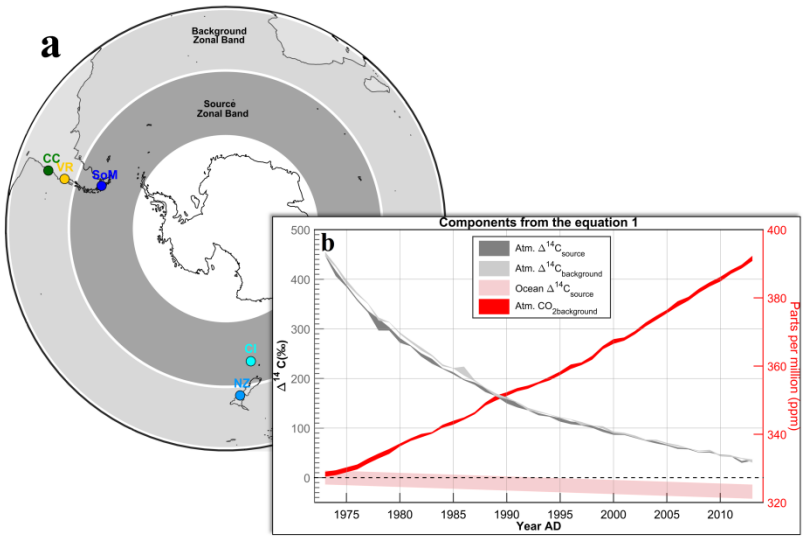

Figure S10. (a) Scheme of the background and source zonal band area. Colored dots are the location of each ^{14}C record used in our CSO estimation. **(b)** Components used to obtain the CSO estimation applying equation 1.

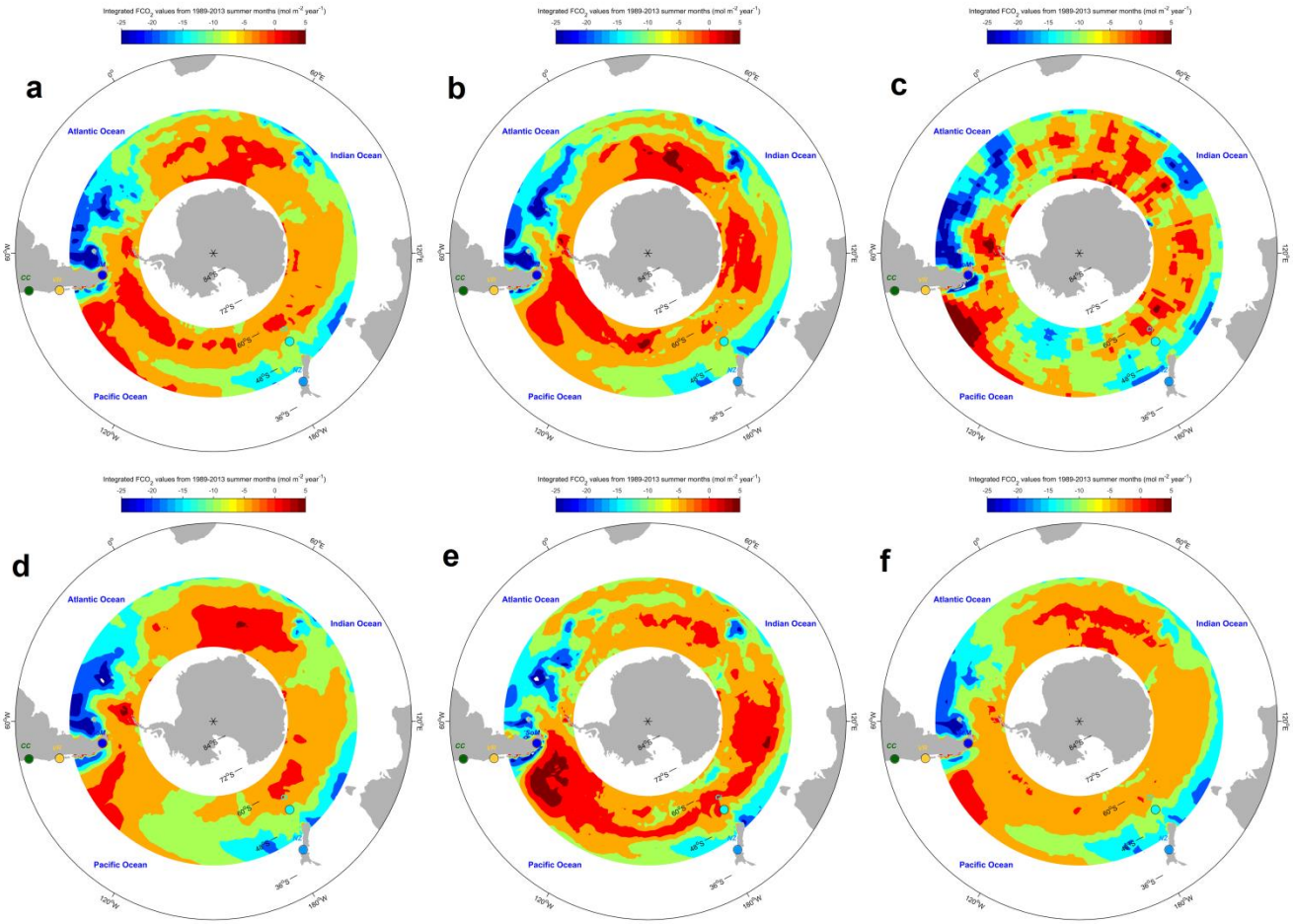

Figure S11. Annual averaged of the integrated air-sea Southern Ocean CO_2 fluxes per grid obtained from summer months (October to March; 1989-2016) from fluxes-product of NCEP2 wind-speed product input (similar results were found using the another wind product as input). This figure remarks the out the Southern Ocean CO_2 flux along the source zonal band obtained from different pCO_2 products: (a) MPI-SOMFFN, (b) JMA-MLR, (c) JENA-MLS, (d) CMEMS-FFNN, (e) NIES-FNN, and (f) CSIR-ML6.

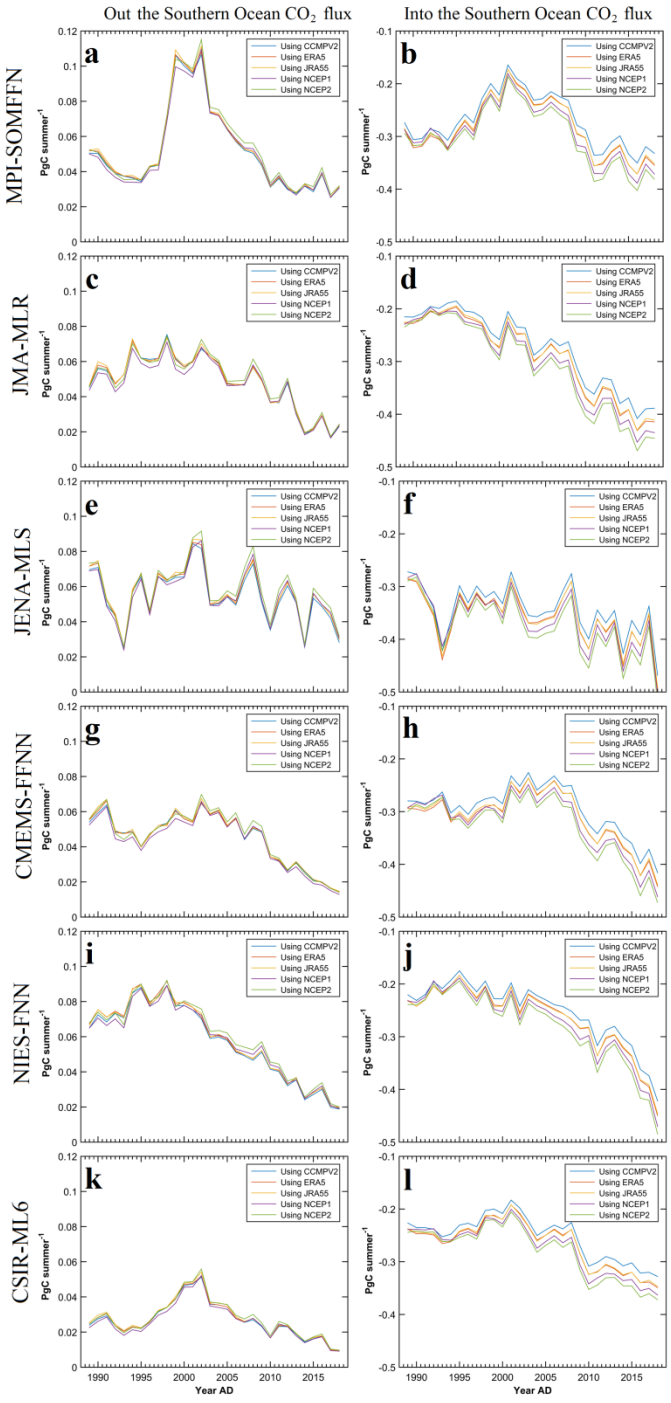

Figure S12. Out the Southern Ocean (left column) and into the Southern Ocean CO_2 (right column) fluxes are calculated from different pCO_2 (each row)

and wind speed products (colored lines). Annual values represent the sum of positive (Out the Southern Ocean or outgassing of oceanic CO_2) and negative (into the Southern Ocean CO_2) CO_2 fluxes occurring during October to March months.

Table S1

Pearson correlation between out the Ocean and into the Ocean CO_2 fluxes ($p < 0.05$)	MPI-SOMFFN	JMA-MLR	JENA-MLS	CMEMS-FFNN	NIES-FNN	CSIR-ML6
CCMPV2	**0.85**	**0.85**	**0.84**	**0.87**	**0.89**	**0.84**
ERA5	**0.84**	**0.85**	**0.83**	**0.86**	**0.88**	**0.84**
JRA55	**0.83**	**0.85**	**0.82**	**0.86**	**0.88**	**0.83**
NCEP1	**0.83**	**0.78**	**0.71**	**0.89**	**0.89**	**0.75**
NCEP2	**0.83**	**0.78**	**0.71**	**0.88**	**0.89**	**0.74**

Note: Significant Pearson correlation value between out the Southern Ocean and into the Southern Ocean CO_2 fluxes derived from different wind products (rows) and pCO_2 products (columns).

Table S2

Estimations	Interannual variability mean SO sea-to-air

	CO_2 flux (1989-2013)
^{14}C based	**0.057 ± 0.0092 (PgC)**
MPI-SOMFFN	**0.0084 ± 0.00042(PgC)**
JMA-MLR	**0.008 ± 0.00041 (PgC)**
JENA-MLS	**0.0139 ± 0.00053 (PgC)**
CMEMS-FFNN	**0.0061 ± 0.00041 (PgC)**
NIES-FNN	**0.0059 ± 0.00046(PgC)**
CSIR-ML6	**0.0042 ± 0.00024 (PgC)**

Note: Interannual variability mean SO sea-to-air CO_2 flux (1989-2013).

Table S3

Outgassing of oceanic	Slope of the trend

CO_2 tracers	
^{14}C based	**-0.0007 (PgCsummer^{1})**
MPI-SOMFFN	**-0.0008 (PgCsummer^{1})**
JMA-MLR	**-0.0013 (PgCsummer^{1})**
JENA-MLS	**-0.0005 (PgCsummer^{1})**
CMEMS-FFNN	**-0.0013 (PgCsummer^{1})**
NIES-FNN	**-0.0021 (PgCsummer^{1})**
CSIR-ML6	**-0.0005 (PgCsummer^{1})**

Note: Slope of the trend calculated from each outgassing of oceanic CO_2 tracer.

5 DISCUSIÓN GENERAL

Las pruebas de armas termonucleares que ocurrieron en el hemisferio norte afectaron fuertemente las concentraciones de $\Delta^{14}C$ atmosférico alrededor del mundo (Manning et al., 1990), quedando fielmente registrado en los anillos de crecimiento de árboles de *P. tarapacana* (20ºS), *A. chilensis* (32ºS), *F. cupressoides* (40ºS) y *P. uviferum* (53ºS). Debido al exceso de ^{14}C generado por la detonación de armas termonucleares, el hemisferio norte alcanzó un máximo valor de $\Delta^{14}C$ atmosférico (*bomb-peak*) en el año 1963 (Hua et al., 2013). Este exceso de ^{14}C fue propagado a través de la circulación atmosférica (Nydal y Lovseth 1965), alcanzando el *bomb-peak* en latitudes tropicales del hemisferio sur en el año 1965 (Hua et al. 2012). Frente a las costas del océano Pacífico sudoriental, nuestros registros de anillos de árboles registraron un abrupto incremento de los niveles de $\Delta^{14}C$ a partir del año 1956, y el valor máximo en el año 1966, lo cual esta en excelente concordancia con las mediciones de $\Delta^{14}C$ atmosférico de Nueva Zelanda (41ºS) y otros registros del hemisferio sur (Santos et al., 2015; Turnbull et al. 2017; Turney et al. 2018). De este modo, el extremo y abrupto incremento de los niveles de $\Delta^{14}C$ atmosférico registrado a lo largo del océano Pacífico sudoriental durante el periodo bomba,

evidenció el extenso alcance de las pruebas de armas termonucleares desarrolladas en el hemisferio norte. Posterior al *bomb-peak*, los niveles de $\Delta^{14}C$ atmosférico registrados frente al océano Pacífico sudoriental disminuyeron, al igual que en todo el globo, demostrando la notable influencia de la quema de combustibles fósiles y el intercambio de carbono entre la atmósfera y los otros reservorios de carbono sobre los niveles de $\Delta^{14}C$ atmosférico (Stuiver y Braziunas 1993; Randerson et al. 2002; Levin et al. 2010; Graven et al. 2012).

Los periodos bomba (1950-1985) y post-bomba (1985-2022) abarcaron una importante y única ventana temporal. La propagación del exceso de ^{14}C bomba a todo el globo y la incorporación de este exceso de ^{14}C bomba al ciclo global del carbono, ha permitido utilizar al ^{14}C bomba como un poderoso trazador del sistema climático y del ciclo global del carbono (Nydal y Lovseth, 1965; Randerson et al. 2002; Levin et al. 2010; Graven et al. 2012). La presente tesis corroboró que la variabilidad de los niveles de $\Delta^{14}C$ atmosférico en el hemisferio sur durante los periodos bomba y post-bomba fue modulada por los pulsos de ^{14}C bomba provenientes del hemisferio norte, el efecto del transporte y mezcla de parcelas de aire y el intercambio de carbono entre los distintos reservorios.

Enfocados en la variabilidad interanual del $\Delta^{14}C$ atmosférico en el hemisferio sur, la presente tesis estudió la proveniencia geográfica de las parcelas de aire y su relación con el cinturón tropical de bajas presiones, encontrando que al Altiplano arribaron parcelas de aire provenientes de la tropósfera superior, de la cuenca Amazónica y del océano Pacífico extratropical. A través de la modelación de la circulación atmosférica en Sudamérica tropical, se encontró una notable variabilidad interanual de la proveniencia geográfica de las parcelas de aire que arribaron al Altiplano durante el periodo bomba. Investigaciones previas estudiaron la proveniencia geográfica de las parcelas de aire que arribaron al Altiplano utilizando datos de reanálisis y una metodología enfocada en la circulación atmosférica en el plano este y oeste (Vuille et al. 2000; Garreaud et al. 2009). De este modo, se ha descrito previamente el arribo al Altiplano de parcelas de aire provenientes del Amazonas las cuales cargan una gran cantidad de humedad, y de parcelas de aire provenientes del Desierto de Atacama las cuales son extremadamente secas (Vuille et al. 2000; Garreaud et al. 2003; Garreaud et al. 2009). La presente investigación halló una interesante y nunca antes descrita variabilidad interanual del flujo atmosférico en el Altiplano, la cual podría estar asociada a eventos de precipitación o sequía. Esta nueva aproximación metodológica, la cual distingue parcelas de aire provenientes de la troposfera inferior y superior,

podría ayudar a entender los forzantes de los recientes cambios en la precipitación sobre el Altiplano, como los eventos de precipitación extrema observados a partir del año 2000 (Morales et al. 2020; Segura et al. 2020).

Por otro lado, la presente tesis encontró excepciones en el gradiente latitudinal de $\Delta^{14}C$ atmosférico esperado durante el periodo bomba, positivo de norte a sur, para el hemisferio sur (Hua et al. 2007; Hua et al. 2013). Para los periodos bomba y post-bomba se encontraron años en que el gradiente latitudinal esperado se invirtió (negativo de norte a sur), evidenciando discrepancias en lo que previamente se ha descrito para el hemisferio sur (Hua et al. 2013). Nuestro estudio reveló que ésta alteración en el gradiente latitudinal positivo de norte a sur ocurrió debido a cambios en la circulación atmosférica sobre Sudamérica tropical y a cambios en la señal isotópica de la biósfera amazónica. De hecho, la presente investigación confirmó lo encontrado en previos estudios de modelación, los cuales proyectaron la ocurrencia de niveles de $\Delta^{14}C$ atmosférico más bajos sobre la cuenca amazónica durante el inicio del periodo bomba, relativo a otras regiones del hemisferio sur (Randerson et al. 2002; Levin et al. 2010). Estos bajos niveles de $\Delta^{14}C$ atmosférico son explicados por la respiración del CO_2 asimilado por la biósfera durante años anteriores (periodo pre-bomba), en los cuales los niveles de $\Delta^{14}C$ atmosférico fueron inferiores a los observados durante el inicio del periodo

bomba. Por otro lado, a fines del periodo bomba y durante el periodo post-bomba, la biósfera Amazónica comenzó a respirar el CO_2 asimilado durante el *bomb-peak*, el cual tenía una mayor concentración de ^{14}C que el $\Delta^{14}C$ atmosférico local. De este modo, la biósfera amazónica comenzó a enriquecer en ^{14}C a la atmósfera incrementando los niveles de $\Delta^{14}C$ atmosférico local, confirmando lo encontrado en previos estudios de modelación, siendo consistente con el patrón observado durante el inicio del periodo bomba (Randerson et al. 2002; Levin et al. 2010). No obstante, nosotros encontramos que esté cambio de señal isotópica ocurrió al menos ocho años antes de lo previsto en estos estudios de modelación, sugiriendo una subestimación de la tasa de intercambio de carbono biósfera-atmósfera de la selva Amazónica. De hecho, actualmente la principal fuente de incerteza en estudios de modelación del ciclo global del carbono es el tiempo de residencia del carbono en la biósfera terrestre (Friend et al. 2013). De manera preliminar, nuevos registros de $\Delta^{14}C$ atmosférico obtenidos en el corazón de la selva Amazónica muestran un patrón similar al reportado en nuestra investigación (Santos et al. 2022 en proceso). Por lo tanto, la evidencia encontrada en nuestra investigación sugiere que el $\Delta^{14}C$ atmosférico registrado en anillos de árboles podría ser un valioso indicador del tiempo de residencia del carbono en la biósfera amazónica, siendo indispensables futuros estudios que aborden este hallazgo.

Por otro lado, esta tesis incorporó el concepto del cinturón tropical de bajas presiones al estudio del $\Delta^{14}C$ atmosférico y potencialmente a otras disciplinas (Fletcher 1945). Es conocido que la zona de convergencia intertropical ocurre sobre los océanos y, en general, en el hemisferio norte, la cual es caracterizada por un alineamiento casi perfecto entre los campos de vientos (convergencia de vientos), presión atmosférica (baja presión) y precipitación (alta precipitación) (Vuille et al. 2012; Marsh et al. 2018). Por lo tanto, es un error conceptual utilizar el término de la zona de convergencia intertropical para representar a la convergencia de vientos, provenientes del hemisferio norte y sur que ocurre sobre los continentes del hemisferio sur (Vuille et al. 2012; Marsh et al. 2018). Investigaciones previas utilizaron erróneamente el concepto de la zona de convergencia intertropical como el área de convergencia entre masas de aire provenientes del hemisferio norte y sur sobre los continentes del hemisferio sur (Hua et al. 2007; Hua et al. 2013). Este uso erróneo del concepto puede llevar a confusiones en el entendimiento interdisciplinario. Basándonos en la necesidad de idear un concepto, el cual describa únicamente la convergencia entre masas de aire provenientes del hemisferio norte y sur, y que sea fácil de calcular, la presente tesis reutilizó la idea de Fletcher (1945) y brindó el concepto del cinturón tropical de bajas presiones al estudio del $\Delta^{14}C$ atmosférico y potencialmente a otras disciplinas. Es así, como en la nueva versión de las curvas de calibración globales para el

periodo bomba y post-bomba (Hua et al. 2021), el concepto de la zona de convergencia intertropical fue reemplazado por el cinturón tropical de bajas presiones.

Al comparar registros de $\Delta^{14}C$ atmosférico de latitudes subtropicales con registros australes, encontramos la ocurrencia de un fuerte y continuo gradiente latitudinal positivo de norte a sur. A través de la modelación del sistema climático y del ciclo global del carbono, estudios previos han reconstruido este gradiente latitudinal, el cual está constituido por bajos niveles de $\Delta^{14}C$ atmosférico sobre el océano austral (Braziunas et al. 1995; Randerson et al. 2002; Turnbull et al. 2009; Levin et al. 2010; Graven et al. 2012). Estos estudios sugieren que los bajos niveles de $\Delta^{14}C$ troposférico observados sobre el océano austral han ocurrido debido a las enormes emisiones de CO_2 del océano a la atmósfera. Este CO_2 de origen oceánico tiene una baja proporción isotópica ^{14}C:^{12}C (debido a la antigüedad de las aguas de surgencia y al decaimiento radioactivo del ^{14}C), por lo que al incorporarse a la troposfera decrecen los niveles de $\Delta^{14}C$ atmosférico sobre el océano austral (Braziunas et al. 1995; Randerson et al. 2002; Key et al. 2004; Turnbull et al. 2009; Levin et al. 2010). Por lo tanto, el gradiente de $\Delta^{14}C$ atmosférico, entre latitudes subtropicales y australes del hemisferio sur, reportado en la presente investigación es la

evidencia empírica del efecto sobre los niveles de $\Delta^{14}C$ atmosférico del flujo de CO_2 del océano a la atmósfera.

Recientes investigaciones han descrito cambios en los flujo de CO_2 entre el océano y la atmósfera sobre el océano austral reportando una marcada variabilidad decadal, la cual presenta un debilitamiento del secuestro de CO_2 atmosférico en 1990s seguido de un fortalecimiento del secuestro de CO_2 atmosférico en los 2000s (Landsctüzer et al. 2013; Rödenbeck et al. 2014; Munro et al. 2015). Estos cambios a escala decadal de los flujos de CO_2 océano-atmósfera han sido atribuidos a cambios en la ventilación oceánica, forzada por los vientos australes del oeste (DeVries et al. 2017). Para estudiar los flujos de CO_2 océano-atmósfera que ocurren sobre el océano austral, se ha utilizado comúnmente la siguiente fórmula (Wanninkhof 2014):

$$Flujo\ de\ CO_2 = k_w * sol * \left(pCO_{2\ océano} - pCO_{2\ atmósfera}\right) * (1 - hielo)$$

En donde *Kw* es la velocidad de transferencia del CO_2, *sol* es la solubilidad del CO_2 en el océano, $pCO_{2\ océano}$ es la presión parcial del CO_2 en la superficie del océano y $pCO_{2\ atmósfera}$ es la presión parcial del CO_2 en la atmósfera de la capa limite atmosférica marina. Finalmente, (1 – *hielo*) representa a la cobertura de hielo sobre los océanos de altas latitudes. El principal problema para estimar los flujos de CO_2 océano-atmósfera es la falta de cobertura

espacio-temporal de los datos de $pCO_{2\ océano}$, lo que sugiere la realización de un monitoreo más extenso. Por otro lado, los datos de $pCO_{2\ atmósfera}$ no suponen un gran problema, debido a la rápida mezcla zonal atmosférica. A través de distintas metodologías, previos estudios han reconstruido los campos de $pCO_{2\ océano}$ a escala mensual para luego estimar cambios en los flujos de CO_2 océano-atmósfera que han ocurrido durante los últimos años a través de la ecuación presentada anteriormente. En general, existe cierto consenso en los resultados encontrados en los estudios basados en $pCO_{2\ océano}$, por ejemplo que el flujo de CO_2 de la atmósfera al océano ha incrementado debido al aumento de $pCO_{2\ atmósfera}$ producido por la quema de combustibles fósiles, el cambio de uso de suelo y la elaboración de cemento. No obstante, debido a la escasa cobertura espacio-temporal de los datos de $pCO_{2\ océano}$, los flujos estimados en estos estudios están basados en la interpolación sistemática de los datos de $pCO_{2\ océano}$ a través de distintas aproximaciones metodológicas, lo cual inherentemente genera una fuente de incerteza en las estimaciones (Fay y Mckinley 2013; Rödenbeck et al. 2013; Fay et al. 2014; Zeng et al. 2014; Gregor et al. 2019; Landschützer et al. 2020; Iida et al. 2020; Chau et al. 2020). De hecho, en el último informe del Panel Intergubernamental sobre el Cambio Climático (PICC; IPCC 2019), los cambios decadales del flujo de CO_2 océano-atmósfera estimado son catalogados como de confianza media. Por lo tanto, es indispensable utilizar nuevas aproximaciones metodológicas, no basadas en la

$pCO_{2\ océano}$, para trazar la variabilidad de los flujos de carbono océano-atmósfera y así alcanzar un consenso universal y/o de alta confianza. En este contexto, las diferencias de $\Delta^{14}C$ atmosférico entre registros subtropicales y australes del hemisferio sur trazan el efecto de las emisiones de CO_2 de origen oceánico. Considerando que el $\Delta^{14}C$ atmosférico no es sensible al flujo de carbono de la atmósfera al océano y si es sensible al flujo de carbono del océano a la atmósfera (Stuiver y Polach 1977), con el objetivo de trazar la variabilidad interanual del flujo de CO_2 del océano a la atmósfera en el océano austral, la presente tesis utilizó una metodología previamente descrita para trazar las emisiones de CO_2 producidas por la quema de combustibles fósiles en las megaciudades del hemisferio norte (Levin et al. 2003; Hou et al. 2020; Niu et al. 2021). De este modo, nuestra investigación utilizó al $\Delta^{14}C$ atmosférico como un novedoso trazador de la variabilidad interanual del flujo de CO_2 del océano a la atmósfera.

Las emisiones de CO_2 del océano austral trazadas con el $\Delta^{14}C$ atmosférico evidenciaron un constante flujo de CO_2 del océano hacia la atmósfera. Este resultado está en acuerdo con previos estudios de estimación del flujo de CO_2 océano-atmósfera basados en datos de *$pCO_{2\ océano}$* (Rödenbeck et al. 2013; Fay et al. 2014; Zeng et al. 2014; Gregor et al. 2019; Landschützer et al. 2020; Iida et al. 2020; Chau et al. 2020; Fay et al. 2021). Estas estimaciones del flujo de

CO_2 océano-atmósfera están basadas en distintas metodologías que abordan la reconstrucción de la pCO_2 sobre el océano: (i) Modelo biogeoquímico acoplado a un modelo atmosférico de inversión que considera la profundidad de la capa de mezcla superficial del océano y mediciones de $pCO_{2\ océano}$ (JENA-MLS: Rödenbeck et al. 2013), (ii) red neuronal de un paso que relaciona no-linealmente a las variables de temperatura superficial, salinidad superficial, latitud, longitud y clorofila-a superficial con mediciones de $pCO_{2\ océano}$ (NIES-FNN; Zeng et al. 2014), iii) red neuronal de dos pasos, uno para desarrollar la climatología y otro para desarrollar las anomalías de $pCO_{2\ océano}$, el cual relaciona no-linealmente a la temperatura superficial, salinidad superficial, latitud, longitud, profundidad de la capa de mezcla, nivel del mar y clorofila-a superficial con mediciones de $pCO_{2\ océano}$ (CMEMS-FFNN; Devin-sommer et al. 2019), iv) estimación de $pCO_{2\ océano}$ usando *machine lerning*, con el cual se divide al océano en provincias biogeoquímicas a través del método *k-means* y luego se utilizan cuatro modelos estadísticos para ajustar los valores proyectados de $pCO_{2\ océano}$ con valores de mediciones *in situ* de $pCO_{2\ océano}$ (CSIR-ML6; Gregor et al. 2019), (v) modelos de regresiones lineales múltiples que asocian a la temperatura superficial, salinidad superficial, latitud, longitud, profundidad de la capa de mezcla, nivel del mar y clorofila-a superficial con el carbono inorgánico disuelto y mediciones de $pCO_{2\ océano}$ (JMA-MLR; Iida et al. 2020), vi) red neuronal de dos pasos acoplado a una división del océano en

provincias biogeoquímicas para posteriormente relacionar diversas variables con mediciones de $pCO_{2\ océano}$ (MPI-SOMFFN; Landschützer et al. 2020).

Por otro lado, nuestra metodología al parecer sobreestima las emisiones de CO_2 del océano austral, lo cual podría deberse a las incertezas asociadas al grosor de la capa límite atmosférica marítima. Esta aparente sobreestimación también podría deberse a una subestimación de los flujos de CO_2 de los estudios comparados. Esta posible subestimación podría explicarse por la naturaleza del parámetro *kw* (velocidad de transferencia del CO_2), el cual depende no linealmente de la velocidad del viento ($kw = U^2 * (Sc/660)^{exp\ -0.5}$; U = velocidad del viento; Wanninkhof 2014), por lo que un promedio mensual de viento enmascara los extremos de la velocidad del viento que ocurren a escala de horas y días afectando directamente al parámetro *kw* (Wanninkhof 2014). Del mismo modo, *kw* probablemente no represente correctamente la velocidad de transferencia del CO_2 en el océano austral debido a que es un parámetro que funciona correctamente entre un rango de velocidad del viento de 3-15 m s^{-1}, y es conocido que en el océano austral los vientos pueden alcanzar velocidades muy superiores (Wanninkhof 2014). Además, encontramos que las emisiones de CO_2 oceánico trazadas con el $\Delta^{14}C$ atmosférico tuvieron una notable variabilidad interanual y ausencia de variabilidad decadal. Esta gran variabilidad interanual es observada sólo en la mitad de los estudios-

comparados de modelación del flujo de CO_2 océano-atmosférico basados en $pCO_{2\ océano}$ (JENA-MLS, JMA-MLR, MPI-SOMFFN). Por otro lado, la aparente ausencia de variabilidad decadal en nuestra estimación está en acuerdo con algunos de los flujos estimados de CO_2 basados en la $pCO_{2\ océano}$ (JMA-MLR, JENA-MLS, CMEMS-FFN, NIES-FNN). Las emisiones de CO_2 del océano austral estimadas muestran la ocurrencia de niveles cercanos a cero durante algunos años, sugiriendo que el océano austral sólo actuó como sumidero de CO_2 durante esos años. Es importante mencionar que en las estimaciones del flujo de CO_2 oceánico basadas en $pCO_{2\ océano}$ no se observaron valores cercanos a cero ni tampoco una gran variabilidad interanual (Rödenbeck et al. 2013; Fay et al. 2014; Zeng et al. 2014; Gregor et al. 2019; Landschützer et al., 2020; Iida et al., 2020; Chau et al., 2020; Fay et al., 2021). Éste contraste sugiere una posible subestimación de estos estudios de la variabilidad interanual del flujo de CO_2 océano-atmósfera, la cual podría estar relacionada a la metodología aplicada en estos estudios con interpolaciones y suavizamientos sistemáticos a través de la latitud, la longitud y el tiempo, o una posible sobrestimación de la variabilidad interanual debido a la variabilidad de la circulación atmosférica, la cual afecta directamente a las concentraciones de $\Delta^{14}C$ atmosférico. En este sentido, para reducir las incertezas asociadas al $\Delta^{14}C$ atmosférico es necesario incorporar más registros, de distintas regiones del hemisferio sur, a nuestra estimación. Finalmente, es importante mencionar que

a pesar de que todas estas estimaciones del flujo de CO_2 océano-atmósfera basadas en *$pCO_{2\ océano}$* se obtuvieron en base a la misma fuente de datos de mediciones *in situ* de *$pCO_{2\ océano}$* (Surface Ocean Carbon Dioxide Atlas; SOCAT; Bakker at al. 2016), el conjunto de estimaciones presenta notables diferencias entre sí, principalmente a escala anual y decadal. Por lo tanto, ya que nuestra estimación se basa en una variable distinta ($\Delta^{14}C$ atmosférico) a la comúnmente utilizada (pCO_2), consideramos que los resultados de la presente tesis brindan un avance significativo al estado del conocimiento de la variabilidad temporal del flujo del carbono en el océano austral, siendo una herramienta fundamental para llegar consensos y certezas respecto a cambios en los flujos de CO_2 entre el océano y la atmósfera (PICC).

Por último, nuestra estimación de las emisiones de CO_2 del océano austral basadas en las concentraciones de $\Delta^{14}C$ atmosférico revelaron una tendencia negativa, la cual ha ocurrido durante las últimas décadas. Esta tendencia negativa también es observada en los estudios del flujo de CO_2 oceánico basado en *$pCO_{2\ océano}$* (Rödenbeck et al. 2013; Fay et al. 2014; Zeng et al. 2014; Gregor et al. 2019; Landschützer et al. 2020; Iida et al., 2020; Chau et al. 2020; Fay et al. 2021). De acuerdo al PICC, esta tendencia negativa está ocurriendo debido al aumento de CO_2 en la atmósfera ocasionado por la quema de combustibles fósiles y el cambio de uso de suelos (IPCC 2019; Le Quere et al.

2018). El incremento de CO_2 atmosférico aumenta la pCO_2 de la atmósfera, lo que facilita el flujo de CO_2 de la atmósfera al océano (Garbe et al. 2014; Wanninkhof 2014). De hecho, varios modelos acoplados proyectan, para un escenario RCP8.5 (elevadas emisiones de CO_2 antropogénico), que cerca del año 2100 la toma de CO_2 atmosférico en el océano austral alcanzará los 2.38 Pg C $año^{-1}$, lo cual es aproximadamente 2.5 veces más que el secuestro de CO_2 atmosférico actual (0.91 Pg C $año^{-1}$). Por lo tanto, el patrón observado en nuestra investigación apoya la ocurrencia de esta tendencia negativa (disminución del flujo de CO_2 del océano a la atmósfera), sugiriendo que el flujo de CO_2 océano-atmósfera va a ser unidireccional debido al posible nulo flujo de CO_2 del océano a la atmósfera.

6 CONCLUSIONES

1) El conocimiento actual respecto a los valores de $\Delta^{14}C$ atmosférico en el hemisferio sur, corresponde parcialmente al observado en los niveles de $\Delta^{14}C$ atmosférico frente al océano Pacífico Sudoriental. Encontramos que los niveles de $\Delta^{14}C$ atmosférico sobre el océano Pacífico Sudoriental siguen un marcado gradiente latitudinal positivo de norte a sur, debido al efecto del océano austral sobre el $\Delta^{14}C$ atmosférico. No obstante, es posible encontrar excepciones a este gradiente debido al efecto del transporte y mezcla de parcelas de aire y de los distintos reservorios que intercambian carbono con la atmósfera. Por lo tanto, nuestra hipótesis I está parcialmente aprobada.

2) Los principales mecanismos que afectan la variabilidad del $\Delta^{14}C$ atmosférico frente al océano Pacífico Sudoriental durante el periodo bomba y post-bomba son: la detonación de armas termonucleares en el hemisferio norte y sus respectivos pulsos anuales en el hemisferio sur, el intercambio de carbono entre reservorios y el transporte y mezcla de parcelas de aire. Debido a la gran magnitud del $\Delta^{14}C$ atmosférico durante

el periodo bomba y post-bomba, la generación natural de ^{14}C en la estratósfera no afecta significativamente la variabilidad interanual del $\Delta^{14}C$ atmosférico frente al océano Pacífico sudoriental. Del mismo modo, debido a que gran parte de la quema de combustibles fósiles ocurre en el hemisferio norte, el efecto de este mecanismo es secundario en comparación a los pulsos anuales de ^{14}C bomba, el intercambio de carbono entre reservorios y el transporte y mezcla de parcelas de aire. Por lo tanto, se aprueba parcialmente la hipótesis II.

3) Debido a los fuertes cambios de *isoflux* de los reservorios de carbono y su impacto sobre la variabilidad interanual del $\Delta^{14}C$ atmosférico frente al océano Pacífico Sudoriental (la cual no es lineal), observados durante el periodo bomba, no encontramos una relación entre la variabilidad del $\Delta^{14}C$ atmosférico en las costas chilenas con las oscilaciones climáticas presentes en el océano Pacífico Sudoriental. De hecho encontramos que el incremento de la presión parcial de CO_2 atmosférico debido a la quema de combustibles fósiles ha producido un decrecimiento sostenido de las emisiones de CO_2 del océano austral, lo cual es contrario al efecto sobre el flujo de CO_2 océano-atmósfera del incremento de la presión

parcial de CO_2 oceánico producido por la reciente tendencia positiva del MAS. Por lo tanto, rechazamos nuestra hipótesis III.

7 SIGNIFICANCIA Y TRABAJO FUTURO

La presente investigación forma parte del primer esfuerzo científico interdisciplinario de determinación y estudio de las concentraciones de $\Delta^{14}C$ atmosférico en el margen Sudoriental delOcéano Pacífico, con el fin de describir y evaluar procesos de circulación atmosférica de gran escala y flujos de CO_2 entre el océano y la atmósfera. De este modo, además de mejorar significativamente las curvas de calibración para datar la materia orgánica en el hemisferio sur, se estudiaron y determinaron los principales mecanismos que modulan las concentraciones de $\Delta^{14}C$ atmosférico en las costas de Sudamérica occidental. Nuestra investigación reveló el potencial de los niveles de $\Delta^{14}C$ atmosférico registrados en los anillos de árboles para trazar distintas dinámicas y mecanismos naturales como por ejemplo el tiempo de residencia del carbono en la biósfera Amazónica, el transporte y mezcla de parcelas de aire, las emisiones de CO_2 del océano austral, entre otros. Profundizar en estos hallazgos es fundamental para entender, proyectar y alcanzar un consenso sobre los cambios presentes y futuros del sistema climático terrestre.

Considerando los hallazgos de la presente investigación en lo que respecta al $\Delta^{14}C$ atmosférico, aún existen muchas preguntas por responder

como por ejemplo: i) ¿Es posible trazar las emisiones de CO_2 de las principales ciudades de Sudamérica utilizando registros de los niveles de $\Delta^{14}C$ atmosférico?, ii) ¿A qué mecanismos se deben las pequeñas variaciones zonales de los niveles de $\Delta^{14}C$ atmosférico en el hemisferio sur?, iii) ¿Por qué las emisiones de CO_2 del océano austral trazadas con radiocarbono presentan, al parecer, una sobre estimación de las emisiones?, iv) ¿Es posible trazar el tiempo de residencia del carbono en la biósfera Amazónica utilizando registros de $\Delta^{14}C$ atmosférico?, v) ¿Cuáles son los niveles de $\Delta^{14}C$ atmosférico en Sudáfrica y si serían similares a Sudamérica?.

Responder éstas interrogantes y continuar investigando los hallazgos asociados a esta tesis ayudaría a contextualizar importantes problemas y amenazas para la humanidad, considerando que el océano es el principal sumidero de CO_2 antropogénico, o que los niveles de ^{14}C pueden trazar eventos de eyección de masa coronal solar capaces de inhabilitar nuestros sistemas de telecomunicaciones. Entender y determinar la variabilidad y ocurrencia de estos mecanismos y eventos hacia el pasado, presente y futuro es fundamental para proyectar nuestro futuro en éste planeta.

8 REFERENCIAS

Ancapichún S., De Pol-Holz R., Christie D., Santos, G., Collado-Fabbri, S., Garreaud, R., et al. 2021. Radiocarbon bomb-peak signal in tree rings from the tropical Andes register low latitude atmospheric dynamics in the Southern Hemisphere. Science of the Total Environment 774 (2021) 145126. doi:10.1016/j.scitotenv.2021.145126.

Ancapichún, S. and Garcés-Vargas. 2015. Variability of the Southeast Pacific Subtropical Anticyclone and its impact on sea surface temperature off north-central Chile. Ciencias Marinas 41(1): 1–20. doi:10.7773/cm.v41i1.2338.

Bakker, D., Pfeil, B., Land, C., Metzl, N., O'Brien, K., Olsen, A., et al. 2016. A multi-decade record of high-quality fCO2 data in version 3 of the Sourface Ocean CO2 Atlas (SOCAT). Earth System Science Data 8: 383-413. doi:10.5194/essd-8-383-2016.

Braziunas, T., I. Fung, and M. Stuiver. 1995. The Preindustrial atmospheric $^{14}CO_2$ latitudinal gradient as related to exchanges among atmospheric, ocean & terrestrial reservoirs. Global Biogeochemical cycles 9: 565-584.doi:10.1029/95GB01725.

Chau, T., Gehlen, M., and F. Chevallier. 2021. Global Ocean Surface Carbon Product MULTIOBS_ GLO_BIO_CARBON_SURFACE_REP_015_008, E.U. Copernicus Marine Service Information, available at: https://resources.marine.copernicus.eu/documents/PUM/CMEMS-MOB-PUM-015-008.pdf, last access: 11 January 2021.

Damon, P., S. Cheng, and T. Linick. 1989. Fine and hyperfine structure in the spectrum of secular variations of atmospheric $\Delta^{14}C$. Radiocarbon 31(3): 704-718. doi: 10.1017/S0033822200012303.

DeVries, T., Holzer, M., and F. Primeau. 2017. Recent increase in oceanic carbon uptake driven by weaker upperocean overturning. Nature 542: 215–218. doi:10.1038/nature21068.

Draxler, R., and D. Taylor. 1982. Horizontal dispersion parameters for long-range transport modeling. Journal of Applied Meteorology and Climatology. 21: 367-372. doi: 10.1175/1520-0450(1982)021<0367:HDPFLR>2.0.CO;2.

Draxler, R., and J. Stunder. 1988. Modeling the CAPTEX vertical tracer concentration profiles. Journal of Applied Meteorology and Climatology 27: 617-625. doi: 10.1175/1520-0450(1988)027<0617:MTCVTC>2.0.CO;2.

Draxler, R., and G. Hess. 1998. An Overview of the HYSPLIT_4 modeling system for trajectories, dispersión, and deposition. Australian Meteorological Magazine. 47: 295-308.

DeVries, T., Holzer, M., and F. Primeau. 2017. Recent increase in oceanic carbon uptake driven by weaker upperocean overturning. Nature 542: 215–218. doi:10.1038/nature21068.

Enting, I. 1982. Nuclear weapons data for use in carbon cycle modeling, Melbourne (Australia), CSIRO Division of atmospheric physics and technology.

Fay, A.., and G. McKinley. 2013. Global trends in surface ocean *p*CO2 from in situ data. Global Biogeochem. Cycles 27: 541–557. doi:10.1002/gbc.20051.

Fay, A., McKinley, G., and N. Lovenduski. 2014. Southern Ocean carbon trends: Sensitivity to methods. Geophysical Research Letter *41*: 6833–6840. doi:10.1002/2014GL061324.

Fay, A., Gregor, L., Landschützer, P., McKinley, G., Gruber, N., Gehlen, M., et al. 2021. Harmonization of global surface ocean pCO2 mapped products and their flux calculations; an improved estimate of the ocean carbon sink. Earth system science data**.** doi:10.5194/essd-2021-16.

Feely, R., R. Wanninkhof, T. Takahashi, and P. Tans. 1999. The influence of the equatorial Pacific contribution to atmospheric CO_2 accumulation. Nature 398: 597-601. doi: 10.1038/19273.

Fletcher, R. 1945. The general circulation of the tropical and equatorial atmosphere. *Journal of meteorology*, 2(3), 167-174. doi:10.1175/1520-0469(1945)002<0167:TGCOTT>2.0.CO;2.

Friend, A., Lucht, W., Rademacher, T., Keribin, R., Betts, R., Cadule, P., Ciais, P., et al. 2013. Carbon residence time dominates uncertainty in terrestrial vegetation responses to future climate and atmospheric CO_2. PNAS. doi:10.1073/pnas.1222477110

Garbe, C., Rutgersson, A., Boutin, J., Leeuw, G., Delille, B., Fairall, C., et al. 2014. Transfer across the air-sea interface, in: Ocean-Atmosphere Interactions of Gases and Particles, edited by: Liss, P. S. and Johnson, M. T., Springer, Berlin, Heidelberg, 55–112, 2014.

Garreaud R., Vuille, M., and C. Amy. 2003. The climate of the Altiplano: observed current conditions and mechanisms of past changes. Palaeogeography, Palaeoclimatology, Palaeoecology 194: 5-22. doi:10.1016/S0031-0182(03)00269-4.

Garreaud, R., Vuille, M., Compagnucci, R., and J. Marengo. 2009. Present-day South American climate. Palaeogeography, Palaeoclimatology, Palaeoecology 281: 180-195. doi:10.1016/j.palaeo.2007.10.032.

Graven, H. D., T. P. Guilderson, and R. F. Keeling. 2012. Observations of radiocarbon in CO_2 at seven global sampling sites in the Scripps flask network: Analysis of spatial gradients and seasonal cycles. Journal of Geophysical Research: Atmospheres 117. doi: 10.1029/2011JD016533.

Gregor, L., Lebehot, A., Kok, S., and P. Scheel Monteiro. 2019. A comparative assessment of the uncertainties of global surface ocean CO2 estimates using a machine-learning ensemble (CSIR-ML6 version 2019a) – have we hit the wall*?.* Geoscience Model Develop. 12: 5113–5136. doi:10.5194/gmd-12-5113-2019.

Heimann, M., and E. Maier-Reimer. 1996. On the relations between the oceanic uptake of CO_2 and its carbon isotopes. Global Biogeochemical Cycle.10: 89-110. doi:10.1029/95GB031.

Hesshaimer, V., and I. Levin. 2000. Revision of the stratospheric bomb $^{14}CO_2$ inventory. Journal of Geophysical Research 105(D9): 11641-11658. doi:10.1029/1999JD901134.

Hogg AG, Heaton TJ, Hua Q, Palmer JG, Turney CSM, Southon J, Bayliss A, Blackwell PG, et al. 2013. SHCal20 Southern Hemisphere calibration, 0-55,000 years cal BP. Radiocarbon 62. doi: 10.1017/RDC.2020.59.

Hou, Y., W. Zhour, P. Cheng, X. Xiong, H. Du, Z. Niu, X. Yu, Y. Fu, and X. Lu. 2020. ^{14}C-AMS measurements in modern tree rings to trace local fossil fuel-derived CO_2 in the greater Xi'an area, China. *Science of the total Environment* 715:136669. doi:10.1016/j.scitotenv.2020.136669.

Hua, Q., M. Barbetti, U. Zoppi, D. Fink, M. Watanasak, and G-E. Jacobsen. 2004. Radiocarbon in tropical tree rings during the Little Ice Age*.* Nuclear Instruments and Methods in physics research 223-224: 489-494. doi:10.1016/j.nimb.2004.04.092.

Hua, Q., and M. Barbetti. 2007. Influence of atmospheric circulation on regional $^{14}CO_2$ differences. Journal Geophysical Research 112: D19102. doi:10.1029/2006JD007898.

Hua, Q., M. Barbetti, V. Levchenko, D. Arrigo, B. Buckley, and A. Smith. 2012. Monsoonal influences on Southern Hemisphere $^{14}CO_2$. Geophysical Research Letter 39: L19806. doi:10.1029/2012GL052971.

Hua, Q., M. Barbetti, and A. Rakowski. 2013. Atmospheric Radiocarbon for the period 1950-2010. Radiocarbon 55(4): 2059-2072. doi:10.2458/azu_js_rc.v55i2.16177.

Hua, Q., J., Turnbull, G., Santos, A., Rakowski, S., Ancapichún, et al. 2021. Atmospheric radiocarbon for the period 1950-2019. Radiocarbon: 1-23. doi:10.1017/RDC.2021.95.

Hughen, K., S. Lehman, J. Southon, J. Overpeck, O. Marchal, C. Herring, and J. Turnbull. 2004. ^{14}C Activity and global carbon cycle changes over the past 50.000 years. Science 303: 202-207. doi:10.1126/science.1090300.

Iida, Y., Takatani, Y., Kojima, A. and Ishii, M. 2020. Global trends of ocean CO2 sink and ocean acidification: an observation based reconstruction of surface ocean inorganic carbon variables. Journal of Oceanography pp.1-36. doi:10.1007/s10872-020-00571-5, 2020.

IPCC. 2019. The Ocean and cryosphere in a changing climate. A special report of the intergovernmental panel on climate change.

Kalnay, E., M. Kanamitsu, R. Kistler, W. Collins, D. Deaven, L. Gandin, M. Iredell, S. Saha, G. White, J. Woollen, Y. Zhu, M. Chelliah, W. Ebisuzaki, W. Higgins, J. Janowiak, K-C. Mo, C. Ropelewski, J. Wang, A. Leetmaa, R. Reynolds, R. Jenne, and D. Joseph. 1996. The NCEP/NCAR 40-Year Reanalysis Project. Bulletin of the American Meteorological Society. 77(3): 437-471. doi:10.1175/1520-0477(1996)077<0437:TNYRP>2.0.CO;2.

Key, R., a. Kozyr, C. Sabine, K. Lee, R. Wanninkhof, J. Bullister, R. Feely, F. Millero, C. Mordy, and T. Peng. 2004. A global ocean carbon climatology: results from global data analysis project (GLODAP). Global Biogeochemical Cyc*cles* 18(4): GB4031. doi:10.1029/2004GB002247.

Kromer, B., W. Manning, P-I. Kuniholm, W. Newton, M. Spurk, and I. Levin. 2001. Regional $^{14}CO_2$ offsets in the troposphere: Magnitude, Mechanism, and Consequences. Science 294: 2529-2532. doi:10.1126/science.1066114.

Landschützer, P., Gruber, N., Bakker, D., Schuster, U., Nakaoka, S., Payne, M., et al. 2013. A neural network-based estimate of the seasonal to inter-annual variability of the Atlantic Ocean carbon sink. Biogeosciences 10, 7793–7815. doi:10.5194/bg-10-7793-2013.

Landschützer, P., Gruber, N., and D. Bakker. 2020. An observation-based global monthly gridded sea surface pCO2 product from 1982 onward and its monthly climatology (NCEI Accession 0160558). Version 5.5. NOAA National Centers for Environmental Information. https://www.ncei.noaa.gov/access/ocean-carbon-data system/oceans/SPCO2_1982_present_ETH_SOM_FFN.html. Dataset. https://doi.org/10.7289/V5Z899N6.

Lal, D., and Rama. 1966. Charasteristics of global tropospheric mixing based on Man-Made C^{14} and Sr^{90}. Geophysical Research 71(12): 2865-2874. doi:10.1029/JZ071i012p02865.

Lara, A., and R. Villalba. 1993. A 3620-year temperature record from *Fitzroya cupressoidess* tree rings in southern South America. Science 260: 1104-1106. doi: 10.1126/science.260.5111.1104.

Le Quéré, C., Rödenbeck, C., Buitenhuis, E., Conway, T., Langenfelds, R., Gomez, A., et al. 2007. Saturation of the Southern Ocean CO2 Sink Due to Recent Climate Change. Science 316, 1735 (2007). doi:10.1126/science.1136188.

Le Quéré, C. 2018. Decadal trends and variability in the Southern Ocean sink of CO_2. EGU general assembly conference abstracts.

Levin, I., Kromer, B., Schmidt, M., and H. Sartorius. 2003. A novel approach for independent budgeting of fossil fuel CO_2 over Europe by $^{14}CO_2$ observation. Geophysical Research Letters 30(23), 2194. doi:10.1029/2003GL018477.

Levin, I., T. Naegler, B. Kromer, M. Diehl, R.J. Francey, A.J. Gomez-Pelaez, L.P. Steele, D. Wagenbach, R. Weller, and D.E. Worthy. 2009. Observations and modeling of the global distribution and long-term trend of atmospheric $^{14}CO_2$. Tellus 62(1): 26-46. doi:10.1111/j.1600-0889.2009.00446.x.

Libby, W.F. 1952. Radiocarbon dating, 2nd ed. The Chicago: University of Chicago Press.

Manning, M., Lowe, D., Melhuish, W., Sparks, R., Wallace, G., Brenninkmeijer, C., and R. Mcgil. 1990. The use of radiocarbon measurements in atmospheric studies. Radiocarbon 32, 37-58. doi:10.1017/S0033822200039941.

Manning, W., M. Barbetti, B. Kromer, I. Kuniholm, I. Levin, W. Newton, and J. Reimer. 2002. No systematic early bias to Mediterranean C-14 ages:

Radiocarbon measurements from tree-ring and air samples provide tight limits to age offsets. Radiocarbon 44: 739-754. doi:10.1017/S0033822200032197.

Marland, G., T. Boden, and R. Andres. 2008. Global, regional and National CO2 emissions. In: Trends: a Compendium of data on global change. Carbon Dioxide information Analysis center, Oak ridge national laboratory. http://cdiac.ornl.gov/trends/emis/tre_glob.html.

Marsh, E., Bruno, M., Fritz, S., Baker, P., Capriles, J., and Hastorf, C. 2018. IntCal, SHCal, or a Mixed Curve? Choosing a ^{14}C Calibration curve for archaeological and paleoenvironmental records from tropical South America. Radiocarbon vol 60, Issue 3, pp. 925-940. doi:10.1017/RDC.2018.16.

Marshall, G. J. 2003. Trends in the Southern Annular Mode from Observations and Reanalyses. Journal of Climate 16(24): 4134–4143. doi:10.1175/1520-0442(2003)016<4134:titsam>2.0.co;.

Masarik, J., and J. Beer. 1999. Simulation of particle fluxes and cosmogenic radionuclide formation in Earth's atmosphere. Journal Geophysical Research 104: 12099-13012. doi:10.1029/1998JD200091.

McCormac, F., A. Hogg, T. Higham, J. Lynch-Stieglitz, W. Broecker, N. Baillie, J. Palmer, L. Xiong, J. Pilcher, D. Brown, and S. Hoper. 1998. Temporal variation in the interhemispheric ^{14}C offset. Geophysical Research Letters 25: 1321-1324. doi:10.1029/98GL01065.

McCormac, G., G. Hogg, G. Blackwell, E. Buck, G. Higham, and J. Reimer. 2004. ShHcal04 Southern hemisphere calibration, 0-11.0 cal Kyr BP. Radiocarbon 46(3): 1087-1092. doi:10.1017/S003382220003301.

Morales, M.S., Cook, E.R., Barichivich, J., Christie, D.A., Villalba, R., LeQuesne, C., Srur, A.M., Ferrero, M.E., González-Reyes, A., Couvreux, F., Matovsky, V., Aravena, J.C., Lara, A., Mundo, I.A., Rojas, F., Prieto, M.R., Smerdon, J.E., Bianchi, L.O., Masiokas, M.H., Urrutia, R., Rodriguez-Catón, M., Muñoz, A.A., Rojas-Badilla, M., Alvarez, C., Lopez, L., Luckman, B., Lister, D., Harris, I., Jones, P.D., Williams, A.P., Velazquez, G., Aliste, D., Aguilera-Betti, I., Marcotti, E., Flores, F., Muñoz, T., Cuq, E. and J.A. Boninsegna. 2020. Six hundred years of South American tree rings reveal an increase in severe hydroclimatic events since mid-20th century. Proceedings of the National Academy of Sciences. doi:10.1073/pnas.2002411117.

Munro, D., Lovenduski, N., Takahashi, T., Stephens, B., Newberger, T., and C. Sweeney. 2015. Recent evidence for a strengthening CO_2 sink in the Southern Ocean from carbonate system measurements in the Drake Passage

(2002–2015). Geophysical Research Letter 42: 7623–7630. doi:10.1002/2015gl065194.

Naegler, T., & I. Levin. 2009. Observation-based global biospheric excess radiocarbon inventory 1963-2005. Journal of Geophysical research 114: D17302. doi:10.1029/2008JD011116.

Niu, Z., Feng, X., Zhour, W., Wang, P., Liu, Y., Lu, X., Du, H., et al. 2021. Tree-ring $\Delta^{14}C$ time series from 1948 to 2018 at a regional background site, China: Influences of atmospheric nuclear weapons tests and fossil fuel emissions. Atmospheric Environment 118156. doi:10.1016/j.atmosenv.2020.118156.

Nydal, R. 1968. Further investigation on the transfer of radiocarbon in nature. Journal of geophysical research 73: 3617-35. doi:10.1029/JB073i012p03617.

Nydal, R., and Lövseth, K. 1965. Distribution of radiocarbon from nuclear tests. *Nature,* 206, 1029-1031. doi:10.1038/2061029a0.

Olsen, A., et al. 2020. An updated version of the global interior ocean biogeochemical data product, GLODAPv2.2020. Earth System Science Data 12: 3653–3678. doi:10.5194/essd-12-3653-2020.

Randerson, J., I. Enting, E. Schuur, K. Caldeira, and I. Fung. 2002. Seasonal and latitudinal variability of troposphere $\Delta^{14}CO_2$: Post bomb contributions from fossil fuels, oceans, the stratosphere, and the terrestrial biosphere. Global Biochemical Cycles 16(4). doi:10.1029/2002GB001876.

Reimer, J., G. Baillie, E. Bards, A. Bayliss, W. Beck, J. Bertrand, G. Blackwell, E. Buck, S. Burr, B. Cutler, E. Damon, R. Edwards, G. Fairbanks, M. Friedrich, P. Guilderson, G. Hogg, A. Hughen, B. Kromer, G. McCormac, S. Manning, B. Ramsey, W. Reimer, S. Remmele, R. Southon, M. Stuiver, S. Talamo, F. Taylor, J. Van der Plicht, and E. Weyhenmeyer. 2004. INTcal04 Terrestrial radiocarbon age calibration, 0-26 cal Kyr BP. Radiocarbon 46(3): 1029-1058. doi:10.1017/S0033822200032999.

Reimer P, Austin WEN, Bard E, Bayliss A, Blackwell PG, Bronk Ramsey C, Butzin M, Cheng H, et al. 2020. The IntCal20 Northern Hemisphere radiocarbon age calibration curve (0-55 cal kBP). Radiocarbon 62. doi:10.1017/RDC.2020.41.

Rödenbeck, C., Keeling, R., Bakker, D., Metzl, N., Olsen, A., Sabine, C., and M. Heimann. 2013. Global surface-ocean pCO2 and sea–air CO2 flux

variability from an observation-driven ocean mixed-layer scheme. Ocean Science 9: 193–216. doi:10.5194/os-9-193-2013, 2013.

Rödenbeck, C., Bakker, D., Metzl, N., Olsen, A., Sabine, C., Cassar, N., et al. 2014. Interannual sea–air CO_2 flux variability from an observation-driven ocean mixed-layer scheme. Biogeosciences 11: 4599–4613. doi:10.5194/bg-11-4599-2014.

Rodgers, K., S. Mikaloff-Fletcher, D. Bianchi, C. Beautien, E. Galbraith, A. Gnanadesikan, A. Hogg, D. Iudicone, B. Lintner, T. Naegler, P. Reimer, J. Sarmiento, and R. Slatter. 2011. Interhemispheric gradient of atmospheric radiocarbon reveals natural variability of Southern Ocean winds. Climate of the past 7: 1123-1138. doi:10.5194/cp-7-1123-2011.

Santos, G., Linares, R., Lisi, C., and M. Tomazello. 2015. Annual growth rings in a simple of Pananá pine (*Araucaria angustifolia*): Toward improving the ^{14}C calibration curve for the Southern Hemisphere. Quaternary Geochronology 25: 96-103. doi:10.1016/j.quageo.2014.10.004.

Schimel, D., J. House, K. Hibbard, P. Bousquet, P. Ciais, P. Peylin, B. Braswell, Apps M., Baker D., Bondeau A., Canadell J., Churkina G., Cramer W., Denning A., Field C., Friedlingstein P., Goodale C., Heimann M., Houghton R., Melillo J., Moore B., Murdiyarso D., Noble I., Pacala S., Prentice I., Raupach M., Rayner P., Scholes R., W. Steffen, and C. Wirth. 2001. Recent patterns and mechanisms of carbon exchange by terrestial ecosystems. Nature 414: 169-172. doi:10.1038/35102500.

Schuur, E., et al. 2016. Radiocarbon and Climate change: Mechanism, Applications and laboratory techniques, Book.

Segura, H., Espinoza, J., Junquas, C., Lebel, T., Vuille, M., and R. Garreaud. 2020. Recent changes in the precipitation-driving processes over the southern tropical Andes/western Amazon. Climate Dynamics. doi:10.1007/s00382-020-05132-6.

Siegenthaler, U., Heimann, M., and H. Oeschger. 1980. ^{14}C Variations caused by changes in the global carbon cycle. Radiocarbon 22: 177–191. doi:10.1017/S0033822200009449.

Stein, A., et al. 2015. NOAA's HYSPLIT atmospheric transport and dispersion modeling system. Bulletin of the american Meteorological society 96: 2059-2077. doi:10.1175/BAMS-D-14-00110.1.

Stuiver, M., and H. Polach. 1977. Discussion: Reporting of ^{14}C Data. Radiocarbon 19(3): 355-363. doi:10.1017/S0033822200003672.

Stuiver, M. and P. D. Quay. 1980. Changes in Atmospheric Carbon-14 attributed to a variable sun. Science 207, 4426: 11–19. doi:10.1126/science.207.4426.11.

Stuiver, M., and P. Quay. 1981. Atmospheric $\Delta^{14}C$ changes resulting from fossil fuel CO_2 release and cosmic ray flux variability. Earth And Planetary Science Letters 53(3): 349-362. doi:10.1016/0012-821X(81)90040-6.

Stuiver, M., T. Braziunas, B. Becker and B. Kromer. 1991. Climatic, solar, oceanic and geomagnetic influences on late-glacial and Holocene atmospheric 14C/12C change. Quaternary Research 35: 1-24. doi:10.1016/0033-5894(91)90091-I.

Stuiver, M., and T. Braziunas. 1993. Sun, ocean, climate and atmospheric $^{14}CO_2$: An evaluation of causal and spectral relationships. The Holocene 3: 289-305. doi:10.1177/095968369300300401.

Stuiver, M., and T. Braziunas. 1998. Anthropogenic and solar components of hemispheric$\Delta^{14}C$. Geophysical research letters 25(3): 329-332. doi:10.1029/97GL03694.

Suess H. 1955. Radiocarbon concentration in modern wood. Science. 122: 415-417. doi:10.1126/science.122.3166.415.b.

Thompson, D. W. J., Solomon, S., Kushner, P. J., England, M. H., Grise, K. M., and D. J. Karoly. 2011. Signatures of the Antarctic ozone hole in Southern Hemisphere surface climate change. Nature Geoscience 4(11), 741–749. doi:10.1038/ngeo1296.

Turnbull, J.C., P.J. Rayner, J.B. Miller, T. Naegler, P. Ciais, and A. Cozic. 2009. On the use of $^{14}CO_2$ as a tracer for fossil fuel CO2: Quantifying uncertainties using an atmospheric transport model. Journal of Geophysical Research. 114: D22302. doi:10.1029/2009JD012308.

Turnbull, J., Mikaloff, S., Ansell, I., Brailsford, G., Moss, R., Norris, M., et al. 2017. Sixty years of radiocarbon dioxide measurements at Wellington, New Zealand: 1954-2014. Atmospheric Chemistry and Physics 17: 14771-14784. doi:10.5194/acp-17-14771-2017.

Turney, C. S. M., and J. G. Palmer. 2007. Does the El Niño–Southern Oscillation control the interhemispheric radiocarbon offset?. Quaternary Research 67(01): 174–180. doi:10.1016/j.yqres.2006.08.008.

Turney, C., Palmer, J., Maslin, M., Hogg, A., Fogwill, C., Southon, J., et al. 2018. Global Peak in Atmospheric Radiocarbon Provides a Potential Definition

for the Onset of the Anthropocene Epoch in 1965. Scientific Reports 8: 1. doi:10.1038/s41598-018-20970-5.

Vuille, M., Bradley, R., F. and Keimig. 2000. Interannual climate variability in the Central Andes and its relation to tropical Pacific and Atlantic forcing. Journal of Geophysical Research 105: 12447-12460. doi:10.1029/2000JD900134.

Vuille, M., Burns, S., Taylor, B., Cruz, F., Bird, B., Abbott, M., et al. 2012. A review of the South American monsoon history as recorded in stable isotopic proxies over the past two millennia. Climate of the Past 8: 1309-1321. doi:10.5194/cp-8-1309-2012.

Wanninkhof, R. 2014. Relationship between wind speed and gas exchange over the ocean revisited. Limnology, Oceanography and Metheorology. 12: 351–362. doi:10.4319/lom.2014.12.351, 2014.

Weaver, A., Marotzke, J., Cummins, P., and E. Sarachik. 1993. Stability and Variability of the Thermohaline Circulation. Journal of Physical Oceanography 23(1): 39–60. doi:10.1175/1520-0485(1993)023<0039:savott>2.0.co.

Zeng, J., Nojiri, Y., Landschützer, P., Telszewski, M., and S. Nakaoka. 2014. A global surface ocean fCO2 climatology based on a feed-forward neural network. Journal of Atmospheric and Oceanic Technology 31: 1838–1849. doi:10.1175/JTECH-D-13-00137.1.